Factors Affecting the Uniaxial Compression Fatigue Performance of Structural Concrete

A dissertation submitted by

Mohsen Minaeijavid

In partial fulfillment of the requirements for the degree of

Doctor of Philosophy
in
Civil and Environmental Engineering

Tufts University

February 2025

Advisor:

Prof. Daniel Kuchma

Abstract

The design and assessment of reinforced concrete (RC) structures subjected to cyclic loading must consider concrete compression fatigue capacity which can control the design for some segments of towers and foundations that support wind turbines. Such structures endure high cyclic stresses due to wind, waves, and operational forces, which progressively degrade concrete's compressive capacity over time. This study involved an experimental investigation of factors affecting the compressive fatigue behavior of various types of concrete including traditional plain and reinforced concrete and 3D-printed concrete. The work also involved collecting and analyzing all publicly available fatigue data, comparing, and assessing existing fatigue models, and developing solutions for advancing fatigue research and the design of more cost-effective and durable towers and foundations that support wind turbines.

The experimental testing consisted of a series of force-controlled fatigue tests that examined the influence of critical factors such as aggregate size and shape, longitudinal reinforcement, load eccentricity, and saturation on the compressive fatigue behavior. Data collected from these experiments provided insights into strain evolution, stiffness degradation, and the appearance of cracks under cyclic loading. Amongst the findings, the tests revealed that the use of larger angular aggregates and saturation significantly reduce fatigue life, that longitudinal reinforcement greatly increases concrete fatigue capacity, and that 3D-printed concrete has greater fatigue capacity relative to normally cast concretes with the same compressive. These findings formed the foundation for developing customized models and testing protocols to improve the understanding and prediction of concrete fatigue performance.

The comparison and assessment of models involved a comprehensive evaluation of existing fatigue models against experimental results and the database of publicly available fatigue data.

The study revealed significant variability in fatigue life predictions across models, highlighting the inadequacy of one-size-fits-all approaches commonly used in design standards. This analysis identified critical gaps, such as insufficient reporting of experimental parameters and limited consideration of material-specific behaviors. The research proposed refined methods for developing S-N (stress-life) curves tailored to specific concrete properties to address these shortcomings.

This study's primary products and contributions were the measured fatigue behavior of large set of new experiments on concrete compressive fatigue that investigated the effect of previous untested or lightly tests effects, a comprehensive experimental database, and recommendations for standardized fatigue testing. The database provides new and existing fatigue test data within an Excel-based dashboard for analysis and visualization; this resource aids engineers and researchers in understanding key trends and variability in fatigue behavior. The study also produced a set of recommendations for standardized testing protocols and methods for developing customized fatigue models. These contributions enable the design of more cost-effective and durable wind turbine support structures, reducing material usage while enhancing safety and longevity. Additionally, the findings highlight the potential of emerging materials, such as 3DPC, for structural applications, fostering innovation in renewable energy infrastructure.

Dedication

To my beloved wife, Nasim, whose unwavering love, support, and sacrifices have been my greatest source of strength and inspiration throughout this journey. Your faith in me — even during the most challenging times — has been a constant reminder of why I chose this path. You have been my wonderful partner, and true friend in every sense, patiently enduring the long hours and countless challenges, and always encouraging me to push forward.

And to my little angel — soon to join this world — whose impending arrival fills my heart with hope, joy, and a renewed sense of purpose. Though you are not here yet, your presence in our lives is already a source of boundless motivation and dreams for a brighter future.

This work is as much yours as it is mine; it is a testament to the love and dreams we share as a family.

Acknowledgments

This research was made possible through the generous support of the U.S. Department of Energy's Office of Energy Efficiency and Renewable Energy (EERE), provided through the Wind Energy Technology Office under award number DE-EE0008961. I am deeply grateful for this funding which has enabled me to pursue and contribute to advancements in wind energy technology. This support has been instrumental in conducting the research and achieving the outcomes presented in this document.

I would also like to express my deepest gratitude to my advisor, Professor Daniel Kuchma, for his exceptional guidance, mentorship, and unwavering support throughout my PhD journey. His profound expertise, insightful feedback, and commitment to excellence have been invaluable in shaping the direction and quality of this research. Professor Kuchma's encouragement and patience — coupled with his ability to inspire critical thinking and innovation — have made this

challenging process rewarding. I am truly grateful for the opportunity to learn and grow under his supervision, and I will carry the lessons which he has imparted throughout my career.

Note of appreciation and recognition

I am deeply grateful to my lab mate, John DeFrancisci, whose dedication, and good sport made the challenges of my PhD journey much easier to navigate. John's assistance and camaraderie throughout my first campaign of experimental testing preparations were invaluable.

I also extend my heartfelt thanks to Guodong Feng, a Master's student, Nasim Partovi Mehr and Hooman Shirzadi, fellow PhD students, for their significant help and contributions during the experimental testing phase.

I am thankful to Monni Rahimi for her invaluable assistance in casting cylindrical specimens and slabs for testing, and to Lara Appleby for her editorial support during the final stage of this journey.

Special thanks to Morten Søgaard Andersen, from DNV, for his insightful consultations and constructive feedback, which significantly contributed to the success of this work.

Table of Contents

Abstract ... ii

Dedication ... iv

Acknowledgments ... iv

Note of appreciation and recognition ... v

List of Figures and Tables ... x

Nomenclature or List of Abbreviations ... xxi

1 Introduction ... 1

1.1 Motivations ... 1

1.1.1 Motivation: Concrete as an attractive alternative to steel for wind turbine support structures ... 1

1.1.2 Motivation: Modeling fatigue for design of support structures ... 2

1.2 Objectives: New data, models, understanding, and recommendations regarding design for concrete fatigue demands ... 5

1.3 Organization of the dissertation ... 6

2 Background (Literature Review) ... 10

2.1 Introduction to compressive fatigue behavior of concrete ... 10

2.1.1 Microcrack formation and propagation ... 10

2.1.2 The three phases of concrete fatigue ... 11

2.1.3 Fatigue Strength and Number of Cycles to Failure ... 12

2.1.4 Classifications of fatigue ... 13

2.1.5 Factors affecting concrete fatigue behavior ... 14

2.2 Introduction to concrete compressive fatigue models ... 24

2.2.1 Existing fatigue models for concrete ... 25

2.3 Factors influencing fatigue capacity of concrete ... 50

2.3.1 Variability in concrete strength and its impact on scatter of fatigue test results ... 51

2.3.2 Aggregate type and size effect ... 52

2.3.3 Specimen size effect ... 55

2.3.4 Saturation and presence of water ... 58

2.3.5 Loading frequency ... 61

2.3.6 Loading waveform ... 65

2.3.7 Other factors ... 66

2.4 Summary and conclusion ... 68

3 **Database for Experimental Data on Concrete Fatigue** 70
3.1 Introduction 70
3.2 List of references for experimental fatigue data 71
3.3 Initial exploration 73
3.3.1 Comparison of data with selected models (based on Smin) 73
3.3.2 Strength 76
3.3.3 Frequency 79
3.3.4 Specimen dimension ratio 80
3.3.5 Saturation level 82
3.3.6 Waveform 82
3.3.7 Summary 84
3.4 Concrete fatigue experimental database spreadsheet / dashboard 85
3.4.1 Introduction 85
3.4.2 How to use the fatigue data excel spreadsheet 93
3.4.3 Evaluation of the existing data, using the plots generated with the experimental database spreadsheet 103
3.4.4 Outliers in the data set 111
3.4.5 Statistical significance of loading frequency effect on fatigue life capacity 113
3.4.6 Linear and polynomial regression 125
3.5 Introduction to empirically-developed models and artificial neural network models . 128
3.5.1 Neural networks in concrete fatigue data sets 135
3.6 Summary and conclusions 138
4 Initial Compressive Uniaxial Fatigue Testing 139
4.1 Test setup and system for data acquisition 140
4.2 Monotonic and fatigue compressive test of plain concrete 142
4.2.1 Characteristics of the plain concrete testing batch 142
4.2.2 Loading protocol #1 (Smax, Smin)=(0.80, 0.05) 144
4.2.3 Loading Protocol #2 (Smax, Smin)=(0.70, 0.05) 146
4.2.4 Visual damage on the plain concrete under fatigue loading 148
4.3 Effect of longitudinal reinforcement on fatigue capacity 152
4.3.1 Assessing fatigue design life of structures made of steel and concrete 152
4.3.2 Behavior of reinforced concrete under monotonic and fatigue loading 154
4.3.3 Constant amplitude test (CAT) on reinforced concrete 163

4.3.4 Plain concrete vs. reinforced concrete 166
4.3.5 Discussion on the effect of reinforcement on fatigue capacity 167
4.4 Effect of saturation on fatigue capacity 174
4.5 Effect of load eccentricity on fatigue capacity 178
4.6 Variability in experimental test data and impact of f'c 179
4.6.1 Significance of concrete compressive strength in fatigue testing 180
4.6.2 Impact — on fatigue capacity — of assumed strength error 181
4.7 Conclusion 181
5 3D-Printed Concrete 184
5.1 Introduction 184
5.2 Research significance 186
5.3 Experimental investigation 186
5.3.1 Materials and specimens 186
5.4 Experimental results, analysis and discussion 191
5.4.1 Monotonic test results 191
5.4.2 Fatigue test results 191
5.5 Conclusions 208
6 Effect of Aggregate Size and Shape on Fatigue Behavior of Concrete 212
6.1 Primary fatigue experimental investigations 212
6.1.1 Riverstone concrete (with 3/8 in maximum aggregate size) 213
6.1.2 Crushed stone concrete (with 3/4 in maximum aggregate size) 215
6.1.3 Primary fatigue test results 217
6.2 Fabrication of specimens for final casting of various concrete batches 218
6.2.1 Aggregate sources and details 218
6.2.2 Selection of desired mix designs by casting trial batches 221
6.2.3 Final selected types of concrete 223
6.3 Experimental testing 226
6.3.1 Overview 226
6.3.2 Introduction 226
6.3.3 Mechanical properties and mix design of material 228
6.3.4 Improved method for estimating the strength 229
6.3.5 Results and discussion 230
6.3.6 Conclusions 249

7 Recommendations for Fatigue Testing 253
7.1 ACI Technote #4 - Recommended Practice for Compression Fatigue Testing of Concrete 253
7.1.1 Introduction 254
7.1.2 Methodology 256
7.1.3 Experimental Testing 261
7.1.4 Discussion and Results 263
7.1.5 Recommended Data Gathering Items 270
7.1.6 Conclusion 270
7.2 ACI Technote #5 - Recommended Procedure for Development of a S-N Curve for a Specific Concrete Mix 273
7.2.1 Overview 273
7.2.2 Introduction 273
7.2.3 Methodology 277
7.2.4 Experimental Testing Example 281
7.2.5 Discussion and Results 282
7.2.6 Probabilistic Approach 285
7.2.7 Conclusion 292
8 Summary of Findings and Recommendations for Future Research 294
8.1 Overview of dissertation objectives and scope 294
8.2 Findings from new experiments 297
8.2.1 Effect of longitudinal reinforcement 297
8.2.2 Effect of saturation 298
8.2.3 Effect of load eccentricity 299
8.2.4 Effect of aggregate size and shape 299
8.2.5 Lightweight aggregate concrete 300
8.2.6 Effect of variability in monotonic compressive strength 301
8.2.7 Performance of 3D-printed concrete 302
8.2.8 Appearance of visual cracks due to fatigue loading 303
8.3 Findings from analysis of the complete fatigue testing database 304
8.3.1 Insufficient reporting in the literature 305
8.3.2 Effect of loading frequency 306
8.3.3 Scatter in fatigue capacity 306

8.3.4 Variability in fatigue models 307
8.4 Recommendations for the advancement of fatigue testing and design practice 308
8.5 **Recommendations for future research** 309
8.5.1 Influence of complex states of stress 310
8.5.2 Assessment of impact — on stress demands — of softening due to fatigue 310
8.5.3 Structural joint test 311
8.5.4 Computed tomography investigation 311
9 References 313

List of Figures and Tables

Figure 1 Examples of different shapes of offshore wind support structures made of concrete. 4
Figure 2 The numerous cylinders casted for the final testing. 8
Figure 3 The strain evolution of concrete under cyclic loading [16]. 12
Figure 4 The Wöhler's curve in the σ-Nf diagram [16]. 13
Figure 5 Behavior of concrete subjected to fatigue under cyclic compression (3DPC) Left side; Stress-strain response of cylinder to monotonic compressive loading, along with a few cycles of hysteresis and peak and valley stress and strain development over the cycles. Right side; The strain evolution plot shows peak and valley strain increments over the cycles of loading up to failure. 15
Figure 6 Stiffness evolution plot, depicting the progressive development (degradation) of concrete fatigue secant stiffness as a function of an increasing number of fatigue loading cycles. [25] 21
Figure 7 Qualitative development of the strain components versus number of load cycles [49]. 23
Figure 8 Model Code 1990 S-N curve for the pure compression stress state with different normalized minimum compressive stress (Scmin) 26
Figure 9 Model Code 1990 S-N curve for the compression-tension stress state. 27
Figure 10 Model Code 1990 S-N curve for pure tension & tension-compression stress state. 27
Figure 11 Model Code 2010 S-N curve for the pure compression stress state with different normalized minimum compressive stress (Scmin). 29
Figure 12 Model Code 2020 S-N curve for the pure compression stress state considering the effect of water with different normalized minimum compressive stress (Scmin). 30
Figure 13 DNV ST C502 S-N curve for the pure compression stress state considering the effect of water with different normalized minimum compressive stress (Scmin). 31

Figure 14 DNV ST C502 S-N curve for the compression-tension stress state considering the effect of water. 31
Figure 15 Eurocode-2 S-N curve for the pure compression stress state with different normalized minimum compressive stress (Scmin). 32
Figure 16 JSCE.15 S-N curve for the pure compression stress state considering the effect of water with different normalized minimum compressive stress (Scmin). 33
Figure 17 Dutch Code 2009 S-N curve for the pure compression stress state with different normalized minimum compressive stress (Scmin). 34
Figure 18 Hsu 1981 S-N curve for the pure compression stress state with different normalized minimum compressive stress (Scmin). 35
Figure 19 Zhang et al. 1996 S-N curve for the pure compression stress state with different normalized minimum compressive stress (Scmin). 36
Figure 20 Zhang et al. 1998 (modified) S-N curve for the pure compression stress state with different normalized minimum compressive stress (Scmin). 36
Figure 21 Kim and Kim 1996 S-N curve for the pure compression stress state with different normalized minimum compressive stress (Scmin). 37
Figure 22 Lantsoght et al. 2013 S-N curve for the pure compression stress state with different normalized minimum compressive stress (Scmin). 38
Figure 23 S-N models at compression-tension stress state. 44
Figure 24 S-N models at pure tension stress state 44
Figure 25 S-N models at pure compression stress state with a minimum stress level of 0. 45
Figure 26 S-N models at pure compression stress state with a minimum stress level of 0.2. 45
Figure 27 S-N models at pure compression stress state with a minimum stress level of 0.2. 46
Figure 28 S-N models at pure compression stress state with a minimum stress level of 0.6. 46
Figure 29 S-N models at pure compression stress state with the minimum stress level of 0.8. ... 47
Figure 30 Evaluation of existing data and S-N models for stress ratio of 0.2. 48
Figure 31 S-N models at pure compression stress state with a stress ratio of 0.8. 49
Figure 32 Conversion of compressive strengths from different specimen types and sizes into a standard compressive strength for shear databases (image from the paper by Reineck et al. 2003 [88]). 57
Figure 33 Screenshot #2 of the experimental test data repository – Specimen Geometry and Material Properties. 71
Figure 34 Screenshot #1 of "List of References for Fatigue Experimental Data" Spreadsheet... 72
Figure 35 Screenshot #2 of "List of References for Fatigue Experimental Data" Spreadsheet... 73
Figure 36 S-N models and experimental data points at pure compression stress state with a minimum stress level of 0.05. 74

Figure 37 S-N models and experimental data points at pure compression stress state with a minimum stress level of 0.25. 75

Figure 38 S-N models and experimental data points at pure compression stress state with a minimum stress level of 0.80. 76

Figure 39 S-N models and experimental data points at pure compression stress state with a minimum stress level of 0.05, data points sorted based on the strength of concrete. 77

Figure 40 S-N models and experimental data points at pure compression stress state with a minimum stress level of 0.05, data points sorted based on the strength of concrete and plotted separately. 78

Figure 41 S-N models and experimental data points at pure compression stress state with a minimum stress level of 0.05, data points sorted based on the frequency of loading. 79

Figure 42 S-N models and experimental data points at pure compression stress state with a minimum stress level of 0.05, data points sorted based on the frequency of loading plotted separately. 80

Figure 43 S-N models and experimental data points at pure compression stress state with a minimum stress level of 0.05, data points sorted based on dimension ratio of concrete specimens (H/D). 81

Figure 44 S-N models and experimental data points at pure compression stress state with a minimum stress level of 0.05, data points sorted based on dimension ratio of concrete specimens (H/D) and plotted separately. 81

Figure 45 S-N models and experimental data points at pure compression stress state with a minimum stress level of 0.05, saturated specimens test results. 82

Figure 46 S-N models and experimental data points at pure compression stress state with a minimum stress level of 0.05, data points sorted based on loading wave form. 83

Figure 47 S-N models and experimental data points at pure compression stress state with a minimum stress level of 0.05, data points sorted based on loading wave form and plotted separately. 83

Figure 48 Screenshot #1 of the experimental test data repository – Tabs definition. 85

Figure 49 Concrete monotonic stress-strain behavior (from the tests conducted at UIUC [25]). 87

Figure 50 Progressive damage in the concrete cylinder specimens under increasing load. 87

Figure 51 Screenshot #2 of the experimental test data repository – Specimen Geometry and Material Properties 88

Figure 52 Screenshot #3 of the experimental test data repository – Material Properties and cyclic fatigue loading regime. 88

Figure 53 Screenshot #4 of the experimental test data repository – table for defining data range to be shown in the plots 90

Figure 54 Comparison of different specified data sets with DNVGL characteristic S-N model. 90

Figure 55 Comparison of different specified data sets with Model Code 2010 characteristic S-N. 91

Figure 56 Comparison of different specified data sets with Model Code 2010 Design S-N model 92
Figure 57 Designed Tabs in the Spreadsheet 93
Figure 58 Table for defining data range to be shown in the plots in each tab. 94
Figure 59 Table for defining Smin levels of the characteristic S-N curves shown on the plot. ... 97
Figure 60 Table for defining Smin levels and other influential parameters, including standard monotonic strength of the concrete of the design S-N curves of model code 2010 shown on the plot. 98
Figure 61 Table for defining Smin level and other influential parameters, including standard monotonic strength of the concrete of the design S-N curves of DNVGL shown on the plot. .. 100
Figure 62 Table for defining Smin level and other influential parameters, including standard monotonic strength of the concrete of the design S-N curves of Euro Code 2 shown on the plot. 102
Figure 63 Defined data ranges to see the effect of Smin level on the fatigue capacity of the concrete specimens under uniaxial cyclic test. 103
Figure 64 Uniaxial concrete fatigue test data with five different Smin ranges compared with characteristic S-N model code with five different average Smin levels. 104
Figure 65 Uniaxial concrete fatigue test data with Smin range of 0-0.1 and with five different strength levels and No fibers. 105
Figure 66 Uniaxial concrete fatigue test data with Smin range of 0-0.1 and with five different strength levels and No fibers, plus model code S-N curves for min and max Smin. 106
Figure 67 Plot of average uniaxial concrete fatigue test data with Smin range of 0-0.1 and with five different strength levels and No fibers. 106
Figure 68 Table of uniaxial concrete fatigue test data with Smin range of 0-0.1 and with five different frequency ranges and No fibers. 107
Figure 69 Plot of uniaxial concrete fatigue test data with Smin range of 0-0.1 and with five different frequency ranges and No fibers, plus model code S-N curves for min and max Smin. 108
Figure 70 Plot of average uniaxial concrete fatigue test data with Smin range of 0-0.1 and with five different frequency ranges and No fibers. 108
Figure 71 Table of uniaxial concrete fatigue test data with Smin range of 0-0.1 and with five different maximum aggregate sizes and No fibers. 109
Figure 72 Plot of uniaxial concrete fatigue test data with Smin range of 0-0.1 and with five different maximum aggregate sizes and No fibers, plus model code S-N curves for min and max Smin. 110
Figure 73 Plot of average uniaxial concrete fatigue test data with Smin range of 0-0.1 and with five different maximum aggregate sizes and No fibers. 110
Figure 74 Uniaxial concrete fatigue test data with five different Smin ranges compared with characteristic S-N model code with five different average Smin levels. 112

Figure 75 Distribution of the fatigue capacity of concrete. 114
Figure 76 Effect of change in loading frequency on fatigue capacity of concrete. 115
Figure 77 Effect of change in loading frequency on the probability density function (pdf) of fatigue capacity of concrete. 115
Figure 78 Effect of change in loading frequency on fatigue capacity of concrete (Smax≥0.8 & Smin≈0.05). 117
Figure 79 Effect of change in loading frequency on the probability density function (pdf) of fatigue capacity of concrete (Smax≥0.8 & Smin≈0.05). 118
Figure 80 Effect of change in loading frequency on fatigue capacity of concrete (Smax≈0.8 & Smin≈0.05). 120
Figure 81 Effect of change in loading frequency on a probability density function (pdf) of concrete fatigue capacity (Smax≈0.8 & Smin≈0.05). 121
Figure 82 The histogram and the normal distribution of the data sets. 123
Figure 83 Histogram of all of the data sets. 124
Figure 84 Histograms of pairs of data sets compared. 125
Figure 85 Comparison among the linear regression models generated based on the data set and the existing models proposed by standards (with the same assumed variables) 127
Figure 86 Comparing the polynomial regression models generated based on the data set with the existing models proposed by standards (having the same assumed variables) 128
Figure 87 Test data and fatigue models for the impact of Scmax on fatigue capacity (Scmin = 0.05). 130
Figure 88 Comparison of strength ratios between U.S. Building Code (no Trend) and ANN. [110] 133
Figure 89 Comparison of strength ratios between U.S. Building Code (with Trend) and ANN. [110] 134
Figure 90 Ratio of predicted fatigue life by DNV model to the actual test data versus Smax ... 136
Figure 91 Ratio of predicted fatigue life by NN model to the actual test data versus Smax 137
Figure 92 Ratio of predicted fatigue life by NN model to the actual test data versus frequency of loading (Hz) 137
Figure 93 Loading setup sketch (left); photo taken from the testing setup (right). 141
Figure 94 Peak strain recorded on both sides of the concrete cylinder over the testing cycles. (3DPC) 141
Figure 95 Stress-strain behavior of PC. 142
Figure 96 Stress-strain difference (Channel A-B) of PC under monotonic loading. 143
Figure 97 Plot of peak strain evolution under (Smax, Smin)=(0.80, 0.05) loading. 145
Figure 98 Plot of valley strain evolution under (Smax, Smin)=(0.80, 0.05) loading. 146

Figure 99 Plot of peak strain evolution under (Smax,Smin)=(0.70,0.05) loading. 147
Figure 100 Valley plot of strain evolution under (Smax,Smin)=(0.70,0.05) loading..... 148
Figure 101 Plan view of the concrete specimen in the machine, along with the sensors and cameras. 149
Figure 102 Peak strain variation at first cycle, at the cycle in which first visual damage was observed, and at last cycle vs. monotonic test results..... 149
Figure 103 Plot of peak strain evolution under (Smax, Smin)=(0.80, 0.05) loading vs. dotted line showing the ε_{PM}..... 151
Figure 104 Plot of peak strain evolution under (Smax, Smin)=(0.70, 0.05) loading vs. dotted line showing the ε_{PM}..... 151
Figure 105 Photos of the CAT#3 (Smax, Smin)=(0.80, 0.05) showing progress of visual damage. 152
Figure 106 Calculating fatigue capacity consumption of a hotspot in a monopile considering an imaginary variable load and specific weld type using DNVGL C203 code [116]. 153
Figure 107 Stress-strain behavior of RC specimen with four #3 longitudinal bars inside. 155
Figure 108 Cross section of RC specimens with four #3 longitudinal bars inside. 155
Figure 109 Stress-strain behavior of RC specimen vs. stiffness in a few selected cycles along the fatigue test up to the failure, RC-CAT#1..... 157
Figure 110 Strain evolution plot of RC specimen under fatigue loading (Smax, Smin)=(0.80, 0.05), RC-CAT#1..... 157
Figure 111 Stress-strain behavior of RC specimen vs. stiffness in a few selected cycles along the fatigue test up to the failure, RC-CAT#2..... 158
Figure 112 Strain evolution plot of RC specimen under fatigue loading (Smax, Smin)=(0.80, 0.05), RC-CAT#2..... 158
Figure 113 Photos of the RC-CAT#1 (Smax, Smin)=(0.80, 0.05) showing visual damage progress..... 159
Figure 114 Photos of the RC-CAT#2 (Smax, Smin)=(0.80, 0.05) showing visual damage progress 160
Figure 115 Peak strain evolution plot of RC specimens under fatigue loading cycle (Smax, Smin)=(0.80, 0.05)..... 161
Figure 116 Stress-strain behavior of #3 rebar that was used in the RC specimens. 162
Figure 117 Stress share of concrete in the RC specimen considering the stress transfer to the reinforcement by strain increment, (Smax, Smin)=(0.80, 0.05). 162
Figure 118 Stress share of concrete in the RC specimen considering the stress transfer to the reinforcement by strain increment, (Smax, Smin)=(0.70, 0.05). 163
Figure 119 Fatigue test results for cylinders made of RC. 165
Figure 120 Overview of the fatigue test results for cylinders made of RC. 166

Figure 121 Plot of peak strain evolution of PC and RC specimens. (Smax, Smin)=(0.80, 0.05)167

Figure 124 a) Monotonic response of RC (Stress-Strain curve) and loading-unloading lines of fatigue test; b) reinforcement cage used for casting cylindrical specimens made of RC (4 in x 8 in) 169

Figure 125 Comparison of the number of cycles to failure in specimens made of PC and RC with S_{max}/S_{min} = 0.80/0.05 170

Figure 126 Compressive stress over the loading history caluclated for S_{max}/S_{min} = 0.80/0.05 tests 171

Figure 127 Bands for calculating fatigue capacity utilization. 172

Figure 128 Fatigue test results for saturated/wet cylinders made of PC..... 176

Figure 129 Effect of saturation on the final fatigue capacity..... 177

Figure 130 Overview of the saturated/wet PC cylinders fatigue test results 177

Figure 131 The setup for eccentric loading. 178

Figure 132 Example of eccentric loading effect on the fatigue capacity..... 179

Figure 133 S-N models and experimental data points for a minimum stress level of 0.05. [21, 23, 32, 37, 39, 41, 51, 58, 59, 65, 78, 117-121] 180

Figure 134 3D-printed beam (left) and the coring procedure for production of cylindrical specimens (right)..... 188

Figure 135 3DPC cylinders..... 189

Figure 136 Monotonic test results for 3DPC. 190

Figure 137 Fatigue test results variation based on the test type (PC; plain concrete, RC; Reinforced concrete, 3DPC; 3D print concrete). 190

Figure 138 Average fatigue capacity of 3DPC material compared to plain concrete (dry and saturated), and S-N models (EuroCode2, DNV-ST-C502, Model Code 2010)..... 192

Figure 139 S-N plot (models compared to test results). 193

Figure 140 Combined fatigue test results of 3DPC; left side) Stress-strain response of cylinder to monotonic compressive loading, along with a few cycles of hysteresis and peak and valley stress and strain development over the cycles. Right side) The strain evolution plot shows peak and valley strain increments over the cycles of loading up to failure. 196

Figure 141 Photos of two sides of the concrete cylinder at certain points during the test (Test #9). 197

Figure 142 Peak strain recorded on both sides of the concrete cylinder across the testing cycles. 198

Figure 143 Strain evolution of 3DPC (peak and valley strain vs. normalized number of cycles to failure); Peak solid lines; Valley dashed lines. 199

Figure 144 Peak strain evolution for (Smax, Smin)=(0.80, 0.05). 199

Figure 145 Normalized peak strain evolution plot 200

Figure 146 Final peak strain due to fatigue loading versus normalized stress-strain monotonic results. 200
Figure 147 Initial and final stiffness versus the logarithm of the number of cycles to failure. .. 202
Figure 148 Peak strain related to the first visual crack appearance on the concrete cylinders final due to fatigue loading versus normalized stress-strain monotonic results. 203
Figure 149 Down-sampled peak strain (Test #9); a) Peak strain evolution plot, b) the gradient of peak strain, c) Zoomed-in gradient of peak strain. 206
Figure 150 Correlation between the number of cycles to failure and peak strain gradient. 207
Figure 151 Correlation between the number of cycles to failure and valley strain gradient. 207
Figure 152 Correlation between the number of cycles to failure and stiffness gradient. 208
Figure 153 The preparation of materials (sieving aggregates) for casting at Tufts University (March 2023). 212
Figure 154 Types of aggregates used in the casting of new concrete cylinders. 213
Figure 155 Aggregate gradation for river pea gravel source used for casting. 214
Figure 156 Monotonic strength of concrete cylinders with smaller round aggregate. 214
Figure 157 Aggregate gradation for crushed blue stone source used for casting. 216
Figure 158 Monotonic strength of concrete cylinders with larger sharp aggregate. 216
Figure 159 Compressive fatigue capacity test results compared to the codes. 217
Figure 160 Gradation results for crushed coarse granite. 219
Figure 161 Gradation results for river based round aggregate. 219
Figure 162 Coarse crushed granite aggregate; Left) max aggregate size of ¾ in; Right) max aggregate size of 3/8 in. 220
Figure 163 River based round aggregate with max size of 3/8 in. 220
Figure 164 Gradation results for sand. 221
Figure 165 Sand. 221
Figure 166 A few photos from the trial batches (mixing process and results of the slump test). 222
Figure 167 A few photos from concrete 10321, with round coarse aggregate and the slab with crushed granite aggregate (mixing process, entrained air test, and results from the slump test). 224
Figure 168 The first two sets of concrete cylinders delivered to Tufts University. 225
Figure 169 Example of plotting the stress-strain response of a concrete cylinder to compressive monotonic loading using ISEM to estimate the actual strength of the cylinder (3DPC). 230
Figure 170 S-N curve plot for uniaxial compressive fatigue testing with Smin of 5%. 231
Figure 171 S-N curve plot for uniaxial compressive fatigue testing with Smin of 20%. 232
Figure 172 Combined fatigue test result plot of 3D-printed concrete; left side) Stress-strain response of cylinder to monotonic compressive loading, along with a few cycles of hysteresis

and peak and valley stress and strain development over the cycles. Right side) Strain evolution plot showing peak and valley strain increment over the cycles of loading up to failure. 239
Figure 173 Photos of two sides of the concrete cylinder at certain points during the test (Test #9). 240
Figure 174 Normalized peak strain evolution plot. 240
Figure 175 Down-sampled peak strain (3DPC Test #9); a) Peak strain evolution plot, b) the gradient of peak strain, c) Zoomed-in gradient of peak strain. 242
Figure 176 Correlation between the number of cycles to failure and peak strain gradient. 243
Figure 177 Correlation between the number of cycles to failure and valley strain gradient. 245
Figure 178 Correlation between the number of cycles to failure and stiffness gradient. 246
Figure 179 Peak strain related to the stag of visual crack appearance due to fatigue loading for river base aggregate concrete. 248
Figure 180 Peak strain related to the stag of visual crack appearance due to fatigue loading for crushed granite coarse aggregate concrete. 248
Figure 181 Peak strain related to the stag of visual crack appearance due to fatigue loading for lightweight coarse aggregate concrete. 248
Figure 182 S-N models and experimental data points for a minimum stress level of 0.05[23, 32, 37, 39, 41, 51, 58, 60, 65, 66, 78, 86, 119-121, 145] 255
Figure 183 3D-printed concrete monotonic test results 259
Figure 184 Monotonic stress-strain test results of the concrete named OCNC 262
Figure 185 Shape of the concrete cylindrical specimen failure under monotonic compressive loading [147] 262
Figure 186 Base test results used to predict the strength using ISEM method 264
Figure 187 Effect of the number of input data on the model error 266
Figure 188 bar-plot comparing the error of the NNISEM model and old-fashioned model 268
Figure 189 Improved Strength Estimate Method 272
Figure 190 Example of development of an S-N Curve by certification by testing procedure 279
Figure 191 Development of Two S-N Curves 281
Figure 192 Developed S-N curve for a particular normal strength concrete at Smin=0.05 & frequency=1 Hz 281
Figure 193 Developed S-N curve for a particular normal strength concrete at Smin=0.20 & frequency=1 Hz 282
Figure 194 S-N curve plot for uniaxial compressive fatigue testing with Smin of 5% 283
Figure 195 S-N curve plot for uniaxial compressive fatigue testing with Smin of 20% 284
Figure 196 Probabilistic S-N curve plot for uniaxial compressive fatigue testing for RBAC 291
Figure 197 Probabilistic S-N curve plot for uniaxial compressive fatigue testing for GCAC 292

Table 1 Existing S-N models for prediction of fatigue life of concrete under pure compression stress state 39
Table 2 Partial fatigue safety factors for the strength of materials 42
Table 3 Partial fatigue safety factors for load cases 42
Table 4 Type of concrete considered in fatigue models 42
Table 5 Saturation type 43
Table 6 Stress states and shear design 43
Table 7 Outliers in the uniaxial concrete fatigue data sets 112
Table 8 Range, mean, and standard deviation of the defined data sets as 2 categories with a different frequency range 114
Table 9 Hypothesis test and significance level for two categories of data set with different loading frequency ranges. 116
Table 10 Range, mean, and standard deviation of the defined data set as two categories with different frequency ranges and (Smax≥0.8 & Smin≈0.05) 117
Table 11 Hypothesis test and significance level for two categories of data set with different loading frequency ranges. (Smax≥0.8 & Smin≈0.05) 119
Table 12 Range, mean, and standard deviation of the defined data sets as two categories with different frequency ranges and (Smax≈0.8 & Smin≈0.05) 119
Table 13 Hypothesis test and significance level for two categories of data set with different loading frequency ranges. (Smax≈0.8 & Smin≈0.05) 121
Table 14 Range, mean, and standard deviation of the defined data sets 122
Table 15 Input parameters/variables for regression models 126
Table 16 Cyclic fatigue loading protocols for plain concrete 144
Table 17 Cyclic fatigue loading protocols 144
Table 18 Number of cycles to failure of PC under (Smax, Smin)=(0.80, 0.05) loading 145
Table 19 Number of cycles to failure of the plain concrete under (Smax, Smin)=(0.70, 0.05) loading 147
Table 20 Visual damage results in fatigue test of the PC specimens 150
Table 21 Cyclic fatigue loading protocols for RC 156
Table 22 Comparison of fatigue test results and fatigue model predictions for cylinders made of RC and cylinders made of dry plain concrete. 164
Table 23 Number of fatigue loading cycles per failure for PC and RC specimens, (Smax, Smin)=(0.80, 0.05). 167
Table 24 Fatigue capacity utilization based on the Model Code. 172

Table 25 Fatigue test results versus fatigue model predictions for saturated/wet and dry 175
Table 26 Impact of assumed strength error on fatigue capacity using three different fatigue models 181
Table 27 Monotonic test results for 3DPC 189
Table 28 Fatigue test results for 3DPC specimens 194
Table 29 Predicted fatigue capacity based on correlations of gradient strains and stiffness 205
Table 30 Monotonic strength of concrete cylinders with smaller round aggregate 215
Table 31 Monotonic strength of concrete cylinders with larger sharp aggregate 217
Table 32 Primary fatigue test results 218
Table 33 Monotonic test results for trial batches of concrete 223
Table 34 Monotonic test results for the final mix designs of concrete 225
Table 35 Concrete specifications and mix design 228
Table 36 Fatigue test results of PC specimens with river base round coarse aggregate (maximum size of 3/8 in) 233
Table 37 Fatigue test results of plain concrete specimens with crushed granite (angular) coarse aggregate (maximum size of 3/4 in) 234
Table 38 Fatigue test results of PC specimens with lightweight coarse aggregate 235
Table 39 Fatigue test results of cored plain concrete specimensfrom slab with crushed granite (angular) coarse aggregate (maximum size of 3/4 in) 236
Table 40 Comparison of the average and minimum fatigue capacity of normal concrete with similar strength but different aggregate type and size (Smin = 5%) 237
Table 41 Comparison of the average and minimum fatigue capacity of normal concrete with similar strength but different aggregate type and size (Smin= 20%) 237
Table 42 Parameters of peak (maximum) strain gradient correlation with fatigue capacity 244
Table 43 Parameters of valley (minimum) strain gradient correlation with fatigue capacity 244
Table 44 Parameters of Stiffness degradation gradient correlation with fatigue capacity 246
Table 45 Ratio of the fatigue life (capacity) at which the first visual crack observed 249
Table 46 Impact of assumed strength error on fatigue capacity using three different fatigue models 256
Table 47 Statistic summary of the monotonic test results of OCNC concrete 261
Table 48 Monotonic test results of concrete (called OCNC) 263
Table 49 Performance of ISEM method compared to old fashioned method (assuming the average strength for all the specimens) 265
Table 50 NN model performance on average 267

Table 51 Performance of NN model compared to old fashioned method (assuming the average strength for all the specimens) 269

Nomenclature or List of Abbreviations

N_f = Number of cycles to failure

$f_{c\_monotonic}$= Monotonic strength of a concrete cylinder

f_{c_max}= Maximum/peak defined stress for fatigue cyclic loading

f_{c_min}= Minimum/valley defined stress for fatigue cyclic loading

$S_{max} = {f_{c\_max}}/{f_{c\_monotonic}}$ Maximum imposed stress/load ratio during fatigue cyclic loading

$S_{min} = {f_{c\_min}}/{f_{c\_monotonic}}$ Minimum imposed stress/load ratio during fatigue cyclic loading

E_{sec} = Secant stiffness

σ_{max} = Maximum/peak compressive stress during fatigue cyclic loading

σ_{min} = Minimum/valley compressive stress during fatigue cyclic loading

ε_{max} = Maximum/peak compressive strain during fatigue cyclic loading

ε_{min} = Minimum/valley compressive strain during fatigue cyclic loading

ε_{PM} = Avg. strain of concrete under monotonic loading at peak stress point

Ncrk = Number of cycles at which first visual crack has been observed

ε_{PC} = Avg. strain at peak at Nc (milli-strain)

ε_{VC} = Avg. strain at valley at Nc (milli-strain)

Ec = stiffness of concrete at Nc (ksi)

PSG = Peak strain gradient

VSG = Valley strain gradient

SG = Stiffness gradient

N: total axial load capacity

Nc: concrete axial load capacity

Ns: steel axial load capacity

Ec: modulus of concrete (stiffness)

Es: modulus of steel (stiffness)

$N = E_s / E_c$: modular ratio

A_g = gross cross-sectional area of a specimen

As: longitudinal steel cross section area

$Ac = A_g - A_s$: concrete cross section area

$A_t = A_c + n * A_s$: transformed (equivalent) concrete area

$P_{RC} = A_t * f_{cm}$: Capacity of cross-section

1 Introduction

1.1 Motivations

1.1.1 Motivation: Concrete as an attractive alternative to steel for wind turbine support structures

The nation's ambitious plans for development of offshore and onshore wind energy [1-4] underscore the need for durable and sustainable support structures, including towers and foundations. Concrete is an attractive alternative to steel, offering extended operational lives for wind farms and reduced Levelized Cost of Energy (LCoE) [5]. As concrete support structures are typically constructed near wind farm sites, they offer additional societal benefits such as local jobs and tax revenues.

For offshore applications, concrete Gravity-Based Foundations (GBFs) are particularly advantageous due to their significantly longer service lives, lasting up to 100 years compared to the 25–35 years typical for steel structures [5]. This increase in longevity is largely attributed to concrete's superior resistance to corrosion, which, given the marine environment of these structures, otherwise compromises steel structures relatively quickly, even if those steel structures have extensive coatings and cathodic protection. Corrosion of steel not only compromises the material's fatigue capacity, but it also creates sharp edges that further reduce the service life of a steel structure. Repairs to such damaged steel structures are often prohibitively expensive or technically infeasible [6-9]. In contrast, well-designed concrete structures have demonstrated exceptional long-term durability, in similar environments [10].

For onshore wind applications, concrete is increasingly being used in segmental construction techniques, a method originally developed for bridges, to construct towers which are very tall — up to 185 meters high. These towers support very large wind turbines, with rotor diameters exceeding 200 meters, and enable the turbines to capture the stronger winds present at higher altitudes[1,2,3] [11]. Compared to their steel counterparts, wind towers made of segmental concrete offer enhanced stability and durability through their increased stiffness and reduced number of bolted connections.

Concrete support structures are cost-competitive with steel, their construction is more labor-intensive and typically needs to occur closer to the wind farm site [5]. These requirements constitute significant advantages, promoting local employment, increasing tax revenue, and offering other economic benefits.

1.1.2 Motivation: Modeling fatigue for design of support structures

Turbines are subject to high-cycle loading due to varying wind and wave loads as well as turbine operation, so fatigue of turbine support structures must be understood and accounted for. The most common fatigue models and rules in design standards for concrete structures lead to unnecessarily conservative designs and uncertainties for long-term performance. The "one-size-fits-all" fatigue models that are dominantly used in current design and assessment practices do not adequately account for the variation in shape, type of concrete (normal strength, high strength, lightweight), types and amounts of reinforcement, and level of prestressing among the

[1] https://concreteproducts.com/index.php/2016/05/10/siemens-commercializes-site-cast-wind-turbine-tower-design/
[2] https://insights.globalspec.com/article/2684/siemens-wind-turbine-towers-to-top-115-meters
[3] https://www.windsystemsmag.com/siemens-introduces-concrete-tower-technology-to-reduce-energy-costs/

various concrete support structures which have been designed, analyzed, constructed, and/or installed for onshore and offshore wind turbines (Figure 1).

(a) Wind Tower Technologies Precast Tall Tower Solution[4]

(b) Floatgen Offshore[5] Foundation

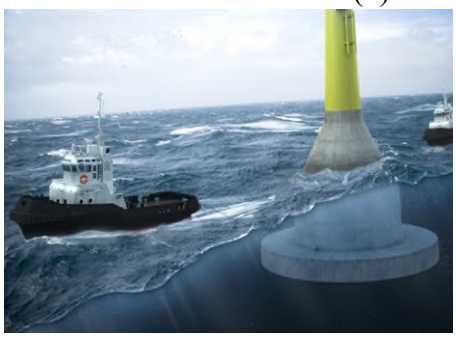

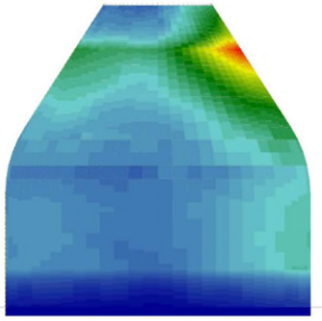

(c) SeaTower Gravity Base Offshore Wind Support Structure with Finite Element Model[6]

(d) ODE Articulating Wind Column[7] (e) Kårehamn Barge-Delivered Offshore Wind [12]

[4] Photo of the Mid-American power company. [Link: https://www.desmoinesregister.com/midamerican-builds-nations-tallest-land-based-wind-turbine]
[5] Photo of the Floatgen project courtesy of EDF Renewables. [Link: https://fowcoe.co.uk/programmes/strategic-programmes/construction-operations-and-maintenance/]
[6] Seatower's gravity-based foundation. [Link: https://www.windpowermonthly.com/article/1308806/seatowers-gravity-based-foundation-baseplate-cast]
[7] ODE Articulating Wind Column. [Link: https://www.offshorewind.biz/2017/04/19/ode-to-test-awc-deep-water-foundation/]

(f) Equinor Spar Floater[8]

(g) Volturnus Floating OWSS[9]

(i) Olav Olsen Star Floater[10]

(j) Esteyco Telescoping OWSS[11]

(k) Blyth Demonstration Project[12]

Figure 1 Examples of different shapes of offshore wind support structures made of concrete.

This dissertation aims to address critical shortcomings in current fatigue analysis and design practices of concrete support structures for wind turbines by developing fatigue models that are tailored to specific concrete properties and structural conditions. Present approaches often apply generalized models that treat all concrete structures, similarly, ignoring key factors such as

[8] Kongsberg EmPower system [Link: https://www.windpowerengineering.com/statoil-chooses-kongsberg-empower-hywind-demo/]
[9] Volturn US design utilizes a concrete semisubmersible floating [Link: https://www.ajot.com/premium/ajot-offshore-floating-a-wind-energy-solution-for-us-energy-gap]
[10] OO Star Wind Floater. [Link: https://www.sintef.no/globalassets/project/eera-deepwind-2018/presentations/closing_landbo.pdf]
[11] [Link: https://www.windpowermonthly.com/article/1491045/turbine-telescopic-tower-installed]
[12] [Link: https://www.offshorewind.biz/2017/01/13/gravity-based-foundations-for-blyth-demo-taking-shape/]

material composition, reinforcement levels, and environmental conditions that significantly influence fatigue performance. These overly conservative models can underestimate the true fatigue capacity of concrete by a factor of 10 or more, leading to inefficient designs that increase costs and thereby compromise the competitiveness of concrete as a structural material to support wind turbines.

1.2 Objectives: New data, models, understanding, and recommendations regarding design for concrete fatigue demands

This dissertation focuses on advancing innovation in concrete support structures for offshore and onshore wind turbines by experimentally quantifying the effects of fatigue on the strength, stiffness, and durability of marine structural concretes. It leverages newly generated data alongside existing experimental data to improve understanding of fatigue models, design standards, and analytical processes. The work provides a publicly accessible experimental database, recommendations for customized fatigue models, and standardized methods for compressive fatigue testing, equipping researchers, designers, and developers with tools to reduce costs, enhance durability, and drive innovation in concrete support structures for wind turbines.

To achieve these objectives, the dissertation includes four key components. First, publicly available data from previous concrete fatigue tests were compiled into a comprehensive database, analyzed for trends and gaps, and used to identify missing key features for improved fatigue modeling. Recommendations were developed to standardize testing and facilitate future model development. Second, extensive experimental fatigue testing was conducted on various concrete types, including normal strength, lightweight, and 3D-printed concrete (3DPC), as well

as concretes with different aggregate types and reinforcement configurations. These tests provided insights into the influence of stress levels, mix designs, and reinforcement on fatigue life, and the findings were incorporated into the database. Third, efforts to create more accurate S-N curves for different concretes revealed limitations due to variability in existing data and missing critical information. Instead, a methodology was developed for targeted fatigue testing to create specific S-N curves with reduced effort, offering a pragmatic approach to addressing these challenges. Finally, based on experimental findings, recommendations for standardized compressive fatigue testing and data presentation were proposed and are set to be published as Technotes by the American Concrete Institute, ensuring broad applicability and public access.

1.3 Organization of the dissertation

This dissertation is organized into eight chapters, each building upon the previous, and together constituting a comprehensive exploration of the fatigue behavior of concrete used in support structures for wind turbines.

Chapter 1 introduces the motivation, objectives, and overall structure of the dissertation. It provides a detailed explanation of why concrete presents a promising alternative to steel in wind turbine support structures and highlights the need for improved fatigue modeling and testing practices. The chapter also outlines critical gaps in existing knowledge, framing the objectives of this research within the broader context of structural durability and cost-efficiency.

Chapter 2 is a literature review covering the fundamentals of concrete fatigue behavior and factors influencing fatigue capacity, including aggregate type, loading conditions, and environment. It includes a critical examination of existing fatigue models and discussion of gaps in the current understanding. This chapter serves as the foundation for the experimental and

analytical work described in later chapters, emphasizing the need for a systematic approach to understanding concrete fatigue.

Chapter 3 focuses on the development of a database for experimental data on fatigue. through consolidation of data from prior studies, organization of an Excel-based dashboard for analysis, and evaluation of trends and inconsistencies in existing datasets. This database forms a critical resource for the experimental program that follows.

Chapters 4 through 6 present the core experimental research, each with a unique focus:

Chapter 4 is about the initial experimental testing phase, in which key factors influencing fatigue capacity were explored through a range of controlled experiments, including tests on plain concrete and reinforced concrete under various loading conditions (e.g., concentric, eccentric, and saturation). The fabrication and testing processes are shown in Figure 2. This phase provided insights into critical parameters and served as the foundation for more extensive testing.

In **Chapter 5,** studies of the fatigue performance of 3DPC — relative to that of concrete formed through casting — to determine the emerging material's potential for structural applications in support systems for wind turbines are described.

Chapter 6 is about the effects of aggregate size, shape, and type on fatigue behavior on the overall performance and durability of concrete under fatigue loading.

(a) Initial testing phase casting, at UIUC

(b) Initial testing phase specimens, at Tufts

(c)Reinforced concrete specimens before casting

(d) Air content test

(e) Final cast concrete samples with different aggregate sizes

Figure 2 The numerous cylinders casted for the final testing.

In **Chapter 7,** presents recommendations for fatigue testing are presented, including standardized methodologies for compressive fatigue tests and procedures for developing S-N curves specific to various concrete mixes. These recommendations, proposed for publication as ACI Technotes, are offered as guidance for both current practice and future research.

Chapter 8 includes a consolidation of the research findings a discussion of their implications for concrete fatigue design and testing, and directions for future work.

2 Background (Literature Review)

2.1 Introduction to compressive fatigue behavior of concrete

Because structures that support wind turbines are subjected to high-cycle fatigue loading, the effect of fatigue on reducing stress capacity much be carefully considered to provide an effective and optimized design. What follows is a literature review on the fatigue process in concrete material to show how the material's behavior (e.g., strain evolution, cracking, other types of damage) is influenced by fatigue loading, as well as to introduce methods for characterizing fatigue behavior in such material.

Fatigue of concrete is a process directly related to the propagation of microcracks inside the material [13-15]. Pre-existing defects like pores and shrinkage microcracks, in addition to the discontinuity of material at the interface between the cement paste and aggregates, act as triggers for the formation and propagation of cracks [16].

Generally, microcracks exhibit a similar formation and origin in both static and dynamic loading. Fatigue-related microcracks typically initiate and propagate around aggregates and in the cementitious material. Cracks run parallel to the loading direction under compression and perpendicular under tension. In both cases, the microcracks show an average orientation perpendicular to the maximum tension/extension direction in the cementitious/mortar matrix [16]. Under cyclic loading, microcracks are more numerous and can spread more extensively, whereas, in static loading, microcracks are fewer but more developed (i.e., larger and wider).

2.1.1 Microcrack formation and propagation

Fatigue microcracking of concrete is irreversible, constituting a slow but progressive deterioration of the inner structure. Crack propagation is quantifiable, enabling evaluation of the

deterioration process and its evolution to failure. When microcracks form in a given specimen under fatigue loading, sounds are produced which can be recorded in the laboratory [17-19]. The crack propagation process can also be monitored using sensors such as strain gauges and extensometers (which track deformation)[20]. Heat dissipation can also quantify the deterioration process, as energy is released as the microcracks propagate [16].

2.1.2 The three phases of concrete fatigue

Deterioration of concrete due to fatigue can be thought of as occurring in a series of phases of accumulation of strain damage. See Figure 3, where strain (ε) is shown as a function of the nominal number of applied loading cycles (n/Nf) where "n" is the number of loading cycles and "Nf" is the number of loading cycles at failure. Thus, a n/Nf value of 0.5 corresponds to being 50% through the measured fatigue capacity.

- **Phase I**: During this phase, small holes within the concrete start to close, and this process initiates some microcracks. This phase covers about 5-10% of the total number of loading cycles (N_F) necessary for fatigue failure.
- **Phase II**: In this phase, microcracks start to propagate at a constant rate, and plastic straining is slow. This phase is the main part of the fatigue capacity/life of the material, accounting for 80-90% of the total number of cycles to failure.
- **Phase III**: During this phase, the concrete deteriorates progressively quicker until it fails. The microcracks merge together and create macrocracks, leading to large crack widths and slip-along crack faces, as measured by the larger level of strain. As the concrete approaches its fatigue life, it deteriorates progressively quicker until it fails.

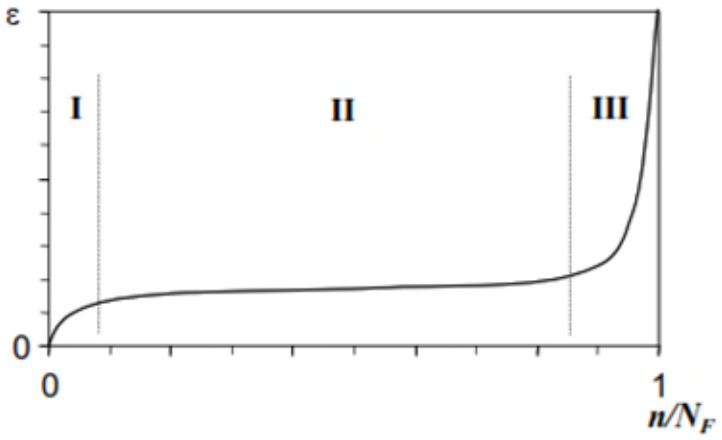

Figure 3 The strain evolution of concrete under cyclic loading [16].

2.1.3 Fatigue Strength and Number of Cycles to Failure

Concrete's resistance to fatigue is typically represented by the relationship between the magnitude of the applied stress and the number of cycles to failure (or estimated fatigue capacity). This relationship is often illustrated using a Wöhler (σ-N) curve, as shown in Figure 4, which only connects the imposed cyclic stress to the fatigue capacity (Nf). This curve represents the stress level, referred to as "endurance limit" or "fatigue strength", plotted against the number of loading cycles (N_f) of fatigue capacity. One of the main assumptions is that by keeping the stress value fixed, it is possible to estimate the number of cycles of failure capacity. Conversely, for a given number of cycles, the corresponding level of stress that will cause failure can be determined. This model is not a perfect representation of concrete behavior under cyclic loading; there are other important parameters that are proven to have an effect, such as loading frequency [21-23], and multiple possible impactful parameters that need to be explored and considered.

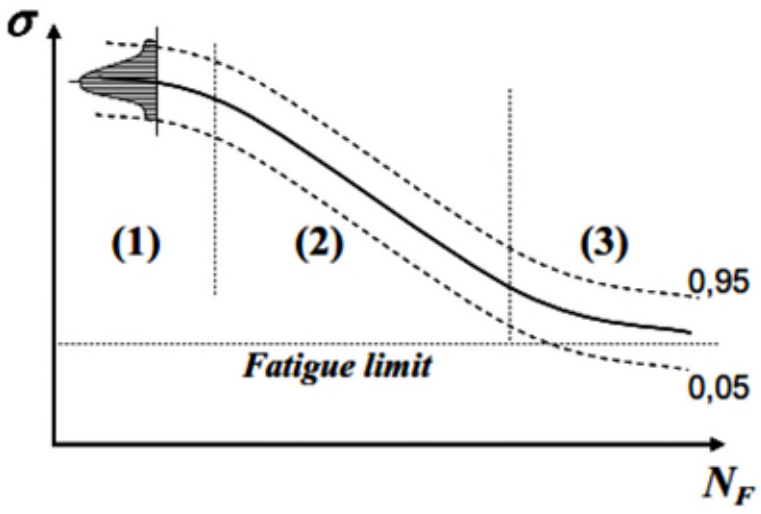

Figure 4 The Wöhler's curve in the σ-Nf diagram [16].

2.1.4 Classifications of fatigue

Cyclic fatigue loading of a structure is generally classified into three categories based on the number of cycles to failure (N_f):

- Low Cycle Fatigue ($N_f \leq 10^3$)
- Large Cycle Fatigue ($10^3 \leq N_f \leq 10^7$)
- Very Large Cycle Fatigue ($N_f \geq 10^7$)

The relationship between stress and the number of cycles to failure is commonly represented by Wöhler's formula, where α and β are constants specific to the material and derived from experimental data:

$$\sigma = \alpha - \beta \, Log \, N_F \text{ (Wöhler's formula)} \qquad \text{Equation 1}$$

The fatigue capacity of concrete is highly variable, often exhibiting significant scatter. For a given loading condition, the number of cycles to failure (N_f) can vary dramatically, with values sometimes differing by a factor of 1000 or more. To account for this variability, fatigue life is

represented probabilistically, often using a Weibull distribution to describe the fatigue strength of concrete at various cycle counts.

2.1.5 Factors affecting concrete fatigue behavior

The fatigue behavior of concrete depends on several parameters, including:

- **Material composition and strength**: The type of cement, water-to-cement ratio, and aggregate characteristics all influence concrete's fatigue resistance.
- **Loading cycle**: The level, frequency, and shape of the loading cycle (sinusoidal, trapezoidal, etc.) also play a critical role.
- **Environmental conditions**: Factors such as temperature and moisture conditions can significantly affect fatigue performance.

The age, method of casting, curing conditions, and porosity of concrete also influence its fatigue capacity. Notably, both static and cyclic strengths of concrete depend on these variables.

Figure 5 presents the behavior of concrete material subjected to cyclic loading. The peak and valley stains are the uniaxial strain related to the maximum and minimum uniaxial compressive stress imposed on the test specimen. The progression of strain across cycles (or the normalized number of cycles) is depicted in a strain evolution plot (see Figure 5, right side). On the left side, the monotonic stress-strain response of the concrete with the same strength is plotted along with a few down-sampled fatigue hysteresis curves (in green). Also depicted are the secant stiffness lines for those hysteresis curves, which are plotted (in blue) by connecting the maximum and minimum stress-strain points (σ_{max}, ε_{max}) and (σ_{min}, ε_{min}). The test failed when the last loading cycle crossed the descending branch of the monotonic test result. This is a typical behavior observed by other researchers [24-27]. The peak and valley strain evolution plots are

shown on the right side of Figure 5. The strain evolution plot has a S-inverted shape. Like other concrete materials, it can be seen that there are three distinctive phases of strain development. *Phase I* has a rapid strain accumulation due to the closing of the holes and pore spaces inside the material, and it usually continues up to about $0.2*N_f$. *Phase II* has a steady and constant linear strain accumulation. In *Phase II*, the microcracks continue to progress. *Phase III* starts at about $0.8*N_f$ and shows a rapid strain increase due to cyclic loading. The S-inverted behavior is normally inferred to be due to the merging of microcracks and initiation of macrocracks and failure zones [23, 25, 26].

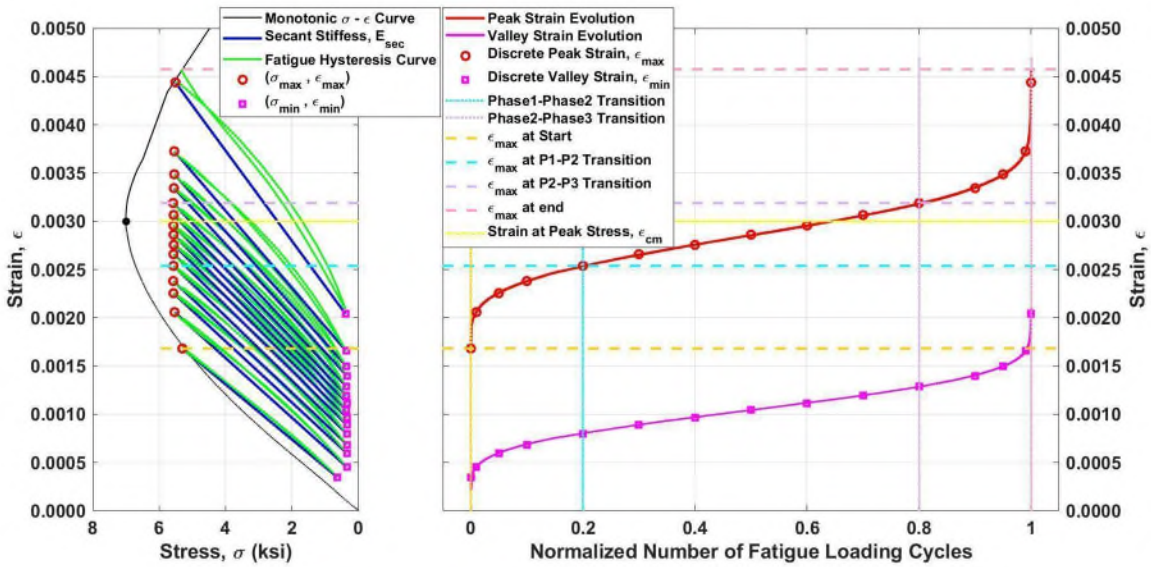

Figure 5 Behavior of concrete subjected to fatigue under cyclic compression (3DPC) Left side; Stress-strain response of cylinder to monotonic compressive loading, along with a few cycles of hysteresis and peak and valley stress and strain development over the cycles. Right side; The strain evolution plot shows peak and valley strain increments over the cycles of loading up to failure.

Both the static and cyclic strengths of the concrete depend on the same parameters [28-32]: type and grading of the aggregates, type of cement, water-to-cement ratio, porosity, method of casting, specimen size and curing conditions during the period of hardening. Thus, a conventional σ-N_f curve is valid for a given concrete based on its specific age and characteristics.

In this formulation, the stress parameter can be normalized by the static strength of the material or the cyclic stress to static strength ratio: $S=\sigma/f_c$. The stress ratio can be represented by S, and Wöhler's curve can be modified to the S-N curve. S is normalized stress by static monotonic compressive strength of the material, and N_f is the number of cycles to failure. With this representation, the fatigue curve only depends on the loading parameters [16]. The S-N curve considers not only the material's static compressive strength but also factors like stress ratios ($S = \sigma/f_c$).

Understanding the fatigue behavior of concrete is crucial to be able to designstructures that can withstand high-cycle cyclic loading, such as turbines for offshore and onshore wind energy. Accurate fatigue models based on experimental data enable more precise prediction of fatigue life and design of structures with increased safety and durability.

Concrete is a nonlinear material, requiring the study of its behavior under fatigue loading. Concrete fatigue involves progressive structural changes, including microcrack initiation and propagation, strain evolution, and stiffness degradation. Petkovic and Lenschow (1992) noted that fatigue loading causes either revealing viscous properties or crack propagation, with each cycle acting on a slightly altered structure [33]. Understanding parameter variations during fatigue loading is critical. Recent research has explored concrete's behavior under fatigue more thoroughly. Key findings are summarized below.

2.1.5.1 Strain evolution and behavior

As shown in Figure 5, while under fatigue / cyclic loading, concrete exhibits three-phase behavior Hsu et al. 1963 linked visible macrocracks to the third phase, noting that continuous cracks did not immediately reduce capacity, extending this phase [34]. Sparks and Menzies 1973

connected strain rates to failure cycles, which is useful for fatigue monitoring [35]. Sparks 1973 & 1982 identified the three-phase strain evolution and noted a constant strain increase rate in the middle phase [35, 36]. Awad and Hilsdorf 1971 observed a rise in Poisson's ratio in the third phase, which was attributed to crack opening [37]. Takhar et al. 1974 found lateral confining pressure mitigated strain increases [38].

Do et al. 1993 also observed increasing strain magnitudes with longer test durations [39]. Grzybowski and Meyer 1993 found fibers delayed large crack formation by promoting smaller cracks, increasing strength, but also increased initial microcrack density, reducing strength [40]. Dyduch and Destrebecq 1994 noted that fatigue failure occurs as microcracks develop and merge into macrocracks. They further reported that fatigue-induced cracks were more numerous and merged into macrocracks under cyclic loading, leading to failure [41]. Kim and Kim 1996 observed these three stages across concrete strengths [29], while Lohaus and Anders 1996 reported brittle fatigue responses in UHPC [42]. Bahn and Hsu 1998 described three strain stages: rapid initial increase, steady-state growth, and a final rapid increase leading to failure [43].

Medeiros et al. 2015 described the middle phase as quasi-linear. They found that in plain concrete (PC), critical cracks led to failure in phase 3. In fiber-reinforced concrete, fiber bridging stabilized these cracks, creating a bump in the cyclic creep curve, appearing to revert stage 3 back to stage 2. [44]. Haar and Marx 2016 highlighted crack growth across phases, noting a rise in Poisson's ratio in the third phase, attributed to crack opening [45]. Oneschkow 2016 identified three phases of strain evolution: an initial disproportionate increase in deformation due to microcracks, a linear increase during stable crack growth, and a disproportionate rise in the third phase caused by unstable crack growth [23]. However, Viswanath et al. 2021 found the middle

phase nonlinear, with strains decreasing until 50% fatigue loading, then increasing [25]. Fan and Sun 2021 noted that higher concrete strength slows fatigue behavior degradation, and all types of fatigue behavior follow a similar trend. They also stated that stress-strain curves exhibit a three-stage progression (uneven-steady-uneven and sparse-dense-sparse), indicating elastic modulus degeneration. The stages are proportioned as 10%-80%-10% [27]. Viswanath et al. 2022 provided a comprehensive investigation into the axial strain behavior of normal-strength concrete under uniaxial compressive fatigue loading. The key findings include the dependency of strain magnitudes on stress levels, the formation of surface cracks during the final phase, and the potential for strain evolution data to predict remaining fatigue life, offering valuable insights for the design of fatigue-critical concrete structures.

2.1.5.1.1 Lengths of the three phases

Viswanath et al. 2021 noted that the length of the three fatigue phases varies based on concrete strength, with the first and third phases generally ranging from 5% to 25% of the failure number of cycles (N_f) and the middle phase spanning 50% to 90% of N_f [25]. Oneschkow 2016 observed phase transitions for normal-strength concrete at 10–20% (first transition) and 80–90% (second transition) of N_f, with shorter first and third phases for higher-strength concrete [23]. Kim and Kim 1996 noted three stages: rapid strain increase (up to 10% of life), uniform increase (10–80%), and rapid increase until failure, with a longer middle phase for higher-strength concrete [29]. Dyduch 1994 reported phase lengths of 10%, 80%, and 10% [41], while Do et al. 1993 and Isojeh et al. 2017 observed lengths of 10%, 70%, and 20% [24, 39]. Medeiros et al. 2015 reported first and third phase lengths of 10–15% [44].

For high-strength concrete, Oneschkow 2016 found phase transitions at 11% and 93%, noting that NfN_f increases prolong phase II [23]. Hümme et al. 2016 (79) identified transitions at 9%

and 92%, while Wefer observed transitions at 5% and 95% for concrete with a strength of 160 MPa [20]. Overall, as concrete strength increases, the first and third phases shorten. Fan and Sun 2021 stated that stress-strain curves exhibit a three-phase progression (uneven-steady-uneven and sparse-dense-sparse), indicating elastic modulus degeneration. The stages are proportioned as 10%-80%-10% [27]

2.1.5.1.2 Effect of concrete strength

Kim and Kim 1996 noted that higher-strength concrete exhibits smaller fatigue strain at failure, indicating that in high-strength concrete in fatigue failure, internal damage is relatively localized. While strains during the process were higher for high-strength concrete (HSC), the strain at failure was actually smaller when normalized against "n" [29]. Oneschkow 2012 observed that the first and third phases of strain evolution were shortened to approximately 5% due to the high strength (115 MPa) of concrete used in their experiments [46]. Li et al. 2016 reported that specimens of ultra-high toughness cementitious composites (UHTCC) did not exhibit explosive failure, unlike specimens of PC, which typically burst into pieces [47].

2.1.5.2 Failure fatigue strain

Kim and Kim 1996 observed that "the total strain at fatigue failure approximately coincides with the strain on the descending branch of the monotonic stress-strain curve," indicating higher failure strains for high-strength concrete (HSC) [29]. Haar and Marx 2016 noted that other studies, including Do et al. 1993, Oneschkow 2012, and Kim and Kim, found ultimate fatigue strains in HSC to be smaller or similar to those under monotonically increasing loads [23, 39, 45]. In normal-strength concrete (NSC) studies, such as Park 1990, fatigue failure strain lies on the decreasing branch of the monotonic curve [48]. Haar and Marx 2018 also observed that, after

correcting for temperature effects, fatigue failure strain in HSC matches the ultimate strain under monotonic loading and shows a linear increase in damage-induced strain with log N_f [49].

Awad and Hilsdorf 1971 reported larger failure strains at lower peak stress levels, exceeding those under standard monotonic loading [37]. Do et al.1993 found similar failure strains in HSC under fatigue and monotonic loading [39]. Studies like Viswanath et al. 2022 confirmed that, at peak stress, failure strain aligns with the strain on the descending branch [26].

Cachim et al. 2002 identified two findings: monotonic stress-strain curves can serve as envelopes for determining fatigue failure strains, and fiber reinforcement increases ductility and failure strains compared to plain concrete [50]. Hümme et al. 2016 and Viswanath et al. 2022 compared fatigue failure strains to monotonic strains and found them within the same range as static tests [20, 26].

2.1.5.3 Stiffness evolution and behavior

Similar to the "strain evolution plot," a "stiffness evolution plot" illustrates the gradual degradation of concrete's fatigue secant stiffness, E_{sec}, as the number of fatigue loading cycles (N) increases. A representative stiffness evolution plot is shown in Figure 6, demonstrating a characteristic "upright-S shape." This behavior can also be divided into three distinct phases of stiffness degradation, analogous to the phases observed in strain evolution.

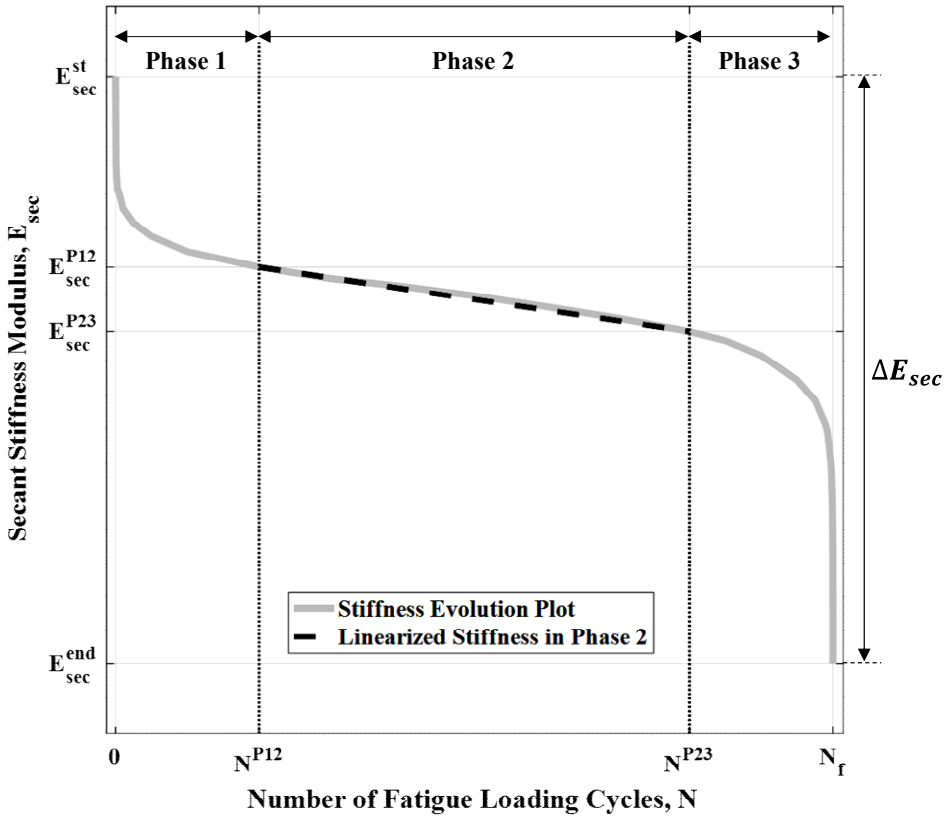

Figure 6 Stiffness evolution plot, depicting the progressive development (degradation) of concrete fatigue secant stiffness as a function of an increasing number of fatigue loading cycles. [25]

2.1.5.3.1 Degree of stiffness degradation

Various studies have quantified stiffness degradation at failure. Holmen 1982 found that the percentage loss of stiffness decreases with higher maximum stress levels (Smax) but that stiffness values before fatigue failure are not influenced by Smax [51]. Similarly, Petkovic 1993 and Haar and Marx 2018 observed greater stiffness degradation at lower Smax [32, 49]. Haar and Marx 2016 also noted that stiffness degradation decreases with increasing log N_f, reflecting the reduced ductility of high-strength concrete (HSC) compared to lower-strength concretes [45].

Holmen 1982 reported a 60% reduction in secant stiffness for normal-strength concrete (40 MPa) over the test period, regardless of Smax [51]. Do et al. 1993 observed that for HSC, the secant modulus converges to a common limit at failure, with values of 75%-85% for 69 MPa concrete

and 85%-95% for 94 MPa concrete [39]. Petkovic et al. 1990 found a 30% reduction in final secant stiffness, reaching about 70% of the initial value for HSC [32].

Bahn and Hsu 1998 illustrated stiffness degradation by unloading at various points along the monotonic stress-strain curve [43]. Zhang et al. 1997 used non-destructive methods to measure residual stiffness in 40 beam specimens under varying fatigue cycles, showing progressive stiffness degradation with increasing fatigue loads [15]. Cachim et al. 2002 observed a 30% reduction in the fatigue modulus for both plain and fiber-reinforced concrete, though final modulus magnitudes varied [50].

Oneschkow 2016 found that lowering Smax increases stiffness loss due to higher N_f. They also noted smaller end stiffness values at lower Smax, without a constant end value being observed. These findings highlight how stiffness degradation varies with stress levels, material strength, and fatigue life [23].

2.1.5.4 Different components of strain

Kim and Kim 1996 categorized strain into initial strain, fatigue strain, and total strain for the first cycle, strain range at cycle N, and total strain at cycle N, respectively [29]. Haar and Marx 2018 noted that fatigue strains consist of elastic and plastic components, with plastic strains resulting from material degradation and crack formation as cycles increase [49]. They also referenced Awad and Hilsdorf 1971 and Whaley 1973, who identified a time-dependent viscous strain component with larger ε_{max} observed in longer tests [37, 52]. Additionally, cyclic loading induces thermal expansion due to specimen heating. Haar and Marx 2018 proposed an additive strain model comprising elastic, damage-induced, time-dependent viscous, and thermal strain components, with plastic deformation arising from damage and viscous strains during fatigue [49].

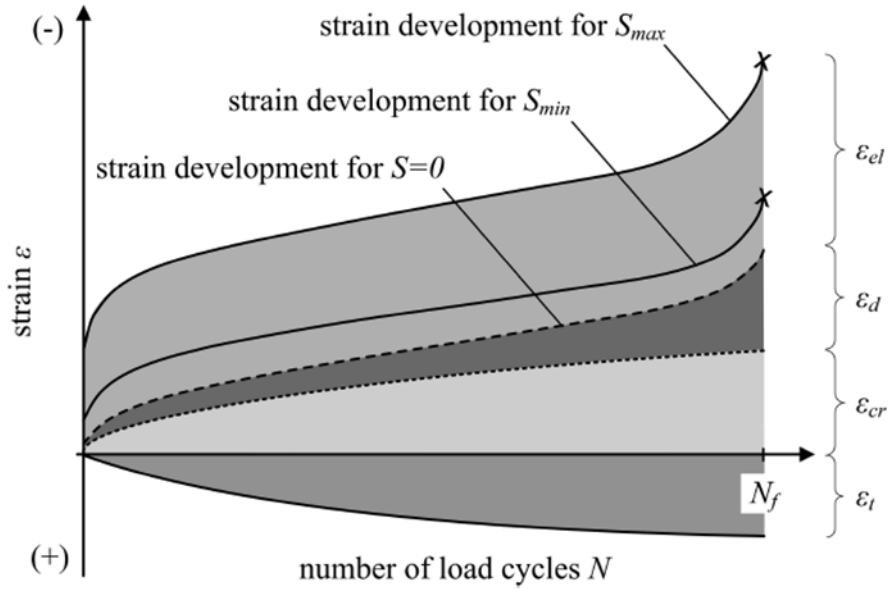

Figure 7 Qualitative development of the strain components versus number of load cycles [49].

Gao and Hsu 1998 divided total strain into irreversible strain (corresponding to valley strain) and strain range. Awad and Hilsdorf 1971 reported higher failure strains in tests with longer failure durations, highlighting a "sustained loading strain component" [37, 53]. Isojeh et al. 2017 classified strain into irreversible and fatigue strain range [24], while Breitenbucher et al. 2007 divided strain into initial and fatigue strains, further subdividing fatigue strain into damage and plastic components [54].

2.1.5.5 Temperature increase effect

Higher loading frequencies are often used to reduce testing time for high-cycle fatigue tests, but this causes specimen heating. Haar and Marx 2018 explained that cyclic loading generates friction, leading to temperature increases, especially at higher frequencies, stress amplitudes, and N_f [49]. Lohaus and Anders 2007 noted that heat-treated specimens can handle higher frequencies without significant temperature rise [42]. Deutscher et al. 2019 observed that high-performance concrete (HPC) and ultra-high-performance concrete (UHPC) specimens warm

significantly during fatigue tests, unlike normal-strength concrete (NSC), which has lower internal friction due to its porous structure and higher water-cement ratio. They found that temperature rise is influenced by factors such as frequency, peak stress level, specimen size, grain size, and concrete strength. At frequencies of 10–20 Hz, heating significantly affects fatigue capacity, with higher heating rates leading to reduced fatigue life [55].

Markert and Laschewski (89) reviewed the factors influencing temperature rise under cyclic loading, including frequency, peak stress, amplitude, strength, surface-to-volume ratio, and aggregate size. They hypothesized that heating may cause cyclic swelling and drying in pores, leading to additional damage. Otto et al. (90) reported that high-strength grout specimens tested at 10 Hz reached temperatures of around 60°C, potentially causing premature fatigue failure below code predictions. Surface temperature increase was dependent on material type, frequency, specimen size, and stress levels. Hümme et al. (79) found that temperature rise was most pronounced in tests at 10 Hz and higher failure cycles, with temperatures reaching 70°C, compared to only 26°C for tests conducted at 1 Hz.

2.2 Introduction to concrete compressive fatigue models

The primary way to determine the reliability of fatigue capacity in design is through the use of S-N curves that are published in codes and standards. These curves depict the relationship between the applied cyclic stress and the number of cycles that concrete is expected to be able to endure before failure. Many models have been proposed over the years, incorporating different stress states and environmental conditions. This project delved into details of existing fatigue models — as well as the origins and application of the data used to generate these models — and then assessed their advantages and limitations before doing additional testing or analysis. This section

presents a summary of the most common fatigue models and their application to concrete fatigue prediction.

2.2.1 Existing fatigue models for concrete

2.2.1.1 Standards

2.2.1.1.1 Model Codes

The International Federation for Structural Concrete (fib) is a pre-normative organization. 'Pre-normative' implies pioneering work in codification. This work has now been realized with the fib model codes. The latest published version of the model code is MC2020. Various versions of the model codes are presented in the following section to shed light on the concrete fatigue models they present.

2.2.1.1.2 Model Code 1990

The MC1990 [56] was published in 1993. The MC1990 covered three different categories of stress state for evaluation of fatigue in concrete, including pure compression, compression-tension, and pure tension and tension-compression. The formulations are presented in Table 1. As the MC1990 stated, the relationships are valid for concrete tested under sealed conditions and large sections of low permeability. The relationships are also valid for concrete that was tested under dry conditions. The fatigue lives given by these equations correspond to a probability of failure p=5% in a log-normal distribution for any given maximum stress. If limited data are available to estimate fatigue strength and number of cycles, the 5% defective fatigue life should be evaluated at a confidence level of 75%. It means that the life estimation would be more conservative since there is less data available. The equations apply for stress level Sc,max and Sct,max<0.9 (Sc,max and Sct,max are maximum normalized stress in compressive and tensile loading, respectively), and frequencies greater than 0.1 cycles/min. For higher stress levels and

lower frequencies (i.e., lower cycle fatigue), lower values of log N may be expected in this model. The model code uses the Sc to represent the normalized compressive strength of material and Sct as the normalized tensile strength of material since it has different formulations for different stress states.

MC1990 does not account for the effect of confinement and longitudinal reinforcement, the impact of saturation, or the effect of loading period/frequency. The fatigue strength and life prediction figures based on the maximum and minimum ratio in the reinforced concrete (RC) section in the three different stress states are presented below. (see Figure 8, Figure 9, and Figure 10)

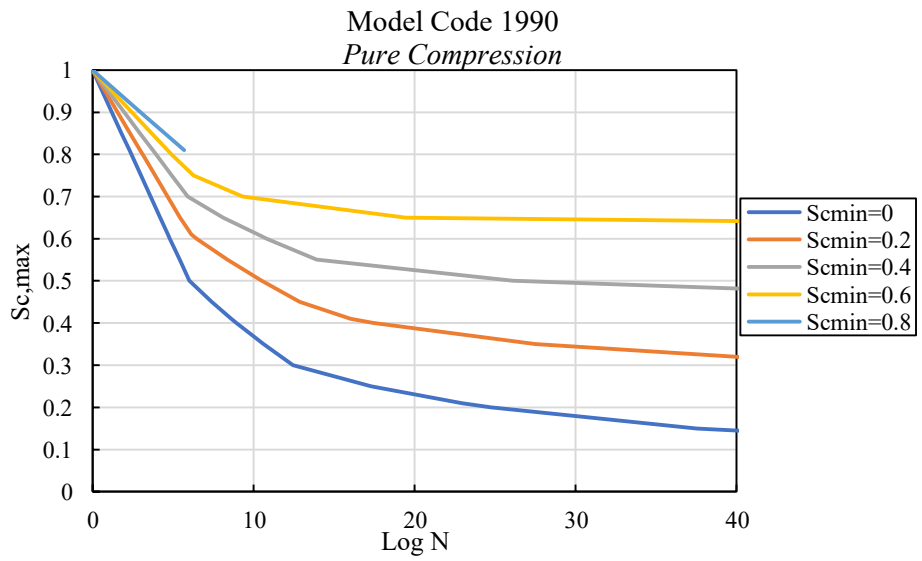

Figure 8 Model Code 1990 S-N curve for the pure compression stress state with different normalized minimum compressive stress (Scmin)

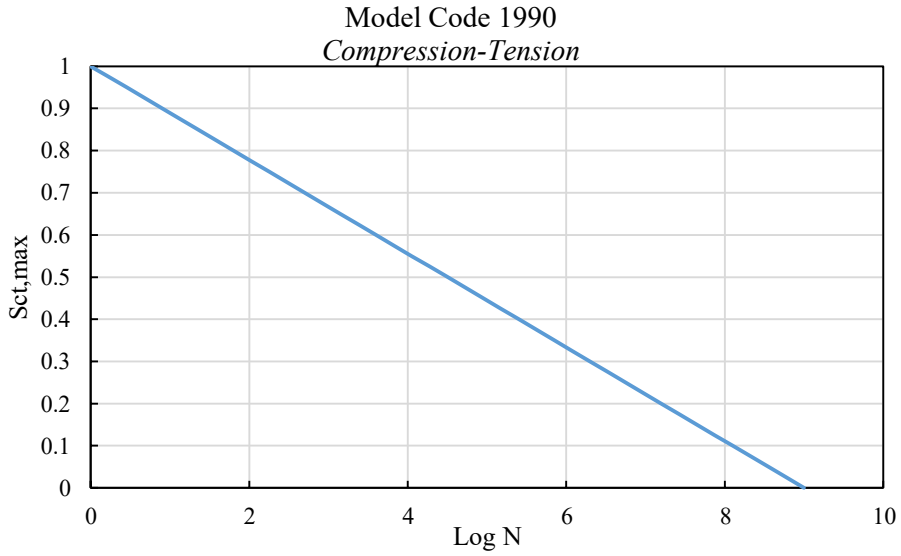

Figure 9 Model Code 1990 S-N curve for the compression-tension stress state.

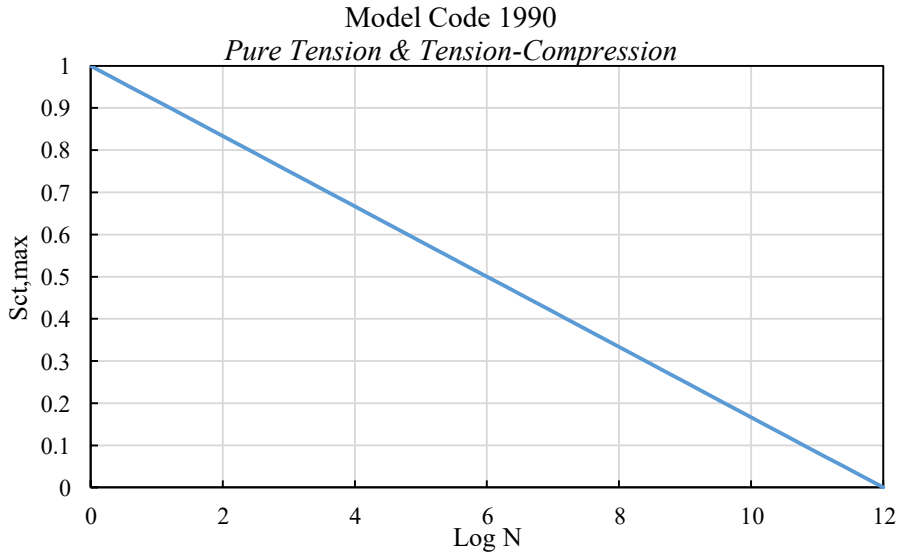

Figure 10 Model Code 1990 S-N curve for pure tension & tension-compression stress state.

2.2.1.1.3 Model Code 2010

The MC2010 [57, 58] was published in 2013. The MC2010, like the previous model code, covers three different stress states for the evaluation of concrete fatigue. The stress states include pure compression, compression-tension, and pure tension & tension-compression. The

formulations are presented in Table 1. The relations are valid for concrete stored in a constant environment of approximately 20 °C and 65 % relative humidity. The relationships between concrete fatigue life and strength are based on experiments with ultra-high strength concrete (up to 200 MPa), and validated for high-strength and normal-strength concrete as well. They have also been verified for up to 10^7 load cycles to failure (*log N = 7)* based on experiments. For higher load cycles, the curves are not verified, and they just asymptotically approach the minimum stress level of the respective curve. The model code expresses that S-N relations can apply to self-compacting concrete due to material considerations, but there is no experimental evidence to prove the idea. There is a large scatter of the experimental results in concrete material, Thus the S-N curves are sometimes the mean curves of the number of load cycles to failure, and sometimes the curve that goes through low 5% percentile of the data. For this particular case, it is the mean curve. So, there is a need to apply a reduction factor to the static strength to take care of safety in design. The equations are applicable for stress levels Sc,max and $S_{ct,max}<0.9$, and for frequencies f>0.1 cycles/min. For higher stress levels and lower frequencies (i.e., lower cycle fatigue), lower values of log N may be expected.

The MC2010 does not account for the effect of confinement and longitudinal reinforcement, the impact of saturation, and the effect of loading period/frequency. Figures of fatigue strength and life prediction based on the maximum and minimum normalized stress ratio in the RC section in the pure compression stress state are presented below (Figure 11). The two other stress states are the same as the previous model code.

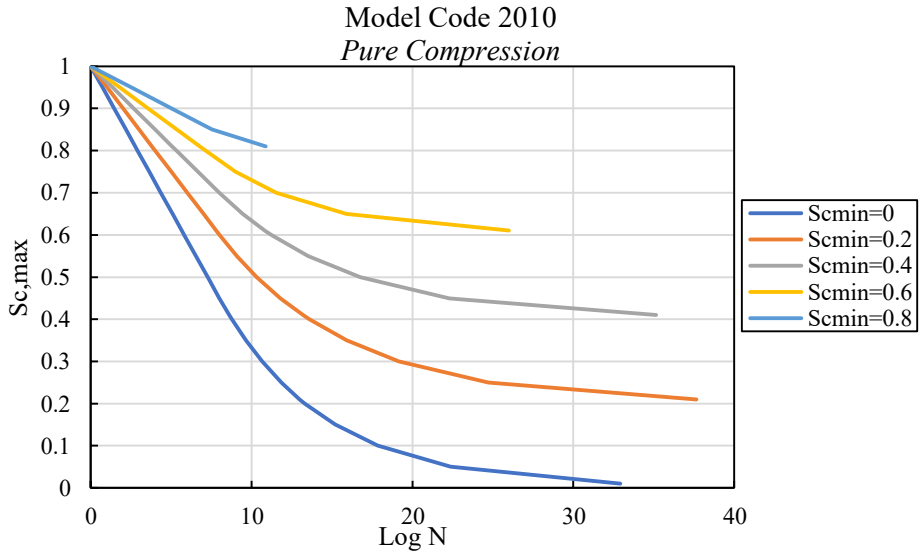

Figure 11 Model Code 2010 S-N curve for the pure compression stress state with different normalized minimum compressive stress (Scmin).

2.2.1.1.4 Model Code 2020

Model Code 2020 considers the effect of water saturation on concrete (the wet concrete vs immersed concrete) by multiplying a factor to the pure compression formulation of MC2010. Characteristic S–N curves for concrete can be used without any restriction for frequencies higher than 0.1 Hz. For lower frequencies, the fatigue life should be reduced. Also, they have added fatigue shear forces verification in their formulations and considerations [59].

Like other models, Model Code 2020 does not consider the effect of confinement and longitudinal reinforcement, the impact of saturation on pure tension and tension-compression state, and the effect of loading period/frequency. Figures showing the fatigue strength and life prediction based on the maximum and minimum ratio in the RC section in the pure compression stress state are presented in Figure 12. The two other stress states are the same as the previous model code.

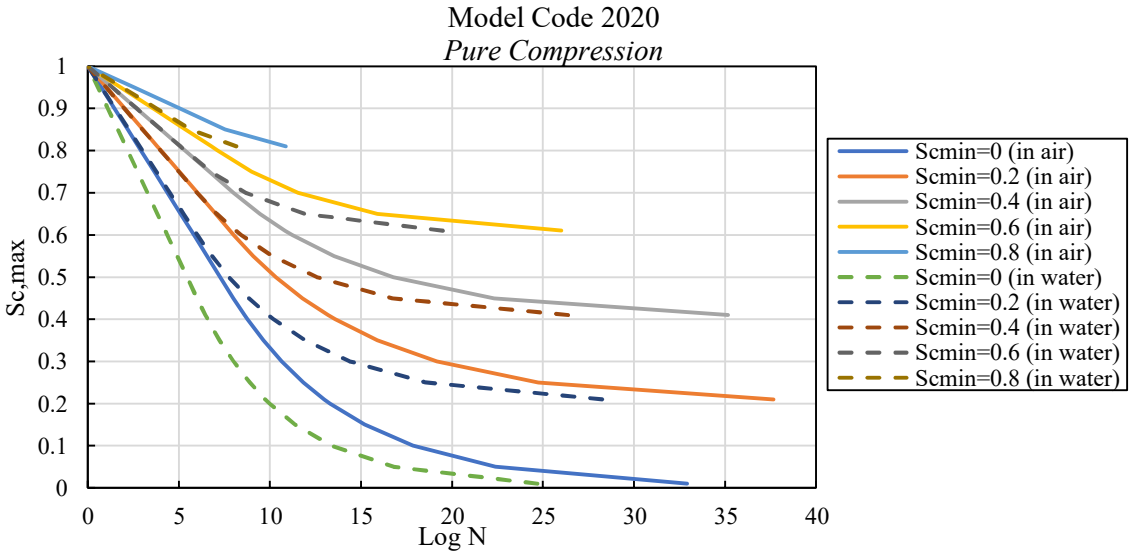

Figure 12 Model Code 2020 S-N curve for the pure compression stress state considering the effect of water with different normalized minimum compressive stress (Scmin).

2.2.1.1.5 DNV-ST-C502

DNV is an internationally accredited registrar and classification society headquartered in Høvik, Norway. They are one of the leading companies in the field of offshore wind. As such, they have a strong knowledge background and are responsible for certifying the design documents of other companies. DNV recommends numerous standards and codes for every aspect of offshore wind. DN-ST-C502 is a standard for offshore concrete structures [60]. The latest version of this code was published in February of 2018. It presents a formulation for pure compression and pure tension fatigue stresses. It also considers the effect of saturation on the estimated fatigue life. It proposes Smin=0 in the compression-tension stress state. Since most codes and research proposed one formulation for fatigue life prediction in different stress states, S is the representative of the normalized strength of the material (compressive, tensile, or flexural).

Similar to the model codes, DNVGL-ST-C502 does not account for the effect of confinement and longitudinal reinforcement or the effect of loading period/frequency. Figures of fatigue strength and life prediction based on the maximum and minimum ratio in the RC section in the

pure compression and compression-tension stress states are presented below (Figure 13 and Figure 14)

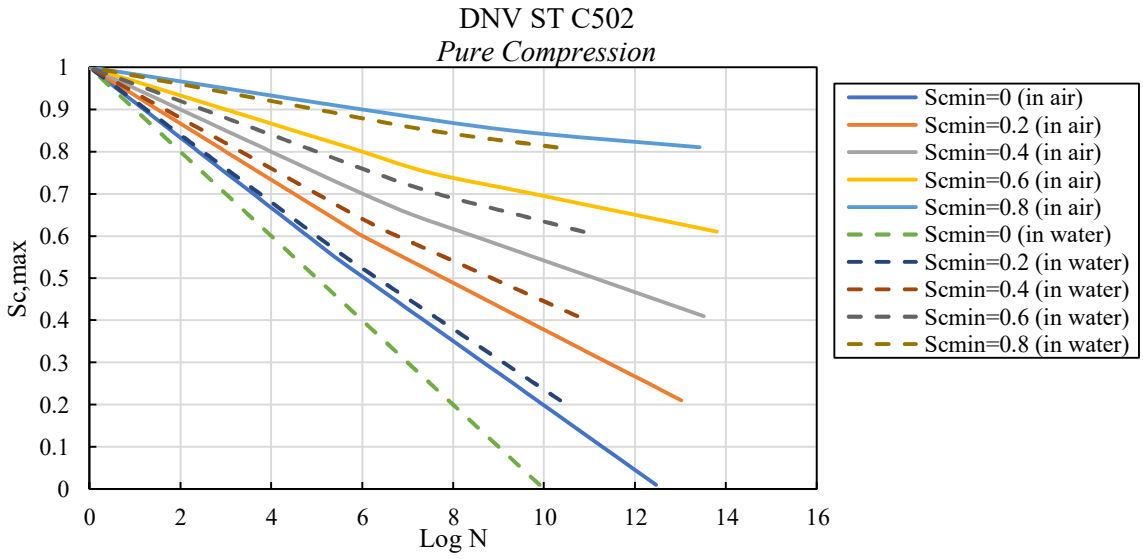

Figure 13 DNV ST C502 S-N curve for the pure compression stress state considering the effect of water with different normalized minimum compressive stress (Scmin).

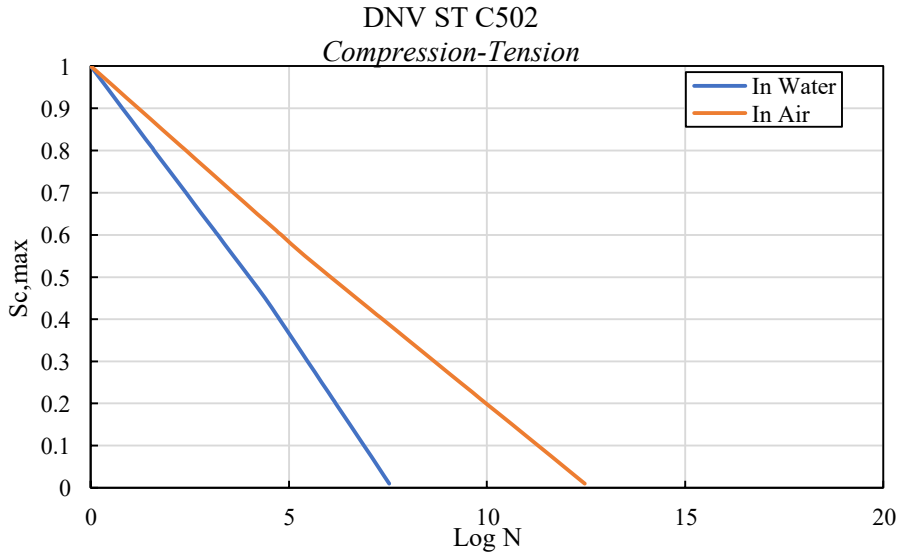

Figure 14 DNV ST C502 S-N curve for the compression-tension stress state considering the effect of water.

2.2.1.1.6 Eurocode 2

The European Standard EN 1992-1-1:2011 [61], called EuroCode2, is a code for the design of concrete structures. There are two different formulas for concrete under compression and shear forces. It also has an equation for the estimation of the concrete fatigue life cycle. This model does not account for the effect of confinement and longitudinal reinforcement, the effect of loading period/frequency, the effect of saturation, and so on. Figures of fatigue strength and life prediction based on the maximum and minimum ratio in the RC section in the pure compression stress state are presented below (Figure 15).

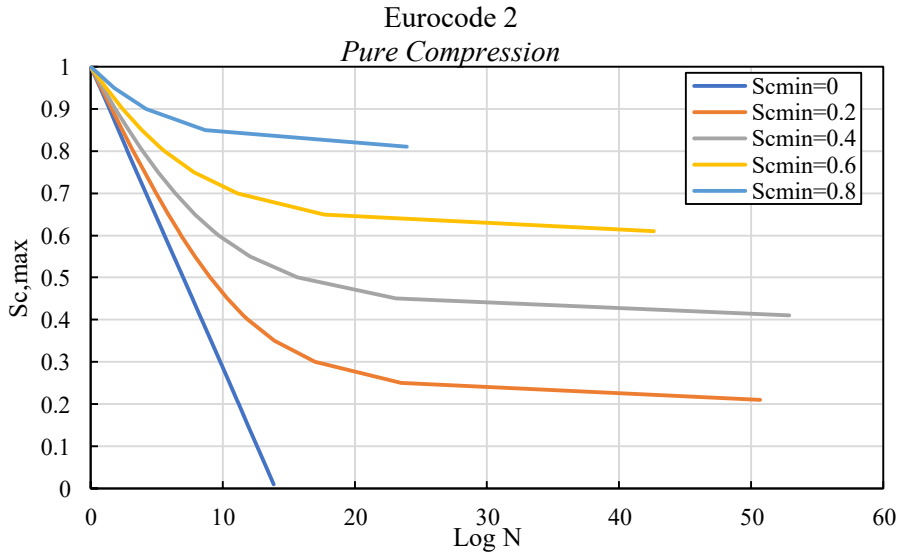

Figure 15 Eurocode-2 S-N curve for the pure compression stress state with different normalized minimum compressive stress (Scmin).

2.2.1.1.7 JSCE 15

The Japanese civil engineering society also has a guideline for designing concrete structures. It was published in 2007. The concrete fatigue formulation given is applicable for the compression and flexural compression, tension, and flexural tension state of stresses. It is applicable for lightweight concrete as well as normal-weight concrete. For high-strength concrete, the code limits the allowable compressive strength of concrete to 50 MPa. For safety reasons, JSCE-15

has four different safety factors for material property and structural elements in the case of fatigue. The code does consider the effect of saturation on the estimation of the life of the concrete. The JSCE.15 [62] has formulations for designing and verifying the structure under fatigue shear forces. This model does not account for the effect of confinement and longitudinal reinforcement, the effect of loading period/frequency, and the effect of compression-tension stress state. Figures of fatigue strength and life prediction based on the maximum and minimum ratio in the RC section in the pure compression stress state are presented (Figure 16).

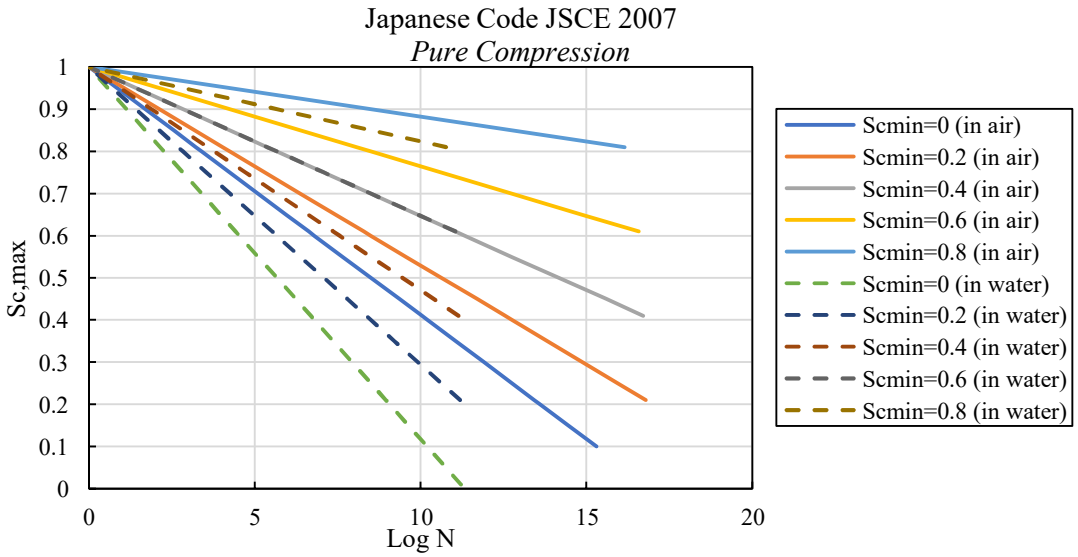

Figure 16 JSCE.15 S-N curve for the pure compression stress state considering the effect of water with different normalized minimum compressive stress (Scmin).

2.2.1.1.8 Dutch Code

The NEN-EN 1992-2+C1 and NEN 6723:2009 [63, 64], known as the Dutch code, have two versions. One was published in 2009, and the other in 2011. Both codes have a formulation to predict the life of concrete under fatigue cyclic loading. The following curves (Figure 17) is derived from those formulations for different maximum and minimum stress levels in the concrete. Fatigue prediction relationships are presented in Table 1. These curves are just for the pure compression stress state because the code does not apply to other stress states. It also does

not account for the effect of confinement and longitudinal reinforcement, the effect of loading period/frequency, and the effect of saturation.

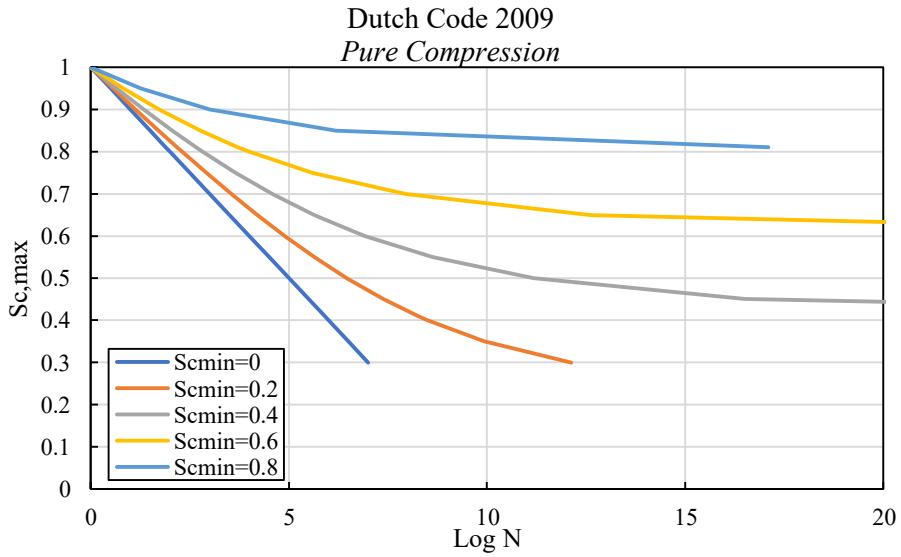

Figure 17 Dutch Code 2009 S-N curve for the pure compression stress state with different normalized minimum compressive stress (Scmin).

2.2.1.2 Papers

There are lots of research publications that present the experimental studies conducted in the field of concrete fatigue, yielding several proposed models for the estimation of material strength under fatigue loading. Most of the proposed models were derived or verified by the results of fatigue tests on some specific concrete materials. These models include all known effective variables in their formulations.

2.2.1.2.1 Hsu et al. 1981

Hsu et al. 1981 [65] gathered existing fatigue compression test data up to the time of the study and proposed a comprehensive relationship among the compressive strength of concrete under cyclic loading, the number of cycles to failure, stress ratio at the concrete cross-section, and the frequency of the loading. There are two different categories of fatigue, including low cycle

fatigue ($N<10^3$) and high cycle fatigue ($10^3<N<10^7$). Hsu et al. proposed two different relationships for the fatigue categories based on the database collected. The equations are presented in Table 1. The following curves are for different maximum and minimum stress levels at pure compression stress state and loading rate of f=1 Hz. (Figure 18)

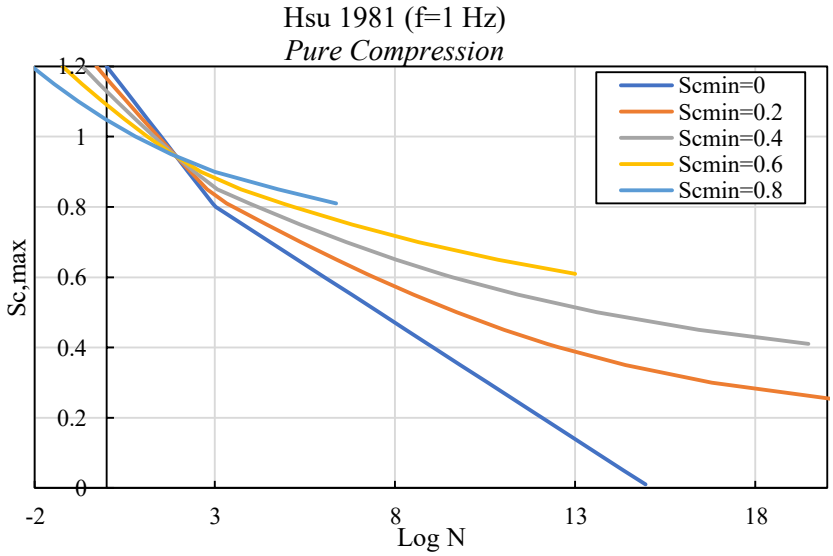

Figure 18 Hsu 1981 S-N curve for the pure compression stress state with different normalized minimum compressive stress (Scmin).

2.2.1.2.2 Zhang et al. 1996 & modified model (1998)

In 1996, Zhang and his colleagues at the University of Glasgow [21] experimented on PC beams under flexural cyclic loads and introduced a model to predict the fatigue life of concrete based on stress ratio and frequency of loading. They considered the effects of different loading regimes, including sinusoidal, triangular, trapezoidal, and square waves [66]. Zhang et al. also investigated the sustained loading effect on the fatigue properties of concrete. Based on the results, the fatigue equation previously proposed by the authors was modified to account for the sustained loading effect. The modified fatigue equations agree well with previous experimental results at high-stress ratios. The fatigue model formulas proposed by Zhang et al. are presented

in Table 1. The following curves also show the relationship between the number of cycles to failure at different stress stages. (Figure 19 and Figure 20)

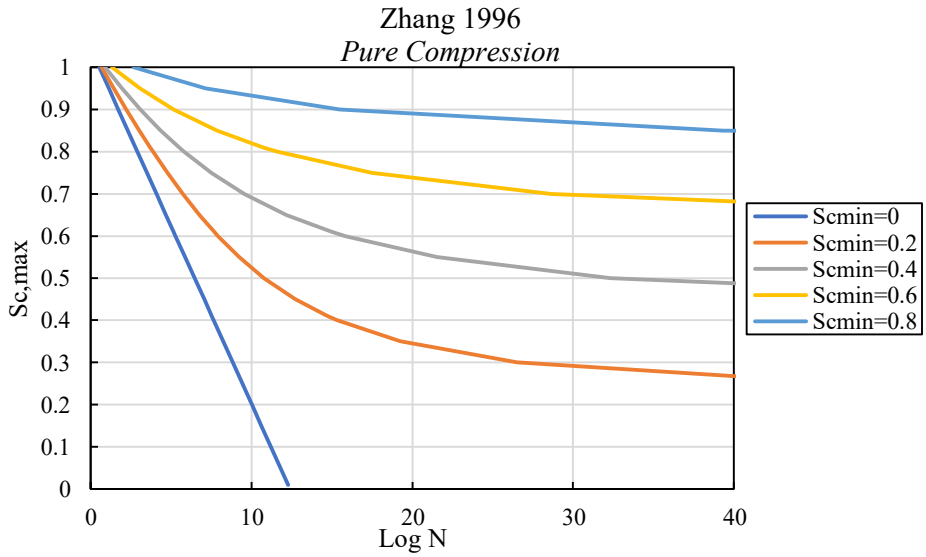

Figure 19 Zhang et al. 1996 S-N curve for the pure compression stress state with different normalized minimum compressive stress (Scmin).

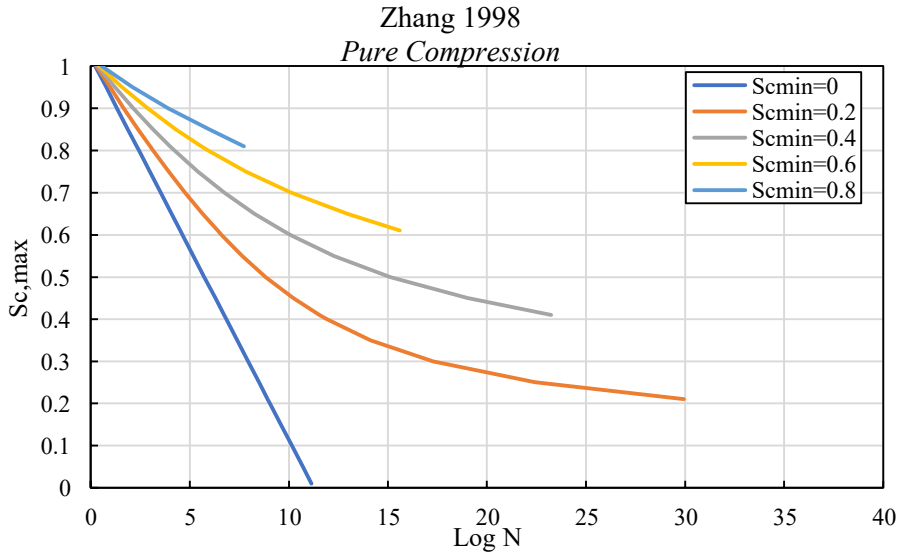

Figure 20 Zhang et al. 1998 (modified) S-N curve for the pure compression stress state with different normalized minimum compressive stress (Scmin).

2.2.1.2.3 Kim & Kim 1998

In 1996, Kim and Kim [29] tested plain cylindrical concrete with different stress levels and a loading frequency of 1 Hz in order to propose a fatigue life prediction model. The proposed model was based on concrete's maximum stress level and static compressive strength. The relationship is presented in Table 1. The following curve shows the relationship between the maximum stress level and the number of cycles to failure. (Figure 21)

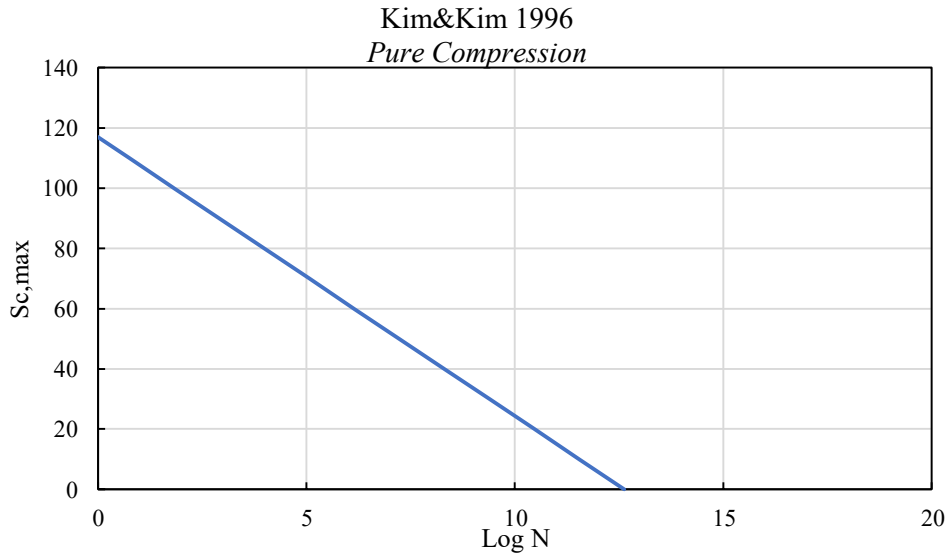

Figure 21 Kim and Kim 1996 S-N curve for the pure compression stress state with different normalized minimum compressive stress (Scmin).

2.2.1.2.4 Lantsoght et al. 2013

Lantsoght [67, 68] et al. gathered data from different research studies to make a comparison between collected data and the few fatigue models — including MC2010 and Dutch Codes — that existed at the time. They proposed a formulation (Table 1) that is a modified version of Dutch code 2011. The formulation, which is for pure compression stress states, can be used to predict the life of concrete under fatigue loading. Figure 22 is for different maximum and minimum stress levels in the section of concrete.

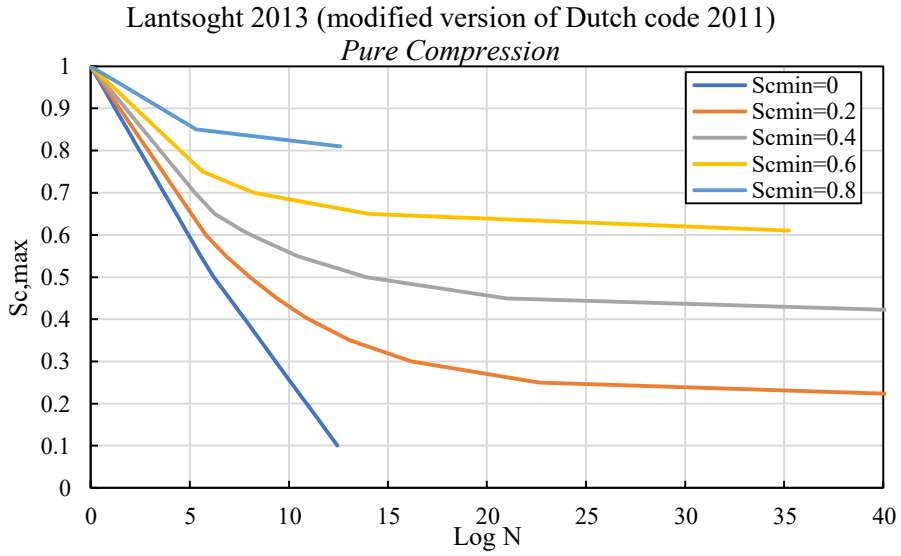

Figure 22 Lantsoght et al. 2013 S-N curve for the pure compression stress state with different normalized minimum compressive stress (Scmin).

2.2.1.3 Evaluation and comparison of design requirements

In order to compare the different models, over 10 of the fatigue S-N models have been organized within a spreadsheet. The relationships of the models in a pure compression stress state are listed in the following table (Table 1). All equations depend on the maximum stress ratio to predict the number of cycles to failure under different stress levels/ratios. Some of the equations are applicable to different loading categories like compression, tension, flexural loading, and shear force (Table 6). Different codes have safety measures, such as partial safety factors, which are presented in Table 2 and Table 3. Almost all of the models are suitable for normal and high-strength concretes. Some codes also consider ultra-high strength and lightweight concretes (Table 4). Only a few codes have considered saturation in their fatigue evaluation (Table 5). All of this information has been gathered in a spreadsheet in order to compare the various models. For the next step, the database explained in task 1 should be merged into the spreadsheet to

evaluate the validity of the S-N models. The curves derived from different S-N models at different stress states are presented in the following figures (see Figure 23, Figure 24, Figure 25, Figure 27, and Figure 28). Model Code 2020 and Dutch Code 2011 are the most conservative S-N models.

Table 1 Existing S-N models for prediction of fatigue life of concrete under pure compression stress state

Reference	Formulation	Comments
Model Code 1990	$logN_1 = 12 + 16 * S_{min} + 8 * S_{min}^2$ $logN_2 = 0.2 * logN_1 * (logN_1 - 1)$ $logN_3 = logN_2 * \frac{(0.3 - 0.375 * S_{min})}{\Delta S}$ *If $logN_1 \leq 6$, then $logN = logN_1$ *If $logN_1 > 6$ & $\Delta S \geq 0.3 - 0.375 * S_{min})$, then $logN = logN_2$ *If $logN_1 > 6$ & $\Delta S < 0.3 - 0.375 * S_{min})$, then $logN = logN_2$	For S_{min}>0.8, use S_{min}=0.8 in the S-N formulation $\Delta S = S_{max} - S_{min}$ $f_{ck,fat}$: Special definition
Model Code 2010	$Y = \frac{0.45 + 1.8 * S_{min}}{1 + 1.8 * S_{min} - 0.3 * S_{min}^2}$ $logN_1 = 8 * \frac{(S_{max} - 1)}{(Y - 1)}$ $logN_2 = 8 + \frac{8 * ln(10)}{(Y - 1)} * (Y - S_{min}) * log(\frac{S_{max} - S_{min}}{Y - S_{min}})$ *If $logN_1 \leq 8$, then $logN = logN_1$ *If $logN_1 > 8$, then $logN = logN_2$	For S_{min}>0.8, use S_{min}=0.8 in the S-N formulation $\Delta S = S_{max} - S_{min}$ $f_{ck,fat}$: Special definition
EuroCode2	$logN = 14 * \frac{1 - S_{max}}{\sqrt[2]{1 - R}}$	Verification: $S_{max} \leq 0.5 + 0.45 * S_{min}$ & $S_{max} \leq 0.9\ for\ f_{ck} \leq 50MPa$ or $S_{max} \leq 0.8\ for\ f_{ck} > 50MPa$ *Valid for $N \leq 10^6$

Table 1 (continued I) Existing S-N models for prediction of fatigue life of concrete under pure compression stress state

Reference	Formulation	Comments
DNVGL St C502	$X = \frac{C_1}{1 - {S_{min}}/{C_5} + 0.1 * C_1}$ $logN_1 = C_1 * \frac{(1 - {S_{max}}/{C_5})}{(1 - {S_{min}}/{C_5})}$ $C_2 = \left(1 + 0.2 * (logN_1 - X)\right) > 1.0$ *If $logN_1 \leq X$, then $logN = logN_1$ *If $logN_1 > X$, then $logN = C_2 * logN_1$	C_1: 12 in the air – 10 in water C_5: 1 for concrete
JSCE15 (2007)	$logN_1 = 17 * \frac{1 - S_{max}}{1 - S_{min}}$ *Dry concrete, then $logN = logN_1$ *Concrete immersed in water, then $logN = \frac{2}{3} * logN_1$	*Valid for $N \leq 2 * 10^6$ *For $N > 2 * 10^6$ experimental studies are required.
DutchCode2009	$logN = 10 * \frac{(1 - S_{max})}{\sqrt[2]{1 - R}}$	*Valid for S_{max}>0.25
DutchCode2011	$logN = \frac{6}{1 - 0.57 * k_l(1 - \frac{f_{ck}}{250})} * \frac{(1 - E_{max})}{\sqrt[2]{1 - R}}$ & $E_{max} = {S_{max}}/{(0.9 + \frac{logN}{60})}$ $logN = 14 * \frac{1 - S_{max}}{\sqrt[2]{1 - R}}$	Eq. (I) for ($N<10^6$) Eq. (II) for ($10^6<N$)
Hsu 1981	$S_{max} = 1.2 - 0.2R - 0.133(1 - 0.779R)logN - 0.053(1 - 0.445R)logT$ $S_{max} = 1 - 0.0662(1 - 0.556R)logN - 0.0294logT$	Eq. (I) for low cycle fatigue ($N<10^3$) Eq. (II) for high cycle fatigue ($10^3<N<10^7$)
Zhang 1996	$S_{max} = C_f(1 - (1 - R)\beta logN)$ $C_f = ab^{-logf} + c$	For normal strength concrete $\beta = 0.0807$ a=0.249 b=0.92 c=0.796

Table 1 (continued II) Existing S-N models for prediction of fatigue life of concrete under pure compression stress state

Reference	Formulation	Comments
Zhang 1998 (modified)	$S_{max} = C_f(1-(1-R)\beta_1 logN + \gamma_1 logT_{max})$ $T_{max} = {N\omega}/{f}$ $\beta_1 = 0.06606 - 0.02258R$ $\omega = \frac{B_{T2} * l}{(-1+B_{T2})(1-R)}\left(1 - R\lvert R\rvert^{-1/B_{T2}}\right) + \frac{(1-l)}{2}(1+\lvert R\rvert^{-1/B_{T2}})$	$C_f = 1$ $\gamma_1 = 2.468 * 10^{-2}$ λ=0.7268 $B_{T2} = -0.0116$
Lantsoght 2013	$logN = \frac{6*(S_{max}-1)}{(S_{max,EC}-1)}$ & $S_{max,EC} = \left(1-\frac{f_{ck}}{400}\right)(1-\frac{3}{7}\sqrt{1-\frac{S_{min}}{S_{max,EC}}})$ $logN = 14 * \frac{1-E_{max}}{\sqrt[2]{1-R}}$ & $E_{max} = {S_{max}}/{(1-\frac{f_{ck}}{400})}$	Eq. (I) for ($N<10^6$) Eq. (II) for ($10^6<N$) For normal-strength concrete
Kim and Kim 1998	$S_{max} = -7.6\left(\frac{f_c'}{f_l'}\right)^{0.066} logN + 126\left(\frac{f_c'}{f_l'}\right)^{-0.025}$	$f_l' = 1\ MPa$
Model Code 2020	$Y = \frac{0.45 + 1.8 * S_{min}}{1 + 1.8 * S_{min} - 0.3 * S_{min}^2}$ $logN_1 = 8 * \frac{(S_{max}-1)}{(Y-1)}$ $logN_2 = 8 + \frac{8 * ln(10)}{(Y-1)} * (Y - S_{min}) * log(\frac{S_{max}-S_{min}}{Y-S_{min}})$ *If $logN_1 \leq 8$, then $logN = \omega_w * logN_1$ *If $logN_1 > 8$, then $logN = \omega_w * logN_2$	For $S_{min}>0.8$, use $S_{min}=0.8$ in the S-N formulation $\Delta S = S_{max} - S_{min}$ $f_{ck,fat}$: Special definition ω_w: 1 for dry concrete 0.75 for wet concrete

Smin and Smax are normalized minimum and maximum stresses due to cyclic loading at the cross-section, and fatigue evaluation is needed. These stresses are normalized with the static strength of the material.

- N is the number of cycles to failure due to cyclic loading.
- R is the ratio of minimum to maximum stress due to cyclic loading at the evaluation point.

Table 2 Partial fatigue safety factors for the strength of materials

Material safety factors				
Standards / Type of material	Plain concrete	Fiber-reinforced concrete	Reinforced Concrete	Steel
DNVGL-st-c502	1.8	1.5 / 1.35*	1.5 / 1.35*	1.1 - 1*
Eurocode2	-	-	1.5	1.15
JSCE.15 (2007)	-	-	1.3	1.05
Model Code 1990	-	-	1.5	1.1
Model Code 2010	-	-	1.5	1.1
DutchCode2009	-	-	1.35	
DutchCode2011	-	-	1.35	
* For accurate design				

Table 3 Partial fatigue safety factors for load cases

Standards	Load safety factors
DNVGL-st-c502	1
Eurocode2	1
JSCE.15 (2007)	1
Model Code 1990	1.1 / 1*
Model Code 2010	1.1 / 1*
DutchCode2009	1
DutchCode2011	1
* For accurate stress analysis	

Table 4 Type of concrete considered in fatigue models

Standards / Type of concrete	Reinforced concrete				Fiber-reinforced concrete
	Ultra-Strength	High Strength	Normal Strength	Lightweight	
DNVGL-st-c502	-	Y	Y	Y	Y
Eurocode2	-	Y	Y	-	-
JSCE.15 (2007)	-	-	Y	-	-
Model Code 1990	-	Y	Y	-	-
Model Code 2010	Y	Y	Y	-	-
DutchCode2009	N/A	N/A	N/A	N/A	N/A
DutchCode2011	N/A	N/A	N/A	N/A	N/A

Table 5 Saturation type

Saturation type			
Standards	wet	submerged	dry
DNVGL-st-c502	Y	Y	Y
Eurocode2	-	-	Y
JSCE.15 (2007)	Y	-	Y
Model Code 1990	-	-	Y
Model Code 2010	-	-	Y
Model Code 2030	Y	Y	Y
DutchCode2009	-	-	Y
DutchCode2011	-	-	Y

Table 6 Stress states and shear design

State of stress				Shear design
Standards	pure compression	compression-tension	pure tension	
DNVGL-st-c502	Y	Y	-	-
Eurocode2	Y	-	-	Y
JSCE.15 (2007)	Y	-	Y	Y
Model Code 1990	Y	Y	Y	-
Model Code 2010	Y	Y	Y	-
DutchCode2009	Y	-	-	-
DutchCode2011	Y	-	-	-

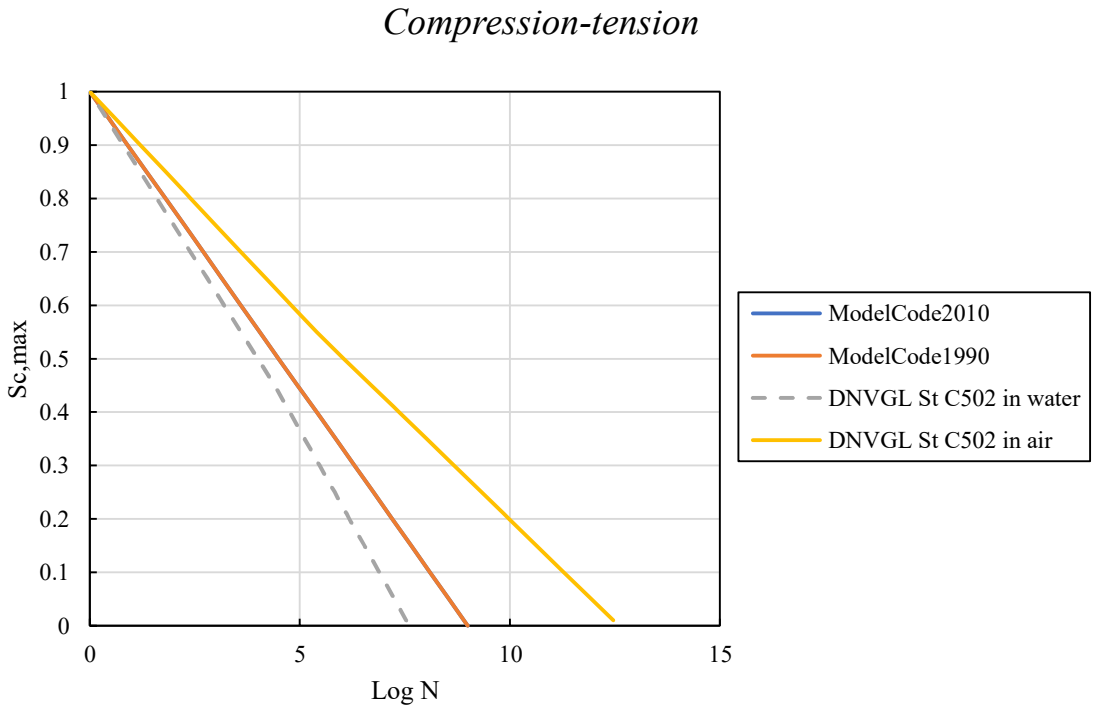

Figure 23 S-N models at compression-tension stress state.

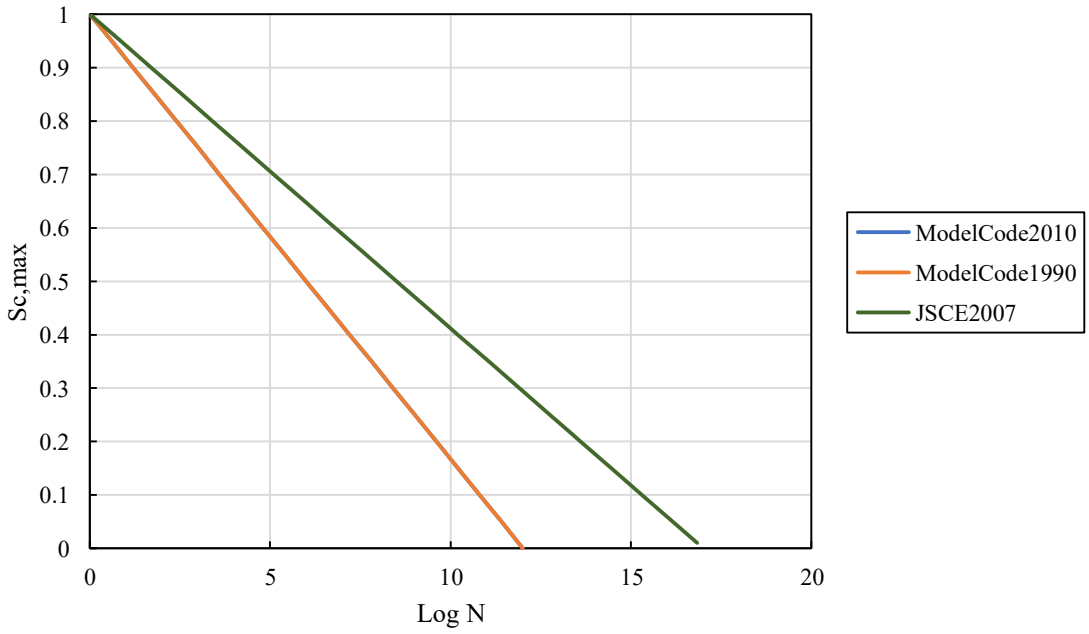

Figure 24 S-N models at pure tension stress state

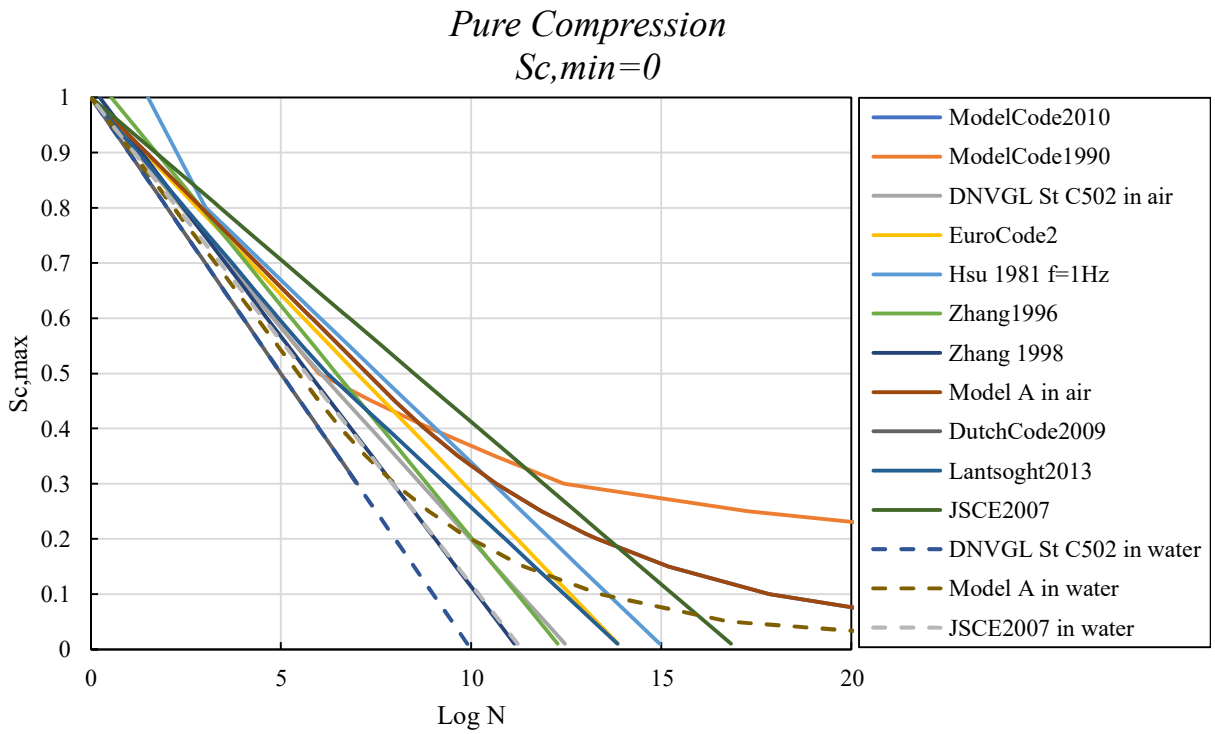

Figure 25 S-N models at pure compression stress state with a minimum stress level of 0.

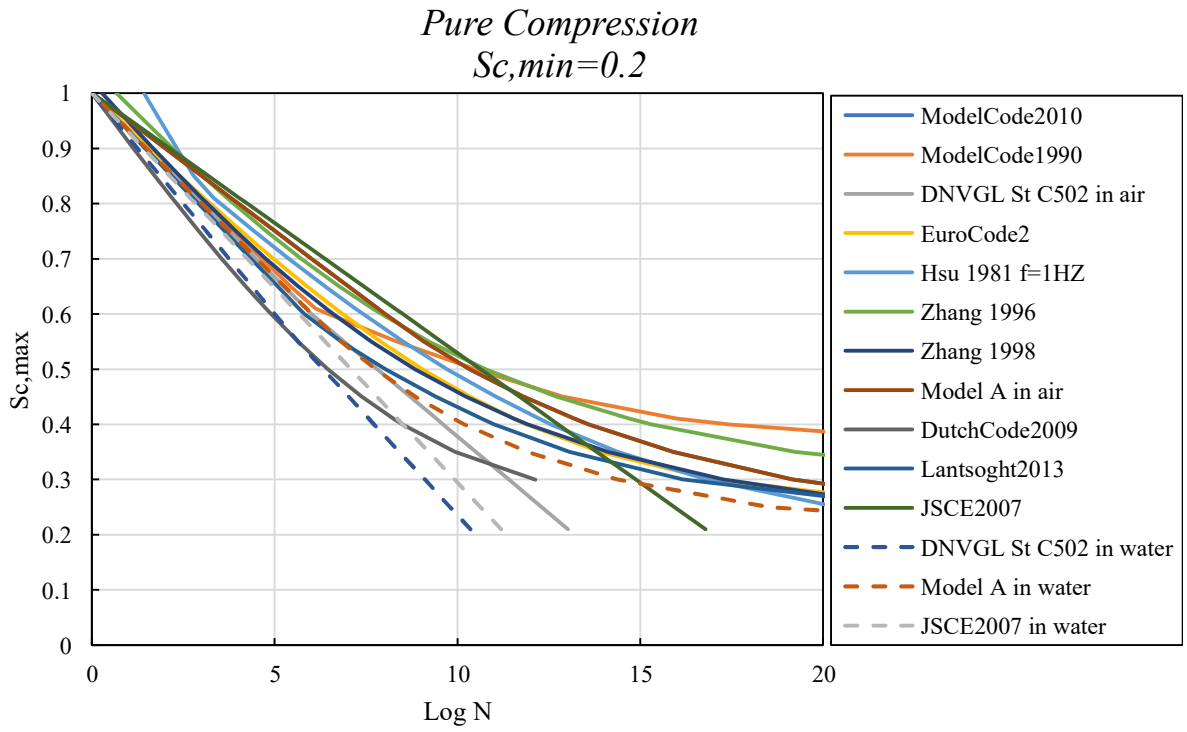

Figure 26 S-N models at pure compression stress state with a minimum stress level of 0.2.

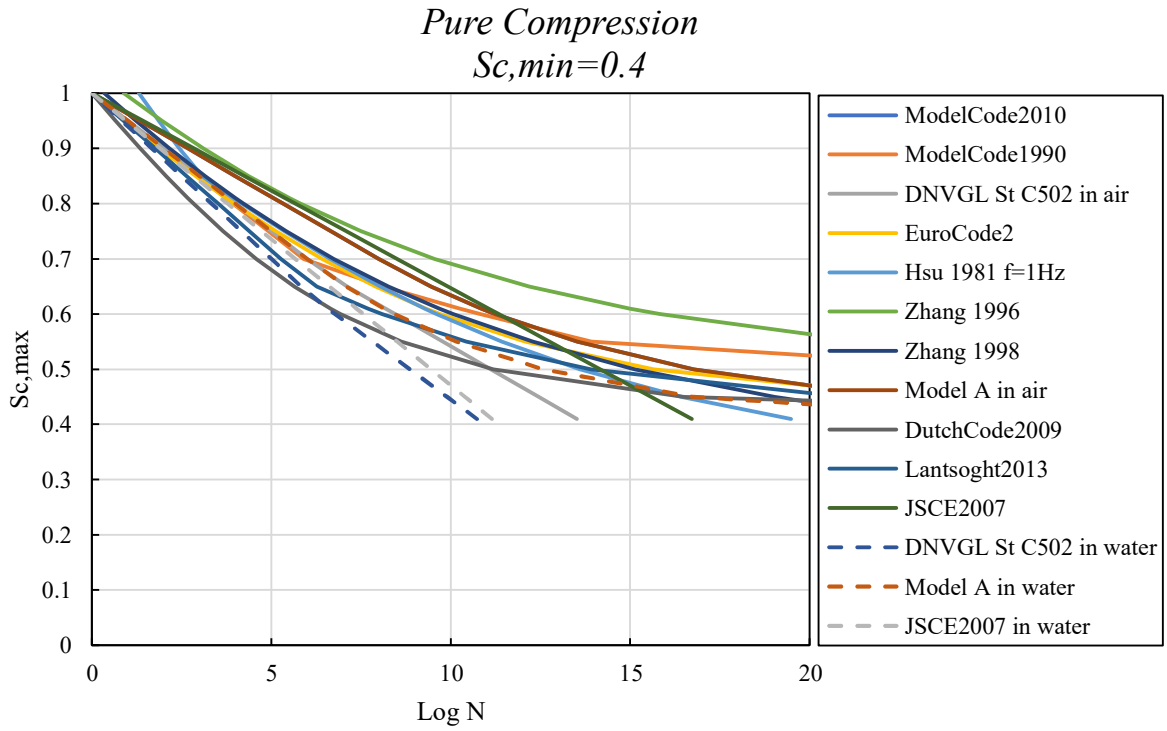

Figure 27 S-N models at pure compression stress state with a minimum stress level of 0.2.

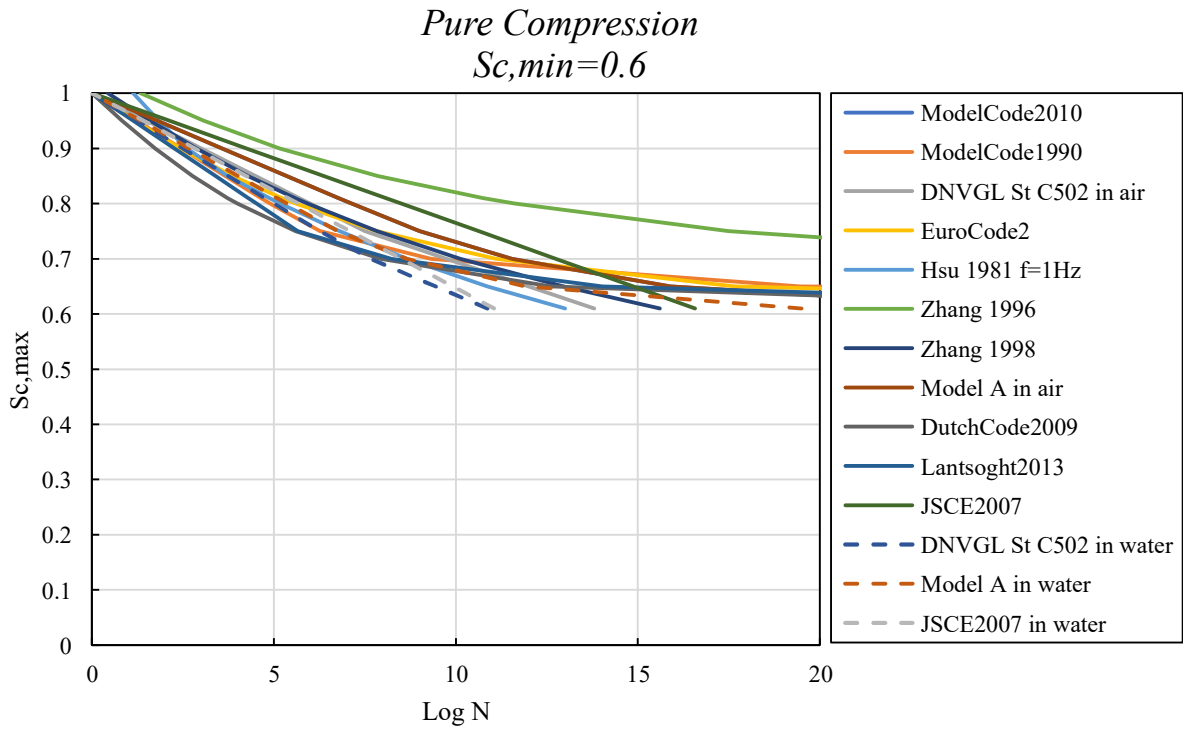

Figure 28 S-N models at pure compression stress state with a minimum stress level of 0.6.

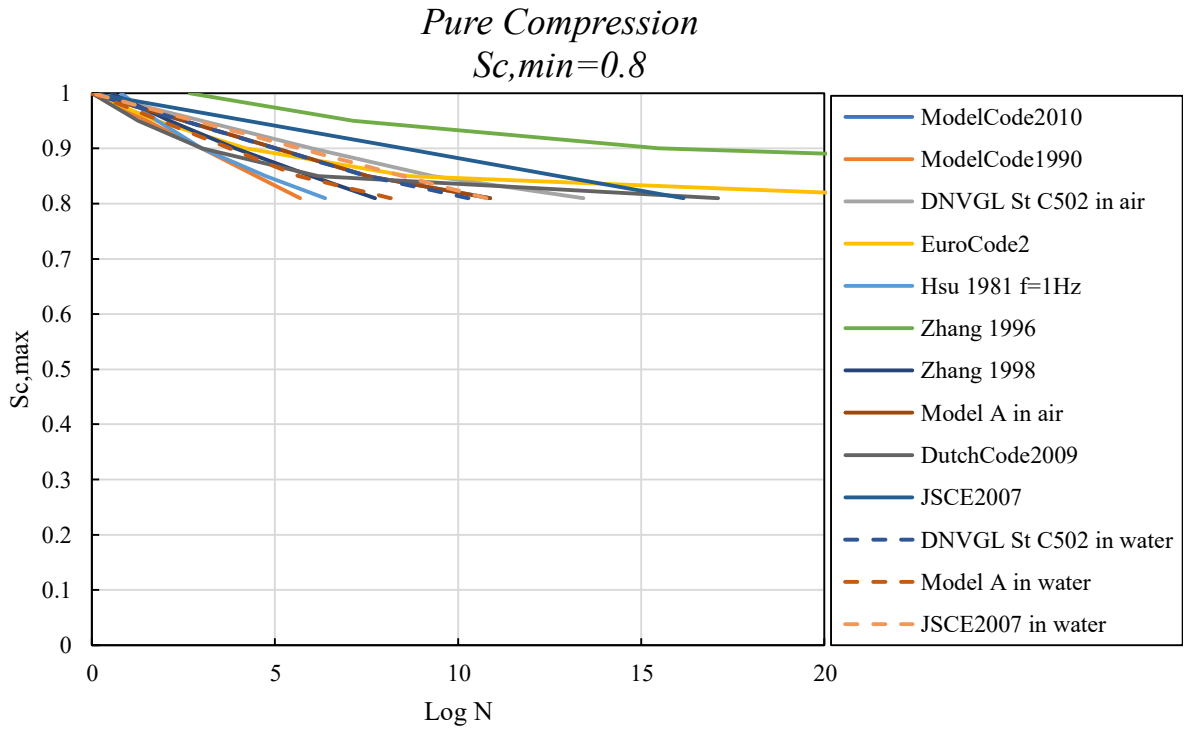

Figure 29 S-N models at pure compression stress state with the minimum stress level of 0.8.

Based on the stress demand evaluation in offshore wind turbine structures in task 4, it can be confirmed that the maximum normalized stress ratio is considerably low (less than 0.6) and the ratio of minimum stress to maximum stress at the point of evaluation (R) tends to be between 0.7-1. On the other hand, almost all of the available data from the previous research have high Smax values (greater than 0.6) and very low R-values (lower than 0.5). Therefore, there is a lack of required data pertinent to the evaluation of stress demand. Figure 30 shows that the high values of maximum stress have fewer cycles to the failure. Also, by considering the safety factors, it is observable that most of the models have a conservative approach for estimating material life under fatigue loads, which is due to a large scatter of existing data and variation of fatigue capacity from one concrete mix to the other one.

As mentioned, the stress demand is different from what was tested before. If the maximum stress value is considered to be around 0.4-0.5 and the stress ratio to be equal to 0.8, there would be

huge variability among models in estimates of the number of cycles and failure (see Figure 31). In this specific case, the estimated N will vary between 10^7 to 10^{40}, which is a very large distribution which would affect the design intensely. So, there is a need to have new tests to cover the lack of knowledge in the aforementioned evaluation and propose an accurate model for estimating the material's fatigue life.

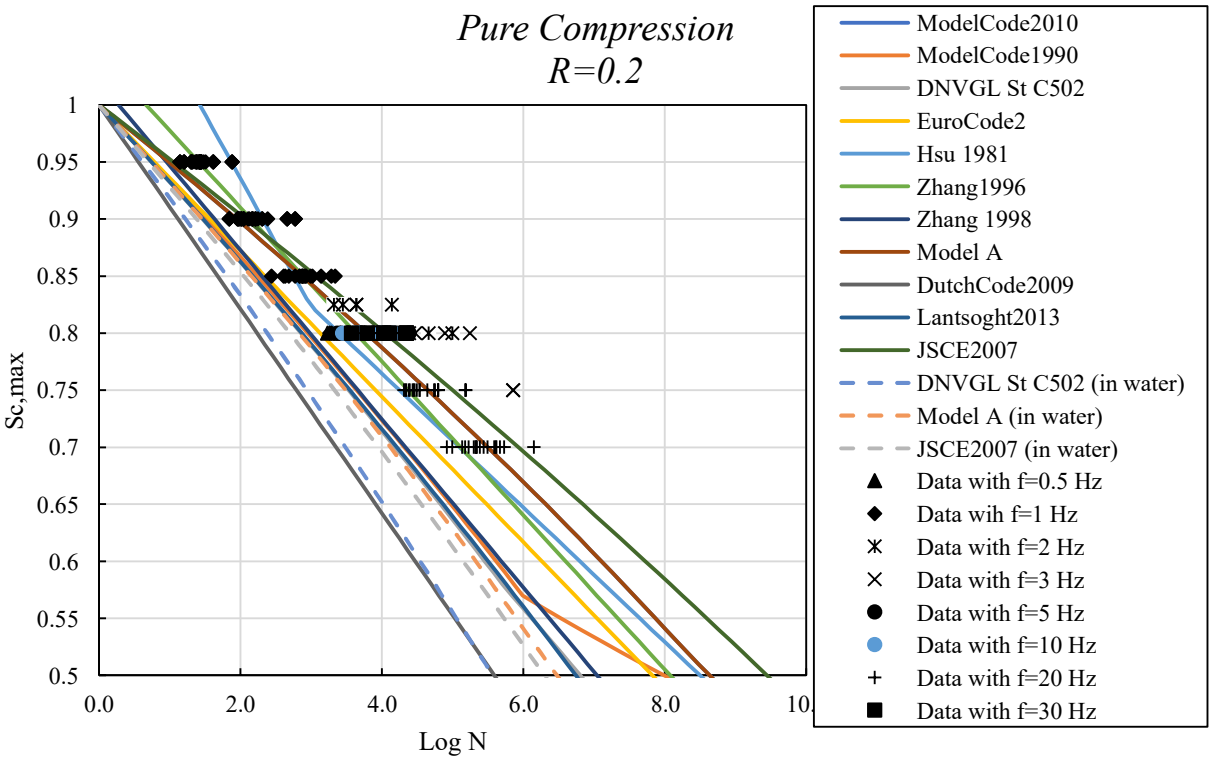

Figure 30 Evaluation of existing data and S-N models for stress ratio of 0.2.

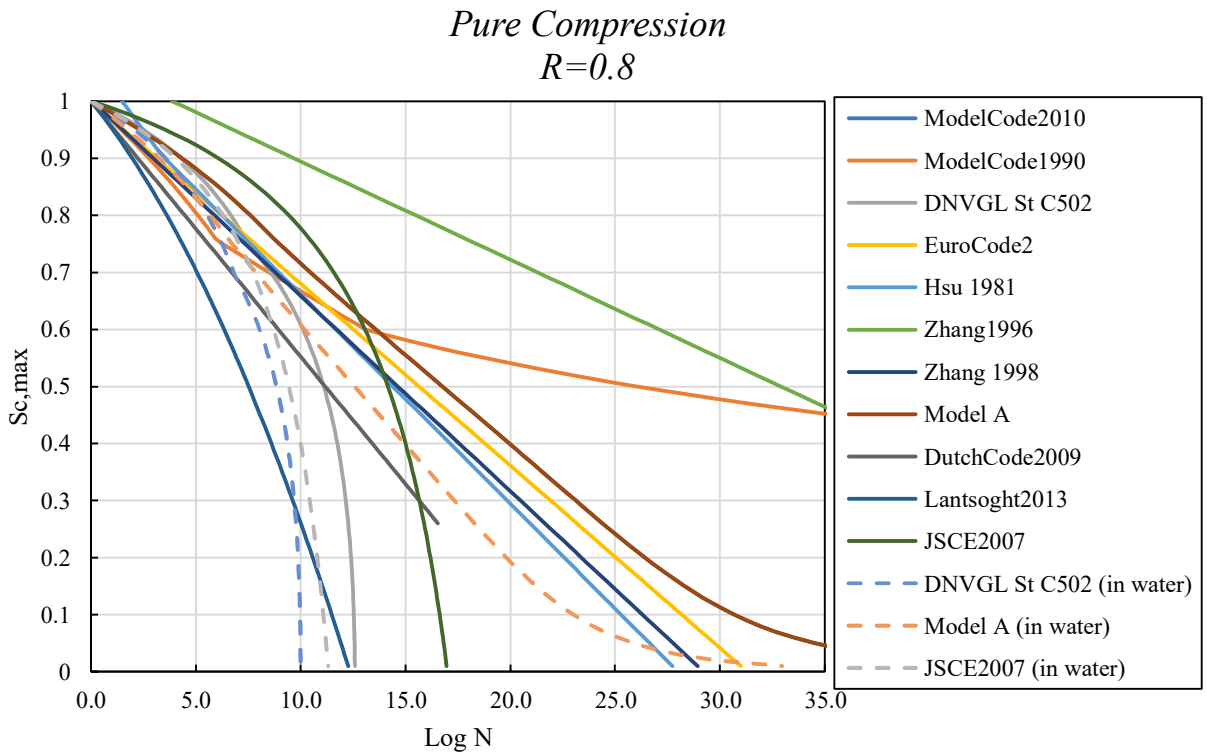

Figure 31 S-N models at pure compression stress state with a stress ratio of 0.8.

2.2.1.4 Summary

Overall, 13 different concrete fatigue life estimation models (S-N models) have been organized within a spreadsheet. The design requirements of these models were extracted from codes, standards, books, theses, and research papers. Almost all of the codes have the same methodology and use Hain's models to evaluate fatigue life in design.

Some of the limitations mentioned could significantly impact the final results, and it is recommended that they be evaluated in the upcoming test series. All of the S-N models are for PC in different stress states, and they do not consider the impact of reinforcement (both longitudinal and transverse) and confinement on the final number of cycles to failure. In static loading, both elements significantly impact the final result of strength. Furthermore, the effect of saturation has not been well-studied.

The stress demand evaluation in offshore wind turbine structures in task 4 showed that the existing test results are irrelevant to the required stress demands. Also, the existing models do not predict the number of cycles at failure at required stress demands.

2.3 Factors influencing fatigue capacity of concrete

Fatigue loading involves subjecting a specimen to repeated stress cycles, where the stress levels (both peak and valley) remain below the material's static strength. Over time, this repeated loading can cause cumulative and irreversible internal damage, leading to structural failure even if the applied stress does not exceed the static capacity. For uniaxial compressive fatigue in plain concrete, the material's strength is tied to its compressive capacity, while flexural fatigue is typically governed by the modulus of rupture due to tensile stress dominance. These internal changes under fatigue loading manifest as crack growth, increased strains, and stiffness degradation. making it essential to study and document concrete's fatigue behavior to ensure the safe design of critical structures such as bridges, pavements, wind turbine foundations, and offshore installations.

Although research on concrete under fatigue loading has been ongoing for decades, the complexity of influencing factors — ranging from material composition and specimen size to loading configurations — has made comprehensive and conclusive studies challenging. Conflicting findings and varying code recommendations further complicate the field. To address these issues, a review of existing literature on concrete fatigue capacity and behavior— along with factors affecting these properties — has been conducted and is presented below.

2.3.1 Variability in concrete strength and its impact on scatter of fatigue test results

Breitenbucher and Ibuk 2006 highlighted that the coefficient of variation in fatigue test outcomes can be extremely high, resulting in significant data scatter and necessitating caution when interpreting results, particularly those based on limited or non-replicated tests [54]. Cornelissen and Reinhardt 1984 demonstrated that the variability in concrete strength is directly linked to its behavior under fatigue testing [69]. According to Tepfers and Kutti 1979, the fatigue capacity is particularly sensitive to deviations in concrete strength from its mean value, especially at higher maximum stress levels (Smax > 0.80). Their findings revealed that reducing Smax from 0.95 to 0.90 (at R = 0) doubled the fatigue life (Nf), while a reduction from 0.80 to 0.76 resulted in a 20% increase in Nf [70].

Lenschow 1982 noted that although fatigue tests generally exhibit greater scatter compared to static tests, the standard deviation for fatigue and static strengths remains similar on average [71]. Siemes 1982 asserted that the variation in the number of cycles to failure in constant amplitude tests is entirely attributable to the variability in static strength [72], a conclusion corroborated by Holmen 1982 [51]. These studies also demonstrated that the fatigue life (Nf) follows a log-normal distribution, where $\log_{10}(\mathrm{Nf})$ exhibits a normal (Gaussian) distribution. Similarly, Petkovic et al. 1990 found that most of the scatter in fatigue test results could be accounted for by the variability in static strength [32], while Lohaus et al. 2012 observed that this static strength variance fully encompasses the tolerance range of fatigue regression lines [58].

Dyduch and Destrebecq 1994 emphasized that the inherent heterogeneity of concrete contributes to experimental scatter — even under static loading — which influences stress levels during fatigue testing. When peak stress exceeds 75% of static strength, the uncertainty in static strength significantly impacts fatigue outcomes. Consequently, these researchers implemented a static

loading test before each fatigue test to assess the specimen's actual static strength, which was then used to normalize fatigue stress levels. Despite these meticulous efforts, the fatigue test results continued to exhibit substantial variability [41].

Recent studies have further explored the variability in concrete fatigue test results and the influence of monotonic strength on fatigue capacity. Becks and Classen (2021) investigated high-strength concrete under mode II loading and found that both monotonic shear strength and fatigue life are significantly affected by concurrent compressive stress. Their results indicated that while fatigue life is sensitive to variations in the shear stress range, it is less affected by changes in compressive stress within the ligament [73].

Additionally, Becks and Classen (2023) conducted an experimental campaign focusing on the monotonic, cyclic, and fatigue responses of high-strength concrete under shear loading. They observed that the scatter in shear fatigue tests decreases with increasing lateral compressive loading, suggesting that higher confinement may lead to more consistent fatigue performance [74].

These findings align with earlier research, reinforcing the understanding that the inherent heterogeneity of concrete and its monotonic strength variability play crucial roles in fatigue behavior. The studies also highlight the importance of considering loading conditions and material properties to accurately predict fatigue life and account for result variability.

2.3.2 Aggregate type and size effect

Sparks and Menzies 1973 explored the effect of different aggregates on concrete fatigue capacity, focusing on normal-weight concrete with gravel and limestone aggregates, as well as lightweight concrete using Lytag. They observed that aggregate stiffness relative to the cement

matrix influenced static strength sensitivity to loading rates. For instance, limestone aggregate concrete exhibited a 4% increase in strength with a hundredfold loading rate rise, while Lytag concrete showed a 16% increase. The fatigue strength regression line for Lytag concrete indicated slightly lower values than gravel and limestone concretes [35]. Continuing this investigation, Sparks 1982 noted that while concrete with gravel aggregates could endure around 10^7 cycles at Smax = 0.55, Lytag concrete was unlikely to exceed 10^5 cycles under the same conditions [36]. Similarly, Raithby and Galloway 1974 reported that limestone aggregate concrete exhibited higher static and fatigue strength compared to flint gravel concrete due to differences in failure modes and crack propagation mechanisms [31].

Klaiber et al. 1978 & 1979 identified that concrete fatigue strength varied with coarse aggregate types, with gravel-based concretes outperforming limestone-based ones at higher stress levels. They noted that limestone aggregate concrete tended to fail through the aggregate, while gravel aggregate concrete predominantly failed around the aggregate. Higher air content shifted the failure pattern to the aggregate-paste boundary, particularly in gravel concretes [75, 76]. Meanwhile, Ramakrishnan and Malhorta 1993 found that lightweight concretes with Haydite and Gravelite aggregates had lower endurance limits than normal-weight concrete [77]. Zhang et al. (1998) observed that while heavyweight concrete demonstrated superior static properties, its fatigue capacity was similar to that of normal-weight concrete at equivalent water-cement ratios. In contrast, lightweight concrete exhibited higher fatigue strength, attributed to improved aggregate-paste bonding due to the porous nature of the lightweight aggregates [66].

However, several studies reported no significant impact of aggregate type on concrete fatigue capacity. Hordijk et al. 1995 found no notable difference in high-strength concrete fatigue performance between limestone and gravel aggregates [78]. Similarly, Tepfers and Kutti 1979

and Gray et al. 1961 concluded that fatigue resistance was independent of coarse aggregate type, even when comparing normal-weight and lightweight concrete [70, 79]. Raithby and Galloway 1974 noted that normalization of static strength to match fatigue testing conditions yielded similar fatigue capacity curves across different variables, including aggregate type [31]. Lohaus et al. 2012 observed no significant effect of grain composition on ultra-high-strength concrete fatigue capacity [58].

Scheiden and Oneschkow 2019 investigated high-strength concretes with basalt and granite aggregates, finding comparable fatigue capacities despite differences in stiffness. However, granite concrete displayed higher strain and lower stiffness under monotonic and fatigue loading, attributed to its lower modulus of elasticity [80].

Codes of practice and standards also address aggregate influence on fatigue capacity. Model Code 2010 notes that crack propagation differs between normal-weight and lightweight aggregate concretes, potentially affecting fatigue life. While lightweight aggregates may absorb more water, leading to wet concrete-like behavior, the overall impact on fatigue strength remains inconclusive [57]. JSCE 15 highlights conflicting findings, with some reports suggesting lightweight aggregate concretes exhibit up to 25% lower fatigue strength than normal concrete [62].

You et al. 2022 have explored the fatigue performance of Recycled Aggregate Concrete (RAC), which incorporates recycled coarse aggregates. Findings indicate that the fatigue life and residual compressive strength of RAC can be comparable to those of natural aggregate concrete (NAC). However, the inherent variability in recycled aggregates may lead to increased scatter in fatigue test results. Factors such as the replacement ratio of recycled aggregates and the quality of the original concrete significantly influence RAC's fatigue behavior [81].

Grassl et al. 2010 stated that larger aggregates can increase the width of microcracks induced by shrinkage, leading to higher permeability in concrete. This is because larger aggregates create more significant stress concentrations at the aggregate-matrix interface, promoting microcrack initiation and propagation [82].

Akçaoğlu 2017 explored how the shape of aggregates affects the mechanical interlock and stress distribution within concrete. Prismatic aggregates, due to their angularity, enhance mechanical interlock but may also lead to higher stress concentrations, influencing microcrack growth. Conversely, spherical aggregates provide more uniform stress distribution but less mechanical interlock, affecting the microcracking process differently [83].

In summary, while there is no consensus on the influence of aggregate type on concrete fatigue capacity, the variability is likely tied to the aggregate's mechanical properties and its interaction with the cement matrix. Future research should incorporate systematic variations in aggregate and concrete composition to clarify the relationship between aggregate type and fatigue capacity and behavior.

2.3.3 Specimen size effect

Petkovic 1990 conducted an extensive experimental study examining various parameters, including specimen size, concrete strength, moisture conditions, and loading sequence. Cylindrical specimens with diameters of 50, 100, and 450 mm were tested, maintaining a length-to-diameter ratio of 3:1. For normal-density concrete tested in air, a clear scale effect was observed, with the fatigue life of 100 mm specimens significantly exceeding that of 450 mm specimens. However, no notable difference was found between the fatigue lives of 50 mm and 100 mm specimens, although this was not further analyzed in the paper. In sealed or submerged conditions, the fatigue lives of all three specimen sizes were similar, leading to the conclusion

that the improved fatigue life of smaller specimens in air conditions is diminished in moist environments [32].

Sinaie et al. 2015 investigated the size effect on concrete cylinder specimens, focusing on diameter (D) and aspect ratio (R = H/D). They found that smaller D and R values increased peak stress and strain, decreased initial tangent stiffness, and enhanced post-peak ductility under monotonic loading, factors that influence fatigue capacity. Additionally, the tangent modulus of the reloading curve was higher for smaller D and R values [84].

Andersen and Ertel 2017 noted unpublished studies indicating that smaller specimens tend to yield better fatigue test results (interpreted as higher fatigue life). They also observed that modern fatigue tests, particularly for high-strength concrete, commonly use smaller specimens (e.g., 60 mm × 180 mm) compared to earlier studies, which often employed larger specimens (e.g., 100 mm × 200 mm) [85]. Oneschkow et al. 2020 compared the fatigue capacities of cylindrical specimens of 60 mm × 180 mm and 100 mm × 300 mm. Smaller specimens showed higher fatigue lives (Nf) under dry conditions, but larger specimens outperformed them under wet conditions, particularly at lower testing frequencies (f = 1 Hz) [86].

Basaldella et al. 2021 examined the influence of specimen production and preparation techniques on the compressive strength and fatigue life of high-performance and ultra-high-performance concretes. While production techniques affected compressive strength, they had minimal impact on the mean number of cycles to failure. However, preparation methods influenced the scatter of test results for both monotonic and fatigue tests [87].

Table 1—Conversion factors of concrete compressive strengths of different control specimens

Specimen strength	Relational equations	Specimen type and size, mm
$f_{c,cyl}$	$f_{1c,cyl} = 0.95 f_{c,cyl}$	cylinder ∅150 × H300
$f_{c,cube}$	$f_{1c,cube} = 0.75 f_{c,cube}$	cube 150 × 150
$f_{c,cyl,100/300}$	$f_{c,cyl} = 1.05 f_{c,cyl,100/300}$	cylinder ∅100 × H300
$f_{c,cyl,70/150}$	$f_{c,cyl} = (1.0/1.06) f_{c,cyl,70/150}$	cylinder ∅70 × H150
$f_{c,cyl,120/360}$	$f_{c,cyl} = (1.0/0.95) f_{c,cyl,120/360}$	cylinder ∅120 × H360
$f_{c,cyl,100/200}$	$f_{c,cyl} = (0.92/0.95) f_{c,cyl,100/200}$	cylinder ∅100 × H200
$f_{c,cube200}$	$f_{c,cube} = 1.05 f_{c,cube,200}$	cube 200 × 200
$f_{c,cube100}$	$f_{c,cube} = 0.90 f_{c,cube,100}$	cube 100 × 100

Figure 32 Conversion of compressive strengths from different specimen types and sizes into a standard compressive strength for shear databases (image from the paper by Reineck et al. 2003 [88]).

Fatigue testing involves a wide variety of specimen types, sizes, and aspect ratios. As highlighted above, these parameters significantly affect the concrete response. Thus, a method to normalize these effects is necessary. Similar challenges were faced by Reineck et al. 2003 , who developed normalization relationships for compressive strengths in shear databases by converting strengths from different specimen types and sizes into a standard compressive strength [88].

Issa et al. 2000 research indicate that larger concrete specimens tend to exhibit lower compressive strengths compared to smaller specimens. This phenomenon, known as the size effect, is attributed to the increased likelihood of flaws and microcracks in larger volumes, which can act as stress concentrators and initiate failure. Additionally, the presence of larger aggregates in bigger specimens can contribute to stress concentrations, further reducing compressive strength [89].

Investigations into the size effect on flexural fatigue behavior by Álvaro, et al. 2024 have shown that larger specimens generally have reduced fatigue strength and shorter fatigue life. This reduction is due to the higher probability of critical flaws in larger volumes and the greater stress gradients present in bigger specimens. Moreover, the addition of steel fibers has been found to mitigate the size effect, enhancing the fatigue performance of larger specimens [90].

Studies by Daneshfar et al. 2023 focusing on the thickness of concrete beams have demonstrated that thicker specimens tend to have a shorter fatigue life under flexural loading. This behavior is linked to the increased stress concentrations and the higher likelihood of defect presence in thicker sections. The incorporation of synthetic fibers can improve fatigue life by bridging cracks and distributing stresses more evenly [91].

Research on UHPC has revealed that the size effect significantly influences its fracture characteristics. Larger specimens exhibit more pronounced brittle behavior and lower fracture toughness compared to smaller specimens. This size-dependent behavior is crucial for designing UHPC structures, as it affects their load-bearing capacity and durability [92].

To address variability in fatigue testing, there is a need for standardized methods to account for variations in specimen types (e.g., cylinders, cubes, prisms, beams), sizes, and aspect ratios. Moving forward, establishing standardized testing guidelines for concrete fatigue would improve the comparability of results and support the development of more consistent and reliable data on concrete fatigue capacity.

2.3.4 Saturation and presence of water

Raithby and Galloway 1974 studied the static and fatigue flexural strengths of concrete under four moisture conditions: fully saturated, lab-dried, curing-tank and oven-dried, and oven-dried

and resoaked. Their findings revealed that oven-dried specimens exhibited the highest flexural strengths and longest fatigue lives, while partially dried specimens had the lowest. Interestingly, partially dried specimens had lower fatigue lives than fully saturated ones. Resoaked specimens showed fatigue capacities similar to fully saturated ones, with the order of fatigue life being oven-dried > saturated (fully or resoaked) > partially dried. The authors suggested that moisture gradients and differential strains might explain these results, but scatter was lowest in fully saturated specimens [31].

Waagaard 1977 and 1994 noted from literature reviews that submerged concrete typically has a shorter fatigue life than air-dried concrete, with the extent of fatigue reduction depending on the degree and duration of saturation [93-95]. Petkovic et al. 1990 evaluated three conditions: air (stored and tested in air), sealed (wrapped with watertight tape), and water (stored and tested in seawater). They found better fatigue capacity in air-dried specimens compared to sealed or submerged conditions. Additionally, for larger cylinders (450 mm diameter), the moisture effect on fatigue capacity diminished, though it remained consistent for smaller sizes (50 and 100 mm). The failure mode also varied: air-dried specimens showed vertical cracking, while sealed and submerged specimens exhibited horizontal toothed cracks [32].

Tomann and Oneschkow 2019 investigated moisture content and its effects on fatigue resistance in high-strength concrete, testing five storage conditions: oven-dried (D), climate chamber (C), intrinsic moisture (M), sealed water-submerged (WS), and submerged and tested underwater (WST). Fatigue resistance decreased with higher moisture content, with external water having a smaller additional effect. The failure cycles (N_f) for the WS and WST conditions were similar, suggesting that microstructural moisture, not the external environment, primarily affects fatigue resistance [96]. Compared to Model Code 2010 [57] predictions for air-dried conditions and

DNV-ST-C502 [60] predictions for submerged conditions, the experimental results showed higher N_f than DNV predictions and varied alignments with MC 2010 predictions, depending on the moisture conditions.

Oneschkow et al. 2020 compared dry and wet environments for high-strength concrete under compressive fatigue. Submerged specimens had significantly lower fatigue capacities, with the effect being more pronounced at lower frequencies (1 Hz vs. 10 Hz) and lower peak stress levels (Smax = 0.70 vs. Smax = 0.80) [86]. They found that Model Code 2010 and Eurocode 2 predictions overestimated fatigue capacity in wet conditions, while DNV-ST-C502 predictions underestimated it, especially for tests at higher frequencies [57, 60, 61].

Standards and codes also provide guidance on moisture's effect on fatigue. Model Code 2010 notes that permeable concrete immersed in water may experience reduced fatigue strength, especially when pores are filled with water due to increased internal water pressure [57]. Model Code 2020 introduced a reduction factor for fatigue capacity for saturated structures [59]. DNV-ST-C502 accounts for environmental effects through a C1 factor, with values of 12 for air and 8–10 for water. JSCE estimates that concrete in water has about two-thirds the fatigue capacity of concrete in air, reflecting this in a reduced S-N equation factor from 17 to 10 [62].

An investigation by Ali et al. 2023 into high-strength concrete subjected to varying moisture levels and load frequencies revealed that increased internal moisture content leads to a significant reduction in fatigue resistance. The study suggests that elevated pore-water pressures and water movement within microcracks may contribute to this decrease in fatigue life [97].

A peridynamic model was developed to analyze the impact failure of wet concrete, considering different saturation levels. The findings indicate that higher saturation levels can exacerbate crack propagation under loading, thereby reducing the material's overall fatigue capacity [98].

In summary, moisture levels significantly influence concrete fatigue capacity, with air-dried specimens generally outperforming saturated ones. Increased moisture content in the microstructure reduces fatigue resistance, likely due to pore-water pressure and water movement causing microstructural damage. While standards provide some adjustments for moisture effects, further research is needed to refine these models for diverse environmental conditions.

2.3.5 Loading frequency

Awad and Hilsdorf 1971 found that fatigue strength depends significantly on loading frequency in the low-cycle region, especially at high peak stress levels (Smax ≥ 0.90). They reported that increasing the stress rate (or frequency) by one order of magnitude led to a near ten-fold increase in fatigue capacity. The effects were more pronounced at higher minimum stress levels (Smin) and diminished at lower Smax values. They emphasized the importance of separating fatigue damage into cycle-dependent and time-dependent components, particularly when stresses exceed the sustained load strength of concrete [37].

Sparks and Menzies 1973 and 1982 observed that faster loading rates enhance fatigue life, with a hundred-fold increase in loading rate resulting in approximately a ten-fold increase in fatigue capacity. However, for Smax levels below 75% of the static strength, frequency variations between 0.1 and 100 Hz had minimal effect on fatigue life [35, 36]. Tepfers and Kutti 1979 corroborated this, noting that creep effects become relevant at Smax > 0.75, making fatigue capacity sensitive to frequency. Below Smax = 0.75, the effect of frequency was negligible, with fatigue life largely unaffected by variations between 0.1 and 200 Hz [70].

Petkovic et al. 1990 reported that at very high stress levels, longer cyclic periods reduced fatigue capacity, implying the need for adjustments to account for real-life loading frequencies, which are generally lower [32]. Similarly, Zhang et al. 1996 introduced a frequency coefficient (C_f) to

modify fatigue equations, showing that C_f increased logarithmically with frequency, confirming that less damage occurs at higher frequencies [21]. Oneschkow 2012 and 2020 found that fatigue life increased with frequency, especially at higher Smax levels (≥0.80), and that the relative change in fatigue life due to frequency was more pronounced in wet environments [46, 86].

Medeiros et al. 2015 demonstrated that decreasing frequency reduced the number of cycles to failure, particularly for PC, while fiber-reinforced concrete showed less sensitivity to frequency [44]. Kesler 1953 and Raithby and Galloway 1974 noted that frequencies within an order of magnitude (e.g., 1–10 Hz) had little influence on fatigue life at lower Smax values [31, 99]. Similarly, Murdock 1965 and Takhar et al. 1974 found no statistically significant differences in fatigue life when comparing frequencies within a narrow range [38, 100].

Zhang et al.1996 reviewed literature indicating that lower frequencies (<0.16 Hz) markedly reduce fatigue life, while frequencies between 1 and 15 Hz had minimal influence at Smax < 75% of static strength [21]. Lantsoght et al. 2016 supported this, emphasizing negligible frequency effects for normal-strength concrete under similar conditions [68].

In general, higher loading frequencies tend to increase fatigue life, particularly at higher peak stress levels. However, real-life loading frequencies are often much lower than those used in laboratory tests, potentially making accelerated fatigue test results unconservative for structural applications, especially at high Smax levels. Partial safety factors in codes partially address this issue.

Model Code 2020 specifies that its equations for fatigue capacity are valid for frequencies above 0.1 Hz and peak stress levels below 0.90. For lower frequencies or higher stress levels, lower fatigue capacities are anticipated, reflecting low-cycle fatigue behavior [59].

A few other research studies explored the influence of loading rate under monotonic loading on concrete strength and its implications for fatigue capacity.

Kim and Kim 1996 observed that regression lines in fatigue tests pass above the static strength (Smax > 1.0) due to higher loading rates during fatigue tests compared to monotonic loading. They also noted that the vertical intercept of these curves decreases with increasing concrete strength [29]. Similarly, Hsu 1981 argued that normalized fatigue stress levels should account for the monotonic strength tested at the same loading rate as fatigue. Hsu reported that the long-term sustained strength of concrete is approximately 75-80% of the ultimate load [65].

Sparks and Menzies 1973 and 1982 hypothesized that fatigue life increases with faster loading rates, but at a diminishing rate. For instance, a hundredfold increase in loading rate results in a tenfold increase in fatigue life. They found that when fatigue stresses were normalized using static strengths at corresponding loading rates, the resulting fatigue capacity curves were consistent across different loading conditions [35, 36]. Murdock 1965, however, found no significant rate effect in tests conducted at loading frequencies of 8 Hz and 16 Hz [100].

Awad and Hilsdorf 1971 observed that failure strains under fatigue and sustained loading were greater than those under monotonic loading, attributed to the higher loading rates during fatigue tests [37]. Raithby and Galloway 1974 found that static strengths increased by 50% when tested at rates comparable to fatigue tests, aligning fatigue capacity curves across varying loading rates [31]. Lenschow 1984 predicted at least a 25% increase in static strength at dynamic loading rates that were significantly higher than standard rates [71].

Petkovic et al. 1990 and Zhang et al. 1986 emphasized that fatigue stress levels normalized by static strength obtained at standard loading rates may lead to unsafe predictions, especially at lower cyclic loading rates. Zhang proposed a loading rate coefficient C_f, dependent on the

logarithm of frequency log f, to adjust fatigue predictions [21, 32]. The coefficient showed that long-term static strength is approximately 75-80% of the standard static strength f_{cm}.

Oneschkow 216 noted discrepancies between experimental data and Model Code 2010 predictions at high stress levels Smax= 0.90-0.95, attributing this to the common assumption that Wohler curves intersect Smax= 1.0. Experimental regression lines, however, typically pass above Smax= 1.0 due to loading rate effects [23].

In summary, fatigue regression lines derived from experimental results generally exceed Smax= 1.0 due to higher loading rates during fatigue testing. However, design S-N curves commonly intersect Smax= 1.0, potentially incorporating a safety margin for high-stress conditions and simplifying data interpretation. This approach emphasizes the need for rate-dependent normalization of fatigue stresses to ensure accurate predictions of fatigue capacity.

A 2022 experimental investigation by Félix et al. evaluated how different loading frequencies (0.125, 0.25, and 0.5 Hz) affect the fatigue behavior of concrete with varying compressive strengths (30, 50, and 70 MPa). The study found that as loading frequency increased, fatigue life also increased exponentially. However, higher-strength concretes exhibited shorter fatigue lives, indicating an inverse relationship between compressive strength and fatigue life [101].

Research by Keerthana and Kishen 2021 examined the micromechanical aspects of concrete fatigue fracture under varying loading frequencies. The study provided insights into how different frequencies influence crack initiation and propagation at the microscale, contributing to a deeper understanding of fatigue behavior in concrete [102].

2.3.6 Loading waveform

Lenschow 1980 noted that while sinusoidal waveforms are representative of wind and wave loadings, tests using other waveforms, such as rectangular and triangular, have also been conducted. Their findings indicate that rectangular waveforms lead to failure after fewer cycles (Nf) compared to sinusoidal waveforms, whereas triangular waveforms allow for a greater number of fatigue cycles [103].

Zhang et al. 1998 reported that square waveforms cause the most damage, triangular waveforms cause the least damage, and sinusoidal waveforms fall between these extremes. They developed a parametric model of a trapezoidal waveform that could transform into other waveforms by adjusting the shape factor, illustrating the effects of different loading waveforms on fatigue behavior [66].

Isojeh et al. 2017 reviewed earlier studies and reported that N_f for sinusoidal waveforms is approximately half of that for triangular waveforms and about one-sixth of that for rectangular waveforms [24]. Similarly, Oneschkow (2012) found that triangular waveforms resulted in higher Nf than sinusoidal waveforms across two peak stress levels and four loading frequencies, providing further evidence of the significant influence of waveform shape on fatigue capacity [46].

A state-of-the-art review by Karna et al. (2024) discusses how different loading waveforms, such as sinusoidal, rectangular, and triangular, affect the fatigue behavior of concrete structures. The review highlights that rectangular waveforms tend to cause failure after fewer cycles compared to sinusoidal waveforms, while triangular waveforms allow for a greater number of cycles before failure [104].

2.3.7 Other factors

McCall 1958, as well as Murdock and Kesler 1958, conducted fatigue tests on plain concrete beams and reported no endurance limit, even after testing up to 20 million and 10 million cycles, respectively [105, 106].

Takhar et al. 1974 studied the effect of lateral confining pressure on fatigue capacity and found it significantly enhanced fatigue life, particularly at lower peak stress levels. For example, at Smax= 0.80, all 11 tests with lateral confining pressure showed $N_f > 15{,}000$ cycles, while all six tests without confining pressure had $N_f < 15{,}000$ cycles. At Smax= 0.90, the average N_f increased with confining pressure, but the effect was less pronounced [38].

The fatigue capacity model by Lohaus et al. 2016, later adopted in Model Code 2010, was developed to meet specific criteria: the curves intersect at Smax= 1.0, remain linear up to about 10^7 cycles, asymptotically approach minimum stress levels at very high cycles, and deviate from test results on the conservative side [20].

Oneschkow et al. 2020 examined storage and testing conditions, loading frequency, and specimen size, concluding that these factors interact and highlight the complexity of the fatigue damage process in concrete [86].

Raithby and Galloway 1974 investigated the effects of loading rate, age, moisture conditions, and aggregate type. They determined static capacity at conditions matching those of fatigue tests, including loading rate and age. Using these updated static strengths for normalizing peak fatigue stresses, they found that the resulting nondimensionalized fatigue capacity curves were consistent across the variables studied [31].

Fatigue testing inherently includes sustained load effects due to the mean stress component, influencing fatigue behavior. Tepfers and Kutti 1979 and Awad and Hilsdorf 1971 highlighted the need to consider creep and time-dependent damage at high Smax levels [37, 70], while Hsu 1981 proposed an extended S-N-R-T model incorporating time effects [65]. Zhang et al. 1996 introduced a frequency coefficient C_f to adjust fatigue equations, aligning long-term strength with experimental data but requiring refinements for high stress ratios [21]. Von der Haar and Marx 2018 linked sustained loading to creep-relevant stress levels through additive strain modeling [49]. Design codes like Model Code [57, 59], Eurocode 2 [61], and JSCE 15 [62] incorporate reduction factors (e.g., 0.85) to account for sustained loading in fatigue strength predictions, ensuring these effects are captured in design models for concrete structures.

Cachim et al. 2002 found that in compressive fatigue tests on concrete cylinders, the addition of 30 mm steel fibers slightly improved fatigue life, whereas 60 mm fibers marginally reduced it, likely due to imperfections, fiber bundling, or size effects [50]. Grzybowski and Meyer (1993) reported that increasing fiber volume by up to 0.25% enhanced cyclic strength for both steel and polypropylene fibers but showed diminishing effects at higher volumes, especially at stress levels exceeding 75% of static strength [40]. Medeiros et al. 2015 noted that fibers enhanced fatigue life at low loading frequencies but showed negligible or even adverse effects at higher frequencies [44]. Li et al. 2016 reported that ultra-high toughness cementitious composites (UHTCC) with polyvinyl alcohol fibers significantly outperformed plain and steel fiber-reinforced concrete in fatigue life due to enhanced crack bridging [47]. Lohaus et al. 2007 found that high- and ultra-high-strength concretes with fibers had lower fatigue capacities than PC, with fibers failing to ensure controllable ductility post-ultimate load [42]. Johnston and Zemp 1991 demonstrated that steel fiber content above 1% and aspect ratios over 70 improved flexural

fatigue [107], while Jun and Stang 1998 identified 1% fiber content as optimal for fatigue capacity, with no additional benefits at higher contents [108]. Lee and Barr 2004 concluded that fibers generally enhance flexural fatigue due to crack-bridging effects but have negligible or adverse effects on compressive fatigue, potentially due to fiber-induced weaknesses [109]. Overall, the inclusion of fibers influences fatigue capacity based on fiber type, volume, aspect ratio, and specimen preparation, with clear benefits in flexural fatigue and mixed outcomes in compressive fatigue.

2.4 Summary and conclusion

There are significant gaps in existing research and data related to the fatigue behavior of concrete. Current studies often fail to capture the influence of crucial parameters — such as loading frequency, environmental conditions — and material-specific characteristics — like aggregate size and reinforcement levels — on the fatigue capacity of concrete. Existing fatigue models are overly generalized, treating all concrete structures under a "one-size-fits-all" approach, which overlooks variations in material properties and loading conditions and has led to inconsistent and often overly conservative predictions of fatigue capacity, hindering the development of cost-effective and efficient designs for concrete support structures.

The lack of a comprehensive and standardized database for concrete fatigue data further exacerbates these issues. A database consolidating experimental results from various sources is critical for identifying trends, validating models, and exploring under-researched areas. Such a resource can facilitate the development of tailored fatigue models and testing protocols that address the unique demands of different concrete structures and loading scenarios. By enabling more precise and practical design methodologies, a well-organized database will provide researchers and engineers with the tools necessary to advance innovation in this field.

The present work prioritizes the development of a robust experimental database and the investigation of key influential factors, such as aggregate size, concrete composition, and reinforcement. It aims to establish a foundation for more accurate fatigue models and design practices.

3 Database for Experimental Data on Concrete Fatigue

3.1 Introduction

Research into the capacity of concrete under fatigue loading has been studied for at least 50 years. Although several relationships exist relating applied stresses (S) and the fatigue life of concrete (N), there is no consensus regarding any specific S-N equation or set of equations that should be used. The first task was to create a test data repository that could be used to examine the accuracy of existing S-N models and understand the differences in the basis of these models. The created repository has a flexible format to accommodate different test data. Both U.S. Customary Units (USUC) and international system metric units (SI) can be used. The test database template accommodates test data entry based on the different independent variables utilized in the research. Conversion factors from previous research were used to accommodate variation in size and/or shape of test specimens (cylinders, cubes, or prisms),.

The database consists of multiple entries for experimental data on fatigue. This is designed to include all possible variables that could give the reader insight into the characteristics of concrete and the variables that could be influential to the material's fatigue response to cyclic loading. The spreadsheet includes the name of the reference document, the type of test (uniaxial or flexural), and information about the geometry of the specimens used in the experimental investigations were added to the spreadsheet, as well as the material properties of the concrete used in the specimens (max aggregate size and type, water-to-cement ratio, cement type, additives name and percent of usage, fibers name and percentage of use, and strength of concrete).

	A	B	C	D	E	F	G	H	I
1	Reference number	Defintion	-	Specimen type	Width/ Diameter	Height	Dimention ratio	Maximum aggregate size	Aggregate type
2	Reference #	Reference	Test Type	Specimen type	b/D (mm/in)	h (mm/in)	DR (h/b or h/D)	d_ag (mm/in)	Aggregate type
3	1	UIUC Test Data 2019 (BFTS) - Individual Test Entries; Uniaxial Compressive Fatigue Loading Tests (with	Uniaxial	Cylinder	4	8	2	0.375	limestone - Coarse aggregate
4	1		Uniaxial	Cylinder	4	8	2	0.375	limestone - Coarse aggregate
5	1		Uniaxial	Cylinder	4	8	2	0.375	limestone - Coarse aggregate
6	1		Uniaxial	Cylinder	4	8	2	0.375	limestone - Coarse aggregate
7	1		Uniaxial	Cylinder	4	8	2	0.375	limestone - Coarse aggregate
8	1		Uniaxial	Cylinder	4	8	2	0.375	limestone - Coarse aggregate
9	1		Uniaxial	Cylinder	4	8	2	0.375	limestone - Coarse aggregate
10	1		Uniaxial	Cylinder	4	8	2	0.375	limestone - Coarse aggregate
11	1		Uniaxial	Cylinder	4	8	2	0.375	limestone - Coarse aggregate
12	1		Uniaxial	Cylinder	4	8	2	0.375	limestone - Coarse aggregate
13	1		Uniaxial	Cylinder	4	8	2	0.375	limestone - Coarse aggregate
14	1		Uniaxial	Cylinder	4	8	2	0.375	limestone - Coarse aggregate
15	1		Uniaxial	Cylinder	4	8	2	0.375	limestone - Coarse aggregate
16	1		Uniaxial	Cylinder	4	8	2	0.375	limestone - Coarse aggregate
17	1		Uniaxial	Cylinder	4	8	2	0.375	limestone - Coarse aggregate
18	1		Uniaxial	Cylinder	4	8	2	0.375	limestone - Coarse aggregate
19	1		Uniaxial	Cylinder	4	8	2	0.375	limestone - Coarse aggregate
20	1		Uniaxial	Cylinder	4	8	2	0.375	limestone - Coarse aggregate

Figure 33 Screenshot #2 of the experimental test data repository – Specimen Geometry and Material Properties.

3.2 List of references for experimental fatigue data

In addition to the Experimental Fatigue Test Data Repository, a "List of References" spreadsheet has also been created, as shown in *Figure 34* and *Figure 35*. This reference list includes some basic information about the papers and reports of experiments that have been conducted on concrete fatigue, including 155 scientific documents. This references list has been attached to this report as an appendix. The list includes the following, for each reference document:

1. Information related to the document itself, such as the document's name, type, publishing year, and author names (*Figure 34*).
2. Information related to the test results, like the number of tests conducted, dimensions of concrete specimens used, and availability of strength of the concrete used, number of cycles to failure of each test, and fatigue strain test data (*Figure 35*).

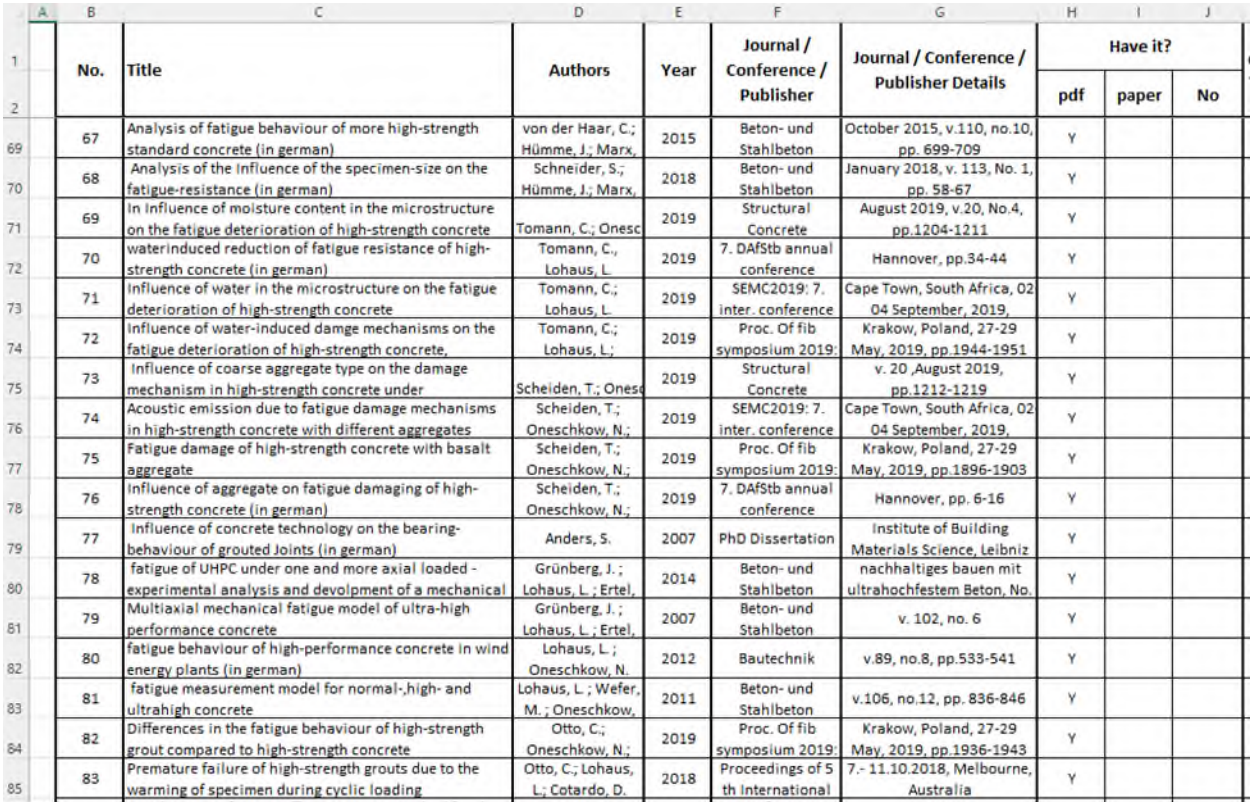

No.	Title	Authors	Year	Journal / Conference / Publisher	Journal / Conference / Publisher Details	Have it?		
						pdf	paper	No
67	Analysis of fatigue behaviour of more high-strength standard concrete (in german)	von der Haar, C.; Hümme, J.; Marx,	2015	Beton- und Stahlbeton	October 2015, v.110, no.10, pp. 699-709	Y		
68	Analysis of the influence of the specimen-size on the fatigue-resistance (in german)	Schneider, S.; Hümme, J.; Marx,	2018	Beton- und Stahlbeton	January 2018, v. 113, No. 1, pp. 58-67	Y		
69	In influence of moisture content in the microstructure on the fatigue deterioration of high-strength concrete	Tomann, C.; Onesc	2019	Structural Concrete	August 2019, v.20, No.4, pp.1204-1211	Y		
70	waterinduced reduction of fatigue resistance of high-strength concrete (in german)	Tomann, C., Lohaus, L.	2019	7. DAfStb annual conference	Hannover, pp.34-44	Y		
71	Influence of water in the microstructure on the fatigue deterioration of high-strength concrete	Tomann, C.; Lohaus, L.	2019	SEMC2019: 7. inter. conference	Cape Town, South Africa, 02 04 September, 2019,	Y		
72	Influence of water-induced damge mechanisms on the fatigue deterioration of high-strength concrete,	Tomann, C.; Lohaus, L.;	2019	Proc. Of fib symposium 2019:	Krakow, Poland, 27-29 May, 2019, pp.1944-1951	Y		
73	Influence of coarse aggregate type on the damage mechanism in high-strength concrete under	Scheiden, T.; Onesc	2019	Structural Concrete	v. 20 ,August 2019, pp.1212-1219	Y		
74	Acoustic emission due to fatigue damage mechanisms in high-strength concrete with different aggregates	Scheiden, T.; Oneschkow, N.;	2019	SEMC2019: 7. inter. conference	Cape Town, South Africa, 02 04 September, 2019,	Y		
75	Fatigue damage of high-strength concrete with basalt aggregate	Scheiden, T.; Oneschkow, N.;	2019	Proc. Of fib symposium 2019:	Krakow, Poland, 27-29 May, 2019, pp.1896-1903	Y		
76	Influence of aggregate on fatigue damaging of high-strength concrete (in german)	Scheiden, T.; Oneschkow, N.;	2019	7. DAfStb annual conference	Hannover, pp. 6-16	Y		
77	Influence of concrete technology on the bearing-behaviour of grouted Joints (in german)	Anders, S.	2007	PhD Dissertation	Institute of Building Materials Science, Leibniz	Y		
78	fatigue of UHPC under one and more axial loaded - experimental analysis and devolpment of a mechanical	Grünberg, J. ; Lohaus, L. ; Ertel,	2014	Beton- und Stahlbeton	nachhaltiges bauen mit ultrahochfestem Beton, No.	Y		
79	Multiaxial mechanical fatigue model of ultra-high performance concrete	Grünberg, J. ; Lohaus, L. ; Ertel,	2007	Beton- und Stahlbeton	v. 102, no. 6	Y		
80	fatigue behaviour of high-performance concrete in wind energy plants (in german)	Lohaus, L. ; Oneschkow, N.	2012	Bautechnik	v.89, no.8, pp.533-541	Y		
81	fatigue measurement model for normal-,high- and ultrahigh concrete	Lohaus, L. ; Wefer, M. ; Oneschkow,	2011	Beton- und Stahlbeton	v.106, no.12, pp. 836-846	Y		
82	Differences in the fatigue behaviour of high-strength grout compared to high-strength concrete	Otto, C.; Oneschkow, N.;	2019	Proc. Of fib symposium 2019:	Krakow, Poland, 27-29 May, 2019, pp.1936-1943	Y		
83	Premature failure of high-strength grouts due to the warming of specimen during cyclic loading	Otto, C.; Lohaus, L.; Cotardo, D.	2018	Proceedings of 5 th International	7.- 11.10.2018, Melbourne, Australia	Y		

Figure 34 Screenshot #1 of "List of References for Fatigue Experimental Data" Spreadsheet.

K	L	M	N	O	P	Q	R	S	T	U	V	W	X	Y	Z
Tests conducted ? If y, then #?	Nf data		Concrete Strength Data			Specimen Info				Fatigue Failure Strain Data			Fatigue Test Strain Data		
	Table	Figure	Table	Figure	Neither	Cylinder	Cube	Prism	Beam	Table	Figure	Neither	Table	Figure	Neither
237					x	100/300	150				Y				x
100						50/150,100/300,450/1350					Y				x
13				Y		100/300						x			x
13		Y	Y			100/300						x			x
13		Y	Y			100/300						x			x
25		Y	Y			100/300						x			x
12		Y	text			60/180				Y				Y	
12		Y	text			60/180						x			x
6		Y	text			60/180						x		Y	
12		Y	text			60/180				Y				Y	
82	Y		Y			60Ø;70Ø	100;75			Y	Y			Y	
	Y	Y				60/180	100	40/40/160			Y			Y	
ca.120		Y			x	60/180		50/50/150				x		Y	
		Y		Y		150/300;60/180						x		Y	
		Y			x	60/180					Y				x
49		Y	Y			60/180						x			x
14		Y				60/180						x			x

Figure 35 Screenshot #2 of "List of References for Fatigue Experimental Data" Spreadsheet.

3.3 Initial exploration

3.3.1 Comparison of data with selected models (based on Smin)

The existing experimental data was used to validate the fatigue models. The vast majority of the existing data points are at an Smin level of 0.05, so a detailed analysis was conducted at this level. Data points were sorted based on the concrete strength, frequency of loading, loading wave form, experimental specimen dimension ratio, and saturation level of concrete specimens. All data points were plotted along with models according to Smin level.

Figure 36 shows experimental data points, and models plotted at Smin=0.05. The Dutch code 2009 stood out as the most conservative model. The Zhang 1996 model almost passes through the mean Nf in all Smax ranges, and the Zhang 1998 model is one of the most conservative

models. Model code 2010 passes through the mean values of data ranges at the Smax range of 0.6-0.8, and it is conservative in Smax>0.9. For the high Smax range (over 0.85), the Hsu model seems to provide relatively reasonable predictions of concrete life.

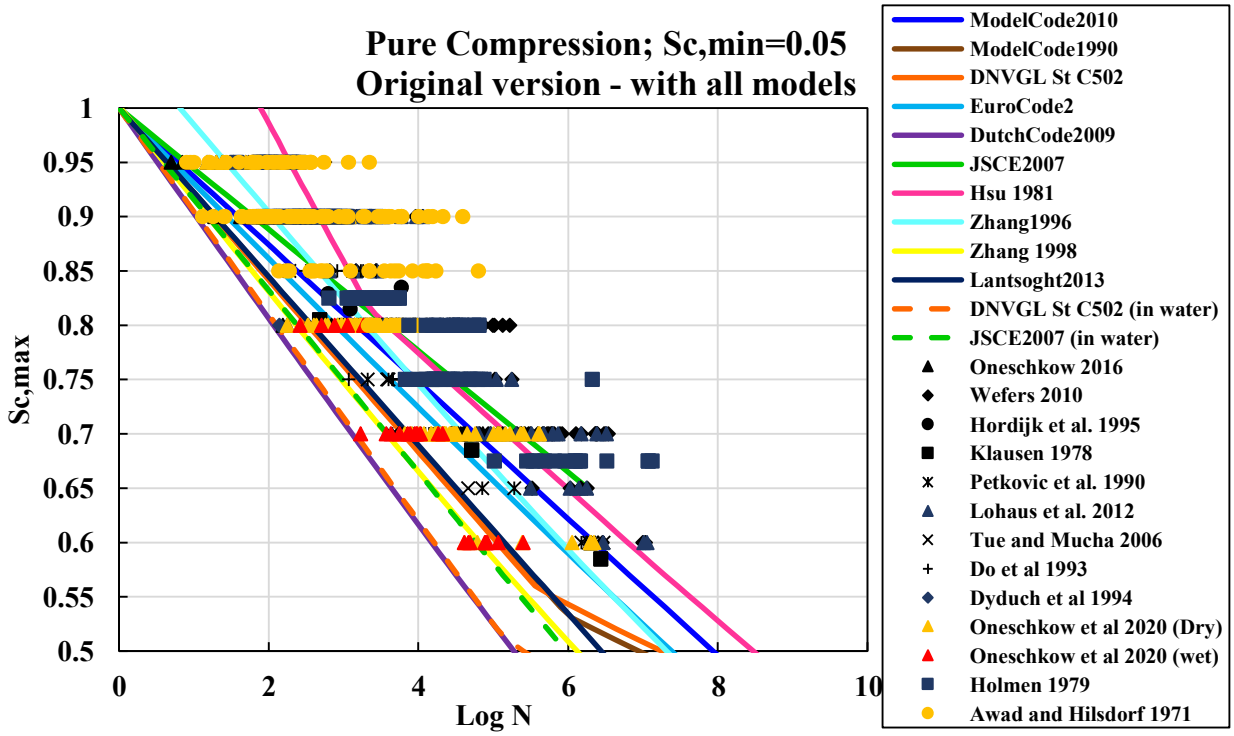

Figure 36 S-N models and experimental data points at pure compression stress state with a minimum stress level of 0.05.

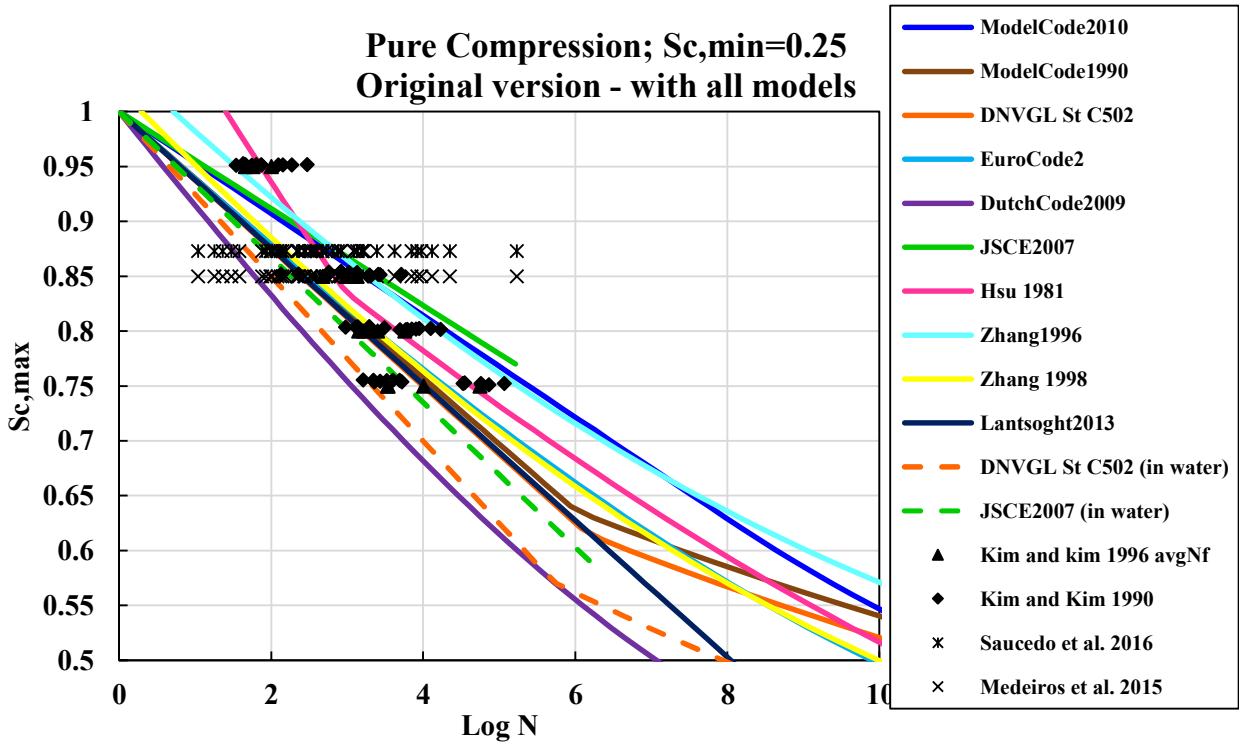

Figure 37 S-N models and experimental data points at pure compression stress state with a minimum stress level of 0.25.

In this higher Smin level, Smin=0.25, Figure 37the DNVGL model seems better in predicting the fatigue life (Figure 36). Model Code 2010 behaves unconservatively in lower Smax levels (<0.8). The Hsu model works well for high Smax levels (>0.85).

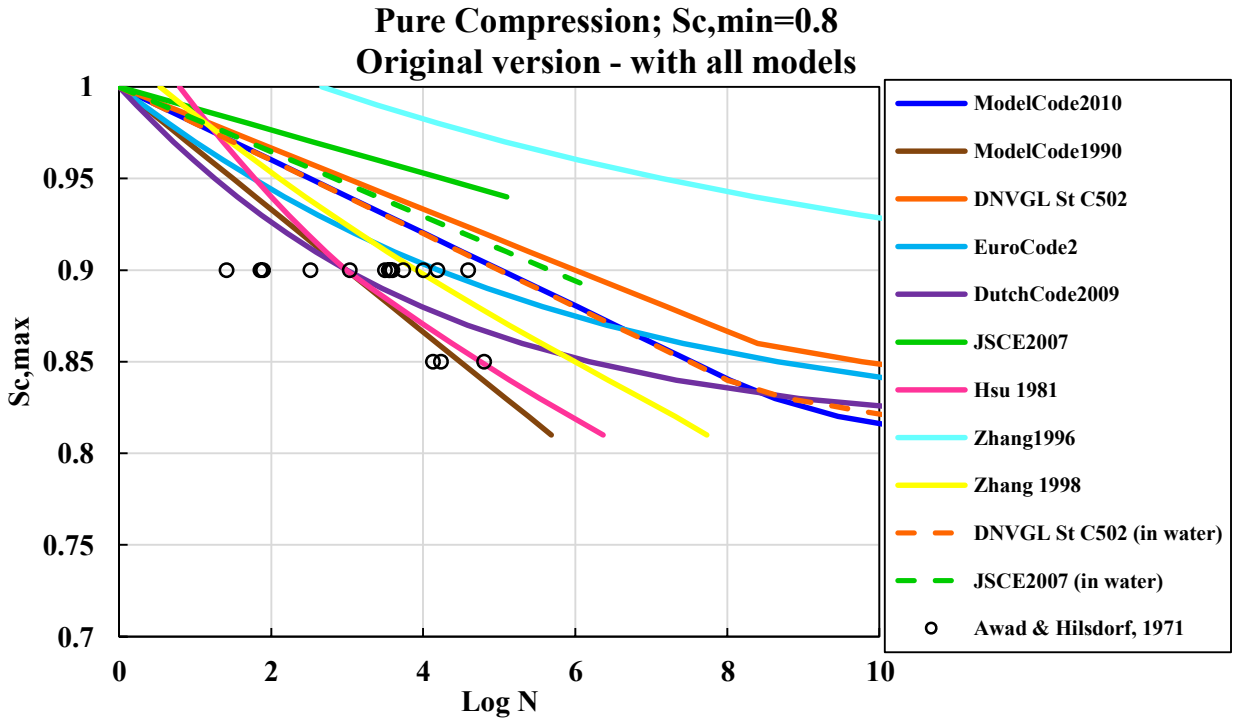

Figure 38 S-N models and experimental data points at pure compression stress state with a minimum stress level of 0.80.

At the high Smin level of 0.8, the only data available was from Awad and Hilsdorf in 1971 (Figure 38). It is not feasible to draw many conclusions from such limited data but the Hsu model does seem to work well in this stage suggesting that the Hsu model works well in Smax>0.85 independent of Smin level.

3.3.2 Strength

One of the key factors affecting the fatigue life of plain concrete material is the material's strengthwhich in turn depends on numerous parameters and conditions. Since there are numerous data points, the number of models was limited to a few, and the strength of the material was categorized into five different ranges to facilitate visual analysis. Color codes for data points are as follows: Light blue for f'c<25 MPa, green for 26<f'c<50 MPa, red for 51<f'c<75 MPa, blue for 75<f'c<100, and black for f'c>100 MPa.

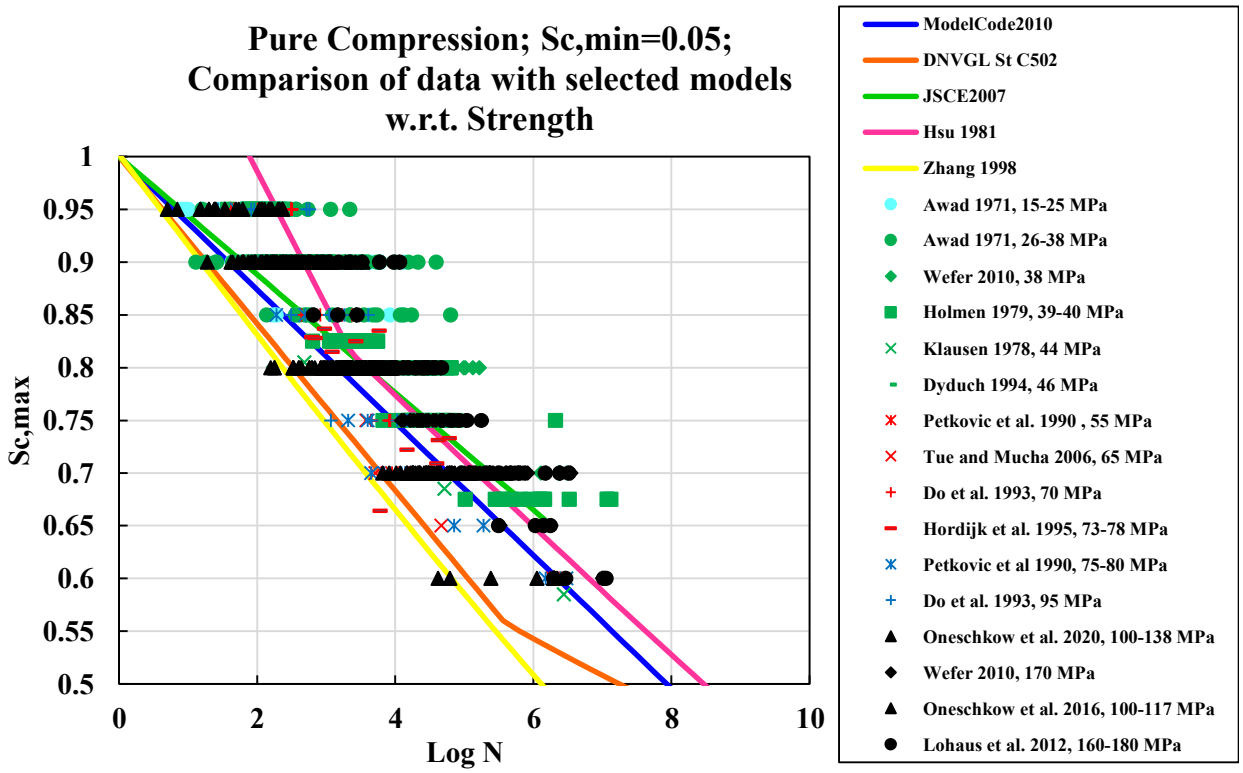

Figure 39 S-N models and experimental data points at pure compression stress state with a minimum stress level of 0.05, data points sorted based on the strength of concrete.

It seems that the mean Nf of different Smax values in higher strength concretes are less than those for concrete of normal strength. This shows itself clearly in lower Smax. But this trend is not observable in f'c>100 MPa. Figure 40 shows the fatigue data points based on the strength of the concrete plotted in separate graphs (the legend of the previous figure may be used for understanding color-marker codes). The main observations are listed below:

- The range of Nf for concrete with f'c<25 Mpa and 26<f'c<50 is nearly identical.
- The fatigue life of concrete specimens with 50<f'c<75 Mpa is less than Nf of concrete with 26<f'c<50 Mpa.
- The mean Nf of different Smax values in higher strength concretes are less than the normal strength concrete, especially in lower Smax.

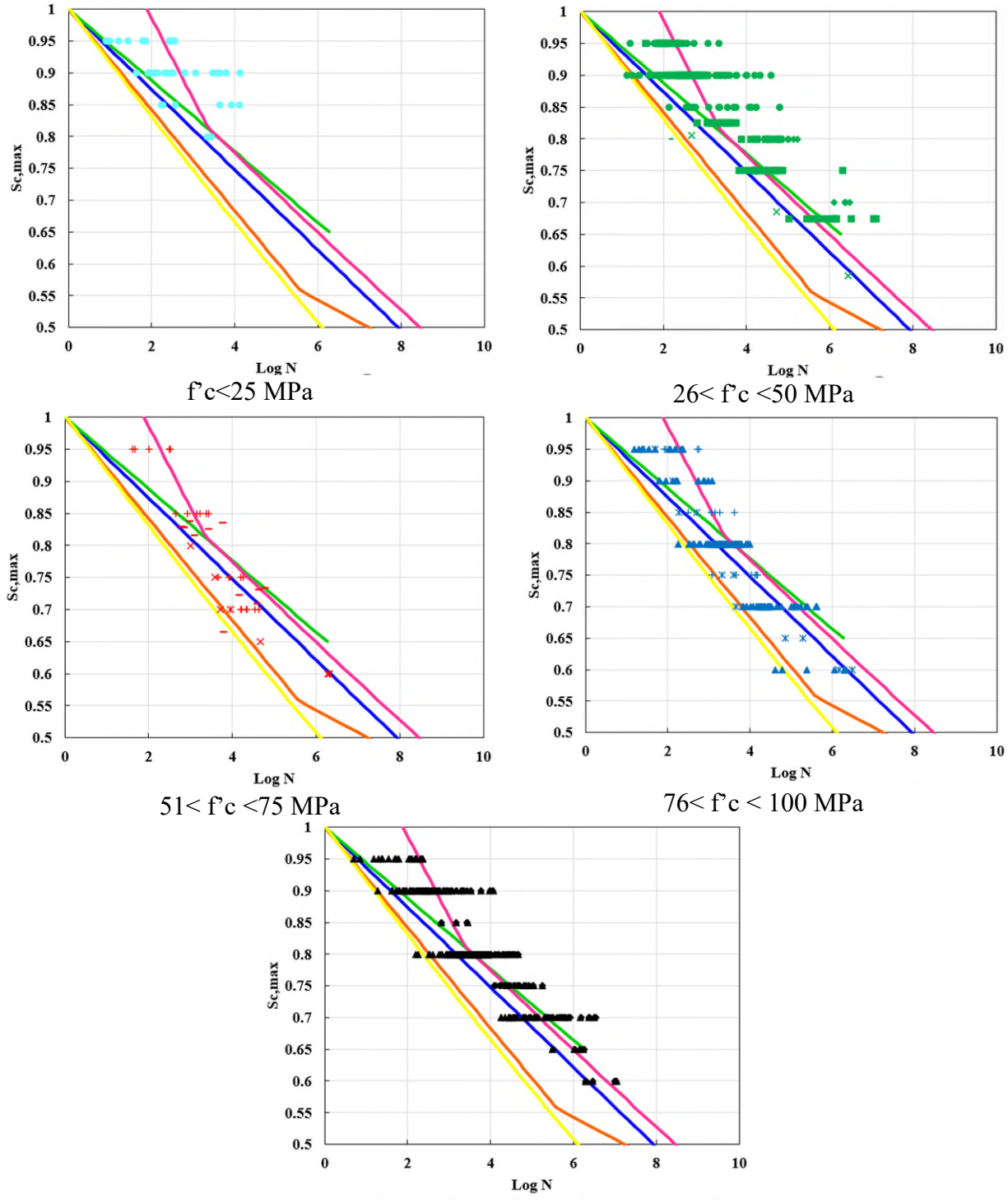

Figure 40 S-N models and experimental data points at pure compression stress state with a minimum stress level of 0.05, data points sorted based on the strength of concrete and plotted separately.

3.3.3 Frequency

The other important factor influencing the fatigue life of PC is the frequency of loading. Generally, the higher the frequency of loading, the lower the number of cycles to failure. Figure 41 shows data points categorized and color-coded based on the frequency of loading. Here are the main observations:

- Data points of f=0.1 Hz match the range of data points with f=1 Hz.
- In f=1 Hz, none of the models match the available data well.
- In f=10 Hz, the data points almost match the results of f=1 Hz.
- Data points of Smax=0.90, 0.825, and 0.80 for f=5 Hz are greater than those for f=1 Hz. No other significant difference is observable.

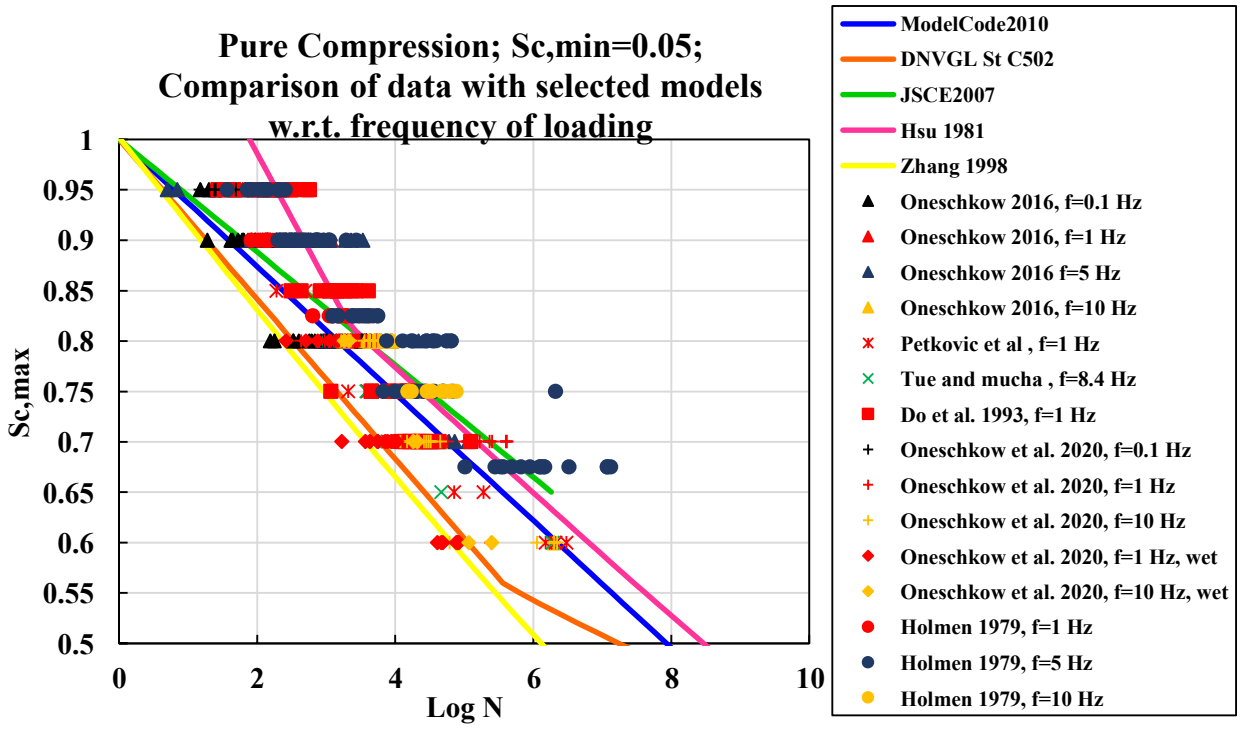

Figure 41 S-N models and experimental data points at pure compression stress state with a minimum stress level of 0.05, data points sorted based on the frequency of loading.

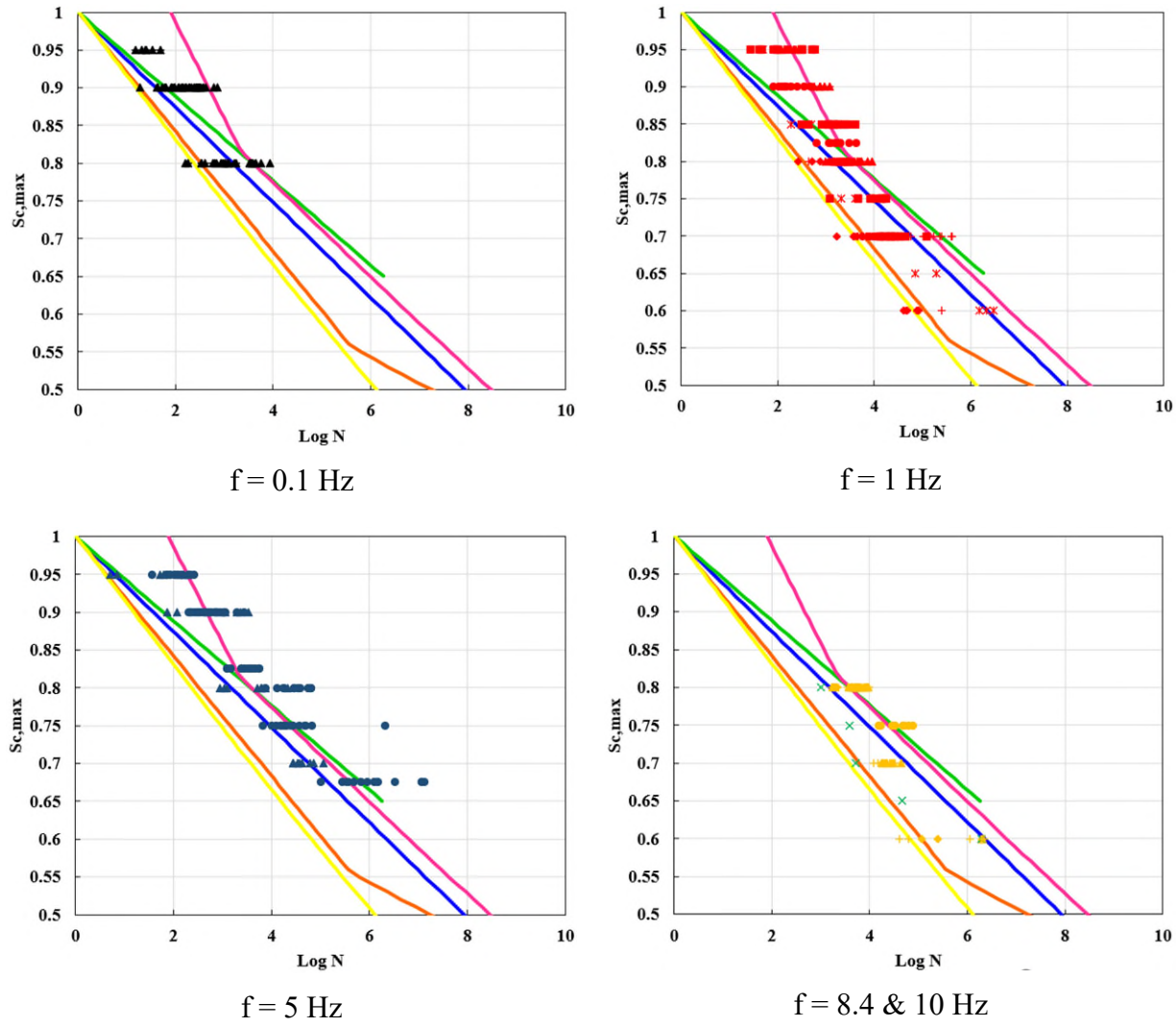

Figure 42 S-N models and experimental data points at pure compression stress state with a minimum stress level of 0.05, data points sorted based on the frequency of loading plotted separately.

3.3.4 Specimen dimension ratio

Another possible factor is the dimension ratio of the specimens of plain concrete used for the fatigue cyclic tests. The available experimental results show that the dimension ratio has no effect on the specimens' fatigue life.

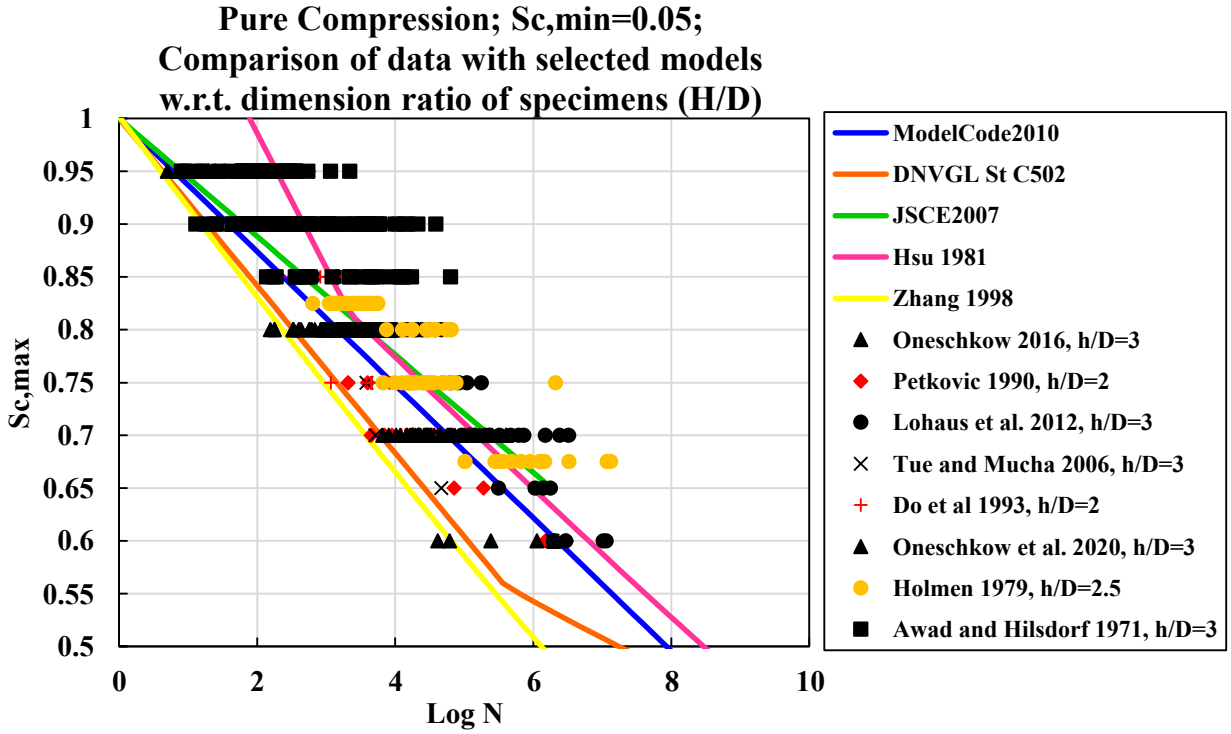

Figure 43 S-N models and experimental data points at pure compression stress state with a minimum stress level of 0.05, data points sorted based on dimension ratio of concrete specimens (H/D).

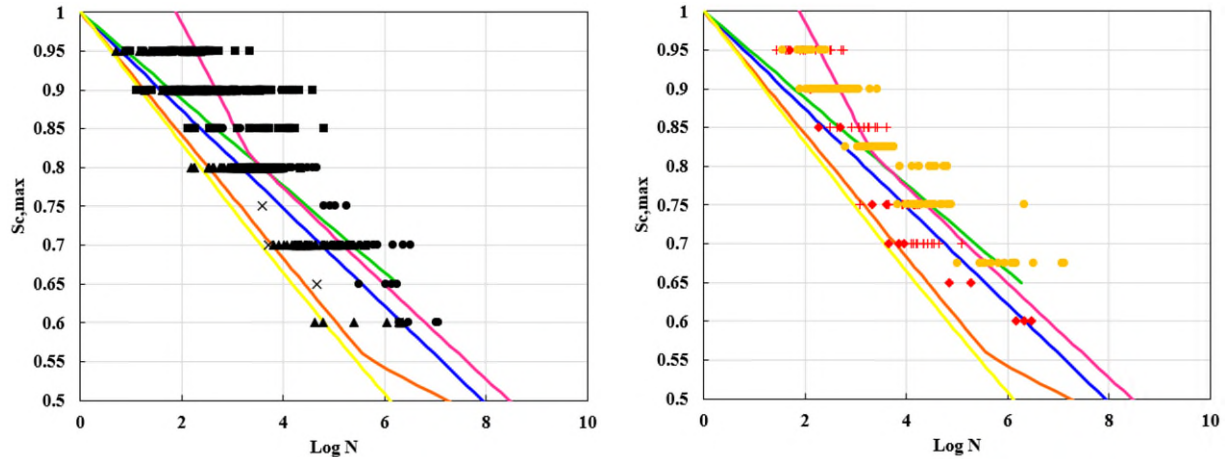

Figure 44 S-N models and experimental data points at pure compression stress state with a minimum stress level of 0.05, data points sorted based on dimension ratio of concrete specimens (H/D) and plotted separately.

3.3.5 Saturation level

The only data points available on cyclic compression of PC were from Oneschkow experiments on concrete with ultra-high strength and some level of saturation during the test. It is not reasonable to draw any conclusions based on these limited data points, but it seems that both the DNVGL and JSCE models work well.

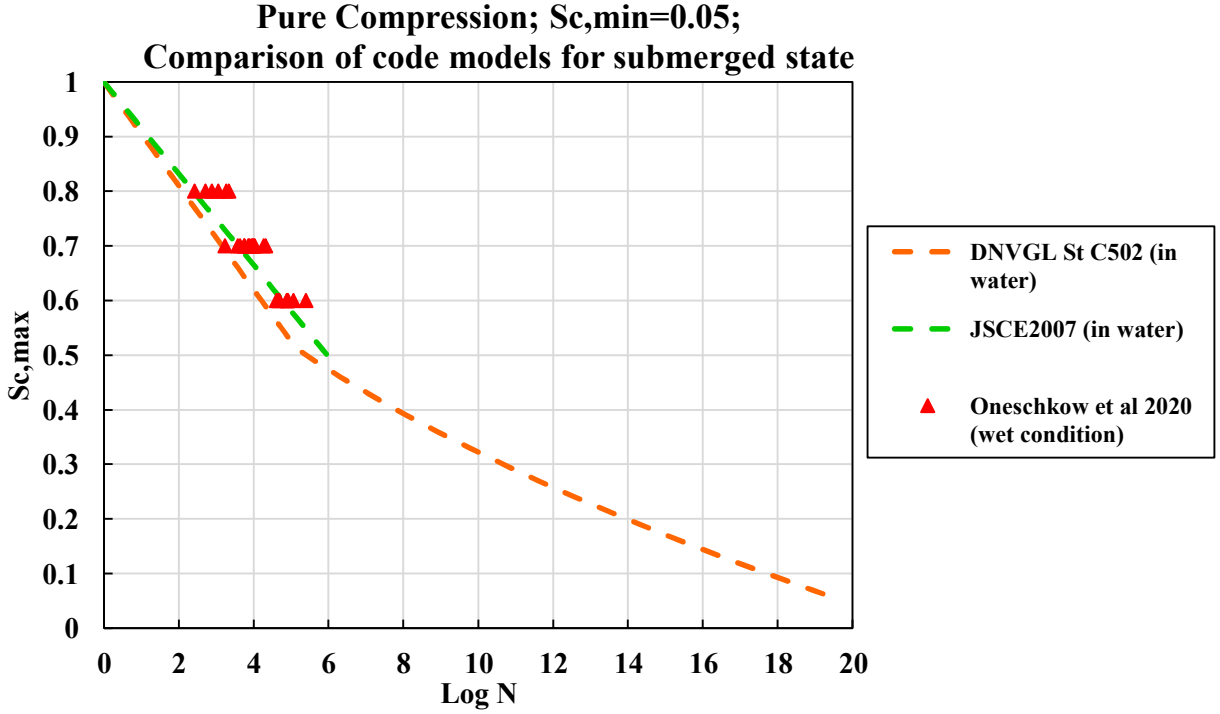

Figure 45 S-N models and experimental data points at pure compression stress state with a minimum stress level of 0.05, saturated specimens test results.

3.3.6 Waveform

A few researchers have indicated that the type of waveform might have an effect on the concrete's fatigue life. This report includes the highest number of data points. No significant effect of wave-form type is apparent.

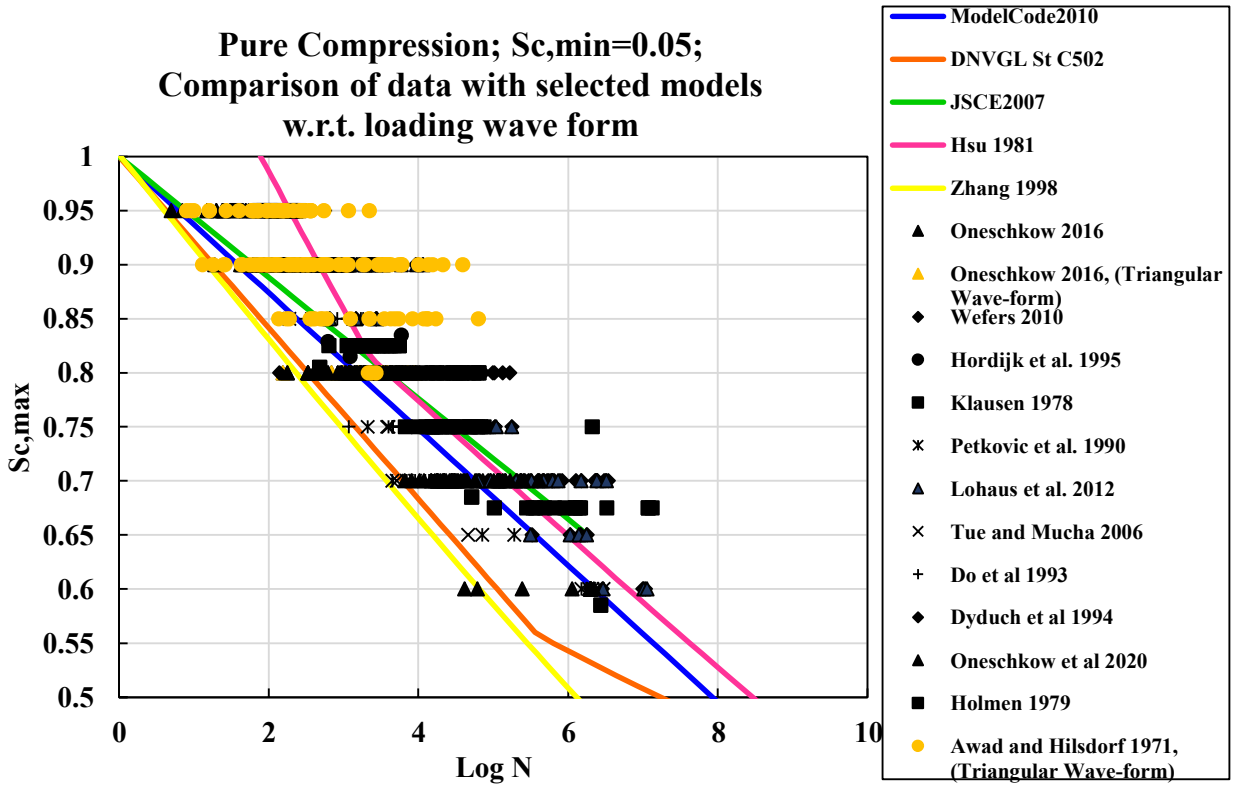

Figure 46 S-N models and experimental data points at pure compression stress state with a minimum stress level of 0.05, data points sorted based on loading wave form.

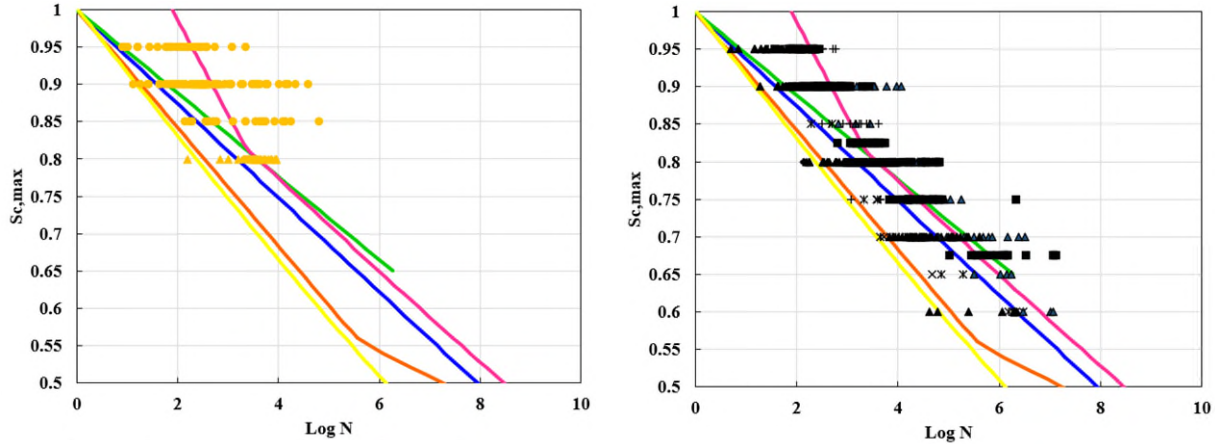

Triangular wave form loading

Sine wave loading

Figure 47 S-N models and experimental data points at pure compression stress state with a minimum stress level of 0.05, data points sorted based on loading wave form and plotted separately.

3.3.7 Summary

Overall, 13 different concrete fatigue life estimation models (S-N models) were organized within a spreadsheet. The design requirements of these models were extracted from codes, standards, books, theses, and research papers. Almost all of the codes use the same methodology to evaluate fatigue life in design: Hain's models.

Some of the limitations mentioned could have a huge impact on the final results, and were therefore evaluated in the test series described later in this document. All of the S-N models are for plain concrete in different stress states and do not consider the impact of reinforcement (both longitudinal and transverse) and confinement on the final number of cycles to failure. In static loading, both of those elements impact the final result of strength significantly. The effect of saturation is also under-studied.

The stress demand evaluation in offshore wind turbine structures in task 4 showed that the existing test results are not relevant to the stress demands typical of that context. The existing models also do not predict the numbers of cycles at failure at the stress demands required of that context. A set of tests at needed stress demand could elucidate which models have a better estimation and the effects of the abovementioned factors.

The evaluation and comparison of with models reveal clear effects of concrete's strength, saturation state, and frequency of loading on the material's fatigue life, but the effect of loading waveform and dimensions of the experimental specimens remain unclear.

3.4 Concrete fatigue experimental database spreadsheet / dashboard

3.4.1 Introduction

The capacity of concrete under fatigue loading has been studied for at least 50 years. Although several relationships exist relating applied stresses (S) to concrete's fatigue life (N), there is no consensus regarding any specific S-N equation or set of equations that should be used. The first task in comparing S-N models was to create a test data repository that could be used to examine the accuracy of existing models and to understand differences in the bases of these models. The presented repository has a flexible format to accommodate different test data. Both U.S. Customary Units (USCU) and international system metric units (SI) can be used. The test database template accommodates the entry of test data based on the different independent variables that were utilized in the research. Since test specimens vary in size and/or shape (cylinders, cubes, or prisms), conversion factors were used based on previous research. This repository was created in the form of an Excel spreadsheet with multiple tabs. The first and second tabs include the concrete fatigue experimental test data both in USCU and SI units. The other tabs include the comparison of the data with S-N models, with each tab focusing on a single model. The salient features that can be found within each tab of the developed experimental test data repository are further explained below (Figure 48).

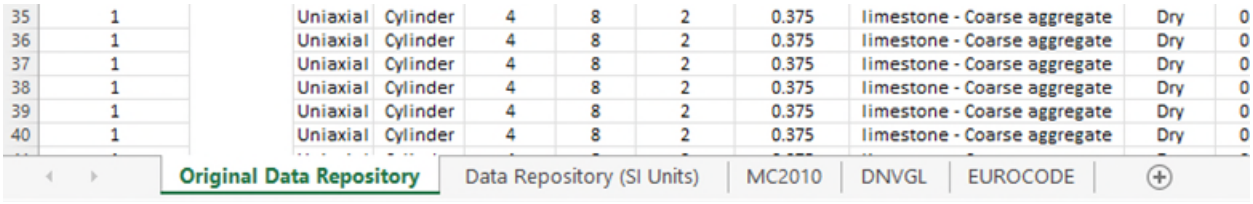

Figure 48 Screenshot #1 of the experimental test data repository – Tabs definition.

The first tab consists of multiple entries for experimental data on fatigue. This tab is designed to include all possible variables that could give the reader insight into concrete characteristics and the variables that control the fatigue response of concrete to cyclic fatigue loading. For example, some basic information about the test data is provided, such as the name of the reference document, type of test (uniaxial or flexural), and information about the geometry of the specimens used in the experimental investigations. Additional data ,including the material properties of concrete used in the specimens listed (max aggregate size and type, water to cement ratio, cement type, additives name and percent of usage, fibers name and percentage of use, and strength of concrete), is also provided if it was publically available. Shown below in Figure 49 are the stress-strain curves of concrete under monotonic compressive loading from the tests conducted at the University of Illinois at Urbana-Champaign (UIUC). Tthe dashed black line in the figure represents an average concrete stress-strain curve. Concrete exhibits an inherently nonlinear material response. Additionally, Figure 50 shows the progressive damage in the concrete cylinder specimens with increasing loads. The letters a, b, and c in Figure 50 roughly correspond to the three last red dots along the concrete stress-strain curves shown in Figure 49. The spreadsheet was developed to request information at the locations of the four red dots seen in Figure 49 (which correspond to strains of 0.1%, 0.2%, 0.3%, and 0.4%, respectively), to more completely capture concrete's behavior. The stress and strain magnitudes at the location of ultimate stress that the concrete cylinders were able to sustain were also recorded and are represented in Figure 49 with the black cross-mark (X).

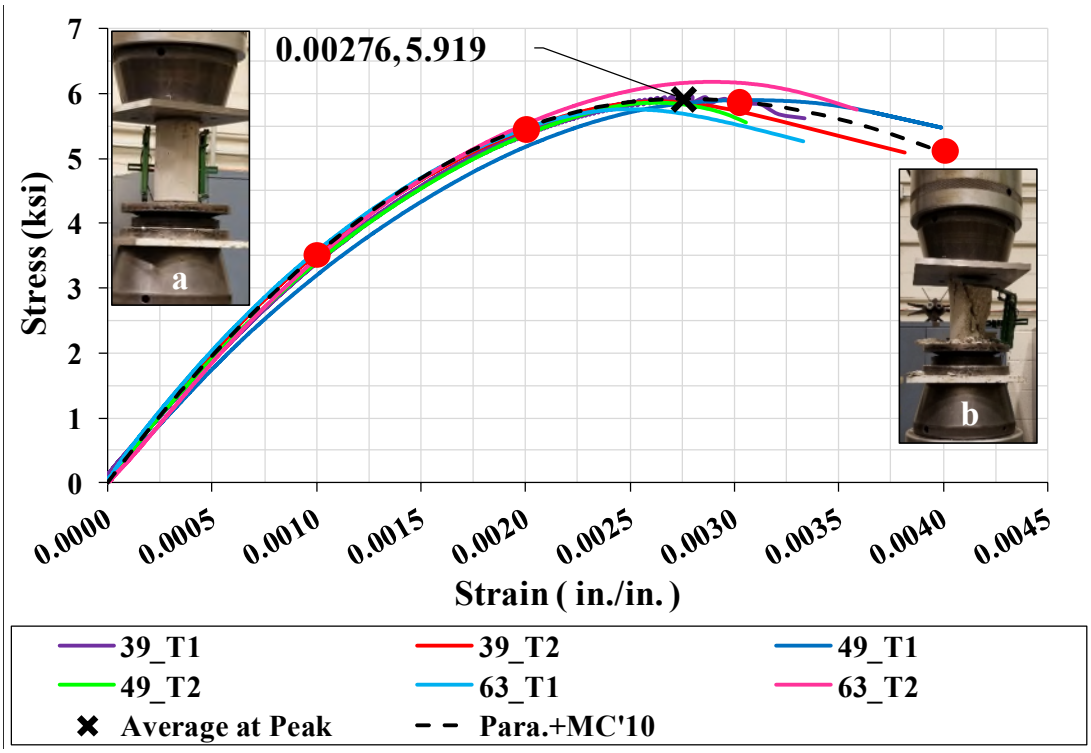

Figure 49 Concrete monotonic stress-strain behavior (from the tests conducted at UIUC [25]).

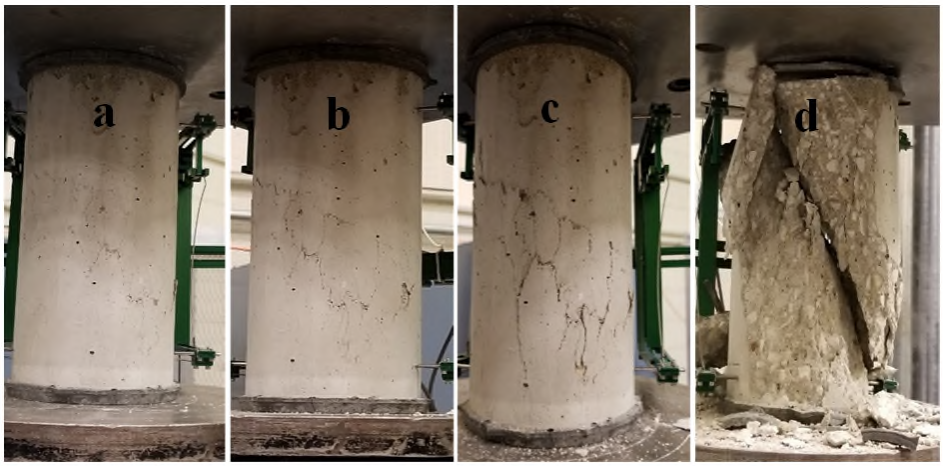

Figure 50 Progressive damage in the concrete cylinder specimens under increasing load.

Figure 51 presents a screen capture of the experimental test data repository, representing information about the geometry and material properties. The various tabs seen at the bottom of the spreadsheet correspond to the various templates that have been created to accommodate the differences in the experiments. Figure 51 shows the populated first tab, which includes concrete

cylinder specimens tested under uniaxial compressive fatigue and referred to the U.S. Customary Units (USCU).

	A	B	C	D	E	F	G	H	I
1	Reference number	Defintion	-	Specimen type	Width/ Diameter	Height	Dimention ratio	Maximum aggregate size	Aggregate type
2	Reference #	Reference	Test Type	Specimen type	b/D (mm/in)	h (mm/in)	DR (h/b or h/D)	d_ag (mm/in)	Aggregate type
3	1	UIUC Test Data 2019 (BFTS) - Individual Test Entries; Uniaxial Compressive Fatigue Loading Tests (with	Uniaxial	Cylinder	4	8	2	0.375	limestone - Coarse aggregate
4	1		Uniaxial	Cylinder	4	8	2	0.375	limestone - Coarse aggregate
5	1		Uniaxial	Cylinder	4	8	2	0.375	limestone - Coarse aggregate
6	1		Uniaxial	Cylinder	4	8	2	0.375	limestone - Coarse aggregate
7	1		Uniaxial	Cylinder	4	8	2	0.375	limestone - Coarse aggregate
8	1		Uniaxial	Cylinder	4	8	2	0.375	limestone - Coarse aggregate
9	1		Uniaxial	Cylinder	4	8	2	0.375	limestone - Coarse aggregate
10	1		Uniaxial	Cylinder	4	8	2	0.375	limestone - Coarse aggregate
11	1		Uniaxial	Cylinder	4	8	2	0.375	limestone - Coarse aggregate
12	1		Uniaxial	Cylinder	4	8	2	0.375	limestone - Coarse aggregate
13	1		Uniaxial	Cylinder	4	8	2	0.375	limestone - Coarse aggregate
14	1		Uniaxial	Cylinder	4	8	2	0.375	limestone - Coarse aggregate
15	1		Uniaxial	Cylinder	4	8	2	0.375	limestone - Coarse aggregate
16	1		Uniaxial	Cylinder	4	8	2	0.375	limestone - Coarse aggregate
17	1		Uniaxial	Cylinder	4	8	2	0.375	limestone - Coarse aggregate
18	1		Uniaxial	Cylinder	4	8	2	0.375	limestone - Coarse aggregate
19	1		Uniaxial	Cylinder	4	8	2	0.375	limestone - Coarse aggregate
20	1		Uniaxial	Cylinder	4	8	2	0.375	limestone - Coarse aggregate

Figure 51 Screenshot #2 of the experimental test data repository – Specimen Geometry and Material Properties

J	K	L	M	N	O	P	Q	R	S	T	U	V	W
Dry / Saturated	water to cement ratio	Cement type	Additives	fiber	Strength (28 days)	Strength at the test day	Maximum stress ratio	Minimum stress ratio	Stress ratio (Smin/Smax)	Frequency of Loading	Type of loading waveform	Number of cycle per failure	-
	w/c				f'c (MPa/psi)	fcm_test (MPa/psi)	Smax	Smin	R	Frequency (Hz)	Waveform	Nf	Log Nf
Dry	0.54	Type I	N/A	N/A	5919	5793	0.85	0.255	0.3	2	Sinusoidal-Wave	277716	5.443600901
Dry	0.54	Type I	N/A	N/A	5919	5793	0.85	0.255	0.3	2	Sinusoidal-Wave	221719	5.345802911
Dry	0.54	Type I	N/A	N/A	5919	5793	0.85	0.255	0.3	2	Sinusoidal-Wave	85307	4.930984669
Dry	0.54	Type I	N/A	N/A	5919	5793	0.825	0.165	0.2	2	Sinusoidal-Wave	13844	4.141261591
Dry	0.54	Type I	N/A	N/A	5919	5793	0.825	0.165	0.2	2	Sinusoidal-Wave	4379	3.641374945
Dry	0.54	Type I	N/A	N/A	5919	5793	0.825	0.165	0.2	2	Sinusoidal-Wave	2819	3.450095076
Dry	0.54	Type I	N/A	N/A	5919	5793	0.825	0.165	0.2	2	Sinusoidal-Wave	2100	3.322219295
Dry	0.54	Type I	N/A	N/A	5293	5293	0.8	0.24	0.3	2	Sinusoidal-Wave	> 852596	5.93
Dry	0.54	Type I	N/A	N/A	5919	5793	0.8	0.16	0.2	3	Sinusoidal-Wave	175523	5.244334033
Dry	0.54	Type I	N/A	N/A	5919	5793	0.8	0.16	0.2	3	Sinusoidal-Wave	77855	4.891286509
Dry	0.54	Type I	N/A	N/A	5919	5793	0.8	0.16	0.2	3	Sinusoidal-Wave	8185	3.913018684
Dry	0.54	Type I	N/A	N/A	5919	5793	0.8	0.16	0.2	3	Sinusoidal-Wave	6835	3.834738519
Dry	0.54	Type I	N/A	N/A	5919	5793	0.8	0.16	0.2	2	Sinusoidal-Wave	99525	4.997932186
Dry	0.54	Type I	N/A	N/A	5919	5793	0.8	0.16	0.2	2	Sinusoidal-Wave	20950	4.321184027
Dry	0.54	Type I	N/A	N/A	5293	5293	0.8	0.16	0.2	2	Sinusoidal-Wave	18571	4.26883529
Dry	0.54	Type I	N/A	N/A	5293	5293	0.8	0.16	0.2	2	Sinusoidal-Wave	9198	3.963693405
Dry	0.54	Type I	N/A	N/A	5919	5793	0.8	0.08	0.1	2	Sinusoidal-Wave	65089	4.813507599

Figure 52 Screenshot #3 of the experimental test data repository – Material Properties and cyclic fatigue loading regime.

Next, information about the fatigue loading plan is requested or added to the spreadsheet. This includes the average concrete monotonic strength (that would be used for determining the

magnitude of the applied stresses), the peak and valley fatigue stress levels, the frequency of loading, and the waveform that was used in the various fatigue experiments. Figure 52 presents another screenshot from the experimental test data repository. The mean concrete strength used for computing the applied fatigue stress levels is represented by “fcm_test”, representing the control value of monotonic strength used in the fatigue tests. As mentioned previously, different fatigue models use different independent variables. For the tests conducted at UIUC, the fatigue model used while selecting the fatigue stress combinations utilized the peak stress level, Smax, and stress ratio, R, (which is the ratio of the valley stress level to the peak stress level), as the independent variables, which is also reflected in this tab of the database. The minimum stress level, Smin, is computed from these two independent variables. The waveform and the frequency of testing used in the experiments are also indicated in the database, as seen in Figure 52.

With the details about the specimen geometry, material properties, and fatigue loading plan obtained, fatigue experimental test results can be populated next in the spreadsheet. The most basic fatigue test result that is reported in almost all fatigue investigations is the number of cycles to failure, $N_{f,}$ also referred to as the fatigue capacity. Additionally, considering the inherently nonlinear material behavior of concrete, it is important to also understand and report the behavior of concrete throughout the fatigue loading history. However, only a small proportion of the papers and investigations have reported this. Therefore, in order to further the understanding of concrete behavior under fatigue loading, it was decided to also request aspects related to concrete fatigue behavior in the database to allow for a complete understanding of the performance of concrete through the duration of fatigue loading.

After having populated the first tab with relevant data, other tabs can be used to compare the data with the existing characteristics and design S-N curves introduced by different standard codes or

researchers. For this purpose, a table has been created to allow the user to filter for specific test data and compare it with the S-N curves. Figure 53 shows a screenshot of the aforementioned table, which includes all the critical variables. Figure 54 and Figure 55 show a comparison of the uniaxial fatigue test data with four different Smin level ranges via two different characteristic S-N models (DNVGL & Model Code 2010) with the same Smin levels.

↓ Define Specified Ranges ↓

Markers and colors		-	Smin	Strength (MPa)	Frequency (Hz)	Waveform	d_ag (mm) max aggregate size	Dimension ratio	Height (mm)	Width/ diameter (mm)	Additives	water/ cement	Test type	Type of specimen	Fiber	Moisture Content	Number of Data points
	A	min	0	0	0	All	0	0	0	0	All	0	Uniaxial	All	All	All	859
		max	0.1	200	60		45	10	1000	500		0.8					
	B	min	0.101	0	0	All	0	0	0	0	All	0	Uniaxial	All	All	All	102
		max	0.2	200	60		45	10	1000	500		0.8					
	C	min	0.201	0	0	All	0	0	0	0	All	0	Uniaxial	All	All	All	351
		max	0.3	200	60		45	10	1000	500		0.8					
	D	min	0.301	0	0	All	0	0	0	0	All	0	Uniaxial	All	All	All	46
		max	0.4	200	60		45	10	1000	500		0.8					
	E	min	0.401	0	0	All	0	0	0	0	All	0	Uniaxial	All	All	All	86
		max	0.8	200	60		45	10	1000	500		0.8					
																Σ	1444

Figure 53 Screenshot #4 of the experimental test data repository – table for defining data range to be shown in the plots.

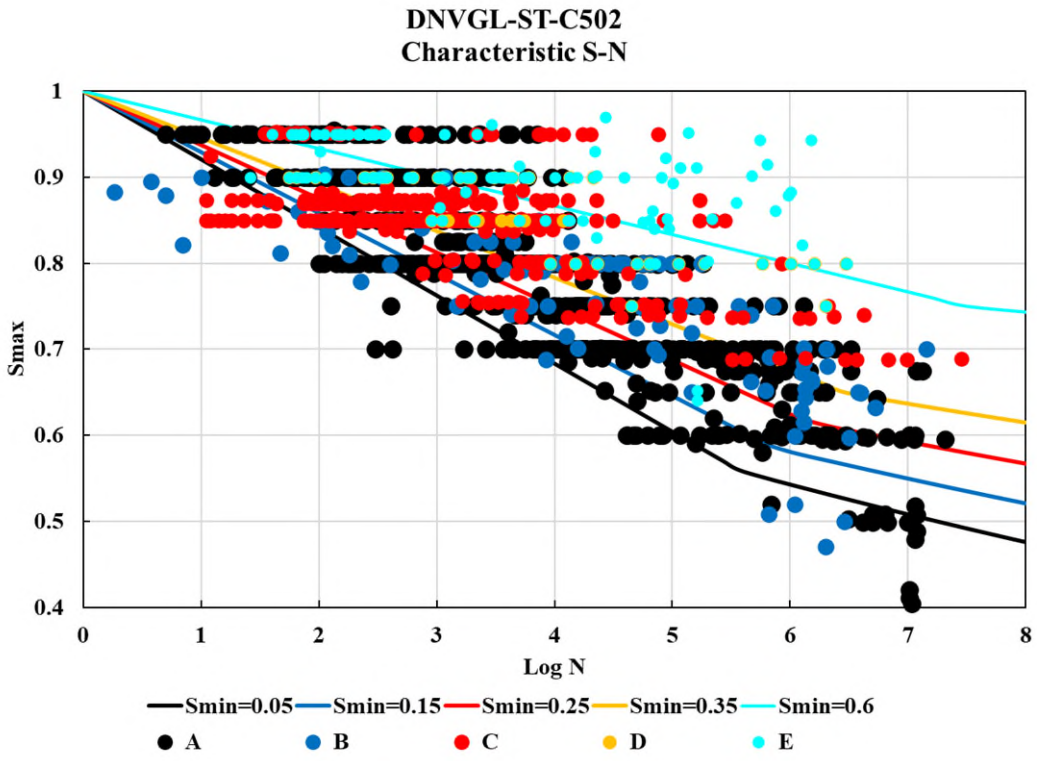

Figure 54 Comparison of different specified data sets with DNVGL characteristic S-N model.

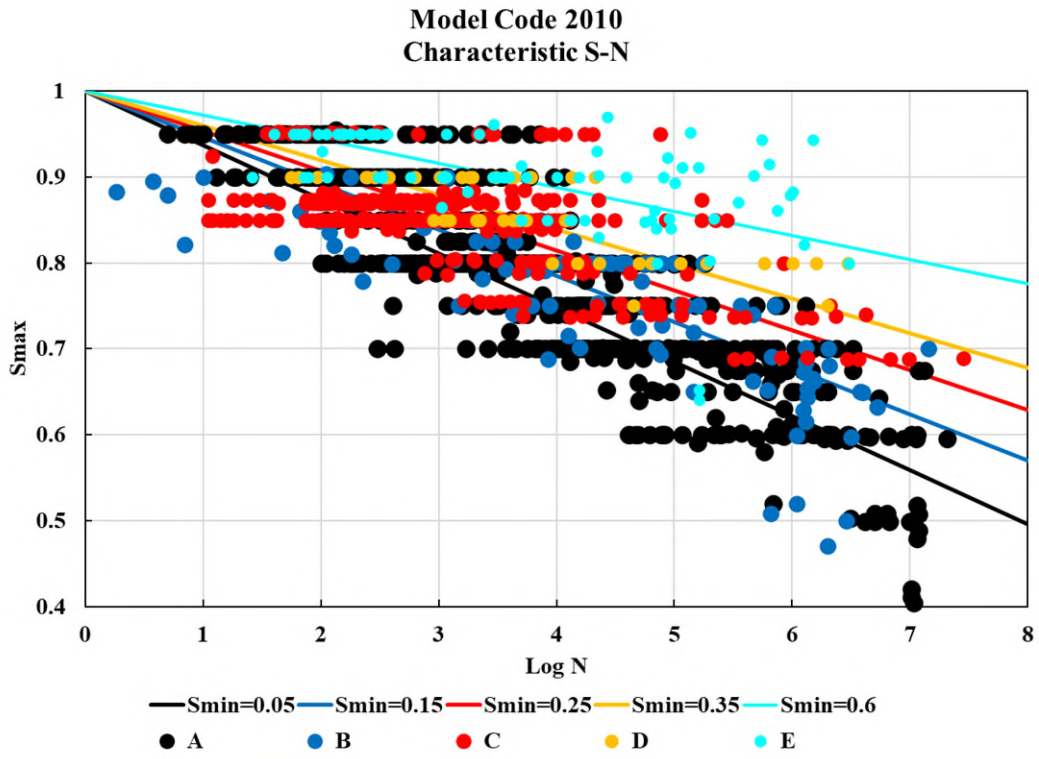

Figure 55 Comparison of different specified data sets with Model Code 2010 characteristic S-N.

The other option that has been included in this tool is the ability to compare the test results to S-N curves of specified designs. Figure 56 shows Model code 2010 design S-N curves with concretes of various reference strengths. These curves have included all of the material reduction factors and partial load factors to enable a reliable and safe design. These capabilities of the spreadsheet are defined in detail in the next section.

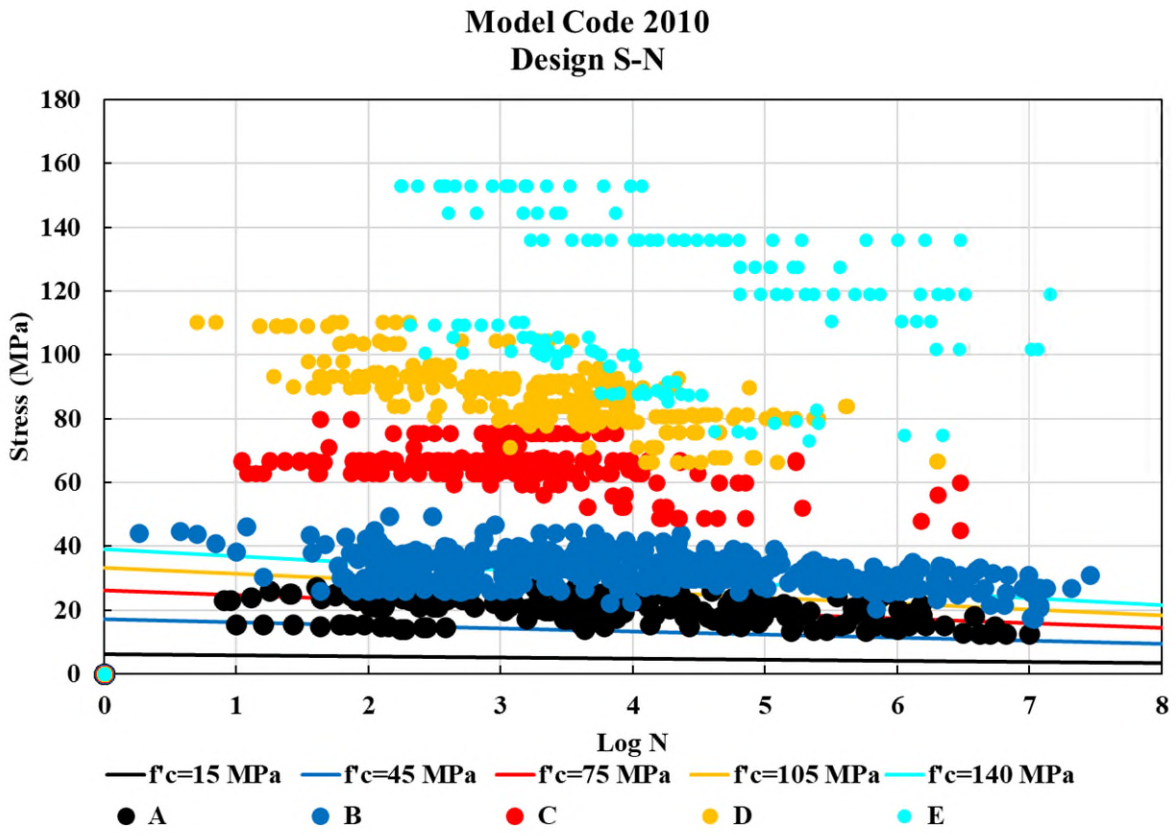

Figure 56 Comparison of different specified data sets with Model Code 2010 Design S-N model

Similar templates were created for the different combinations of the independent variables (units – USCU vs. SI, independent variables – S_{max} and R vs. S_{min}, specimen shapes – cylinders, cubes, or prisms). The experimental test data repository has been populated with data on the failure number of cycles, N_f, including specimen details, material properties, fatigue loading plan, and fatigue capacity, N_f from more than 2400 different tests. Information about strain behavior is unavailable in the public domain for many of these already conducted investigations, though. Efforts are underway to procure the necessary reports to further populate this database with more detailed information. An additional challenge to creating such a database that compares tests conducted around the world is the variation in specimen shape and size, since the compressive strength of concrete is sensitive to specimen geometry. In order to permit comparisons across

specimen geometries, the following concrete compressive strength conversion factors may used to standardize the strength values (Figure 32). The effect of the control specimen geometry was investigated by the PI in a previous research effort that included the creation of a database regarding concrete shear strengths, and these conversion factors were determined as a part of that investigation.

3.4.2 How to use the fatigue data excel spreadsheet[13]

The goal for the design of the Concrete Fatigue Experimental Database Spreadsheet is to be easily used by others to explore the data and derive improved fatigue models. This section includes an overview of the steps that the user needs to take to see the specified results in the plots. The spreadsheet consists of two sheets of data that the user does not need to modify — except to include new data — and three sheets that are designed to create the opportunity for the user to compare the specified data points with three chosen concrete fatigue S-N models (including Model Code 2010, DNVGL-ST-C502, and Eurocode 2) (Figure 57).

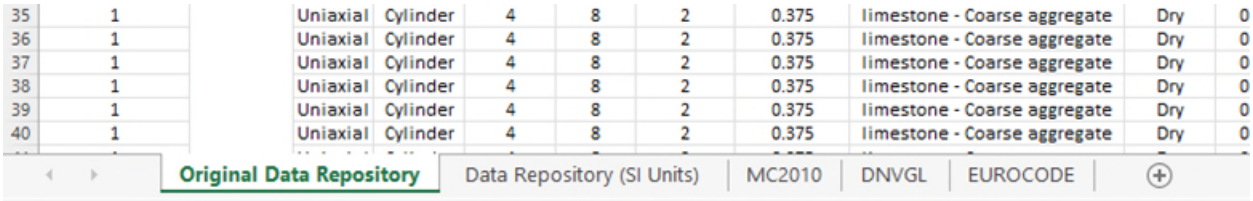

Figure 57 Designed Tabs in the Spreadsheet

3.4.2.1 Table To Filter Data

In each sheet designed for an S-N models, there is a colored table that the user needs to use to define the desired range of data (Figure 58).

[13] https://tufts.box.com/s/rimeao5efwblmcdecr2gopiq5i47phj1

↓ Define Specified Ranges ↓																
Markers and colors	-	Smin	Strength (MPa)	Frequency (Hz)	Waveform	d_ag (mm) max aggregate size	Dimension ratio	Height (mm)	Width/ diameter (mm)	Additives	water/ cement	Test type	Type of specimen	Fiber	Moisture Content	Number of Data points
A	min	0	0	0	All	0	0	0	0	All	0	Uniaxial	All	All	All	859
	max	0.1	200	60		45	10	1000	500		0.8					
B	min	0.101	0	0	All	0	0	0	0	All	0	Uniaxial	All	All	All	102
	max	0.2	200	60		45	10	1000	500		0.8					
C	min	0.201	0	0	All	0	0	0	0	All	0	Uniaxial	All	All	All	351
	max	0.3	200	60		45	10	1000	500		0.8					
D	min	0.301	0	0	All	0	0	0	0	All	0	Uniaxial	All	All	All	46
	max	0.4	200	60		45	10	1000	500		0.8					
E	min	0.401	0	0	All	0	0	0	0	All	0	Uniaxial	All	All	All	86
	max	0.8	200	60		45	10	1000	500		0.8					
															Σ	1444

Figure 58 Table for defining data range to be shown in the plots in each tab.

This table includes the following variables and content (from left to right):

1. *Markers name and color:* Five different markers with specific colors have been chosen to show the data in the plots.

2. *Smin:* The minimum stress level of the experimental data to be displayed may easily be set for each marker type by typing the minimum and maximum desired value.

3. *Strength (MPa):* The monotonic strength of the concrete that has been tested may be defined by typing the minimum and maximum strength in MPa.

4. *Frequency (Hz):* This column defines the frequency range of cyclic loading in Hertz.

5. *Waveform:* This tab is to define the loading waveform type imposed on the concrete material. For each marker type, the user may click on the cell under the waveform and select one of the following options from the drop-down menu: All, Sinusoidal-wave, Triangular-wave.

6. *d-ag (mm):* This option has been defined to give the user the ability to visually explore the effect of maximum aggregate size (in millimeters) on the concrete's fatigue capacity. The user may type the minimum and maximum desired max aggregate size they wish to plot.

7. *Dimension Ratio:* It includes the ratio of the height of the specimen to the width or diameter, and it enables the user to explore the effect of specimen size on the concrete fatigue capacity.

8. *Height (mm):* This variable is defined to explore the effect of specimen height on the concrete fatigue capacity.

9. *Width or Diameter (mm):* This variable is defined to explore the effect of specimen height on the concrete fatigue capacity. Some specimens are cylinders, and others are prisms and cubes.

10. *Additives:* This tab enables the user to explore the effect of the use of additives in the concrete mix on the fatigue capacity. The user could click on the cell and choose one of the following from the drop-down menu: All, Yes, No. "Yes" stands for the experimental results of the concrete that had additives in the mix, and "No" stands for the concrete mixes that had no additives.

11. *Water-to-cement ratio:* The water-to-cement ratio is one of the key elements that strengthen concrete material.

12. *Test Type:* Generally, a concrete fatigue test can be done in different ways (flexural, uniaxial, biaxial, triaxial). Up to now, this spreadsheet only includes the flexural and uniaxial fatigue test results.

13. *Type of Specimen:* The existing experimental test had been executed on cylindrical, prism, and cubic concrete specimens. The user could choose one of those three options from the drop-down menu and investigate the effect of the test type on the concrete fatigue capacity.

14. *Fiber:* Some concrete mixes have used fibers to improve the mechanical behavior of concrete. By clicking on these cells, the user can choose to see the concrete with or without fibers from the drop-down menu.

15. *Moisture Content:* One of the influential parameters in the literature on the fatigue capacity of concrete is the presence of water. For this purpose, a tab has been defined so that the user can choose one of the following from the drop-down menu to filter the desired data points: All, Dry, Partially Saturated, and Saturated.

16. *The number of Data points:* Finally, an option has been defined in this table that shows the number of remaining data after all these filtrations, and it could be a piece of good information for the user to see the reliability of any conclusions that he/she could draw based on the number of data points. (more data, more realistic and reliable conclusions)

3.4.2.2 Model Code 2010

In the sheet of "MC2010", parameters of Model Code 2010 have been defined to have the characteristic and design S-N curves on the plots and compare them with the existing data points. The parameters can be changed by the user to make their version of the model, and any modifications or improvements to the models can be suggested to better represent the concrete fatigue behavior. Figure 59 shows the table in which the user could define five different Smin levels and automatically see the characteristic S-N model in the plot with the defined color. The user also would be able to modify the model's equation including the variable "Y" to further observe the effect of those modifications.

Model Code 2010 (Characteristic S-N Model)										
S_min_i	0.05	0.15	0.25	0.35	0.6	← Inputs				
Y_i	0.4958	0.5700	0.6288	0.6779	0.7759					
	S_max_A	S_max_B	S_max_C	S_max_D	S_max_E	Log_Nf_A	Log_Nf_B	Log_Nf_C	Log_Nf_D	Log_Nf_E
	1	1	1	1	1	0.000	0.000	0.000	0.000	0.000
	0.99	0.99	0.99	0.99	0.99	0.159	0.186	0.216	0.248	0.357
	0.98	0.98	0.98	0.98	0.98	0.317	0.372	0.431	0.497	0.714
	0.97	0.97	0.97	0.97	0.97	0.476	0.558	0.647	0.745	1.071
	0.96	0.96	0.96	0.96	0.96	0.635	0.744	0.862	0.993	1.428
	0.95	0.95	0.95	0.95	0.95	0.793	0.930	1.078	1.242	1.785
	0.94	0.94	0.94	0.94	0.94	0.952	1.116	1.293	1.490	2.142
	0.93	0.93	0.93	0.93	0.93	1.111	1.302	1.509	1.738	2.498
	0.92	0.92	0.92	0.92	0.92	1.269	1.488	1.724	1.987	2.855
	0.91	0.91	0.91	0.91	0.91	1.428	1.674	1.940	2.235	3.212
	0.9	0.9	0.9	0.9	0.9	1.587	1.860	2.155	2.483	3.569
	0.89	0.89	0.89	0.89	0.89	1.745	2.046	2.371	2.732	3.926
	0.88	0.88	0.88	0.88	0.88	1.904	2.232	2.586	2.980	4.283

Figure 59 Table for defining Smin levels of the characteristic S-N curves shown on the plot.

Figure 60 shows the parameters of Model Code 2010 for the design S-N model for concrete fatigue. In this table, the user could define the Smin level, standard concrete strength (5 different strengths for 5 different colored lines in MPa), reduction and increasing factors (like β_{sus} which is for the effect of sustained load, β_{cct} which is defined to see the effect of strength increase over time and has its formulation, and so on). The user also could change the formulation of the fatigue strength of concrete "fck,fat" to make modifications or improvements to the model.

Model Code 2010 (Design S-N Model)							
S_min_MC2010	Y_MC2010	fck_MC2010	betta_sus_MC2010	Betta_cct_MC2010	Gamma_c_MC2010	Gamma_ed_MC2010	fcd,fat_MC2010
0.1	0.5353	40	0.85	1	1.5	1.1	20.4
		fck_MC	15	45	75	105	140
		fcd,fat_MC	8.18	22.63	34.53	43.88	51.57
S_max_MC2010	LogNf_MC2010	etta_c	Smax_A	Smax_B	Smax_C	Smax_D	Smax_E
1	0.000	0.690	6.206	17.169	26.196	33.289	39.120
0.99	0.172	0.690	6.147	17.003	25.943	32.968	38.742
0.98	0.344	0.690	6.087	16.837	25.690	32.646	38.364
0.97	0.516	0.690	6.027	16.671	25.437	32.325	37.986
0.96	0.689	0.691	5.967	16.506	25.184	32.004	37.609
0.95	0.861	0.691	5.907	16.340	24.932	31.682	37.231
0.94	1.033	0.691	5.847	16.174	24.679	31.361	36.853
0.93	1.205	0.691	5.787	16.008	24.426	31.040	36.476
0.92	1.377	0.692	5.727	15.843	24.173	30.718	36.098
0.91	1.549	0.692	5.667	15.677	23.920	30.397	35.721
0.9	1.721	0.692	5.607	15.511	23.667	30.076	35.343
0.89	1.894	0.693	5.547	15.345	23.414	29.754	34.965

Figure 60 Table for defining Smin levels and other influential parameters, including standard monotonic strength of the concrete of the design S-N curves of model code 2010 shown on the plot.

The formulation of Model Code 2010 for PC is provided below:

Considering the stress ratios as $S_{c,max} = (\sigma_{c,max}/f_{ck,fat})$, $S_{c,min} = (\sigma_{c,min}/f_{ck,fat})$

$$f_{ck,fat} = \beta_{cc}(t) \times \beta_{c,sus}(t,t_0) \times f_{ck} \times (1 - f_{ck}/400)$$

$For\ 0 \le S_{c,min} \le 0.8$:

$$\log_{10} N_1 = \frac{8}{(1-Y)} \times (1 - S_{c,max})$$

$$\log_{10} N_2 = 8 - \frac{8 \times \ln 10}{(1-Y)} \times (Y - S_{c,min}) \times \log_{10}\left(\frac{S_{c,max} - S_{c,min}}{Y - S_{c,min}}\right)$$

$$where: Y = \frac{0.45 + 1.8 \times S_{c,min}}{1 + 1.8 \times S_{c,min} - 0.3 \times {S_{c,min}}^2}$$

$Fatigue\ Capacity = \log_{10} N$;

$if\ \log_{10} N_1 \le 8, \quad \log_{10} N = \log_{10} N_1$; $if\ \log_{10} N_1 > 8, \quad \log_{10} N = \log_{10} N_2$

$For\ S_{c,min} > 0.8, the\ S-N\ relations\ can\ be\ used, with\ S_{c,min} = 0.8$

where:

$\log_{10} N$	Fatigue capacity, with "N" representing the number of cycles to failure
$S_{c,max}$	Peak (or maximum) compressive fatigue stress level (normalized)
$S_{c,min}$	Valley (or minimum) compressive fatigue stress level (normalized)
$\sigma_{c,max}$	The magnitude of peak (or maximum) compressive fatigue stress
$\sigma_{c,min}$	The magnitude of the valley (or minimum) compressive fatigue stress
$f_{ck,fat}$	Reference concrete fatigue compressive strength
f_{ck}	Reference concrete static compressive strength.
$\beta_{cc}(t)$	The coefficient for the age of concrete at the beginning of fatigue loading
$\beta_{c,sus}(t, t_0)$	The coefficient for the effect of high mean stresses (i.e., sustained stresses) during loading; for fatigue loading, this coefficient can be taken as equal to 0.85
$\gamma_{c,fat}$	Partial safety factor for concrete (it is considered equal to 1.5)
γ_{Ed}	Partial safety factor for loads (If the stress analysis is sufficiently accurate or conservative, and this fact is verified by in-situ observations, it may be possible to take it equal to 1)
η_c	Average factor considering strain gradient

3.4.2.3 DNVGL-ST-C502

The sheet of "DNVGL" is designed to allow the users to compare the S-N model introduced by DNVGL-ST-C502 standard for plain concrete with the existing data set. As mentioned, each sheet has a table for filtering data sets in five different desired parts with separate markers and colors in the plot. For having the design S-N model incorporated in the spreadsheet, the formulation and all the partial safety factors have been included in the spreadsheet (see Figure 61). The user could adjust these factors to see the effect of the modifications on the curve and compare it with the filtered data sets.

DNVGL-ST-C502 (Design S-N Model)							
S_min_DNV		fcck	fck,fat	Gamma_f	Gamma_C	frd,fat	
0.1		40	37.333	1	1.5	24.889	
		fcck_DNV	15	45	75	105	140
		frd,fat_DNV	9.75	27.75	43.75	57.75	71.56
S_max_DNV	LogNf_DNV		Smax_A	Smax_B	Smax_C	Smax_D	Smax_E
1	0.000		9.750	27.750	43.750	57.750	71.556
0.99	0.133		9.653	27.473	43.313	57.173	70.840
0.98	0.267		9.555	27.195	42.875	56.595	70.124
0.97	0.400		9.458	26.918	42.438	56.018	69.409
0.96	0.533		9.360	26.640	42.000	55.440	68.693
0.95	0.667		9.263	26.363	41.563	54.863	67.978
0.94	0.800		9.165	26.085	41.125	54.285	67.262
0.93	0.933		9.068	25.808	40.688	53.708	66.547
0.92	1.067		8.970	25.530	40.250	53.130	65.831
0.91	1.200		8.873	25.253	39.813	52.553	65.116
0.9	1.333		8.775	24.975	39.375	51.975	64.400
0.89	1.467		8.678	24.698	38.938	51.398	63.684
0.88	1.600		8.580	24.420	38.500	50.820	62.969

Figure 61 Table for defining Smin level and other influential parameters, including standard monotonic strength of the concrete of the design S-N curves of DNVGL shown on the plot.

The S-N model formulation of DNV code is as follows:

$$f_{cn} = f_{cck} \times \left(1 - {}^{f_{cck}}/_{600}\right) ;$$

$$with: \;\; S_{c,max} = \left(\sigma_{c,max}/f_{rd,fat}\right), \qquad S_{c,min} = \left(\sigma_{c,min}/f_{rd,fat}\right), \qquad f_{rd,fat} = C_5 \times f_{rd}$$

$$\log_{10} N = C_1 \times \left(\frac{1 - S_{c,max}}{1 - S_{c,min}}\right)$$

$$X = \frac{C_1}{1 - S_{c,min} + 0.1 \times C_1}$$

$$if \;\; \log_{10} N \,\{from\ (15)\} \geq X, \qquad \log_{10} N = C_2 \times \left[C_1 \times \left(\frac{1 - S_{c,max}}{1 - S_{c,min}}\right)\right]$$

$$where: C_2 = 1 + 0.2 \times (\log_{10} N - X)$$

$$C_1 = \begin{cases} 12 \; for \; concrete \; in \; air \\ 10 \; for \; concrete \; in \; water \; and \; in \; compression - only \; stress \; domain \\ 8 \; for \; concrete \; in \; water \; and \; in \; compression - tension \; stress \; domain \end{cases}$$

C_5 *is the fatigue strength parameter;* $C_5 = 1.0$ *for concrete;* $C_5 = 0.8$ *for grout*

where:

$\log_{10} N$	Fatigue capacity, with "N" representing the number of cycles to failure
$S_{c,max}$	Peak (or maximum) compressive fatigue stress level (normalized)
$S_{c,min}$	Valley (or minimum) compressive fatigue stress level (normalized)
$\sigma_{c,max}$	The magnitude of peak (or maximum) compressive fatigue stress
$\sigma_{c,min}$	The magnitude of the valley (or minimum) compressive fatigue stress
f_{cck}	Characteristic concrete compressive cylinder strength
f_{cn}	The normalized compression strength
f_{rd}	The compression strength for the type of failure in question (here equal to f_{cn})
$f_{rd,fat}$	Reference concrete fatigue compressive strength
γ_c	The material factor for concrete (is considered equal to 1.8 for PC in FLS and 1.5 for RC in FLS)
γ_f	Partial load factor (for fatigue failure limit state, FLS, the partial load factor shall be 1.0 for all loads)

3.4.2.4 Eurocode 2

The last sheet of the spreadsheet is for comparing the Euro code 2 fatigue model with the data set. After filtering the data set with the provided tools in the sheet, the user can also edit the Euro Code 2 formula and factors to see the effect of each parameter on the final plot and compare the new curve with the desired data sets (see Figure 62). The parameters and formulations are presented below.

Euro Code 2 (Design S-N Model)							
S_min_EC	k1	Gamma_c_EC	betta_cct_EC	fcd,fat_EC			
0.1	0.85	1.5	1				
		fck_EC	15	45	75	105	140
		fcd,fat_EC	7.99	20.91	29.75	34.51	34.91
S_max_DNV	LogNf_DNV		Smax_A	Smax_B	Smax_C	Smax_D	Smax_E
1	0.000		7.990	20.910	29.750	34.510	34.907
0.99	0.133		7.910	20.701	29.453	34.165	34.558
0.98	0.267		7.830	20.492	29.155	33.820	34.209
0.97	0.400		7.750	20.283	28.858	33.475	33.859
0.96	0.533		7.670	20.074	28.560	33.130	33.510
0.95	0.667		7.591	19.865	28.263	32.785	33.161
0.94	0.800		7.511	19.655	27.965	32.439	32.812
0.93	0.933		7.431	19.446	27.668	32.094	32.463
0.92	1.067		7.351	19.237	27.370	31.749	32.114
0.91	1.200		7.271	19.028	27.073	31.404	31.765
0.9	1.333		7.191	18.819	26.775	31.059	31.416
0.89	1.467		7.111	18.610	26.478	30.714	31.067

Figure 62 Table for defining Smin level and other influential parameters, including standard monotonic strength of the concrete of the design S-N curves of Euro Code 2 shown on the plot.

The S-N model formulation of Eurocode 2 is as follows:

$$\log_{10} N = 14 \times \left\{ \frac{\left(1 - S_{c,max}\right)}{\sqrt{(1-R)}} \right\}$$

$$with: \;\; S_{c,max} = \left(\sigma_{c,max}/f_{cd,fat}\right), \qquad S_{c,min} = \left(\sigma_{c,min}/f_{cd,fat}\right), \qquad R = S_{c,max}/S_{c,min}$$

$$f_{cd,fat} = k_1 \times \beta_{cc}(t_0) \times f_{cd} \times (1 - f_{ck}/250) \;\; ; \;\; f_{cd} = {}^{f_{cd}}/_{\gamma_c}$$

where:

$\beta_{cc}(t_0)$ The coefficient for concrete strength at first load application [similar to $\beta_{cc}(t)$]

k_1 Coefficient, recommended value is 0.85 [similar to $\beta_{c,sus}(t, t_0)$]

$$S_{cd,max} \leq \begin{cases} 0.5 + 0.45 \times S_{cd,min} \\ 0.9 \; for \; f_{cd} \leq 50 \; MPa \\ 0.8 \; for \; f_{cd} > 50 \; MPa \end{cases}$$

where:

$\log_{10} N$	Fatigue capacity, with "N" representing the number of cycles to failure
$S_{c,max}$	Peak (or maximum) compressive fatigue stress level (normalized)
$S_{c,min}$	Valley (or minimum) compressive fatigue stress level (normalized)
$\sigma_{c,max}$	The magnitude of peak (or maximum) compressive fatigue stress
$\sigma_{c,min}$	The magnitude of the valley (or minimum) compressive fatigue stress
$f_{cd,fat}$	Reference concrete fatigue compressive strength
f_{cd}	The design's compressive strength
f_{ck}	Reference concrete static compressive strength.
$\beta_{cc}(t)$	The coefficient for concrete strength at first load application
K_1	The coefficient, recommended value is 0.85
γ_c	Partial safety factor for concrete (it is considered equal to 1.5)

3.4.3 Evaluation of the existing data, using the plots generated with the experimental database spreadsheet

A few plots were generated to examine the functionality of the Concrete Fatigue Data Spreadsheet. *Figure 63* shows that the vast majority of the uniaxial concrete fatigue test data is for the Smin level of 0-0.1. The cyclic loads in offshore wind turbine structures, however, consist of different Smin levels, including considerably higher levels.

↓ Define Specified Ranges ↓																
Markers and colors	-	Smin	Strength (MPa)	Frequency (Hz)	Waveform	d_ag (mm) max aggregate size	Dimension ratio	Height (mm)	Width/ diameter (mm)	Additives	water/ cement	Test type	Type of specimen	Fiber	Moisture Content	Number of Data points
A	min	0	0	0	All	0	0	0	0	All	0	Uniaxial	All	All	All	859
	max	0.1	200	60		45	10	1000	500		0.8					
B	min	0.101	0	0	All	0	0	0	0	All	0	Uniaxial	All	All	All	102
	max	0.2	200	60		45	10	1000	500		0.8					
C	min	0.201	0	0	All	0	0	0	0	All	0	Uniaxial	All	All	All	351
	max	0.3	200	60		45	10	1000	500		0.8					
D	min	0.301	0	0	All	0	0	0	0	All	0	Uniaxial	All	All	All	46
	max	0.4	200	60		45	10	1000	500		0.8					
E	min	0.401	0	0	All	0	0	0	0	All	0	Uniaxial	All	All	All	86
	max	0.8	200	60		45	10	1000	500		0.8					

Figure 63 Defined data ranges to see the effect of Smin level on the fatigue capacity of the concrete specimens under uniaxial cyclic test.

Figure 64 is the plot generated based on the data filtered in *Figure 63*. Some low and high data points are far from the main cluster of the test results (shown with red arrows on the plot). To narrow down the scatter of the data points to the main data cluster, would require redoing a few tests in each of these load combinations (Smax, Smin). There is a need for careful examination of this dataset (f'c, aggregate, geometry, saturation) to determine what to retest. For the tests

requiring large numbers of load cycles, some of the tests can be stopped after the number of loading cycles to failure, which is just of academic interest.

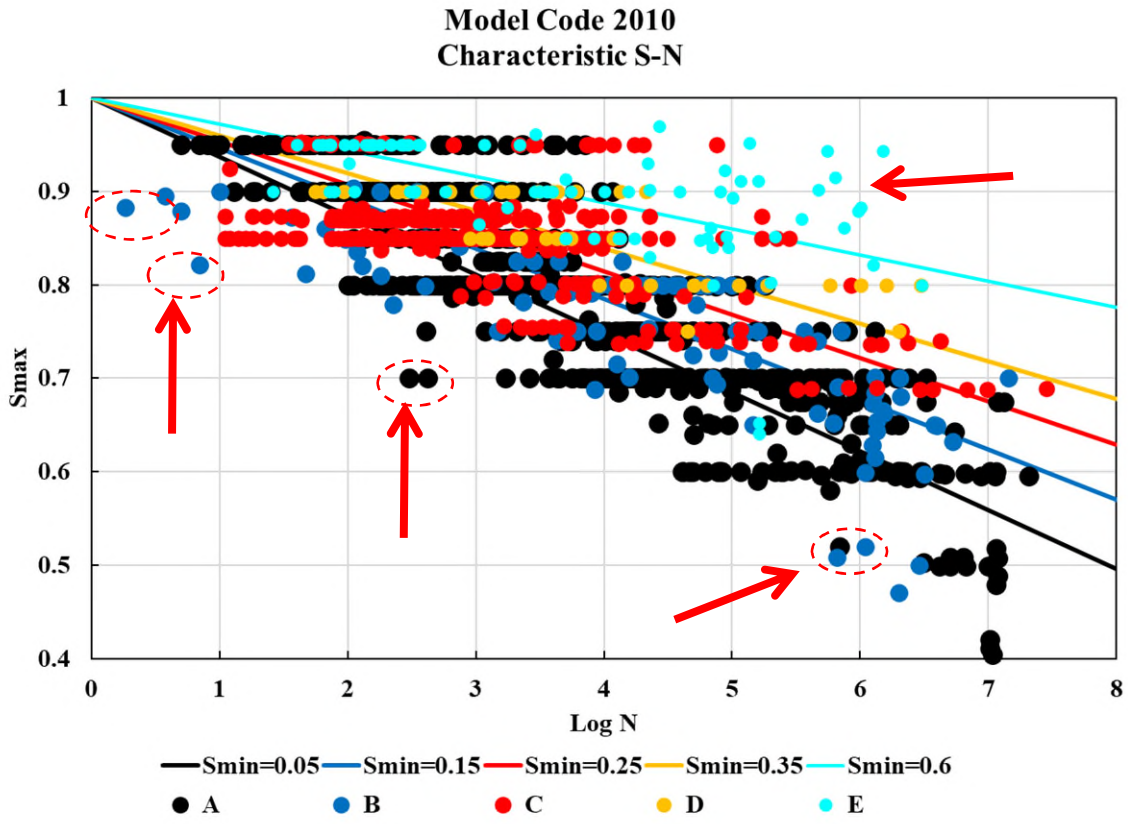

Figure 64 Uniaxial concrete fatigue test data with five different Smin ranges compared with characteristic S-N model code with five different average Smin levels.

Below, a few more examples of use of the tool to assessm data are listed and explained:

3.4.3.1 Exploring the effect of concrete strength

The data points were filtered in a way to show the uniaxial test results with no fiber, for four different strength levels (A: 0-30, B: 30-60, C: 60-90, D: 90-120, E: 120-200 MPa) (see Figure 65).

↓ Define Specified Ranges ↓																	
Markers and colors		-	Smin	Strength (MPa)	Frequency (Hz)	Waveform	d_ag (mm) max aggregate size	Dimension ratio	Height (mm)	Width/ diameter (mm)	Additives	water/ cement	Test type	Type of specimen	Fiber	Moisture Content	Number of Data points
	A	min	0	0	0	All	0	0	0	0	All	0	Uniaxial	All	No	All	76
		max	0.1	30	60		45	10	1000	500		0.8					
	B	min	0	30.01	0	All	0	0	0	0	All	0	Uniaxial	All	No	All	244
		max	0.1	60	60		45	10	1000	500		0.8					
	C	min	0	60.01	0	All	0	0	0	0	All	0	Uniaxial	All	No	All	36
		max	0.1	90	60		45	10	1000	500		0.8					
	D	min	0	90.01	0	All	0	0	0	0	All	0	Uniaxial	All	No	All	158
		max	0.1	120	60		45	10	1000	500		0.8					
	E	min	0	120.01	0	All	0	0	0	0	All	0	Uniaxial	All	No	All	60
		max	0.1	200	60		45	10	1000	500		0.8					
																∑	774

Figure 65 Uniaxial concrete fatigue test data with Smin range of 0-0.1 and with five different strength levels and No fibers.

Figure 66 shows the abovementioned filtered data points compared to the S-N curves of Model Code 2010. This plot shows that the data points have a larger scatter than the model. Generally, in the lower Smax levels, higher strength of concrete result in lower fatigue capacity. To more fully explore the effect of strength on fatigue capacity, Figure 66 was drawn to include only the average value of any specific load combination. Higher strengths result in a higher number of cycles to failure at higher Smax levels (Smax>0.85), and at lower Smax levels (Smax<0.85), high and ultra-high strength concretes have less fatigue capacity than does normal concrete. Higher strength concretes can endure more load and will result in smaller structural elements for the same load. Therefore, comparing only the same (Smax, Smin) combination would not be realistic; rather, comparisons should be made with the design of S-N models.

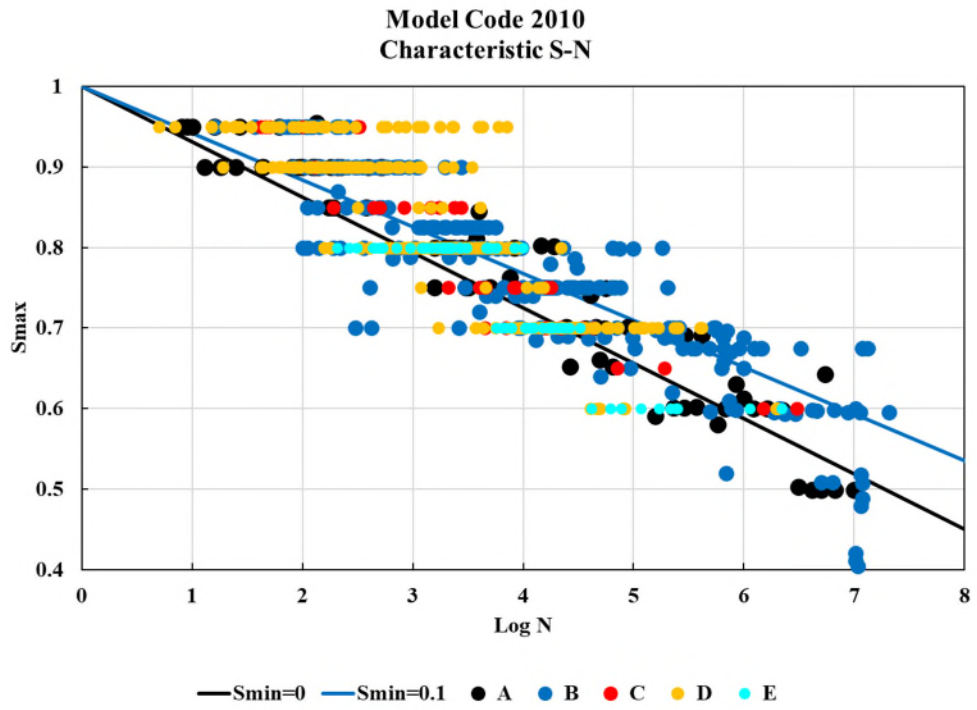

Figure 66 Uniaxial concrete fatigue test data with Smin range of 0-0.1 and with five different strength levels and No fibers, plus model code S-N curves for min and max Smin.

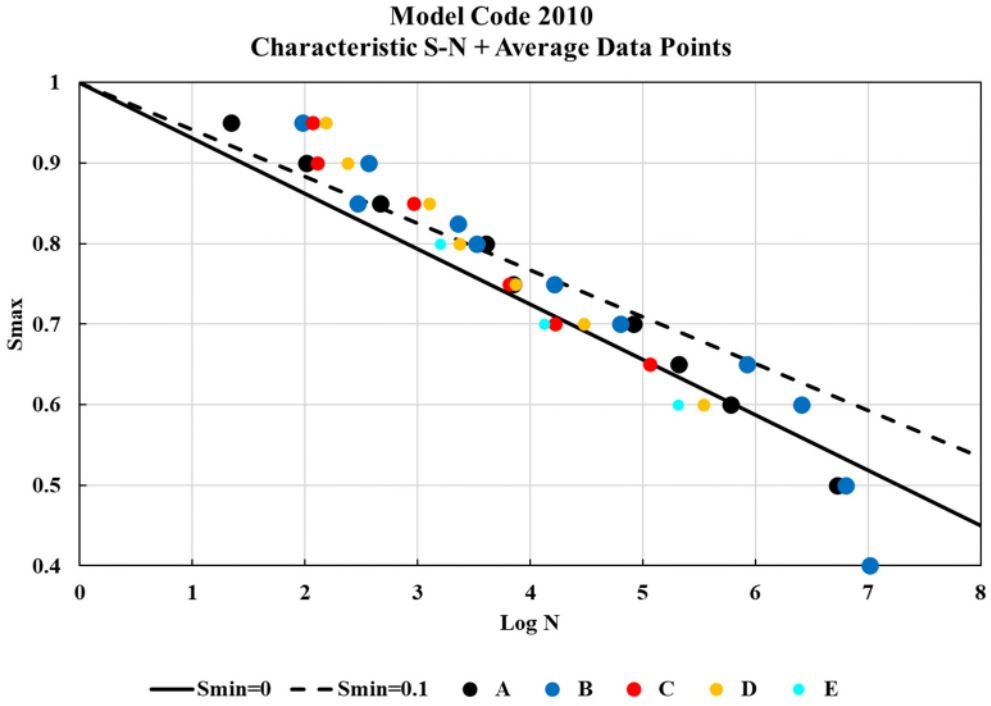

Figure 67 Plot of average uniaxial concrete fatigue test data with Smin range of 0-0.1 and with five different strength levels and No fibers.

3.4.3.2 Exploring the effect of loading frequency

To evaluate the effect of the frequency of loading and explore the functionality of the spreadsheet, the data points were filtered to show the uniaxial concrete test results in the Smin range of 0-0.1 and five different frequency levels (A: 0-0.99, B: 1-1.99, C: 2-4.99, D: 5-9.99, and E: greater than 10 Hz) (See Figure 68).

↓ Define Specified Ranges ↓																
Markers and colors	-	Smin	Strength (MPa)	Frequency (Hz)	Waveform	d_ag (mm) max aggregate size	Dimension ratio	Height (mm)	Width/ diameter (mm)	Additives	water/ cement	Test type	Type of specimen	Fiber	Moisture Content	Number of Data points
A	min	0	0	0	All	0	0	0	0	All	0	Uniaxial	All	All	All	139
	max	0.1	200	0.99		45	10	1000	500		0.8					
B	min	0	0	1	All	0	0	0	0	All	0	Uniaxial	All	All	All	254
	max	0.1	200	1.99		45	10	1000	500		0.8					
C	min	0	0	2	All	0	0	0	0	All	0	Uniaxial	All	All	All	88
	max	0.1	200	4.99		45	10	1000	500		0.8					
D	min	0	0	5	All	0	0	0	0	All	0	Uniaxial	All	All	All	140
	max	0.1	200	9.99		45	10	1000	500		0.8					
E	min	0	0	10	All	0	0	0	0	All	0	Uniaxial	All	All	All	238
	max	0.1	200	60		45	10	1000	500		0.8					
															Σ	859

Figure 68 Table of uniaxial concrete fatigue test data with Smin range of 0-0.1 and with five different frequency ranges and No fibers.

Figure 69 shows that a higher frequency of loading results in a higher number of cycles to failure. To better understand this effect, another plot with only the average data points in each loading combination has been generated, as shown in Figure 70. With an increase of the loading frequency from A (0-0.99) to C (2-4.99), the number of cycles per failure in uniaxial testing increases. However, going beyond 5 Hz affects the fatigue capacity, lowering the number of cycles per failure. In the literature, this effect is mentioned as a heating effect: in higher frequencies of loading, the concrete material starts to heat up and lose its mechanical characteristics [46].

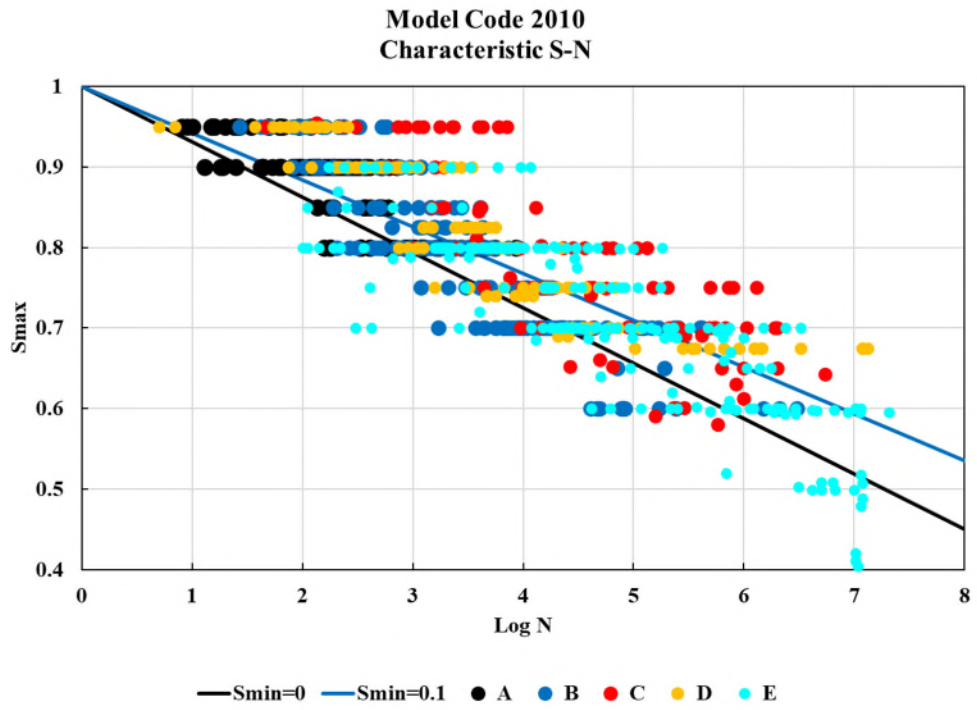

Figure 69 Plot of uniaxial concrete fatigue test data with Smin range of 0-0.1 and with five different frequency ranges and No fibers, plus model code S-N curves for min and max Smin.

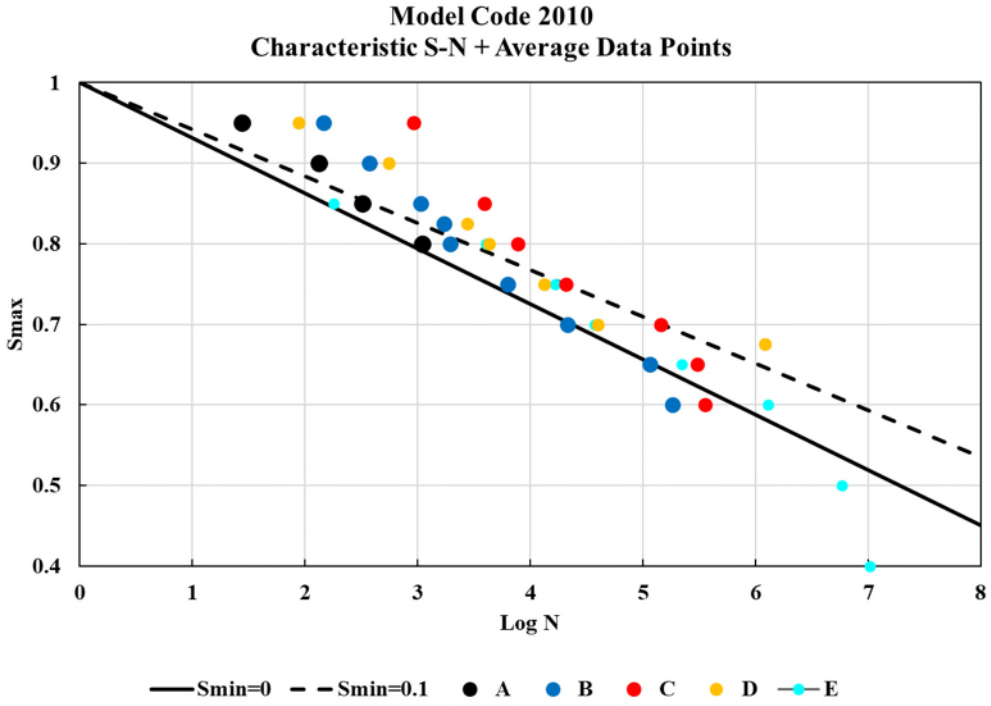

Figure 70 Plot of average uniaxial concrete fatigue test data with Smin range of 0-0.1 and with five different frequency ranges and No fibers.

3.4.3.3 Exploring the effect of maximum aggregate size

The maximum aggregate size of the concrete material was also considered. The data was filtered to show the uniaxial test results in the Smin range of 0-0.1 and five different aggregate sizes (A: 0-0.01, B: 0-7, C: 7-9, D: 9-11, and E: greater than 11 mm) (see *Figure 71*).

↓ Define Specified Ranges ↓

Markers and colors	-	Smin	Strength (MPa)	Frequency (Hz)	Waveform	d_ag (mm) max aggregate size	Dimension ratio	Height (mm)	Width/ diameter (mm)	Additives	water/ cement	Test type	Type of specimen	Fiber	Moisture Content	Number of Data points
A	min	0	0	0	All	0	0	0	0	All	0	Uniaxial	All	All	All	264
	max	0.1	200	60		0.01	10	1000	500		0.8					
B	min	0	0	0	All	0.01	0	0	0	All	0	Uniaxial	All	All	All	0
	max	0.1	200	60		7	10	1000	500		0.8					
C	min	0	0	0	All	7.01	0	0	0	All	0	Uniaxial	All	All	All	433
	max	0.1	200	60		9	10	1000	500		0.8					
D	min	0	0	0	All	9.01	0	0	0	All	0	Uniaxial	All	All	All	86
	max	0.1	200	60		11	10	1000	500		0.8					
E	min	0	0	0	All	11.01	0	0	0	All	0	Uniaxial	All	All	All	76
	max	0.1	200	60		45	10	1000	500		0.8					
															Σ	859

Figure 71 Table of uniaxial concrete fatigue test data with Smin range of 0-0.1 and with five different maximum aggregate sizes and No fibers.

Figure 72 shows that a higher aggregate size increases the number of cycles to failure. Note that the black marker (A) is representative of the data points, and there was no information about the maximum aggregate size. The blue marker (B) also has no data in this specific Smin range. Figure 73 shows the average data point for each specific Smax level. With an increase in maximum aggregate size from (C: 7-9 mm) to (D: 9-11 mm), the fatigue capacity increases, but for a higher max aggregate size (E: greater than 11 mm) this trend is reversed. There is a need to explore the effect of specimen dimension and other parameters.

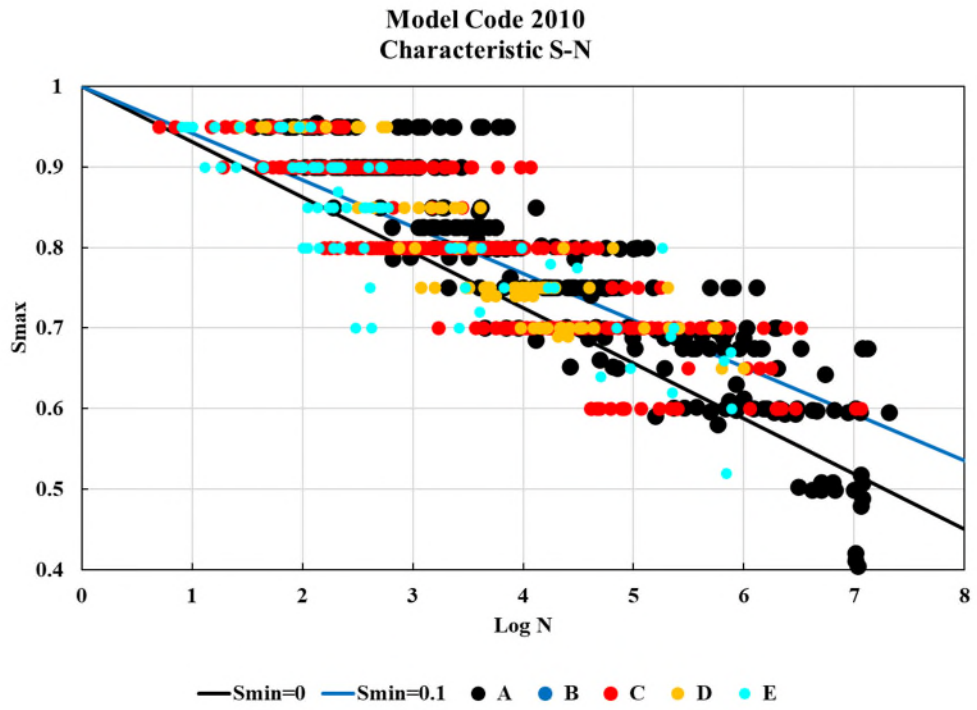

Figure 72 Plot of uniaxial concrete fatigue test data with Smin range of 0-0.1 and with five different maximum aggregate sizes and No fibers, plus model code S-N curves for min and max Smin.

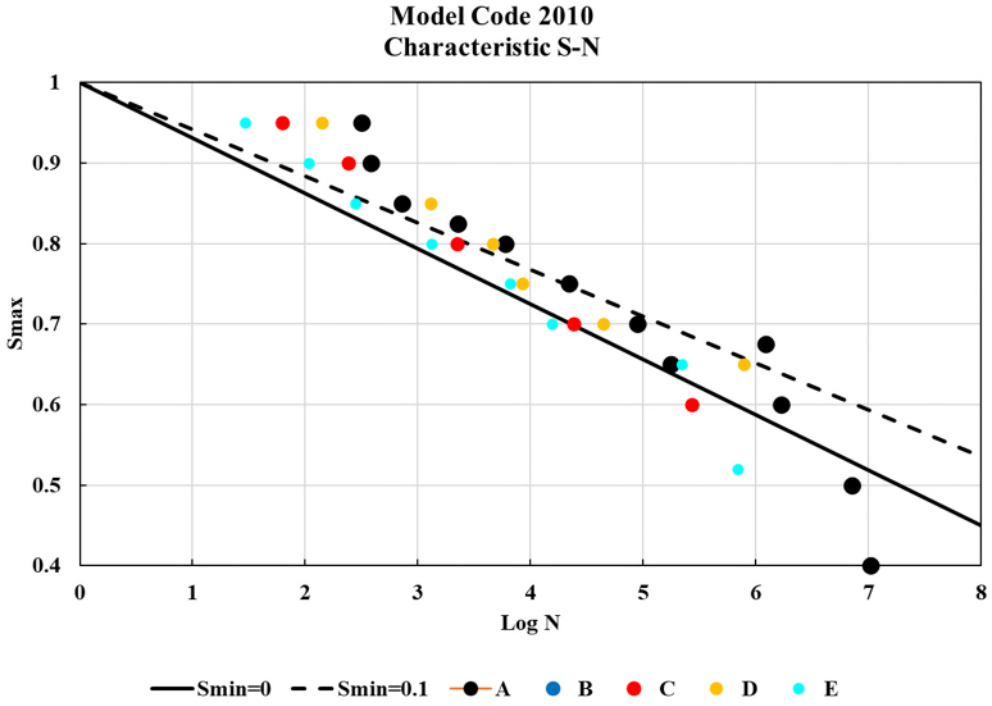

Figure 73 Plot of average uniaxial concrete fatigue test data with Smin range of 0-0.1 and with five different maximum aggregate sizes and No fibers.

3.4.4 Outliers in the data set

The main goal is to use this dataset to gain some idea about the behavior of concrete material under cyclic fatigue loading and to be able to estimate the fatigue capacity of a new design concrete structure. Concrete fatigue capacity depends on several factors, including material properties, testing specimen geometry, existence of water and reinforcement steel, and loading protocol. Almost all of the available experimental data is on PC tested in dry conditions.

One of the concerns with the dataset is the existence of outliers, which can lead to a very conservative estimate of the fatigue capacity of concrete material. These outliers have been defined by two main definitions: 1. They have very low or high numbers of cycles to failure; 2. They are apart from the main cluster of the dataset.

Figure 74 shows the uniaxial experimental dataset on PC and Model Code 2010 prediction model curves. The vertical axis shows the maximum stress ratio (Smax) of loading, and the horizontal axis shows the logarithm of the number of cycles to failure. There are five different markers, which differ in their minimum stress ratios (Smin) of loading, and five different model code 2010 curves, which differ in their Smin and the averages of each marker Smin range. The same colors were used to tie the markers and prediction S-N curves. The wide spectrum of the results is due to different influential factors discussed in previous reports and reflects the nature of concrete behavior. A few examples of the outliers are shown with red arrows. These so-called outliers can have some known or unknown causes, or they may be a fault in the testing (Table 7). That final possiblity can be confirmed or ruled out by redoing the tests.

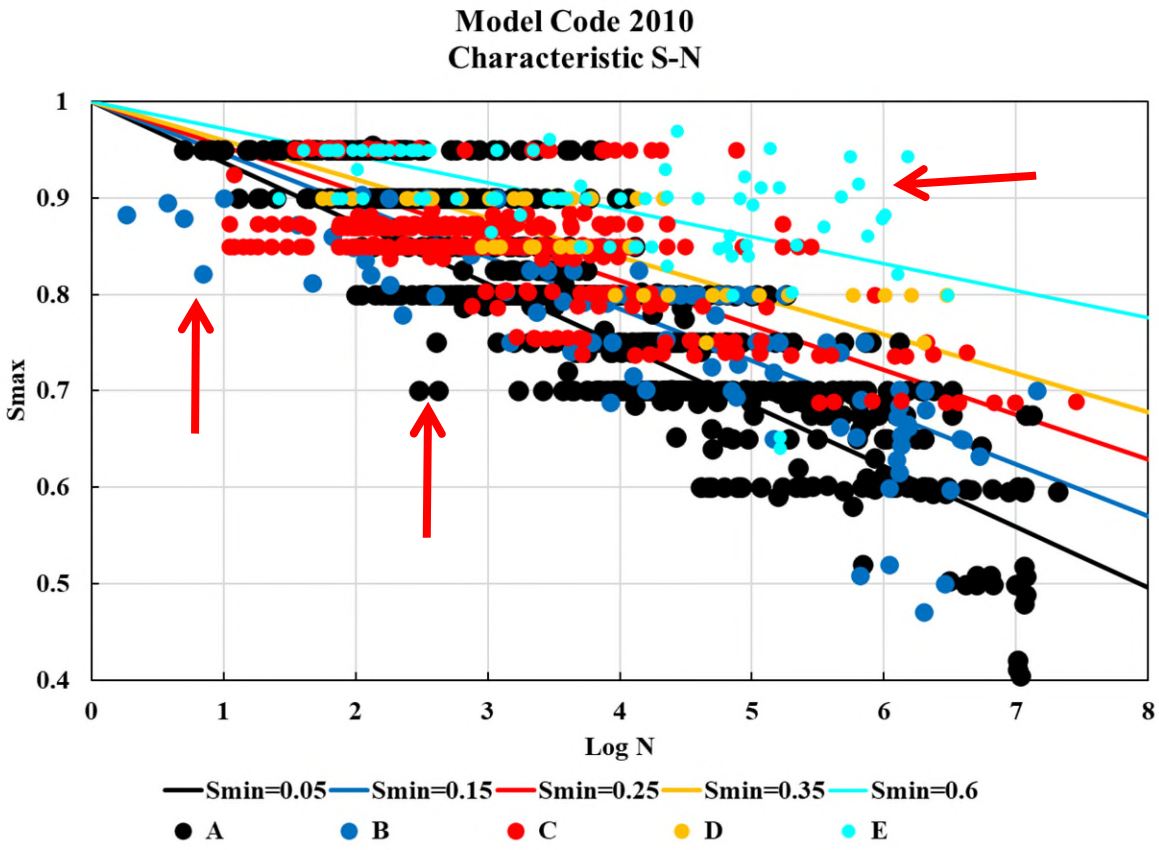

Figure 74 Uniaxial concrete fatigue test data with five different Smin ranges compared with characteristic S-N model code with five different average Smin levels.

Table 7 Outliers in the uniaxial concrete fatigue data sets

Year	Test Type	f'c (MPa)	Smax	Smin	Frequency (Hz)	Log Nf	Low or High
1994	Uniaxial	52.7	0.70	0.10	10	2.5	Low
1967	Uniaxial	50	0.48	0.10	-	5.5-6.5	High
1994	Uniaxial	52.7	0.90	0.12	10	1	Low
1967	Uniaxial	50	0.82	0.18	6	0.25-1	Low
2006	Uniaxial	65	0.60	0.40	8.4	6.5	High
1962	Uniaxial	28	0.87	0.75	11	5.5-6	High
1934	Uniaxial	23.05	0.95	0.75	4.3	5	High
1936	Uniaxial	23.05	0.94	0.75	4.3	5.5-6	High

3.4.5 Statistical significance of loading frequency effect on fatigue life capacity

A few papers have explored the effect of frequency and saturation level and include some statements on the effect of these parameters, but those statements were made based on the limited number of tests on just one concrete material. Therefore, there was a need to investigate the effect of the frequency with a larger dataset.

3.4.5.1 Assumptions

Generally, when somebody wants to explore the statistical effect of a parameter, the other parameters should remain the same to have a reliable conclusion. Unfortunately, there are a number of parameters in this dataset that vary case by case. For the sake of this project, and to be able to do some statistical analysis on the scale of the course project, all the other parameters are assumed to be the same in the entire data set. This analysis was focused on the uniaxial cyclic test data. It was also assumed that the data were normally distributed, though they are not exactly normally distributed. (Figure 75)

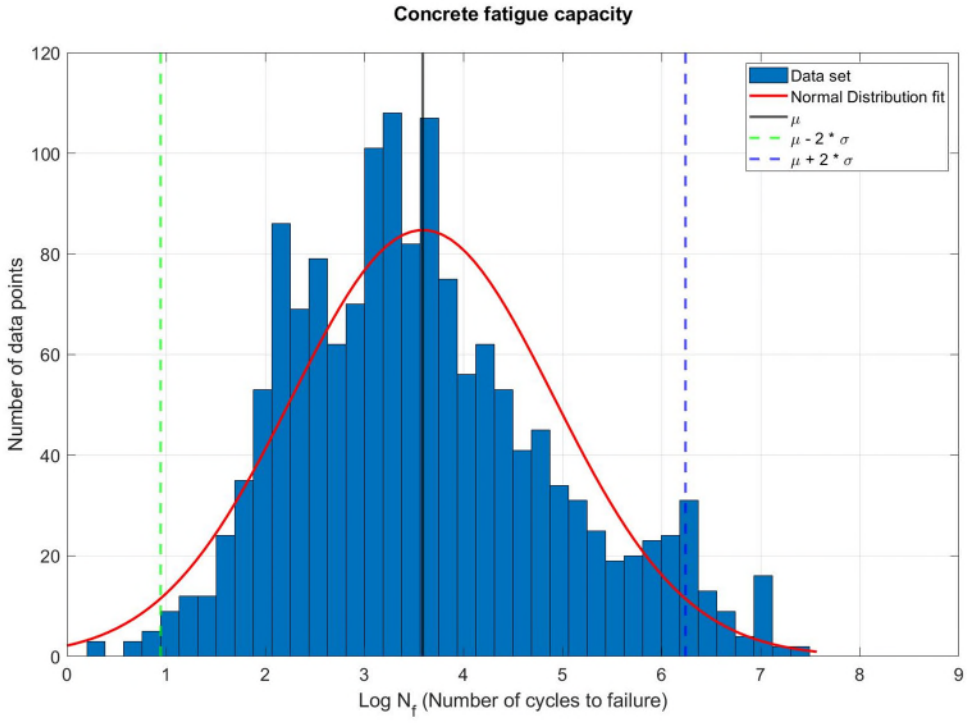

Figure 75 Distribution of the fatigue capacity of concrete.

3.4.5.2 Dividing the data into two big clusters

A general hypothesis is that, in low-frequency cyclic loading (less than 1 Hz), concrete microcracks will have a chance to propagate more effectively — and quickly — to macrocracks, accelerating the process to failure compared to high-frequency cycling loading. The analysis of the results shows that to be true. Table 8 shows a considerable difference between the datasets A1 and A2 in the mean and standard deviation.

Table 8 Range, mean, and standard deviation of the defined data sets as 2 categories with a different frequency range

Nametag of the data bins	Number of data points	Frequency range (Hz)	Mean of Log (Nf)	Standard Deviation of Log (Nf)
Whole data set	1505	[0-60)	3.592	1.325
A1	365	[0-1)	2.514	0.711
A2	761	[1-60)	4.213	1.338

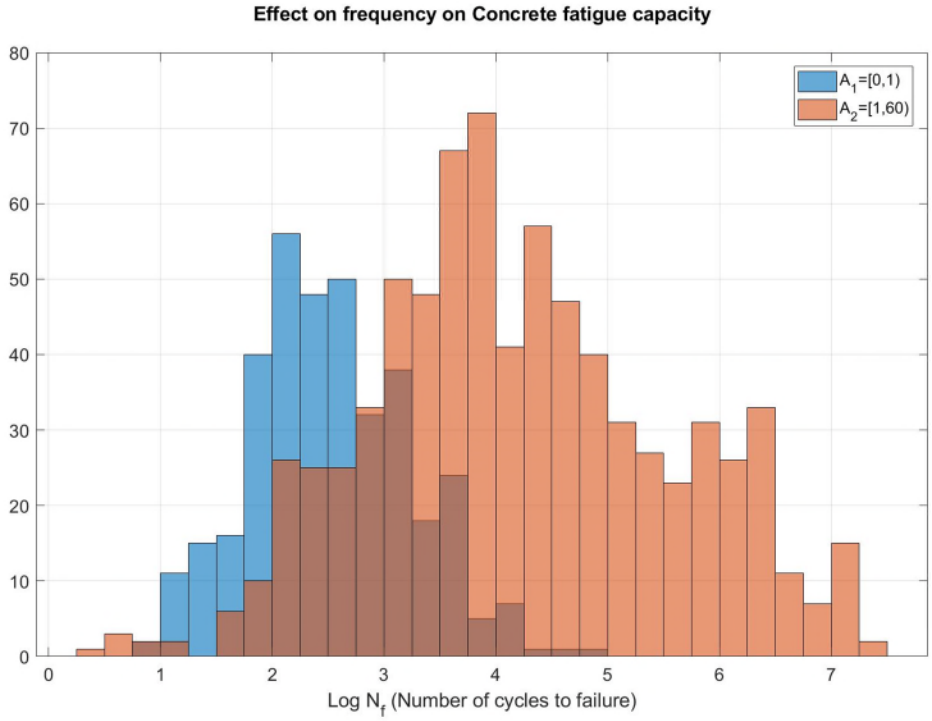

Figure 76 Effect of change in loading frequency on fatigue capacity of concrete.

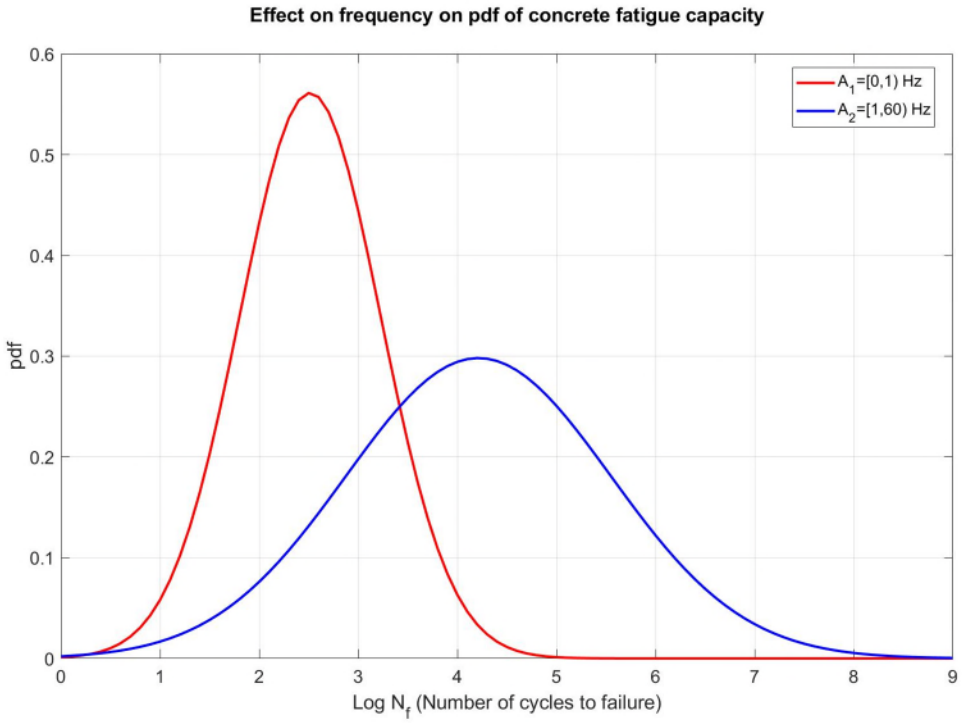

Figure 77 Effect of change in loading frequency on the probability density function (pdf) of fatigue capacity of concrete.

Figure 76 shows the histogram and distribution of each dataset, and Figure 77 shows the probability density of both datasets in one plot assuming a normal distribution. Figure 5 shows that the maximum anticipated fatigue capacity for concrete under cyclic loading with a frequency of less than 1 Hz is about 45000 cycles (regardless of the stress range). The null hypothesis is that any fatigue capacity above Xi belongs to the dataset with high loading frequency. (See Table 9)

Table 9 Hypothesis test and significance level for two categories of data set with different loading frequency ranges.

Parametric value	Xi	Probability of failure for Log (N_f)<Xi in Category A1	Probability of failure for Log (N_f)<Xi in Category A2	Null Hypothesis H0	Alternative Hypothesis H1
				Significance threshold α (False positive)	False negative rate β
$X_0 = \mu_{A1}$	2.514	50%	10%	0.1	0.50
$X_1 = \mu_{A1} + \sigma_{A1}$	3.225	84%	23%	0.23	0.16
$X_2 = \mu_{A1} + 2 * \sigma_{A1}$	3.936	98%	42%	0.42	0.02
$X_3 = \mu_{A1} + 3 * \sigma_{A1}$	4.647	99.9%	63%	0.63	0.001

3.4.5.2.1 Considering the effect of Smax & Smin level

As mentioned before, a relationship has been previously noted between the loading range (Smax and Smin levels) and fatigue capacity. The spreadsheet tool was used to consider this parameter and two more analysis with smaller datasets were performed.

3.4.5.2.2 Data sets with Smax≥0.8 and Smin≈0.05

The uniaxial concrete fatigue dataset was filtered to a smaller dataset, including only data with a maximum loading stress ratio over 80% and a minimum stress ratio equal to or around 5%. Table 10 shows that there is still a considerable difference between the mean values of the A1 and A2 datasets.

Table 10 Range, mean, and standard deviation of the defined data set as two categories with different frequency ranges and (Smax≥0.8 & Smin≈0.05)

Nametag of the data bins	Number of data points	Frequency range (Hz)	Mean of Log (N_f)	Standard Deviation of Log (N_f)
A1	96	[0-1)	2.419	0.660
A2	170	[1-60)	3.231	0.760

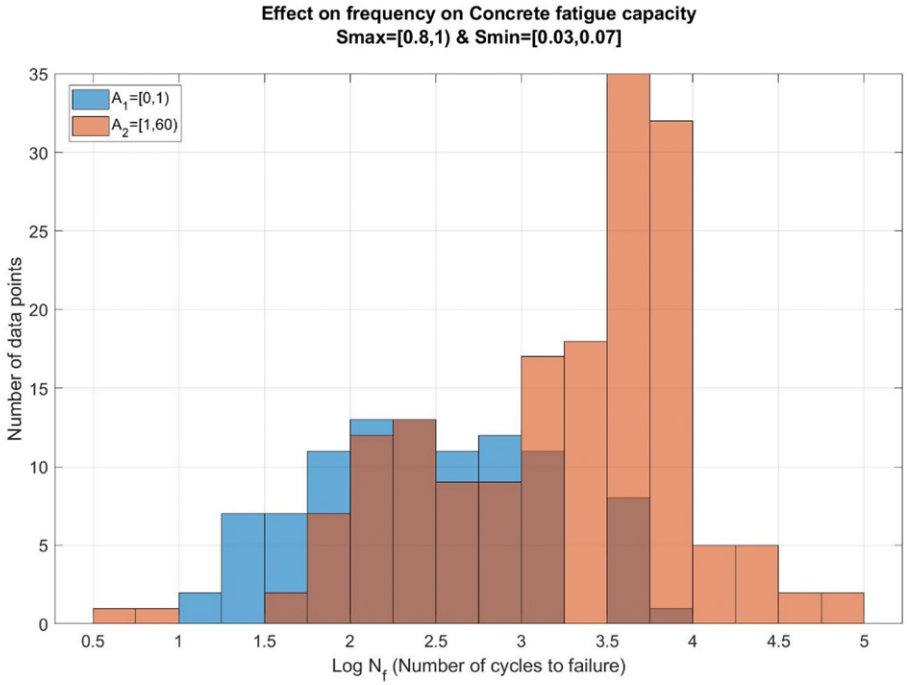

Figure 78 Effect of change in loading frequency on fatigue capacity of concrete (Smax≥0.8 & Smin≈0.05).

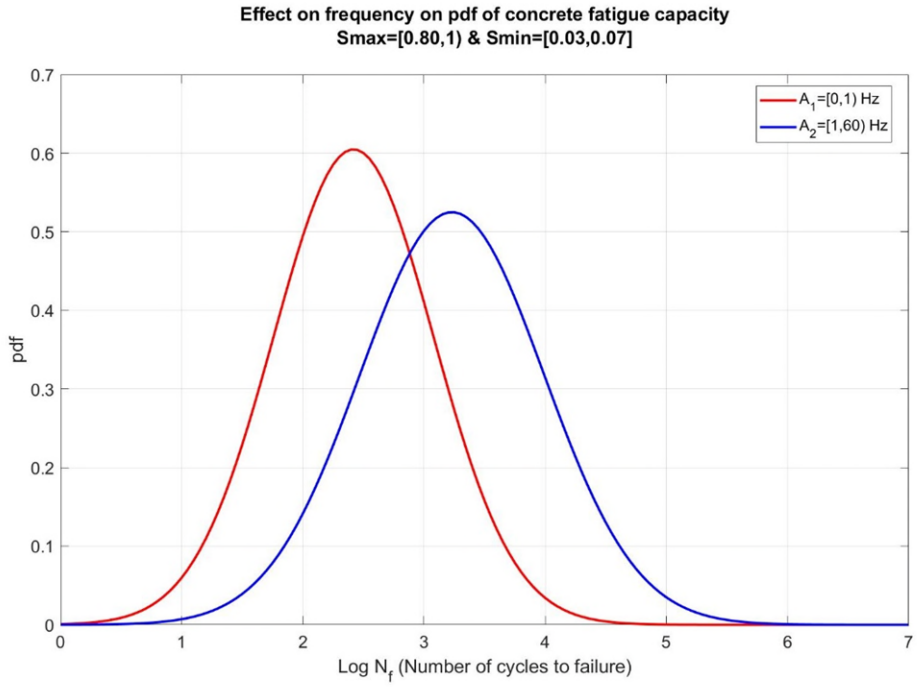

Figure 79 Effect of change in loading frequency on the probability density function (pdf) of fatigue capacity of concrete (Smax≥0.8 & Smin≈0.05).

Figure 78 shows the histogram and distribution of each dataset. The dataset does not seem normal. Figure 79 shows the probability density of both data sets in one plot assuming a normal distribution (for simplicity of the analysis). Figure 79 shows that the maximum anticipated fatigue capacity for the concrete material under uniaxial cyclic loading (with Smax≥0.8 & Smin≈0.05) with a frequency of less than 1 Hz is about 25000 cycles. This is almost half of the previous analysis, in which the threshold was 45000 cycles regardless of loading stress range. The null hypothesis is that any fatigue capacity above Xi belongs to the data set with high loading frequency. (See Table 11)

Table 11 Hypothesis test and significance level for two categories of data set with different loading frequency ranges. (Smax≥0.8 & Smin≈0.05)

Parametric value	Xi	Probability of failure for Log (N_f)<Xi in Category A1	Probability of failure for Log (N_f)<Xi in Category A2	Null Hypothesis H0	Alternative Hypothesis H1
				Significance threshold α (False positive)	False negative rate β
$X_0 = \mu_{A1}$	2.418	50%	14%	0.14	0.50
$X_1 = \mu_{A1} + \sigma_{A1}$	3.078	84%	42%	0.42	0.16
$X_2 = \mu_{A1} + 2 * \sigma_{A1}$	3.737	98%	75%	0.75	0.02
$X_3 = \mu_{A1} + 3 * \sigma_{A1}$	4.397	100%	94%	0.94	0.001

3.4.5.2.3 Data Sets with Smax≈0.8 and Smin≈0.05

The uniaxial concrete fatigue dataset was again filtered to a smaller dataset, this time to include just data with a maximum loading stress ratio equal to or around 80% and minimum stress ratio equal to or around 5%. Table 12 shows that the difference in the meA1 and A2 datasets, was lowered, and there is almost no difference in standard deviation.

Table 12 Range, mean, and standard deviation of the defined data sets as two categories with different frequency ranges and (Smax≈0.8 & Smin≈0.05)

Nametag of the data bins	Number of data points	Frequency range (Hz)	Mean of Log (N_f)	Standard Deviation of Log (N_f)
A1	39	[0-1)	3.018	0.435
A2	86	[1-60)	3.723	0.425

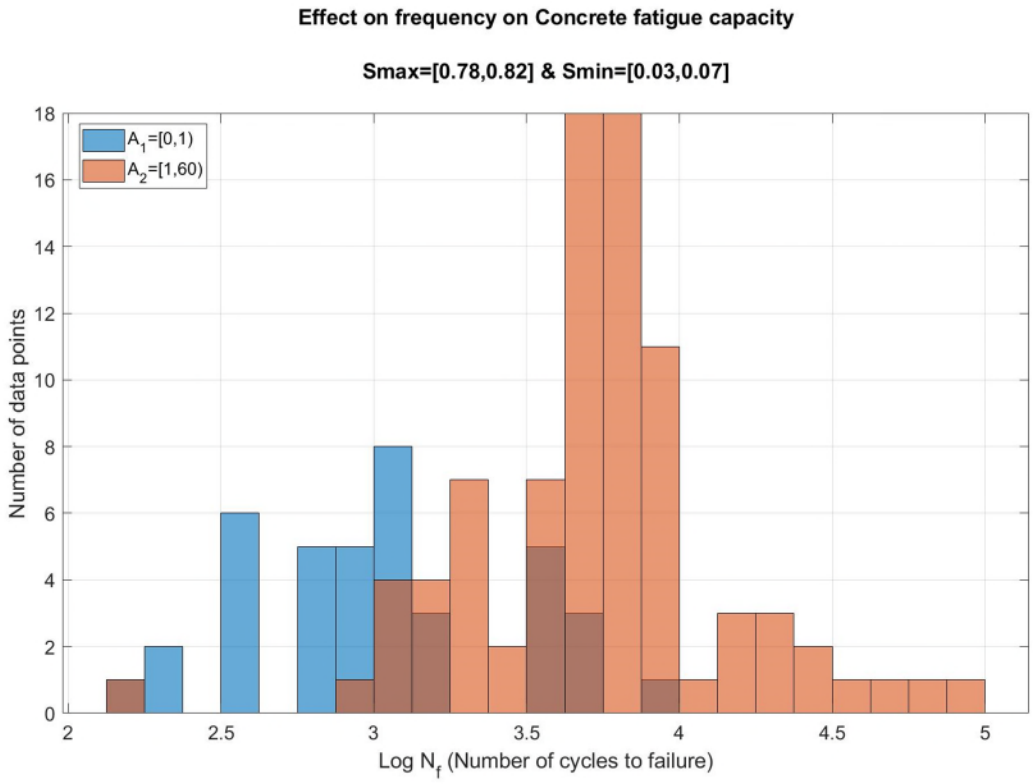

Figure 80 Effect of change in loading frequency on fatigue capacity of concrete (Smax≈0.8 & Smin≈0.05).

Figure 80 shows the histogram and distribution of each dataset, and again, it does not seem normal. *Figure 81* shows the probability density of both datasets in one plot assuming a normal distribution. *Figure 81* shows that the maximum anticipated fatigue capacity for the concrete material under uniaxial cyclic loading (with Smax≈0.8 & Smin≈0.05) with a frequency of less than 1 Hz is about 21000 cycles. The null hypothesis is that any fatigue capacity above Xi belongs to the data set with high loading frequency (see Table 13).

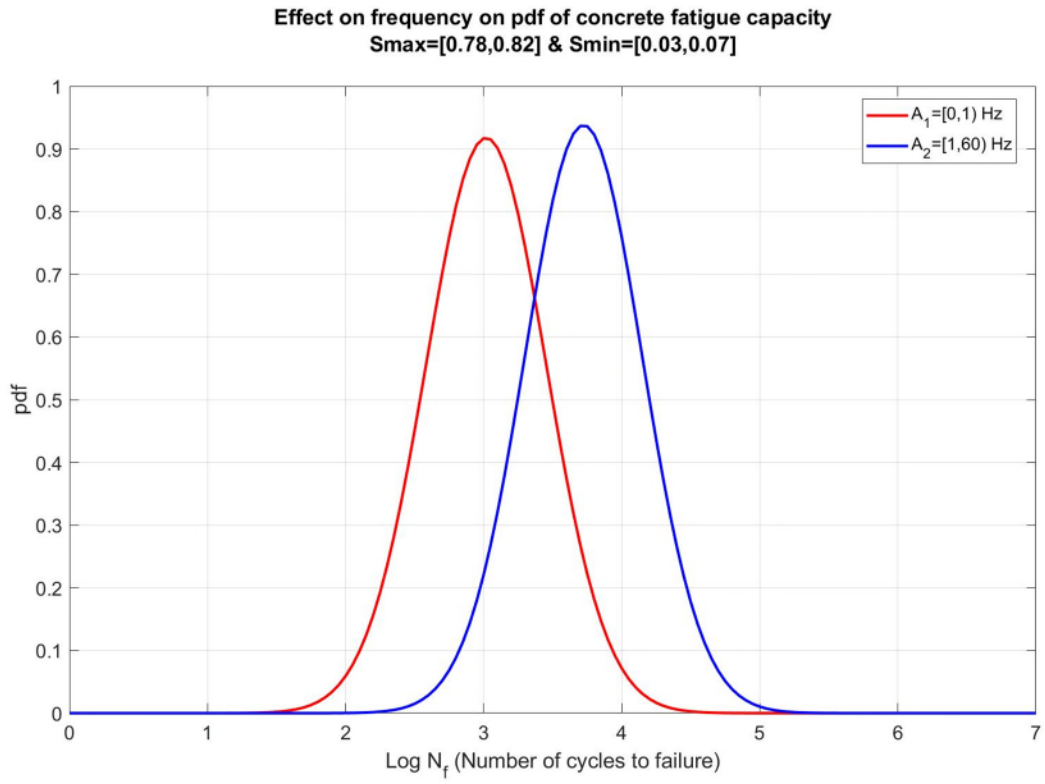

Figure 81 Effect of change in loading frequency on a probability density function (pdf) of concrete fatigue capacity (Smax≈0.8 & Smin≈0.05).

Table 13 Hypothesis test and significance level for two categories of data set with different loading frequency ranges. (Smax≈0.8 & Smin≈0.05)

Parametric value	Xi	Probability of failure for Log (N_f)<Xi in Category A1	Probability of failure for Log (N_f)<Xi in Category A2	Null Hypothesis H0	Alternative Hypothesis H1
				Significance threshold α (False positive)	False negative rate β
$X_0 = \mu_{A1}$	3.018	50%	5%	0.05	0.50
$X_1 = \mu_{A1} + \sigma_{A1}$	3.453	84%	26%	0.26	0.16
$X_2 = \mu_{A1} + 2 * \sigma_{A1}$	3.887	98%	65%	0.65	0.02
$X_3 = \mu_{A1} + 3 * \sigma_{A1}$	4.322	99.9%	92%	0.92	0.001

3.4.5.3 Conclusion

According to these analyses, loading frequency has a considerable effect on the fatigue capacity of concrete. However, other parameters need to be investigated statistically to discern the scale

of effects. In the end, there might be a need to introduce a new model to consider the combined effect of all the significant parameters for estimating the fatigue capacity of the concrete material, which has been done in the following sections.

3.4.5.4 Effect of loading frequency

To explore the effect of frequency, the uniaxial concrete fatigue test data were divided into five data sets, each with a distinct frequency. This table (Table 14) shows that — with the increase in the loading frequency — the standard deviation of the log of the number of the cycles to failure increases along with the mean, resulting in a tighter band range of results for low-frequency (vs. high-frequency) loading. Nevertheless, in this case, the higher frequencies have a very wide range of cycles to failure, as well.

Table 14 Range, mean, and standard deviation of the defined data sets

Nametag of the data bins	Number of data points	Frequency range (Hz)	Mean of Log(Nf)	Standard Deviation of Log(Nf)
F1	365	[0-1)	2.514	0.711
F2	379	[1-2)	3.384	0.978
F3	186	[2-5)	4.161	1.136
F4	234	[5-10)	3.701	1.350
F5	341	[10-60)	4.588	1.317

Figure 82 and Figure 83 show that as the range of frequency increases from dataset F1 to dataset F5, the mean of the results increases and the spread of the data increases as well.

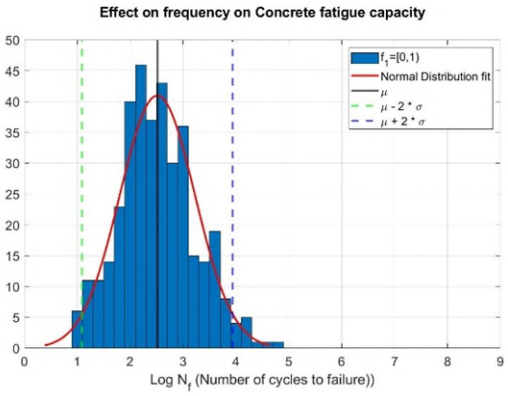

(a) Data set F1

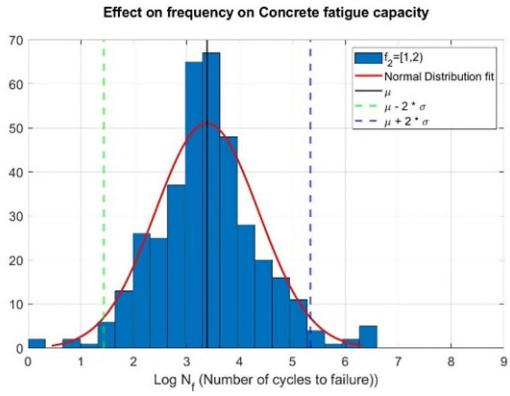

(b) Data set F2

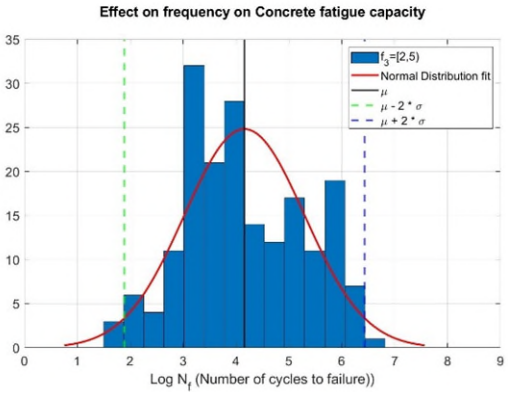

(c) Data set F3

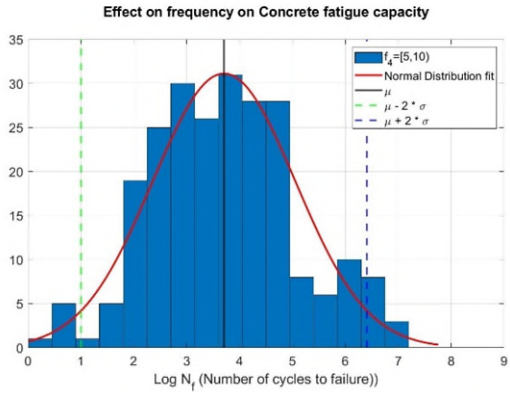

(d) Data set F4

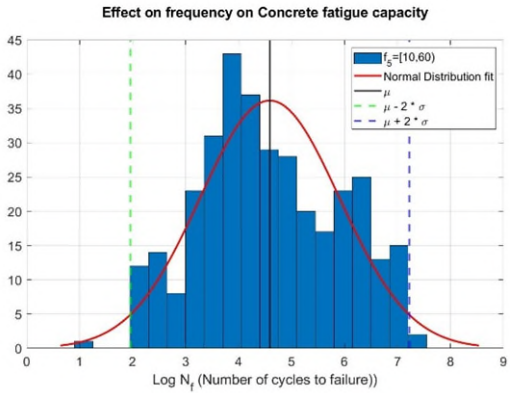

(e) Data set F5

Figure 82 The histogram and the normal distribution of the data sets.

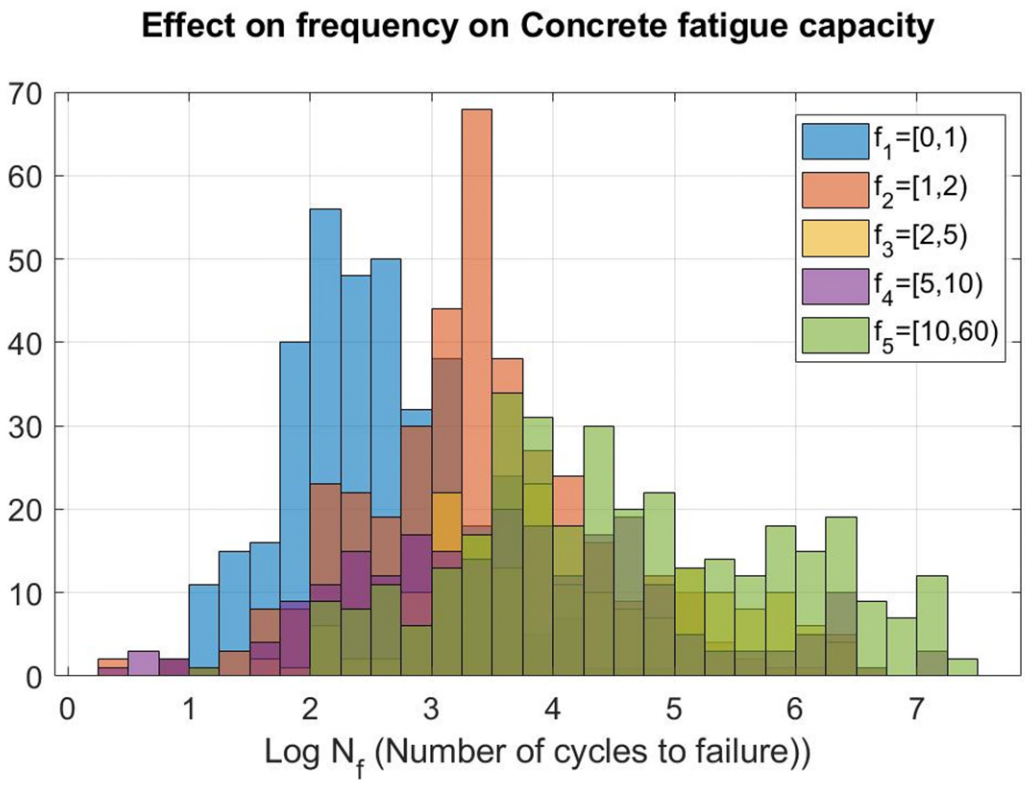

Figure 83 Histogram of all of the data sets.

Figure 83 and Figure 84 show that there is a clear effect of the frequency of loading on the results of the fatigue tests (number of cycles to failure). Though these datasets have different material properties, loading characteristics, and geometry, the codes and provisions have only considered the loading frequency and so have dismissed a discernable effect. Other studies have recognized the effect of the frequency [21].

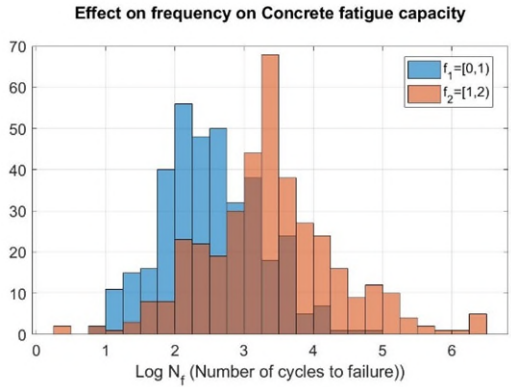

(a) F1 & F2

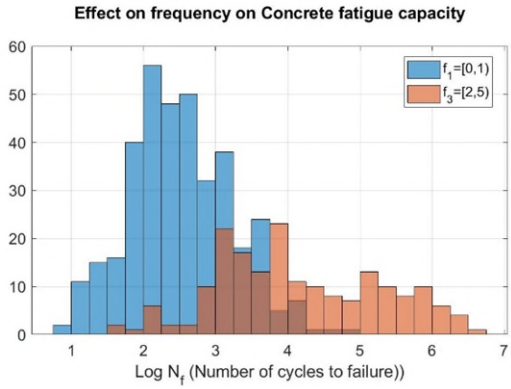

(b) F1 & F3

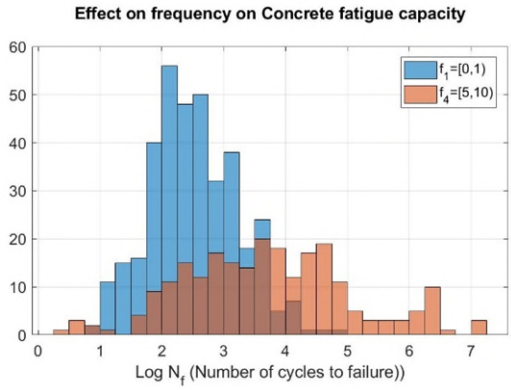

(c) F1 & F4

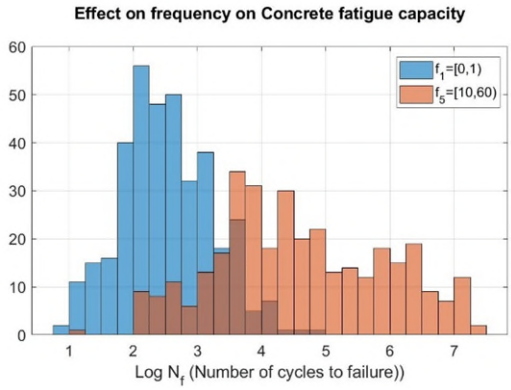

(d) F1 & F5

Figure 84 Histograms of pairs of data sets compared.

3.4.6 Linear and polynomial regression

3.4.6.1 Linear regression

One of the usual methods of assessing a dataset is to look for linear regression among the variables. In this case, linear regression was assessed for the logarithm of the number of cycles to failure and one or more of various parameters. The coefficient of determination (R^2) and Mean Squared Error (MSE) were used to compare various models. Models were validated via a five-fold cross-validation method. wherein the dataset is divided into five equal portions, and then,

the model is calibrated with 4/5 of the data (called “train” data in this report) and validated by the remaining 1/5 (which is called “test” data in this report).

In this case, by increasing the number of input parameters, the R^2 decreased, and MSE increased, suggesting that the logarithm of the number of cycles to failure for plain concrete is influenced by the maximum and minimum stress levels. Even though the other parameters have smaller coefficients in the linear regression models, they too have some influence on the final estimation of fatigue life. Table 15 shows the model number — which is related to the number of input parameters — and the parameters themselves.

Table 15 Input parameters/variables for regression models

Model #	Parameters
2	Smax, Smin,
3	Smax, Smin, Frequency
4	Strength, Smax, Smin, Frequency
5	Max Aggregate Size, Strength, Smax, Smin, Frequency
6	Max Aggregate Size, w/c, Strength, Smax, Smin, Frequency

To have a visual sense of the differences between the newly generated linear regression models and existing standard models, some assumptions were made for the input parameters. The results, plotted as a line in Figure 85, indicate that if a single linear regression is desirable, these models will go through the point (Smax=1.2, LogNf=0). The existing data suggests that in the standard models, the curve or line will go through the point (Smax=1, LogNf=0), but that may not be a good line for the lower Smax levels. The assumed input parameters for this figure are Smin equal to 0, frequency of loading equal to 1 Hz, Max aggregate size of 20 mm, water to cement ratio of 0.4, and finally, the strength of 40 MPa.

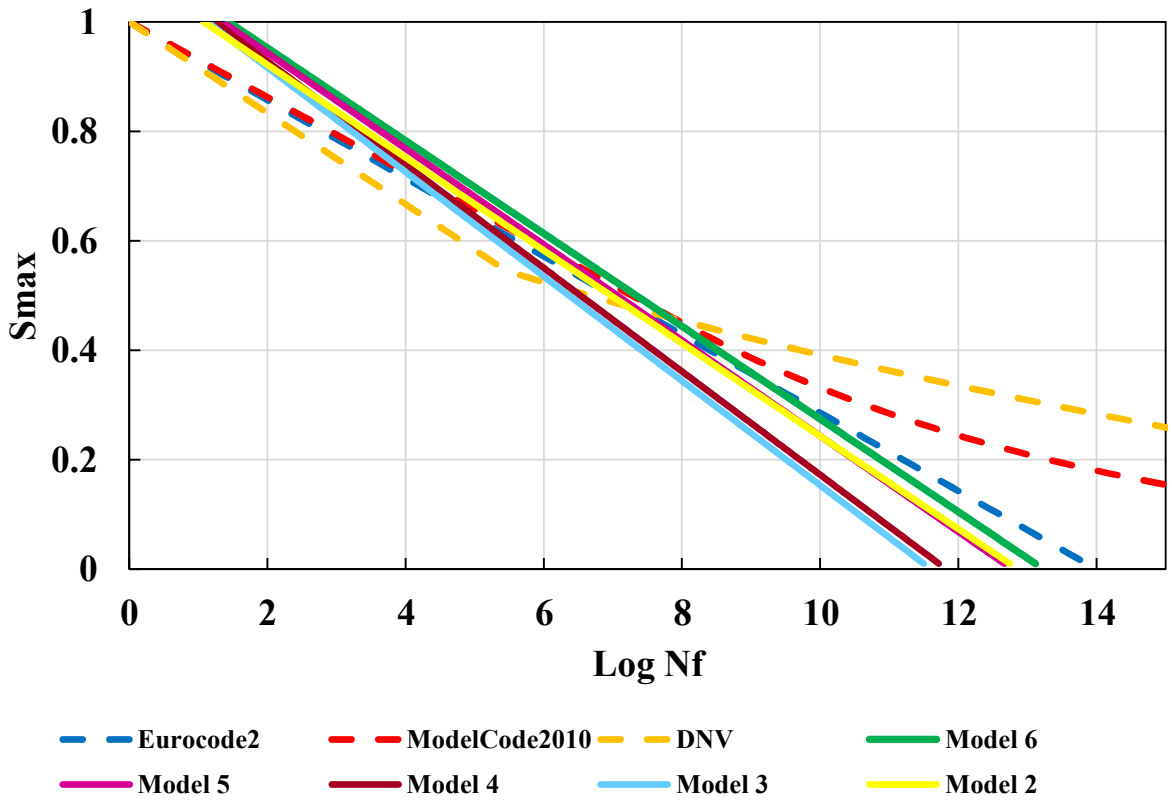

Figure 85 Comparison among the linear regression models generated based on the data set and the existing models proposed by standards (with the same assumed variables).

3.4.6.2 Polynomial Regression

Polynomial regression — which considers the combination of input parameters — is another method that can be used to evaluate the relationship between input parameters and the number of cycles to failure. In this case, polynomial regression helped to increase R^2 and decrease the MSE for the models (a little bit). Figure 86 shows the comparison between the polynomial regression models and standard models. The polynomial models are a little bit curved, which may be more realistic in the lower Smax levels as there is agreement between these models and standard models in those levels. The polynomial model with two input parameters (model 2-2) shows more realistic estimates of the log number of cycles to failure for the higher Smax levels as well (very close to the mean of the datasets).

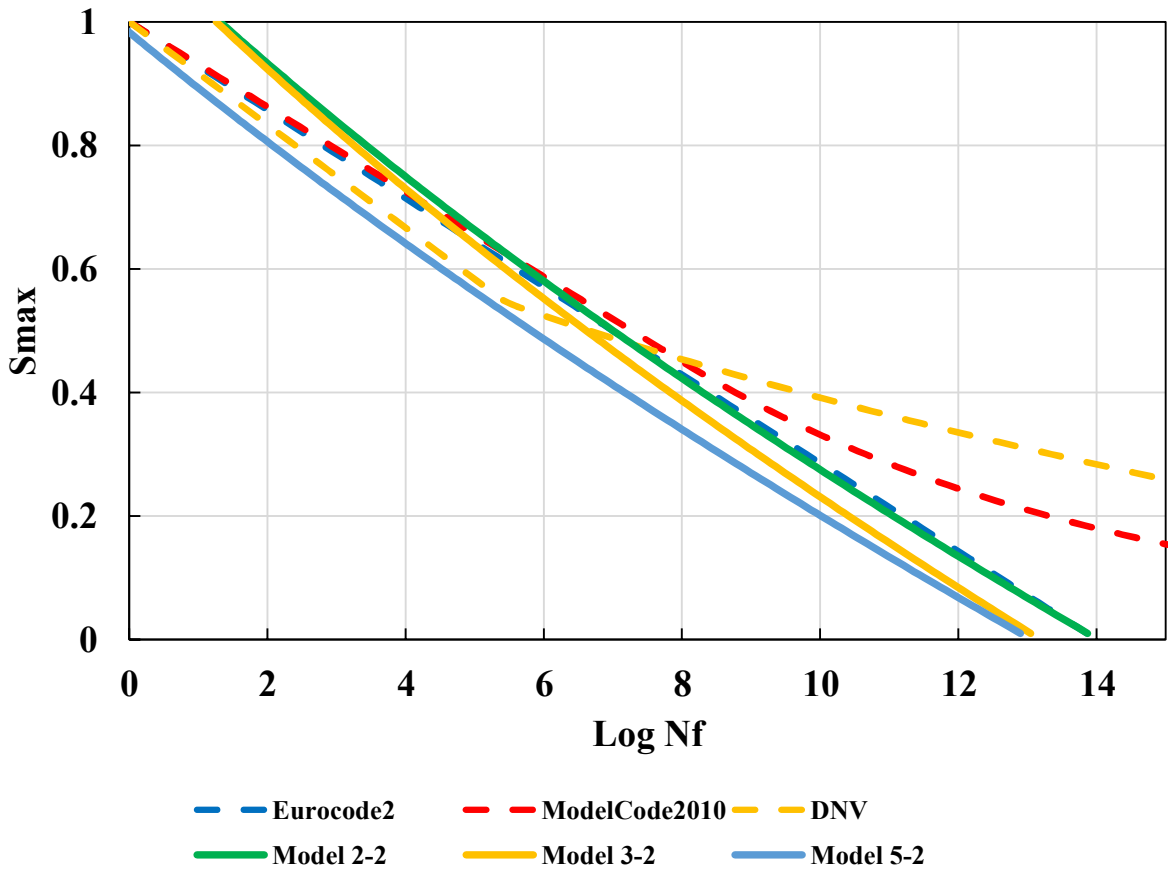

Figure 86 Comparing the polynomial regression models generated based on the data set with the existing models proposed by standards (having the same assumed variables)

3.5 Introduction to empirically-developed models and artificial neural network models

The study of concrete fatigue behavior has historically relied on empirically developed models, which are grounded in observed experimental data. These models predict fatigue life (Nf) based on input variables such as stress ratios, loading frequencies, and the applied stress amplitude. While practical and widely applied, empirical models often rely on simplified assumptions and generalized relationships, which limit their accuracy and applicability to complex or variable conditions. For instance, these models are typically derived from data obtained under controlled

laboratory conditions, which may not fully represent the diversity of factors influencing fatigue performance in real-world scenarios.

One of the major limitations of empirical models is their inability to capture the inherent variability in concrete fatigue behavior, which arises from multiple factors, including material properties, loading conditions, and environmental influences. Aggregate size and shape, reinforcement types, moisture levels, and other variables introduce significant variability in test results, yet empirical models often fail to consider these complex interactions comprehensively. As a result, predictions made using these models may exhibit significant scatter and reduced reliability when applied to concrete mixes or structures outside the specific experimental conditions used to derive them. For complex phenomena, there may be a variety of models which vary in the characteristics they consider and in their calibration values. The accuracy of an empirical model is assessed by R-squared (R^2) fit or Coefficients of Variation (COVs) of the predicted to measured values ratio.

Another type of model that can be used to calculate a material's performance value, such as strength, is an Artificial Neural Network Model. This model is a statistical fit that relates a set of characteristic input parameters to the outcome of an experiment, such as measured strength. Such a model is labeled Artificial because it is just a statistical fit, and not an actual equation. A given ANN model iteratively weights and biases the effect of the inputed parameters until there is as close fit as possible with the particular outcome of the experiment; this is referred to as "model training". This trained ANN Model can then be used to predict an outcome using "test" data (i.e. results that were not used to train the model). The accuracy of an ANN Model is — like an empirical model — evaluated using R^2 and COVs. Since an ANN Model is not constrained, very

high R^2 and low COVs can be achieved compared to empirical models. However, if the considered characteristics are insufficient (i.e., parameters of great influence are omitted), or the uncertainty is aleatory (due to randomness), it is impossible to achieve high R^2 and low COVs even with an ANN.

An ANN model was used to investigate potential causes of the the inaccuracy and differences amongst existing empirical relationships (fatigue models) for concrete fatigue, as conveyed in Figure 87 to determine whether these relationships were just poorly formulated and calibrated, or key characteristics were omitted from the models, or there is a high degree of randomness (aleatory uncertainty), or some combination of those possibilities. An ANN model was trained with some of the available data, and then the model was used to predict the fatigue capacity for "test" data.

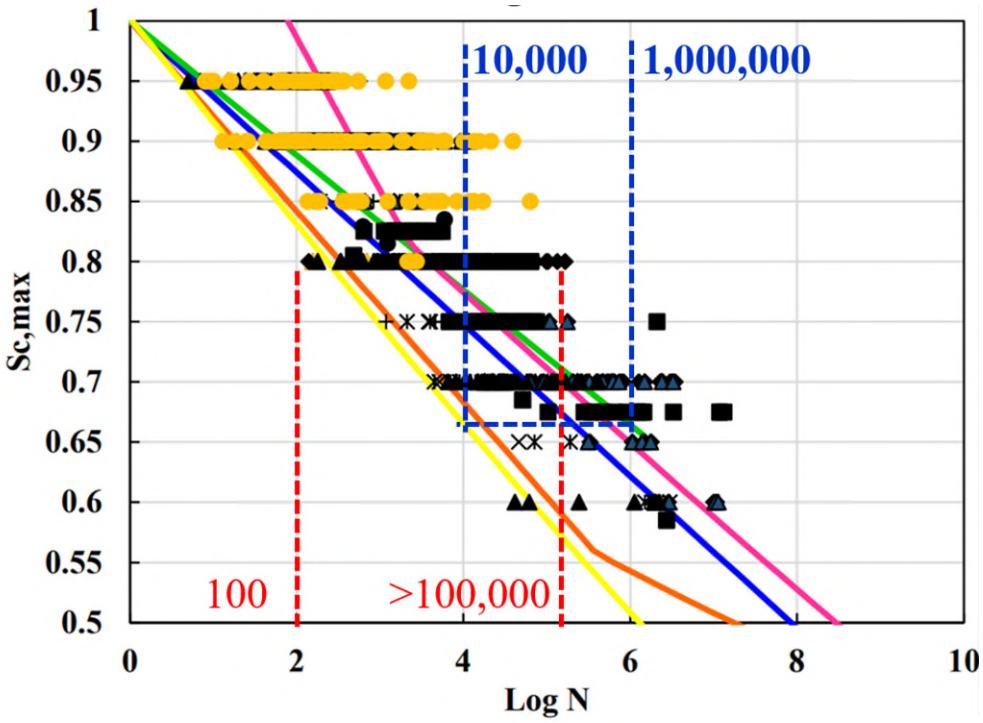

Figure 87 Test data and fatigue models for the impact of Scmax on fatigue capacity (Scmin = 0.05).

There is some precident to these method and approach. The shear database developed Kuchma et al. 2014 serves as a critical resource for advancing the understanding and prediction of concrete shear behavior, particularly under complex loading conditions. That database consolidated experimental data from a wide range of studies, including parameters such as shear strength, reinforcement details, aggregate properties, and loading configurations. By incorporating the shear extensive dataset, Artificial Neural Networks (ANNs) can be effectively utilized to analyze the non-linear relationships between these parameters and shear capacity. ANNs, with their ability to handle large and diverse datasets, offer a powerful tool to uncover patterns and trends that traditional empirical models often fail to capture. The application of ANNs to the shear database has demonstrated improved predictive accuracy compared to conventional methods, enabling the development of more reliable models for assessing shear performance.

Prior to presenting this assessment for concrete compressive fatigue, it is useful to present the results for another example where it is particularly clear that the ANN Model provides for a much better prediction of capacity than empirically developed mathematical relationships. The example that will be used is the shear strength of RC beams that do not contain shear reinforcement [88, 110-113]. These advancements provide a robust foundation for optimizing the design and safety of concrete structures, bridging the gap between experimental findings and practical engineering applications.

The relationship's accuracy for calculating the U.S.'s one-way shear strength is now compared between Building Code provisions as of 2014 [114] and an ANN. The values on the y-axis in Figure 88 and Figure 89 are the ratios of the (experimentally measured strength, Vexp) divided by the capacity (Vpred) calculated using the relationship in the 1999 U.S. Building Code which

remained the same through the 2014 code. Each dot represents one test result. If the y-value is equal to 1, then the measured strength is exactly equal to the "predicted" strength. If the y-value is equal to 2.0, then the measured strength was twice that "predicted" (building code is conservative or safe), and if the y-value is equal to 0.5 then the measured strength is one-half of that "predicted" (building code is unconservative or unsafe). The ratios shown in the left-side figures are from the U.S. Building Code, and the ratios shown on the right-side images are from when an ANN [110] is used. Figure 88(a) is for when these ratios (on the y-axis) are plotted against the monotonic compressive strength of the concrete (f_{1c}) on the x-axis. Figure 88(b) is for when ANN used for predictions. The vertical spread in the results is an indicator of the accuracy of the "prediction."In this case, the ANN is much better than the U.S. Building Code. Since there is no trend in the mean strength ratio for the building code with either f_{1c}, then adjusting how this is considered in the code will have no value. In comparison, the spread of the results in the ANN model is very small for a phenomenon as complex as the shear strength of beams made of RC. While many strength ratios are less than 1.0 in the ANN Model, this could be easily addressed by multiplying the predicted strength by about 0.80. To make the strength ratios for the U.S. building code greater than 1.0, it would be necessary to multiply the predicted strengths by about 0.2.

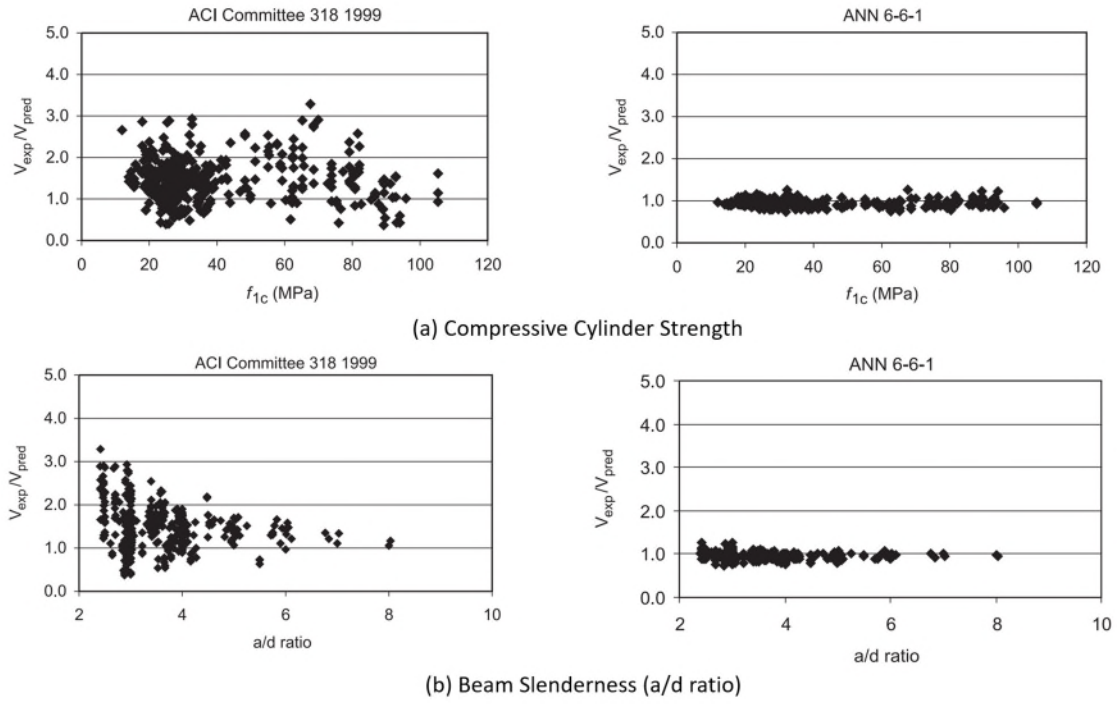

Figure 88 Comparison of strength ratios between U.S. Building Code (no Trend) and ANN. [110]

Figure 89 presents the same results as shown in Figure 88, but this time the strength ratios are plotted versus (a) the Depth of the Beam and (b) the Percentage of Longitudinal Reinforcement. In this case, there is a trend in the strength ratio between the depth of the beam and the percentage of longitudinal reinforcement.

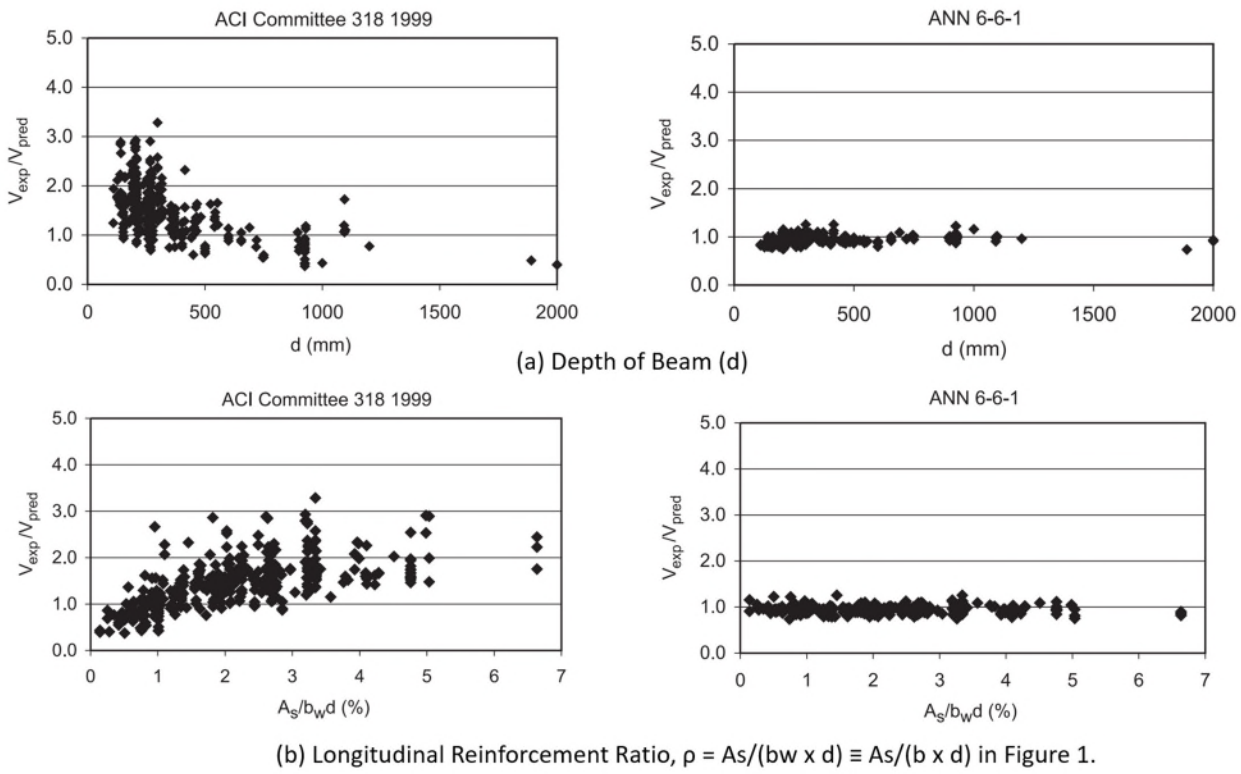

Figure 89 Comparison of strength ratios between U.S. Building Code (with Trend) and ANN. [110]

Another limitation lies in the generalization of fatigue behavior using S-N (stress-life) curves, which are often the backbone of empirical fatigue models. These curves establish a relationship between applied stress levels and the number of cycles to failure, but they inherently simplify fatigue performance as a linear or logarithmic function. This oversimplification neglects critical factors such as strain evolution, stiffness degradation, and crack propagation, which are essential for understanding the mechanisms driving fatigue failure. Consequently, empirical models often underestimate or overestimate fatigue life, leading to overly conservative or unsafe designs.

Given these challenges, the need for more advanced predictive tools has become increasingly evident. Artificial Neural Networks (ANNs), as discussed in the next section, offer a promising

alternative to overcome the limitations of empirical approaches by leveraging data-driven methodologies to capture the non-linear and multifactorial nature of concrete fatigue behavior.

3.5.1 Neural networks in concrete fatigue data sets

As has been discussed previously, design code provisions — in the form of an equation or an S-N fatigue curve — are frequently empirical and result in conservatives estimate of capacity. A neural network was used to complement these other approaches by using the existing data sets to predict the logarithm of the number of cycles to failure for PC.

Most of the uniaxial test data include at least six parameters (Max Aggregate Size, water-to-cement ratio, Strength, Smax, Smin, Frequency of loading). The larger the number of parameters, the better the chance of having a better predictive NN model. The number of parameters influencing capacity is often very large, but the number of parameters that can be included in a design formula for practical reasons is limited. Like the regression models, the neural network model was validated via five-fold cross-validation. A sensitivity analysis of the number of layers, size of layers, and type of activation function was performed to identify the model with the lowest MSE. If there is a relationship between collected metadata and a result, then this will be picked up by an Artificial Neural Network (ANN).

In this case, the NN was not able to perform any better than regression models, and yielded a higher MSE and lower R^2 than did the regression models. Unfortunately, an ANN does not lead to a general formula that is suitable for use in design practice due to the complexity of the models. Son and Yan 2022 later explored the removal of outliers and got a better but not perfect correlation coefficient [115].

As mentioned before, predictions from the standard models are mostly conservative. Figure 90 shows the level of variation in the predictions in the higher Smax level (higher than 0.8), where most of the experimental test data are, and conservativeness and un-conservativeness of predictions over various Smax levels using the DNV fatigue model. Figure 91 shows the same comparison for the NN model generated based on the available data set. Unfortunately, the variation of the prediction is still high. Based on the literature review on the concrete beam shear study, a tight band cluster around the prediction capacity ratio of 1 is expected. Even though it is tighter, there is still significant variation, suggesting that there are other influential parameters that we are missing from the dataset.

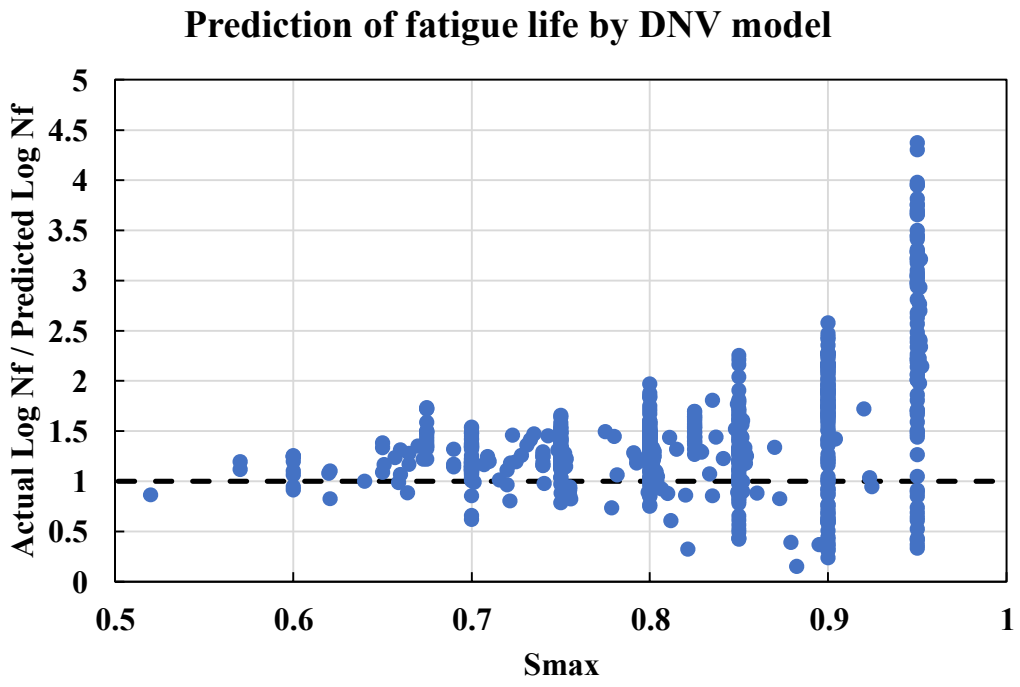

Figure 90 Ratio of predicted fatigue life by DNV model to the actual test data versus Smax

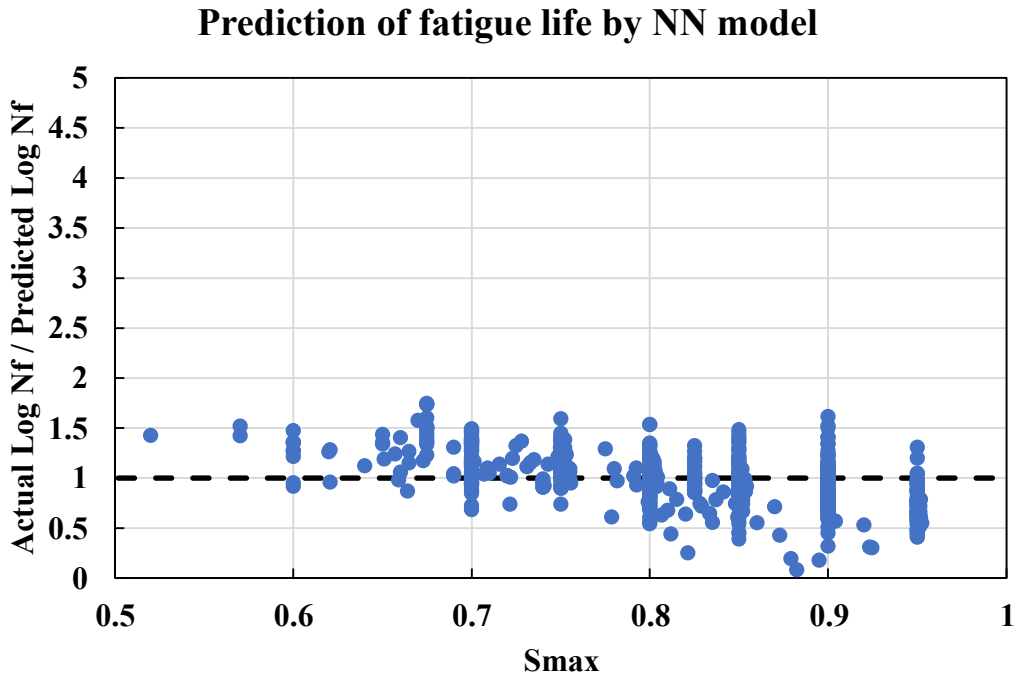

Figure 91 Ratio of predicted fatigue life by NN model to the actual test data versus Smax

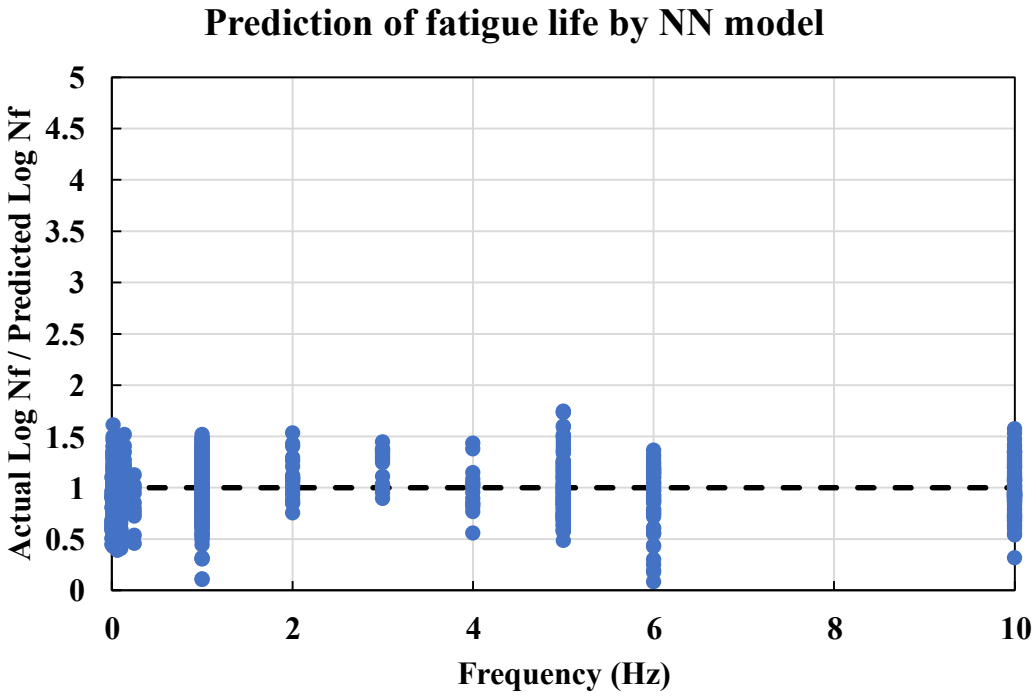

Figure 92 Ratio of predicted fatigue life by NN model to the actual test data versus frequency of loading (Hz)

3.6 Summary and conclusions

This chapter introduced the development and implementation of a comprehensive database of publicly available experimental fatigue data, to identify key gaps in understanding of the fatigue behavior of concrete. The database has a user-friendly Excel-based dashboard for analysis and visualization. By organizing data across parameters such as stress level, material composition, and environmental condition, the database provides critical insights into trends and inconsistencies in existing data on fatigue.

Significant gaps exist in understanding the effects of certain parameters, including loading frequency, specimen geometry, and aggregate type, on fatigue performance. Existing data often lack standardization and comparability, making it challenging to use them to develop fatigue models that are applicable universally. Variability in testing methods and reporting standards further limits the utility of existing datasets for advancing predictive models.

The need for a centralized and accessible database is therefore critical. Such a resource not only facilitates the identification of trends and knowledge gaps but also provides a foundation for developing improved fatigue models and testing methodologies. By enabling more precise analysis and comparison, the database supports the creation of tailored design solutions, thereby improving the reliability and cost-effectiveness of concrete structures.

The scope of this research acknowledges these gaps but is focused on a subset of the broader issues. Rather than addressing all the missing elements, this study prioritizes developing a functional database, exploring the impact of selected influential factors, and evaluating existing fatigue models. These efforts aim to establish a robust platform for future research while addressing practical and immediate needs in concrete fatigue analysis and design.

4 Initial Compressive Uniaxial Fatigue Testing

This chapter presents experimental testing to evaluate the fatigue behavior of plain concrete (PC) and reinforced concrete (RC) under uniaxial compressive loading. The primary goal is to establish a baseline understanding of how concrete responds to fatigue stresses, focusing on critical factors such as reinforcement, saturation levels, and load eccentricity. These experiments aim to identify general trends in fatigue capacity, quantify performance variability, and assess the influence of environmental and material-specific conditions.

While Chapters 5 and 6 delve into specific variables, such as aggregate size, and other materials such as 3DPC, Chapter 4 provides foundational insights into the broader factors influencing fatigue behavior. It sets the stage for more specialized investigations by offering a comparative understanding of how material-specific factors affect fatigue performance. This chapter's findings serve as a reference point, enabling the interpretation of experimental results in subsequent chapters.

The fatigue behavior of concrete is influenced by a multitude of factors that complicate the development of reliable comprehensive models. For instance, loading rate significantly affects monotonic strength, with faster rates producing higher strength and stiffness values. Variability in monotonic compressive strength among concrete cylinders cast from the same batch further contributes to scatter in fatigue test results, sometimes by orders of magnitude. Additionally, larger aggregates reduce fatigue capacity due to stress concentrations and crack propagation along their boundaries. Degree of saturation also plays a significant role, with saturated concrete exhibiting reduced fatigue capacity due to its weakened internal structure.

This chapter addresses these complexities by presenting the results of tests on PC under various conditions, including concentric and eccentric loading, specimen saturation, and the presence of

reinforcement. These experiments provide critical data to better understand how different parameters influence fatigue capacity, justify the need for standardized testing, and guide future research directions. By addressing these foundamental issues, this chapter establishes a robust framework for investigating more specialized aspects of concrete fatigue in the subsequent chapters.

4.1 Test setup and system for data acquisition

A 200-kip compressive servo-hydraulic testing machine was employed. Monotonic tests were conducted using a quasi-static displacement-controlled loading protocol to capture the post-peak stress-strain response of concrete under compressive loading. For fatigue loading, a force-control mode was used to maintain peak and valley stress targets within an acceptable range, using a sinusoidal waveform for cyclic loading. Two extensometers, mounted on opposite sides of the cylinder (see Figure 93), measured length changes over a gauge length of 6 inches (150 mm) to capture the axial strain evolution over the material's fatigue life (see Figure 94). Stress and strain hysteresis data were collected at a frequency of 25 Hz using a separate data acquisition system.

The loading protocol was defined based on the average monotonic strength of the batch of concrete for the first initial round of testing (Figure 95). The compressive loading protocol consisted of maximum and minimum loading ratios (S_{max}, S_{min}) where:

$$S_{max} = {f_{c\_max}}/{f_{c\_monotonic}} \;\&\; S_{min} = {f_{c\_min}}/{f_{c\_monotonic}}$$

$f_{c\_monotonic}$ represents the monotonic strength.

f_{c_max} represents the maximum imposed stress during fatigue cyclic loading.

f_{c_min} represents the minimum imposed stress during fatigue cyclic loading.

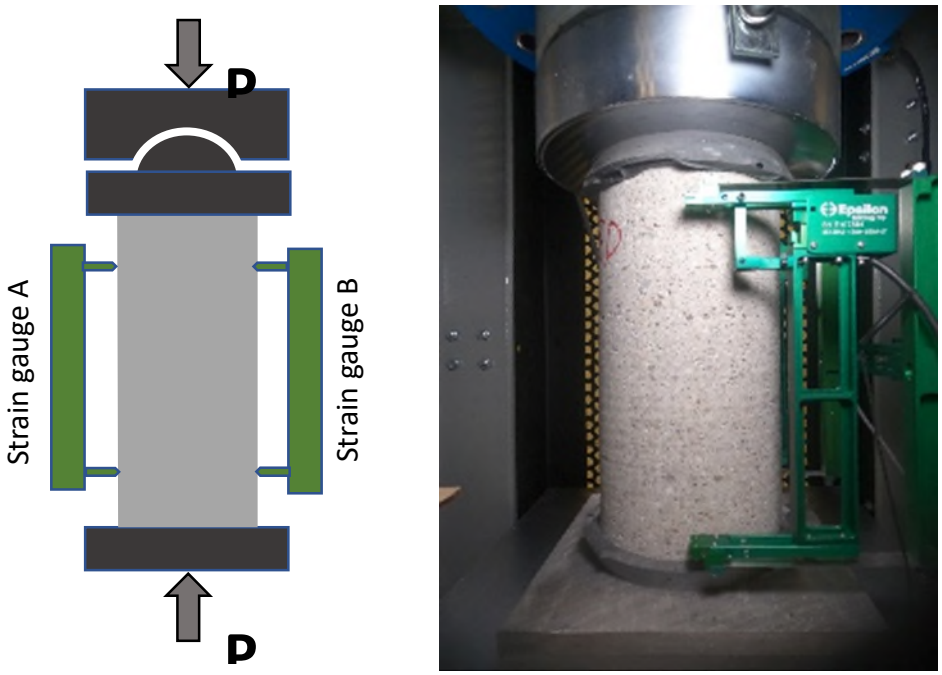

Figure 93 Loading setup sketch (left); photo taken from the testing setup (right).

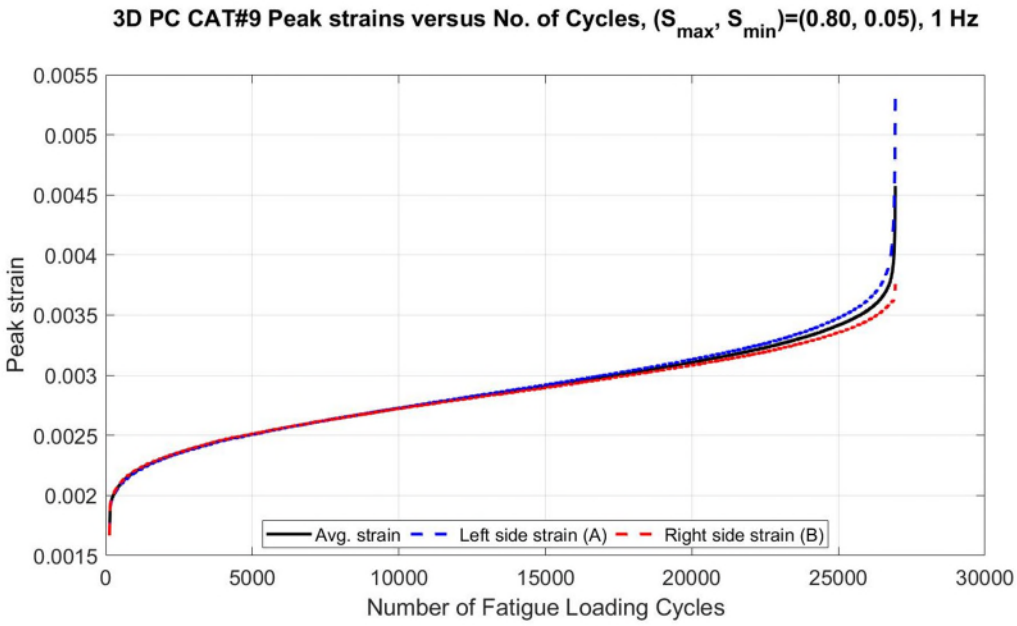

Figure 94 Peak strain recorded on both sides of the concrete cylinder over the testing cycles. (3DPC)

4.2 Monotonic and fatigue compressive test of plain concrete

4.2.1 Characteristics of the plain concrete testing batch

In the early stages of testing, 271 concrete specimens were prepared and cast with different percentages of reinforcement. Casting was done at the University of Illinois at Urbana-Champaign (UIUC). The static strength of this batch of concrete was designed to be about 5000 psi at 28 days. The monotonic test was conducted on a few specimens to find the specimens' average strength immediately prior to the constant amplitude tests (*Figure 95*). These monotonic tests were conducted 55-56 days after casting.

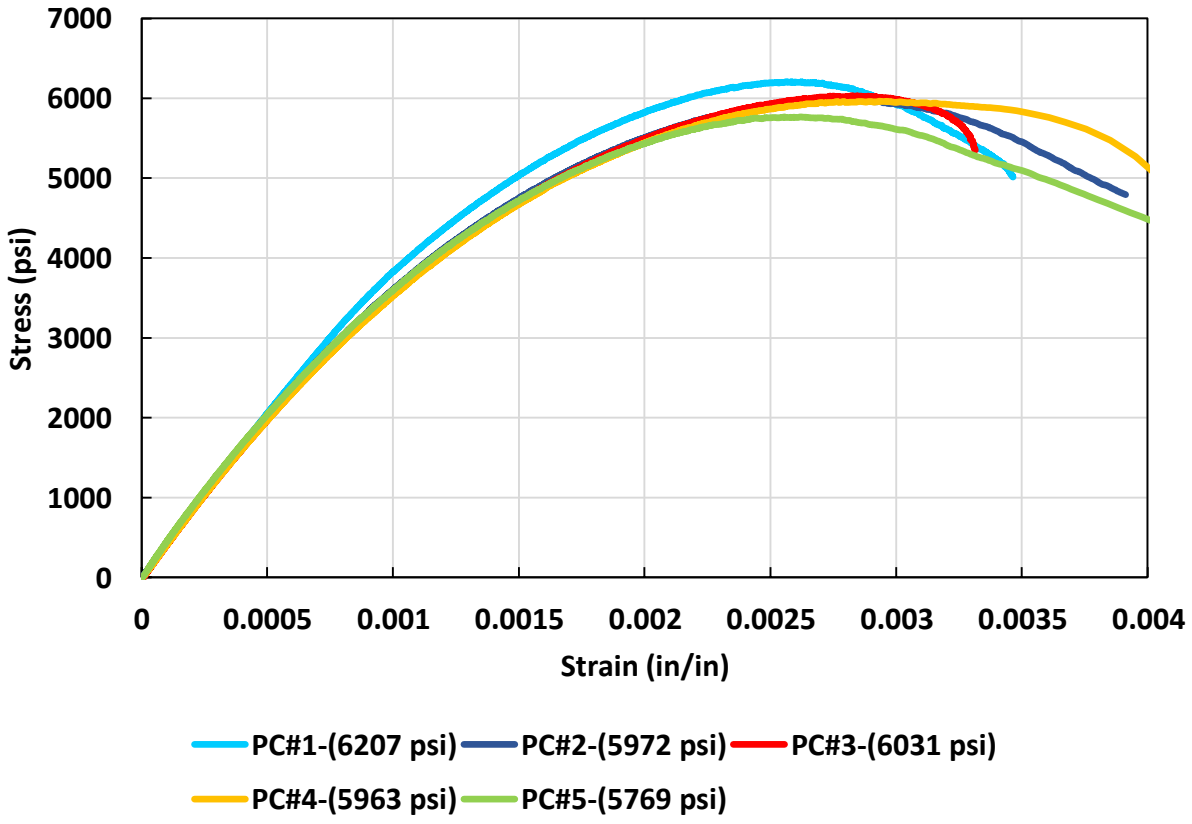

Figure 95 Stress-strain behavior of PC.

In these tests, the strains are measured via extensometers (called Channel A and B in this document) located on opposite sides of the specimen around the perimeter. As might be expected, the strength was lower when there was a greater strain difference between opposite sides of the cylinder. The result for PC#5 (green) supports this quite strongly, but the results from PC#4 (gold colored) are less convincing (Figure 96). Measuring the strain at more locations around the perimeter of the cylinder would provide greater insight into effect of strain variation around the perimeter on the final strength. The plots presented in this document display the average strain value from those two separate readings, unless otherwise noted.

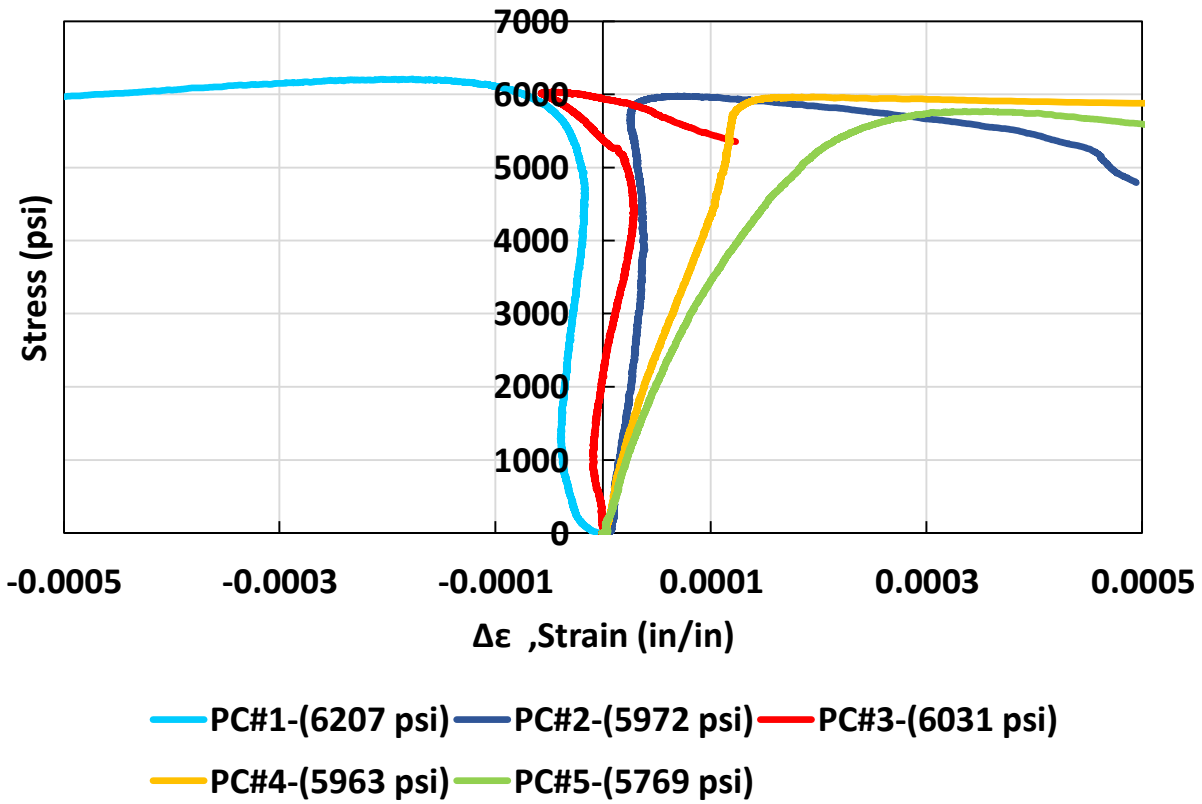

Figure 96 Stress-strain difference (Channel A-B) of PC under monotonic loading.

Identifiers used in this section (PC#1, etc.) are local to this section. As presented in Figure 96, the average compressive strength of concrete at this age was selected to be 6000 psi for the

cyclic testing. The loading characteristics are presented in *Table 16*. The sinewave loading protocol was used for this purpose.

Table 16 Cyclic fatigue loading protocols for plain concrete

	f'c (psi)	Smin	Smax_1	Smax_2	frequency (Hz)
ratio	-	0.05	0.8	0.7	1
Stress (psi)	6000	300	4800	4200	-

Table 17 shows the sensitivity of the fatigue capacity (# of cycles, N_f) by the Model Code to a 5% variation in concrete strength. As shown, for Smax_1, the N_f varies between 328-5786.For Smax_2, the N_f varies between 15615-185049. This corresponds to a 12-18 times variation in the duration of fatigue testing.

Table 17 Cyclic fatigue loading protocols

real f'c (psi)	real Smin	real Smax_1	Nf_1	estimated time_1 (hour)	real Smax_2	Nf_2	estimated time_2 (hour)
5700	0.053	0.842	328	0.09	0.737	15615	4.34
5800	0.052	0.828	554	0.15	0.724	24508	6.81
5900	0.051	0.814	917	0.25	0.712	37832	10.51
6000	0.05	0.8	1490	0.41	0.700	57489	15.97
6100	0.049	0.787	2379	0.66	0.689	86068	23.91
6200	0.048	0.774	3739	1.04	0.677	127049	35.29
6300	0.048	0.762	5786	1.61	0.667	185049	51.40

4.2.2 Loading protocol #1 (Smax, Smin)=(0.80, 0.05)

The first loading protocol was constant amplitude test (CAT) using (Smax,Smin)=(0.80,0.05) with a frequency of 1 Hz. A few results are presented in *Table 18.* The band of test results is very tight (i.e., a small range with a max/min ratio of less than 2), tighter than what has generally been observed by others. *Figure 97* and *Figure 98* show the peak and valley strain evolution plots of the specimens under the (0.80,0.05) loading protocols, respectively. The vertical axes show the strain in the specimen (corresponding to the peak and valley of the sinewave loading), and the

horizontal axes show the number of fatigue loading cycles and the fatigue loading cycle normalized to 1, respectively.

Table 18 Number of cycles to failure of PC under (Smax, Smin)=(0.80, 0.05) loading

Test No.	Nf
CAT#1	2,860
CAT#2	4,790
CAT#3	2,875
CAT#7	2,529

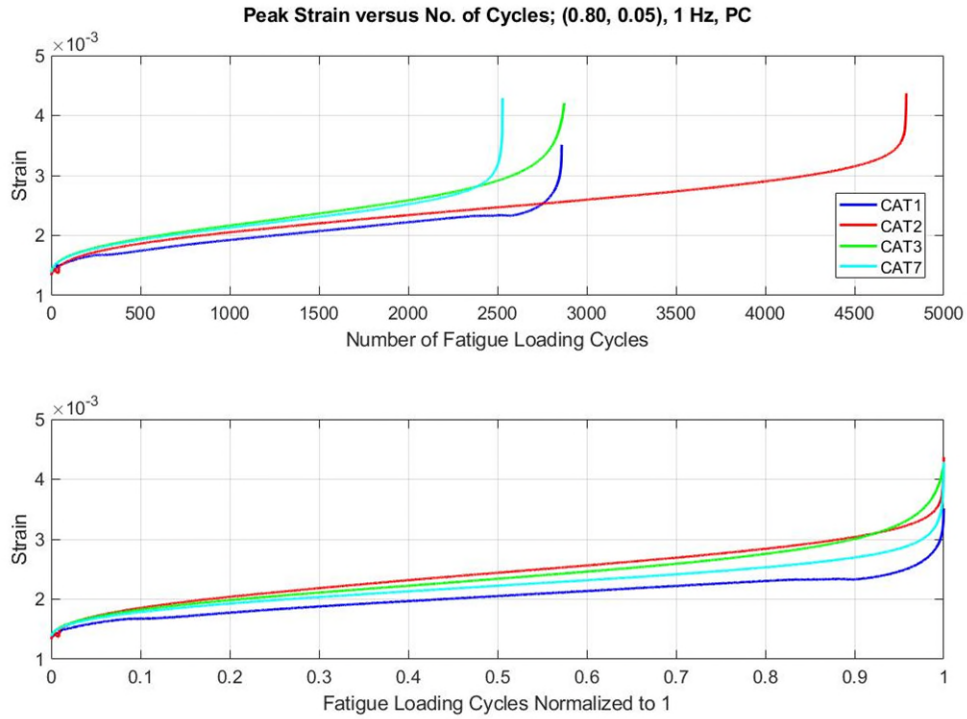

Figure 97 Plot of peak strain evolution under (Smax, Smin)=(0.80, 0.05) loading.

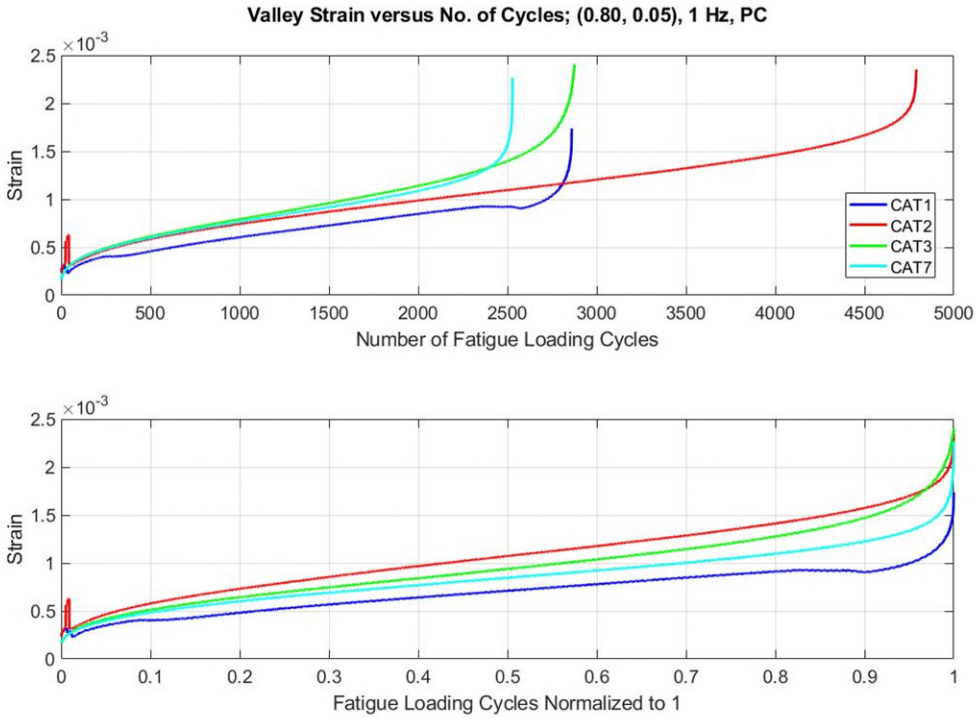

Figure 98 Plot of valley strain evolution under (Smax, Smin)=(0.80, 0.05) loading.

CAT#2 (red) supported twice the number of cycles to failure compared to other specimens. There was no obvious physical difference among these specimens in term of surface texture (honeycombing or shrinkage crack). Based on the aforementioned difference in strength, with the assumed average strength, this degree of variation is very modest. As shown in Figure 98, CAT#2 (red) had light valley strain for a few cycles in the beginning. That was because of a technical issue in setting up the correct Smin value. Since it had less amplitude of loading compared to what should have been imposed for just a few cycles, it had less of an impact on concrete life (N_f) than did the correct Smin.

4.2.3 Loading Protocol #2 (Smax, Smin)=(0.70, 0.05)

The second loading protocol was a constant amplitude test with a loading protocol identical to loading protocol #1 but with a lower Smax value (Smax, Smin)=(0.70, 0.05). *Table 19* shows the number of cycles that each test took to reach its failure point. The N_f results had about four times

variation in whole, which can be considered a tight band compared to the 12-times variation estimated by Model Code 2010. It shows that the concrete specimens had more coherency in terms of strength value and there is not a large variation. *Figure 99* and *Figure 100* show the peak and valley strain evolution plots of the specimens under the (0.70,0.05) loading protocols, respectively.

Table 19 Number of cycles to failure of the plain concrete under (Smax, Smin)=(0.70, 0.05) loading

Test No.	Nf
CAT#4	86,220
CAT#5	129,355
CAT#6	163,164
CAT#8	48,217

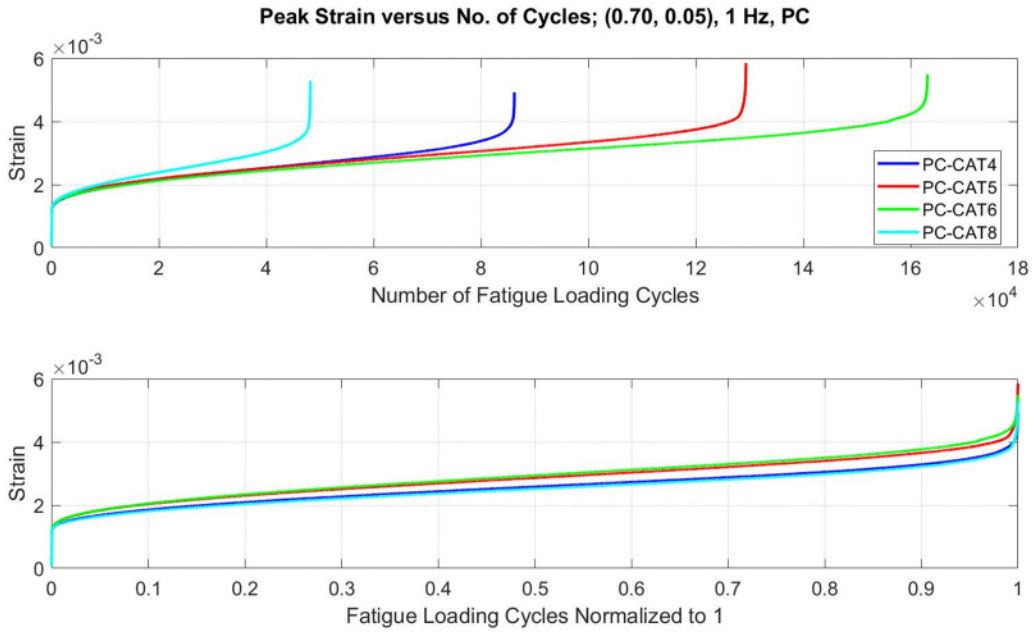

Figure 99 Plot of peak strain evolution under (Smax,Smin)=(0.70,0.05) loading.

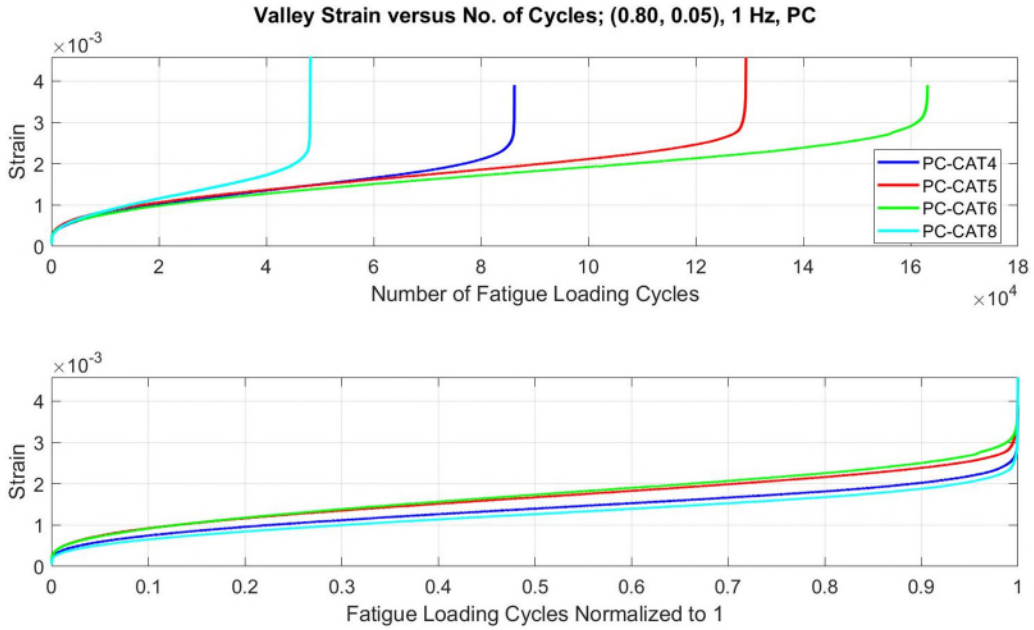

Figure 100 Valley plot of strain evolution under (Smax,Smin)=(0.70,0.05) loading.

These results adequately characterize the fatigue capacity and behavior of the PC cylinders of the first cast.

4.2.4 Visual damage on the plain concrete under fatigue loading

The evolution of surface damage on specimens was recorded by two high-resolution cameras located on opposite sides of the test cylinder. (*Figure 101*). These two cameras took high-resolution photos in preset time intervals (5 seconds, 2 minutes, 5 minutes, etc., depending on the specimens' total number of cycles to failure), and those time intervals were set based on the estimated number of cycles to failure for each test (the longer the estimated test duration, the larger the preset time intervals).

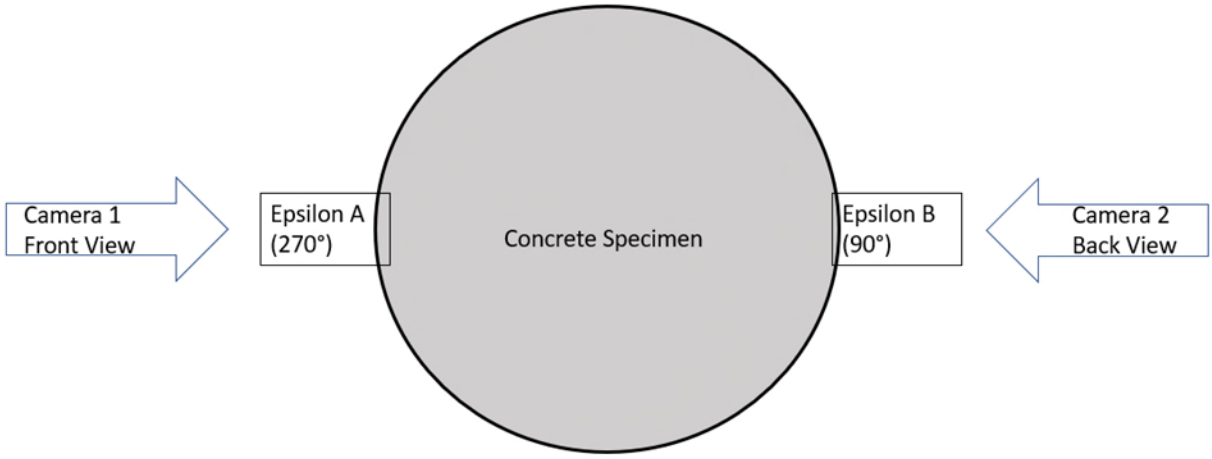

Figure 101 Plan view of the concrete specimen in the machine, along with the sensors and cameras.

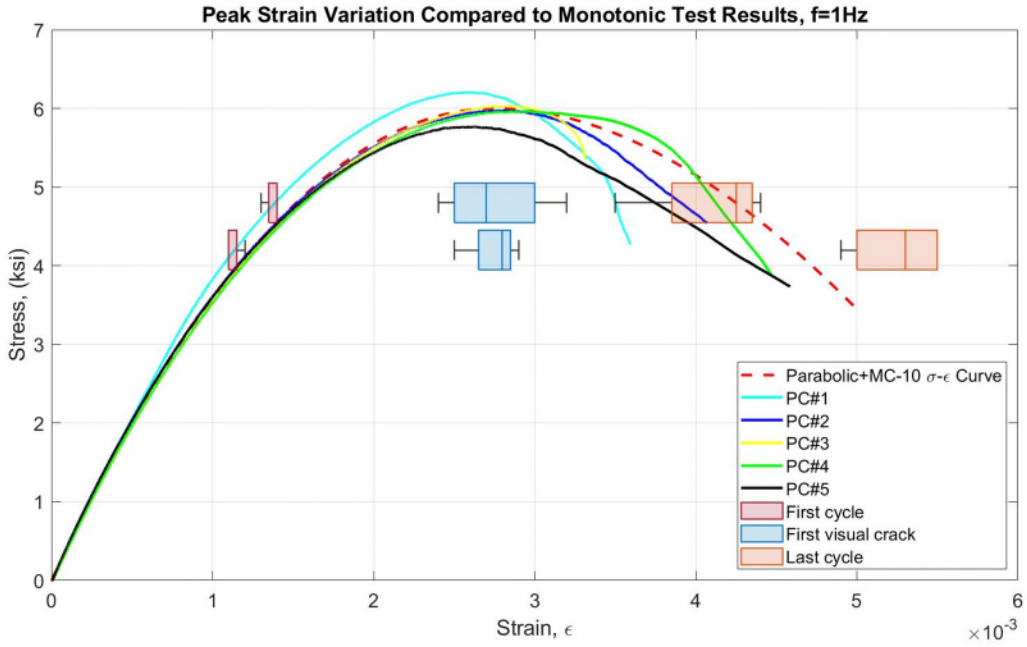

Figure 102 Peak strain variation at first cycle, at the cycle in which first visual damage was observed, and at last cycle vs. monotonic test results.

As might be expected, the internal/external damage in concrete specimens under monotonic test occurred at and after peak point of stress-strain curve, and one of the indications for this damage was load capacity loss. Figure 102 presents the variation of peak strain values of fatigue loading tests at three different points, including at first cycle, the cycle at which the first crack or visual

damage was observed, and the last cycle. The fatigue tests had two different loading protocols (same Smin and two different Smax) that were defined in previous pages. *Figure 102* shows that the first visual damage occurred around the strain related to the peak strength of concrete in the monotonic tests. Thus, the visual macrocracks seem to have had a strong tie with strain related to the peak monotonic strength (ε_{PM}).

Table 20 shows the results related to the point at which the first crack or visual damage was observed. The definitions of the variables are listed below:

N_f = fatigue loading number of cycles per failure

ε_{PM} = Avg. strain of concrete under monotonic loading at peak stress point (0.00273)

Ncrk = Number of cycles at which first visual crack was observed

ε_{PC} = Avg. strain at peak at Nc (milli-strain)

ε_{VC} = Avg. strain at valley at Nc (milli-strain)

Ec = stiffness of concrete at Nc (ksi)

Table 20 Visual damage results in fatigue test of the PC specimens

Test No.	(Smax, Smin)	N_f	N_{crk}	N_{crk}/N_f	ε_{PC}	$\varepsilon_{PC}/\varepsilon_{PM}$	ε_{VC}	Ec (ksi)
CAT#1	(0.80, 0.05)	2,860	2670	93%	2.4	0.89	0.95	3103
CAT#2	(0.80, 0.05)	4,790	4505	94%	3.2	1.19	1.7	3000
CAT#3	(0.80, 0.05)	2,875	2300	80%	2.8	1.04	1.3	3000
CAT#7	(0.80, 0.05)	2,529	2165	86%	2.6	0.96	1.2	3214
CAT#4	(0.70, 0.05)	86220	60000	70%	2.9	1.07	1.7	3250
CAT#5	(0.70, 0.05)	129355	60000	46%	2.8	1.04	1.6	3250
CAT#6	(0.70, 0.05)	163164	70000	43%	2.8	1.04	1.6	3250
CAT#8	(0.70, 0.05)	48217	23040	48%	2.5	0.93	1.2	3000

The ratio of N_c/N_f shows that the visual damage appeared earlier in the fatigue loading with lower Smax.

Figure 103 and Figure 104 prove this point by showing the ratio of the fatigue loading cycle to N_f at the point the stress evolution plot intersects the horizontal (dotted black) line which represents the ε_{PM}, strain related to the peak strength of concrete under monotonic load.

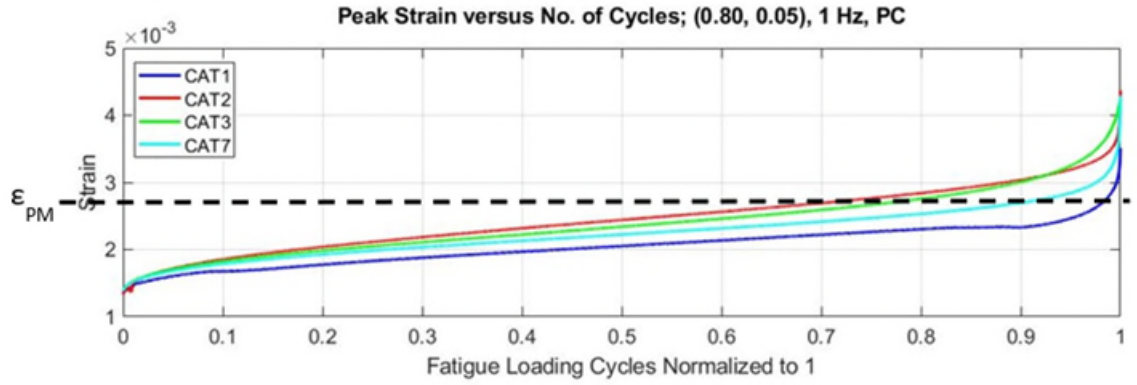

Figure 103 Plot of peak strain evolution under (Smax, Smin)=(0.80, 0.05) loading vs. dotted line showing the ε_{PM}

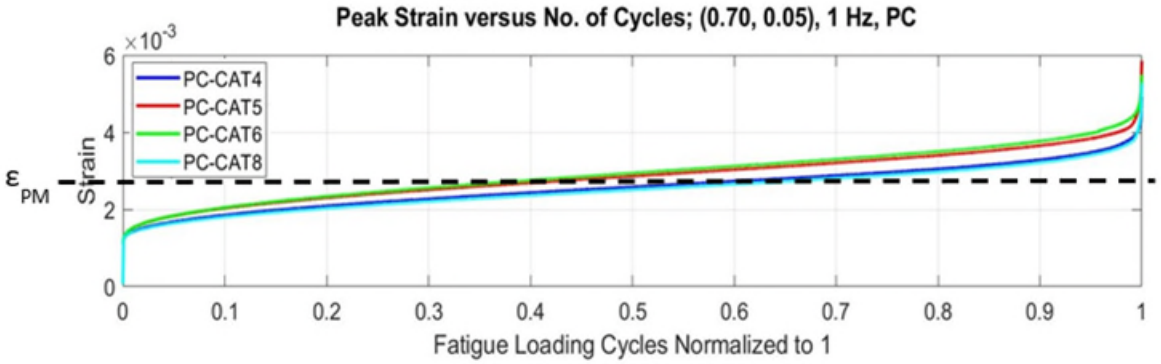

Figure 104 Plot of peak strain evolution under (Smax, Smin)=(0.70, 0.05) loading vs. dotted line showing the ε_{PM}

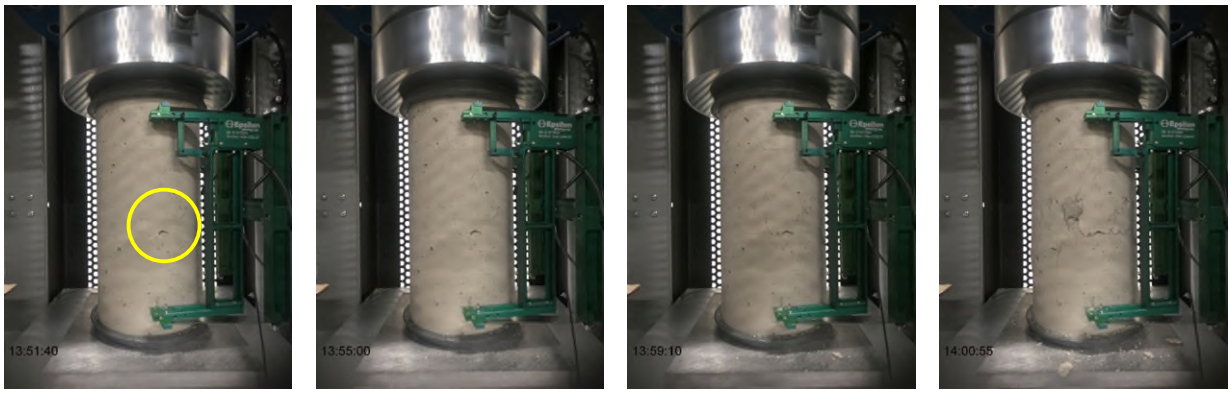

a) N=2300, first visual cracks b) N=2500 c) N=2750 d) N=2875, last cycle

Figure 105 Photos of the CAT#3 (Smax, Smin)=(0.80, 0.05) showing progress of visual damage.

4.3 Effect of longitudinal reinforcement on fatigue capacity

The impact of fatigue on structural concrete is, by standards, currently typically treated the same for all concretes regardless of the type of concrete material, neglecting the benefits of fibers, bar reinforcements, and other effects. The resulting large scatter in test data has led to models that are extremely conservative for many designs which detracts from the competitiveness of concrete design solutions. The new data, models, and standards that this document aims to help deliver offers designers and developers the necessary tools to drive innovation, reduce costs, and produce more resilient concrete support structures for wind turbines.

4.3.1 Assessing fatigue design life of structures made of steel and concrete

The fatigue capacity of concrete structures is characterized in a similar way as it is for steel structures, even though some of the assumptions inherent to that approach are inappropriate for concrete. *Figure 106* shows the so-called S-N relationship for steel structures. A stress range is shown on the vertical axis, the number of cycles of fatigue capacity is shown on the horizontal axis, and both scales are in log base 10. To assess the number of cycles of fatigue capacity for a particular stress range (e.g. 100 MPa), one would go to the point on the vertical axis

corresponding to this stress range, and then move along a horizontal line to the right (e.g. blue line for 100 MPa range) until intersecting the "curve" corresponding to the particular base metal or weld type under evaluation. For example, for a D-Class weld, one would trace the blue line until reaching the horizontal axis, identifying a fatigue capacity of about 550,000 cycles. Imposing this stress range for 100,000 cycles would use up 0.18 (100,000/550,000) or 18% of the available fatigue capacity. To assess the total capacity utilization for a series of different stress ranges, one would sum these via Palmgren-Miner's rule given in the equation shown in Figure 1. Figure 1 shows an example of a loading of 50 MPa for $3e^{+06}$ cycles, 100 MPa for 100,000 cycles, and 200 MPa for 20,000 cycles. Given a sum less than 1.0 (or a more conservative total as some cases require), the design is considered satisfactory.

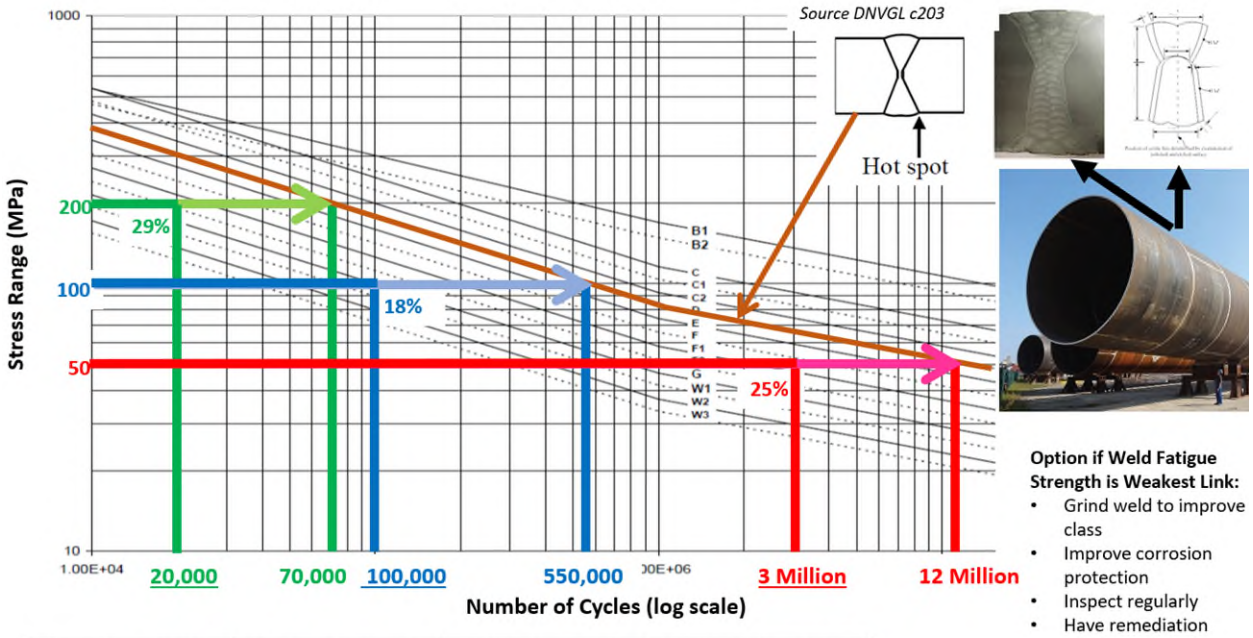

Stress Range (MPa)	# of Load Cycles (n_i)	# of Load Cycles to Fatigue (N_i)	Ni/Nf
50	3 million	12 million	0.25
100	100,000	550,000	0.18
200	20,000	70000	0.29
		Total Utilization	0.72

Palmgren-Miner's Rule

$$D = \sum_{i=1}^{k} \frac{n_i}{N_i} = \frac{1}{a} \sum_{i=1}^{k} n_i \cdot (\Delta\sigma_i)^m \leq \eta$$

Figure 106 Calculating fatigue capacity consumption of a hotspot in a monopile considering an imaginary variable load and specific weld type using DNVGL C203 code [116].

A typical fatigue model for concrete in compression is the Model Code. This model differs somewhat from the S-N curve for steel in that the vertical axis value is the fraction that the maximum compressive stress is of the monotonic compressive strength (S_{max}), and the particular curve to use is defined by the fraction that the minimum compressive stress is of the monotonic strength (S_{min}). Palmgren-Miners' linear damage accumulation model is used to assess the impact of multiple stress ranges.

4.3.2 Behavior of reinforced concrete under monotonic and fatigue loading

Figure 107 shows the monotonic response (stress on the vertical axis and strain on the horizontal axis) of an RC specimen with D=4 in and H=8 in and four longitudinal #3 bars that were part of the first cast. The measurements of two different readings from channel A and channel B of the extensometer (on opposite sides of the cylinder) were plotted alongside the average strain. The nearly identical strains suggest that the presence of the reinforcing bars ensured a similar variation in straining around the perimeter of the test cylinder. Figure 119 shows the cross section of the RC specimen with four #3 bars inside.

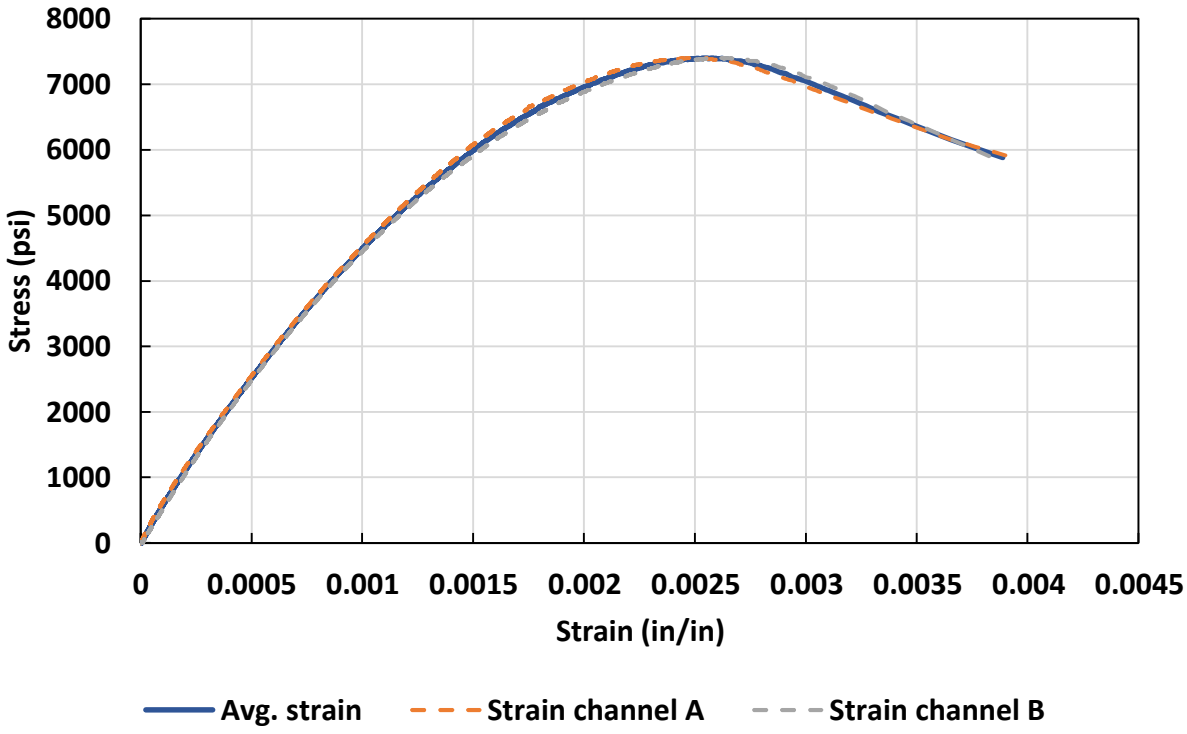

Figure 107 Stress-strain behavior of RC specimen with four #3 longitudinal bars inside.

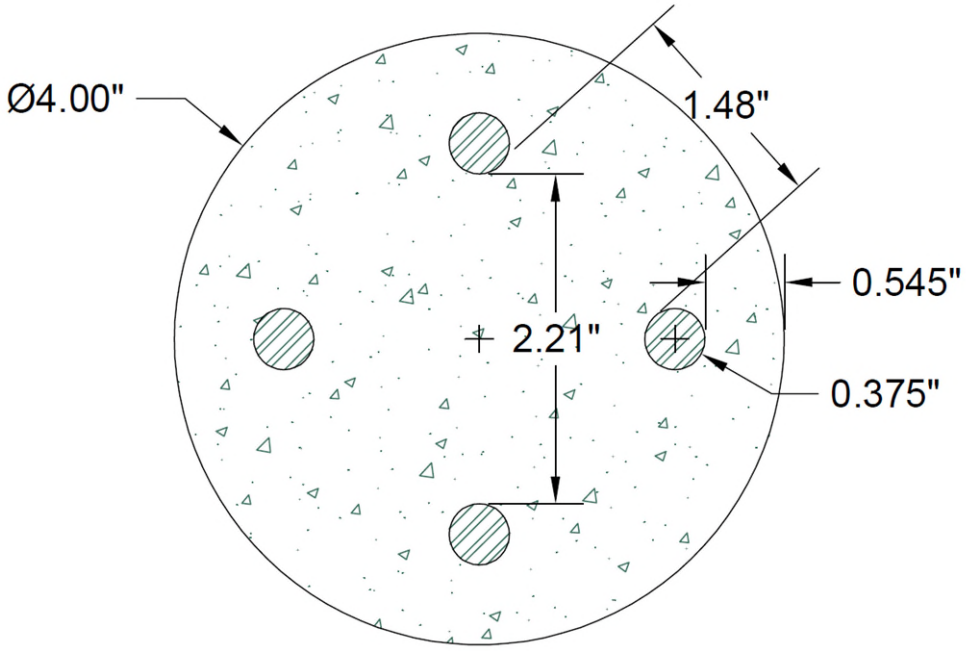

Figure 108 Cross section of RC specimens with four #3 longitudinal bars inside.

The strength of RC specimens with four #3 longitudinal bars and under monotonic load was about 7,400 psi. The maximum and minimum load limits for cyclic loading were calculated and are presented in Table 21.

Table 21 Cyclic fatigue loading protocols for RC

	Strength (psi)	Smin	Smax_1	Smax_2	frequency (Hz)
ratio	-	0.05	0.8	0.7	1
Stress (psi)	7400	370	5920	5180	-

4.3.2.1 Loading Protocol #1 (Smax, Smin)=(0.80, 0.05)

This part presents the results on two tests completed on the RC specimens using the (Smax,Smin)=(0.80,0.05). Figure 109 and Figure 111 present the stiffness degradation along the fatigue test in RC specimens CAT#1 and CAT#2 respectively. In these plots, the stiffness lines are plotted by using the Smax and Smin values and the related peak strain and valley strain of a few cycles along the test to show the stiffness degradation versus the monotonic response of the concrete. Figure 110 and Figure 112 present strain-N_f results of the two mentioned tests, and Figure 113 and Figure 114 show the visual crack and damage progress during the tests. The images are from after the first crack appeared.

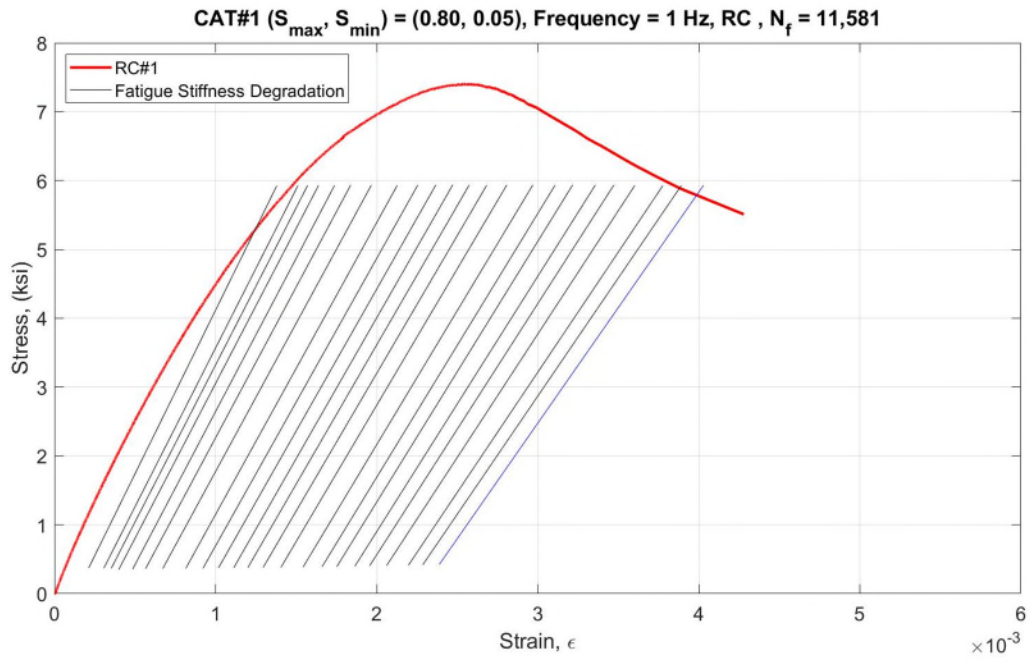

Figure 109 Stress-strain behavior of RC specimen vs. stiffness in a few selected cycles along the fatigue test up to the failure, RC-CAT#1.

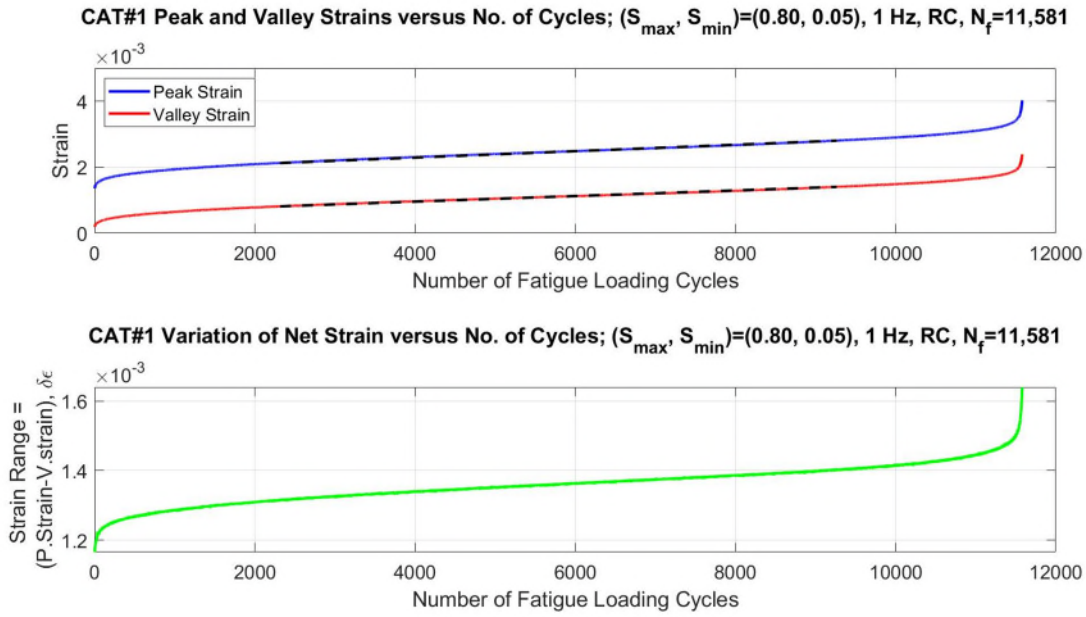

Figure 110 Strain evolution plot of RC specimen under fatigue loading (Smax, Smin)=(0.80, 0.05), RC-CAT#1.

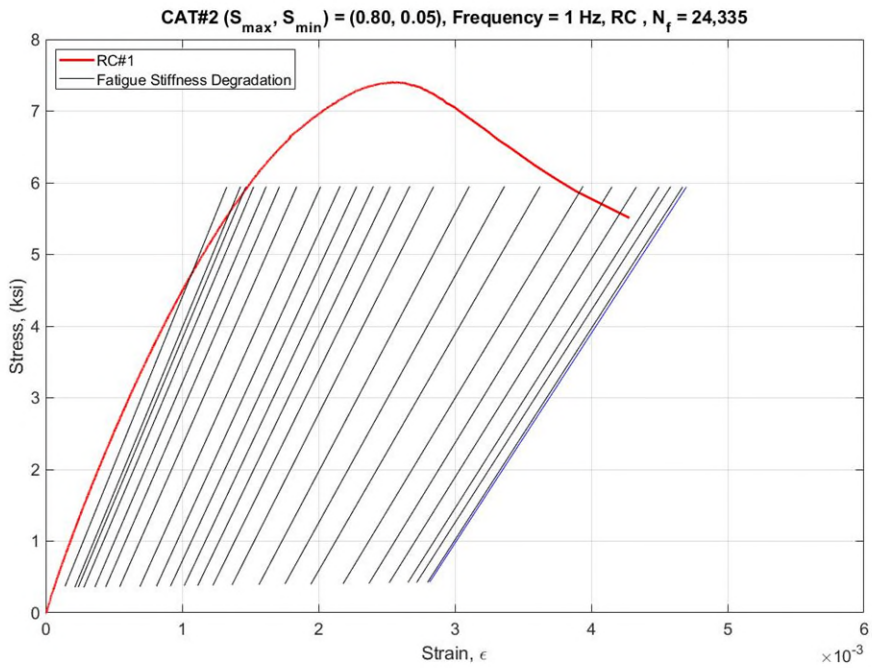

Figure 111 Stress-strain behavior of RC specimen vs. stiffness in a few selected cycles along the fatigue test up to the failure, RC-CAT#2.

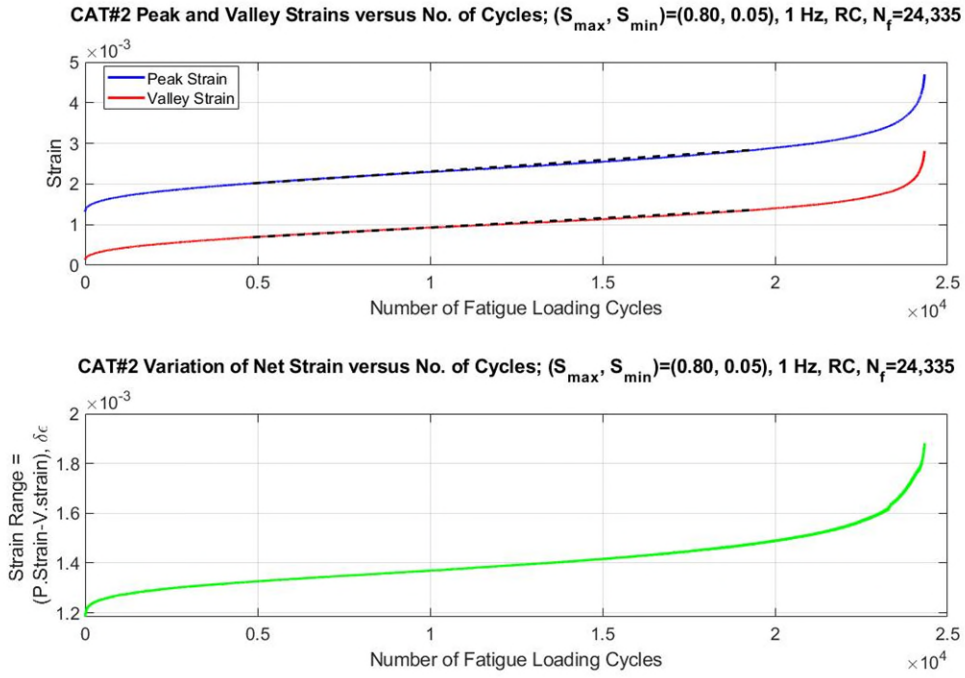

Figure 112 Strain evolution plot of RC specimen under fatigue loading (Smax, Smin)=(0.80, 0.05), RC-CAT#2.

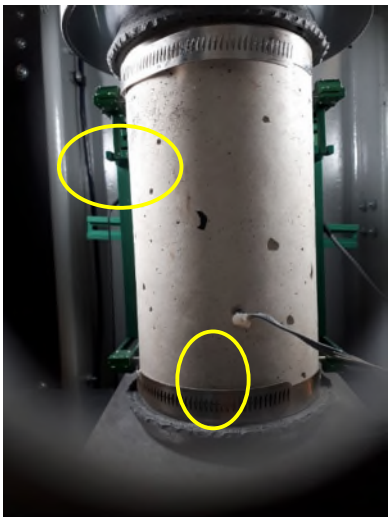

a) N=7,300 first visual cracks

b) N=9,400

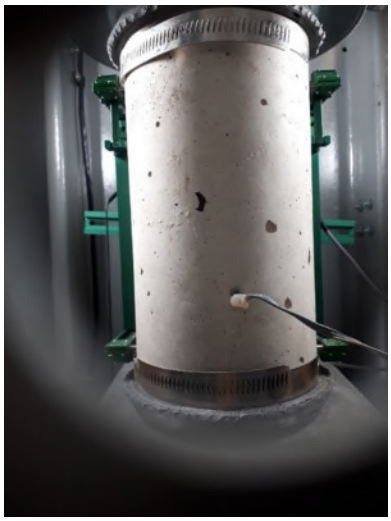

c) N=10,400

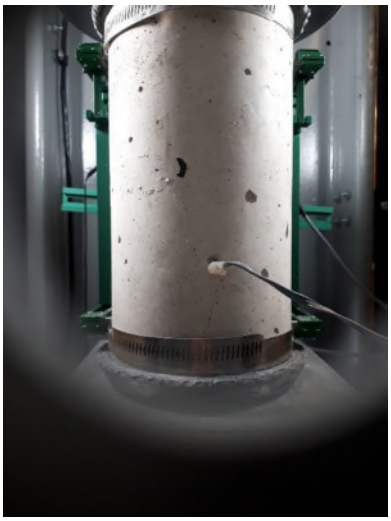

d) N=10,900

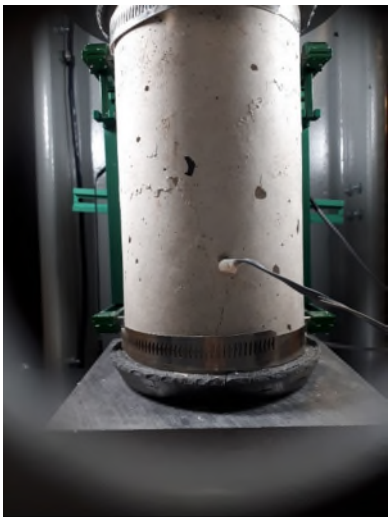

e) N=11,300, few hundreds of cycles before failure

Figure 113 Photos of the RC-CAT#1 (Smax, Smin)=(0.80, 0.05) showing visual damage progress.

a) N=14,400 first visual cracks

b) N=15,300

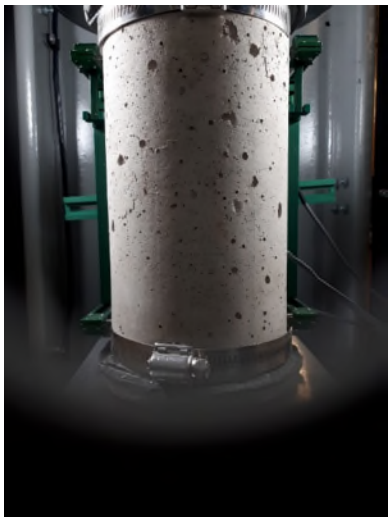

c) N=18,600

d) N=22,100

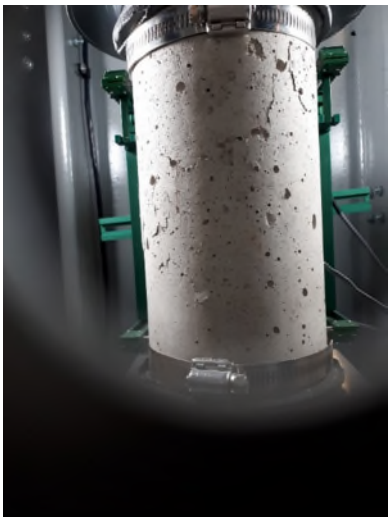

e) N=23,500, a few hundreds cycles before failure

Figure 114 Photos of the RC-CAT#2 (Smax, Smin)=(0.80, 0.05) showing visual damage progress

Figure 115 presents the strain evolution plot of two RC specimens, each with four #3 longitudinal bars, under the fatigue loading test.

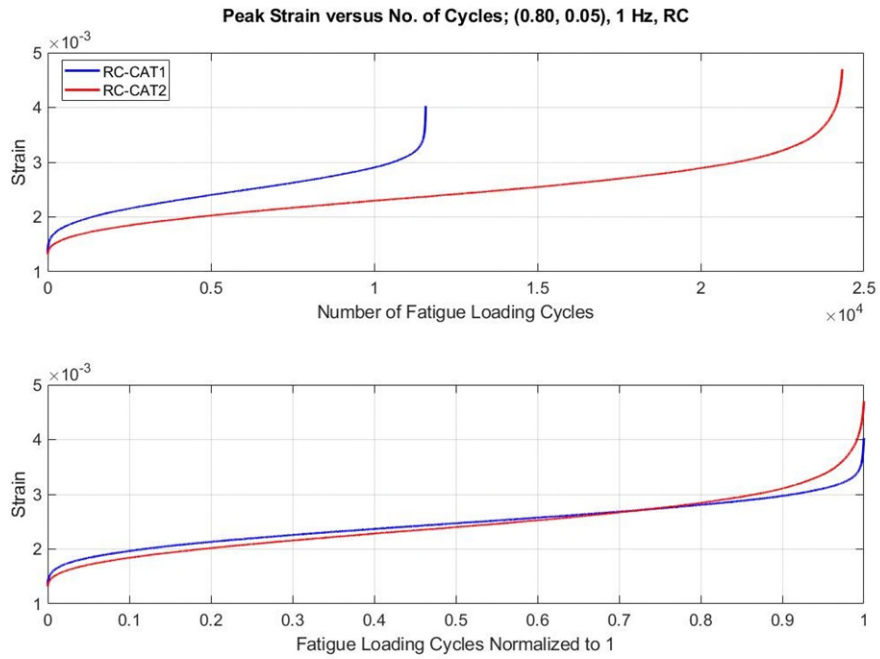

Figure 115 Peak strain evolution plot of RC specimens under fatigue loading cycle (Smax, Smin)=(0.80, 0.05).

The analysis of the load share change of reinforcement steel and concrete required the mechanical characteristics of #3 bars that have been used. The measured stress-strain response of the steel rebars is presented (Figure 116). The average yield strength of the #3 bars was taken as 65 ksi and at a yield strain of 2.32 milli-strain on average. Taking the stress-strain behavior of steel bars into account, Figure 117 and Figure 118 show the stress share change in concrete due to increment in strain along the fatigue loading. Reinforcing the concrete decreases the concrete load share and, consequently, increases the life of the concrete under fatigue loading. These changes in load share happen fast and early in the fatigue testing of RC specimens with high Smax value. For instance, in the (Smax,Smin)=(0.80,0.05) loading regime, the stress in the concrete portion of the structure decreases from $0.8xf'_c$ to $0.633xf'_c$ after only a few hundred cycles.

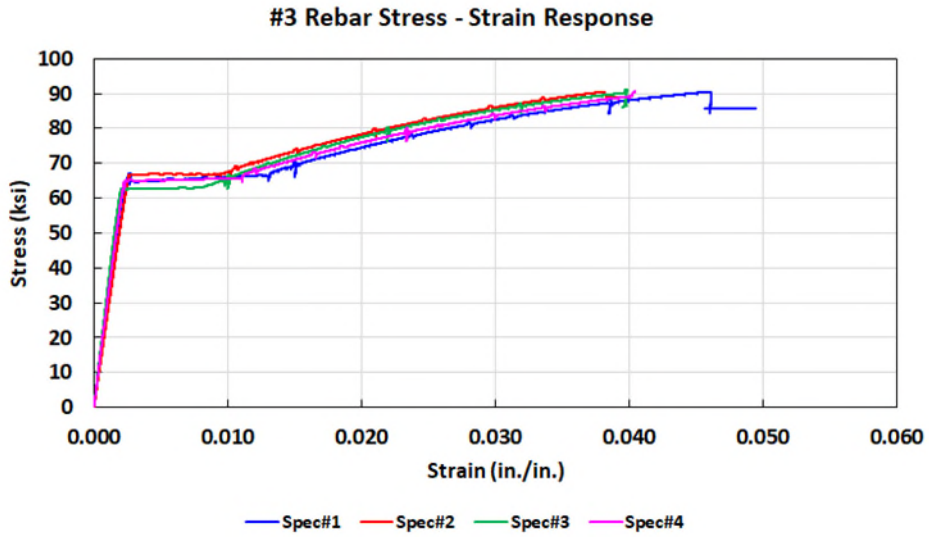

Figure 116 Stress-strain behavior of #3 rebar that was used in the RC specimens.

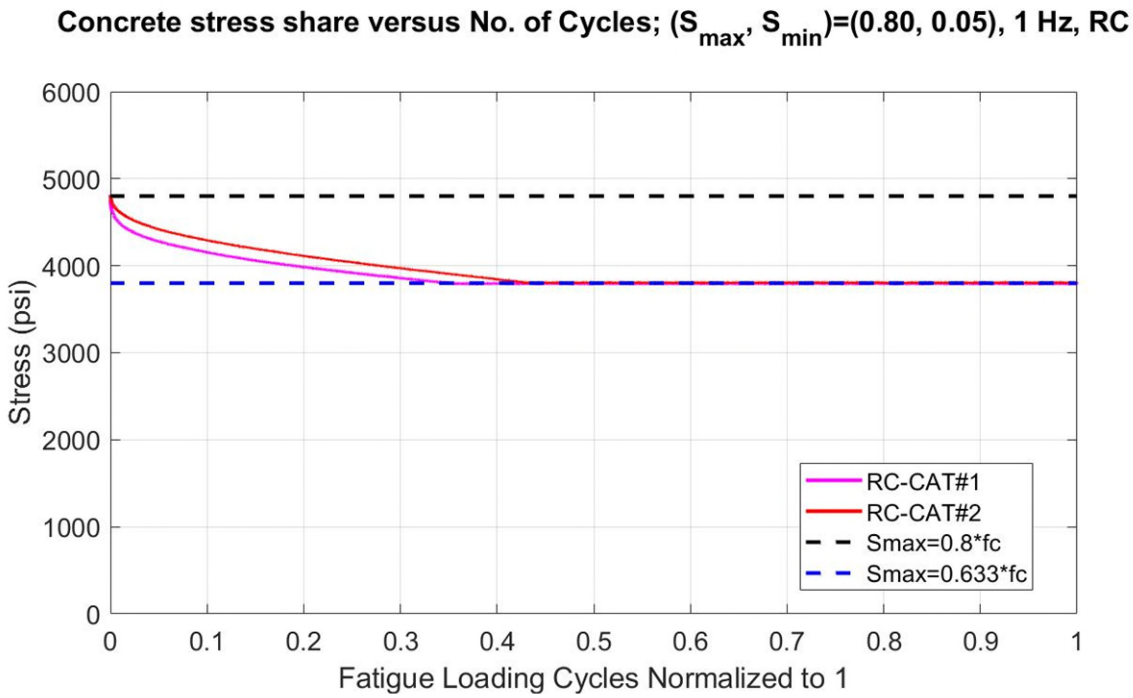

Figure 117 Stress share of concrete in the RC specimen considering the stress transfer to the reinforcement by strain increment, (Smax, Smin)=(0.80, 0.05).

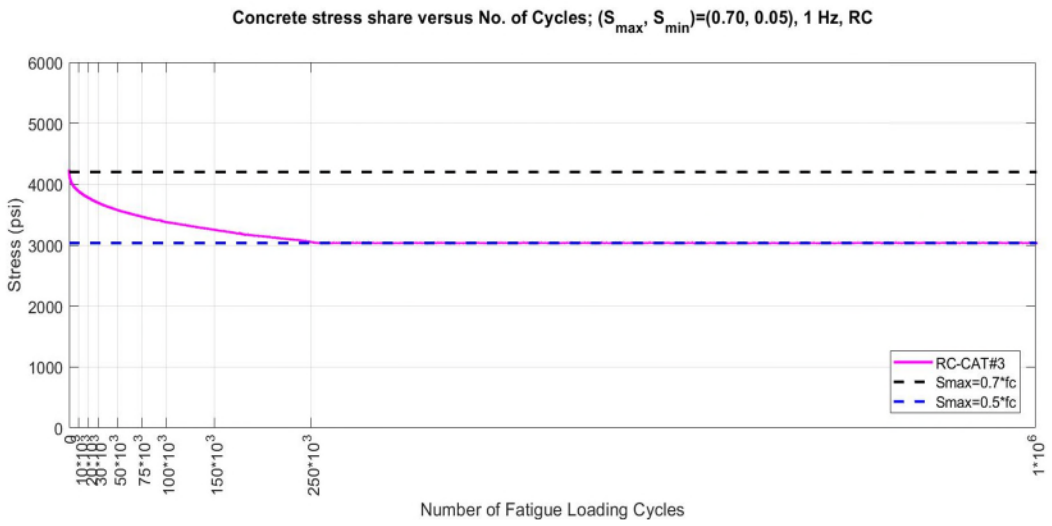

Figure 118 Stress share of concrete in the RC specimen considering the stress transfer to the reinforcement by strain increment, (Smax, Smin)=(0.70, 0.05).

4.3.3 Constant amplitude test (CAT) on reinforced concrete

The constant amplitude test on the RC cylinders with four #3 bars was administered with a load combination of (Smax, Smin) = (0.80, 0.05) at a frequency of 1 Hz. The results (number of cycles to failure) are listed in Table 22. This table also includes the previous test results, with the same load combination, on the specimens made of PC and the model predictions for the fatigue capacity. The last three columns of Table 22 show the ratio of the predicted/recorded number of cycles to failure to the predicted number of cycles to failure of three fatigue models of "Model Code 2010", "DNVGL-ST-C502", and "Eurocode 2". These ratios show the conservativeness of the fatigue models. In some cases, the ratio of the actual test results to the predicted number of cycles to failure approaches 150-fold, and at minimum, the actual capacity is about 5.6 times the predictions.

Table 22 Comparison of fatigue test results and fatigue model predictions for cylinders made of RC and cylinders made of dry plain concrete.

Type	Name	N_f	N_f / N_{f_MC2010}	N_f / N_{f_DNVGL}	$N_f / N_{f\_EuroCode2}$
Code	Model Code 2010	1489.5	1.0	4.4	1.9
	DNVGL-ST-C502	336.0	0.2	1.0	0.4
	Eurocode 2	779.5	0.5	2.3	1.0
Dry PC	PC-CAT#1-F1-80-5	2,860	1.9	8.5	3.7
	PC-CAT#2-F1-80-5	4,790	3.2	14.3	6.1
	PC-CAT#3-F1-80-5	2,875	1.9	8.6	3.7
	PC-CAT#4-F1-80-5	2,529	1.7	7.5	3.2
RC	RC4#3-CAT#1-F1-80-5	38,883	26.1	115.7	49.9
	RC4#3-CAT#2-F1-80-5	43,320	29.1	128.9	55.6
	RC4#3-CAT#3-F1-80-5	8,279	5.6	24.6	10.6
	RC4#3-CAT#4-F1-80-5	10236	6.9	30.5	13.1
	RC4#3-CAT#5-F1-80-5	52,576	35.3	156.5	67.4
	RC4#3-CAT#6-F1-80-5	9,024	6.1	26.9	11.6
	RC4#3-CAT#7-F1-80-5	26,535	17.8	79.0	34.0

Naming guide: Plain Concrete (PC) – Constant amplitude test number 1 (CAT#1) – Frequency of loading (Hz) # (F1) – Smax percent % (80) - Smin percent % (5)

Figure 119 shows a considerable increase in fatigue capacity through reinforcement, highlighting the conservativeness of the fatigue models that are defined for PC. There is a need for large-scale testing on joints and structural elements to explore the effect of reinforcement better due to high concentration of reinforcement in those elements.

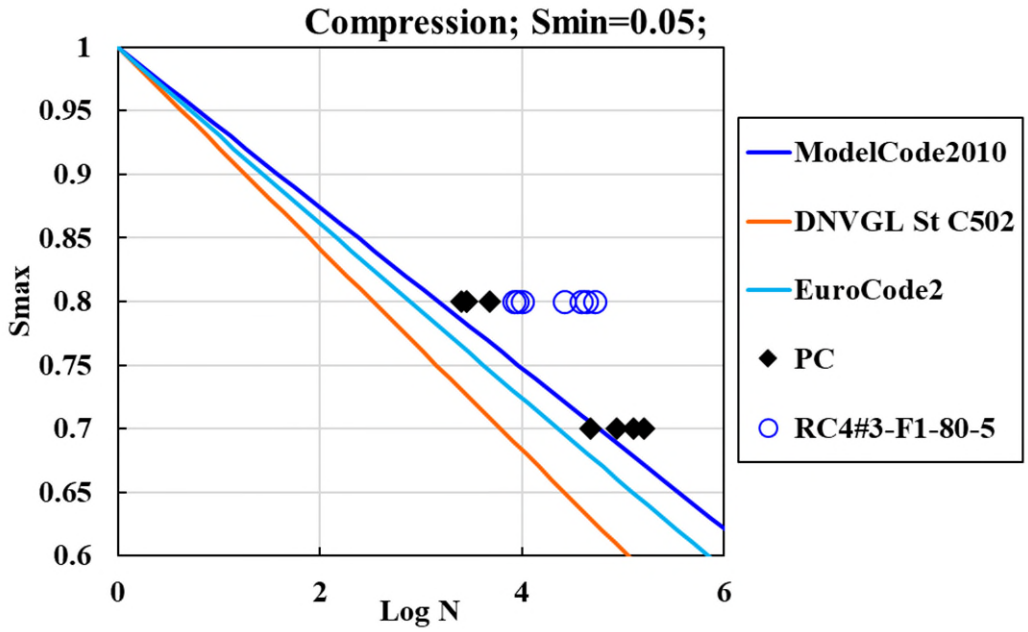

Figure 119 Fatigue test results for cylinders made of RC.

Figure 120 shows the final testing results, which consist of three parts. The first of the three parts is the number of cycles to failure (N_f). More than seven tests had been conducted to obtain the measured number of cycles to failure. The minimum, average, and maximum of the measured number of cycles to failure are listed here. Tests that were observed to fail prematurely due to boundary conditions or other obvious reasons for disqualification have been omitted. The average strain at failure for the last time that the peak load was sustained was presented.

The second part is for the strain and the portion through the testing that there was the first visible damage. This is the average for all tests in this series that were not disqualified. The first visible damage occurred at a strain of 0.2%, which is close to the yield strain of the reinforcing steel. The first visible damage occurred at around 59% of the number of cycles to failure in this particular load combination. These kinds of observations can inform probabilistic methods for determining the remaining fatigue capacity (life) of an existing structure and advance structural health monitoring and inspection techniques.

The third part is the portion of the peak load and valley load taken by the concrete at four different points through the loading history: 10 cycles into the loading, at 10% of the total N_f through the loading history, at 50% of N_f, and 10 cycles before N_f. The load portion between concrete and reinforcing steel changes throughout the test, complicating the design process. The load combination for the load share of PC portion of the structure (i.e. the cyclic load carried out by the PC) changes constantly. Thus, the actual load history is like a variable amplitude test.

1. Constant Amplitude Tests (CATs) on Reinforced Concrete (RC)

Smax (ratio)	Smin (ratio)	Freq (Hz)	Longitudinal Reinforcement	Number of Cycles to Failure (Nf) Minimum	Average	Maximum	Average Strain at Failure
0.8	0.05	1	4 #3 bars	8279	26979	52576	0.0041633

Notes: Minimum is the lowest number of cycles to failure (Nf) from all legitimate test results
Average is the mean number of cycles to failure (Nf) from all legitimate test results
Maximum is the largest number of cycles to failure (Nf) from all legitimate test results

	Average
Ratio of (Number of Cycles to First Visible Damage, Nv) /(Number of Cycles to Failure, Nf)	0.59
Strain at which the first visible damage shows up	0.0020434

An entry of 0.60 in the first row would suggest that visible first visible damage occurs at 60% of the measured Nf
e.g. If Nf is measured to 6212 for a test, then an entry of 0.60 would indicate first visible damage at 0.6(6212) = 3727 cycles

	Cycle Number (Values in Green Cells are Averages) Ni = 10 cycles	Ni/Nf = 0.1	Ni/Nf = 0.5	Ni = Nf - 10
Portion of Peak Load Taken by Concrete	80%	77%	73%	68%
Portion of Valley Load Taken by Concrete	66%	37%	8%	0%

Ni = Number of Cycles
An entry of 0.70 would imply that 70% of the loading is taken by the concrete
The "Portion of Load" will be calcluated as (Load - Asfs)/(Load) where fs is calculated from the measured strain over the height of the cylinder and the fs-εs relationship that was presented in Figure 8 of the competition description document.

Figure 120 Overview of the fatigue test results for cylinders made of RC.

4.3.4 Plain concrete vs. reinforced concrete

To have a sense of the effect of the longitudinal reinforcement on increment of concrete life under fatigue loading, results of two specimens made of PC and two made of RC are presented in Table 23. Both the PC and RC were tested with a (Smax, Smin)=(0.80,0.05) fatigue loading protocol. Figure 121 shows that the longitudinal reinforcement had huge effect on the fatigue life of concrete under compression, with the RC specimens experiencing a longer life with the same loading protocol.

Table 23 Number of fatigue loading cycles per failure for PC and RC specimens, (Smax, Smin)=(0.80, 0.05).

Specimen Type	Test No.	Nf
PC	CAT#2	4,790
PC	CAT#3	2,875
RC	CAT#1	11,581
RC	CAT#2	24,335

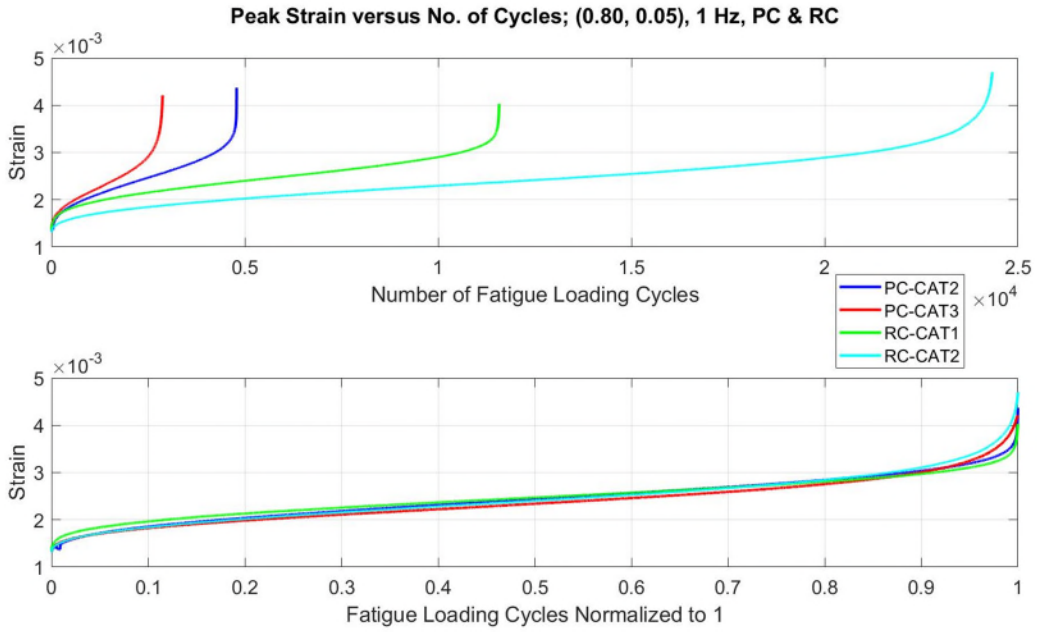

Figure 121 Plot of peak strain evolution of PC and RC specimens. (Smax, Smin)=(0.80, 0.05)

4.3.5 Discussion on the effect of reinforcement on fatigue capacity

This section presents selected test data on fatigue capacity, stress-strain response, and visual observations of damage from the testing of the cylinders made of RC. Four of the most significant findings are presented below.

4.3.5.1 Procedure for determining load-share between concrete and reinforcing steel in RC

The following procedure was utilized for determining the load-share, i.e., the proportion of applied load, $(P_{max}, P_{min})_{RC}$, that was resisted by concrete, $(P_{max}, P_{min})_{Conc}$, and by reinforcing steel, $(P_{max}, P_{min})_{Steel}$:

I. The peak and valley strain magnitudes, $(\varepsilon_{max}, \varepsilon_{min})_{RC}$, were determined from the extensometer readings for every cycle of fatigue loading (see Figure 93).

II. The stress in the reinforcing steel, σ_{St}, was determined as the product of strain and its Young's Modulus, E_s, i.e., $(\sigma_{St})_{max/min} = E_s * \varepsilon_{max/min} \leq f_y$ (where: f_y = yield stress of reinforcing steel = 60 ksi).

III. The proportion of the applied load that was resisted by the reinforcing steel, $(P_{st})_{max/min}$ was computed as the product of the stress and the area, i.e., $(P_{st})_{max/min} = A_s * (\sigma_{St})_{max/min}$

IV. The proportion of the applied load that was resisted by the concrete, $(P_C)_{max/min}$ was computed as the difference between the applied load and that resisted by steel, i.e., $(P_C)_{max/min} = (P_{RC})_{max/min} - (P_{st})_{max/min}$

The load share between concrete and steel (or, the proportion of applied load, $(P_{max}, P_{min})_{RC}$, that was resisted by concrete, $(P_{max}, P_{min})_{Conc}$, and by reinforcing steel, $(P_{max}, P_{min})_{Steel}$) was determined for the conducted uniaxial fatigue experiment on the reinforced concrete specimen. The next section highlights some of the associated results.

4.3.5.2 Reinforcement strain yield capacity and RC fatigue

Figure 122 presents the monotonic and fatigue response of a concrete cylinder when $S_{max} = 0.80$, and $S_{min} = 0.075$. As previously indicated, the peak and valley strains increase with the number

of cycles of loading. Figure 122 (a) also shows the stresses expected in the longitudinal reinforcement at strains of 0.0010, 0.0015, and 0.0020 using an E_s = 29000 ksi (200000 MPa).

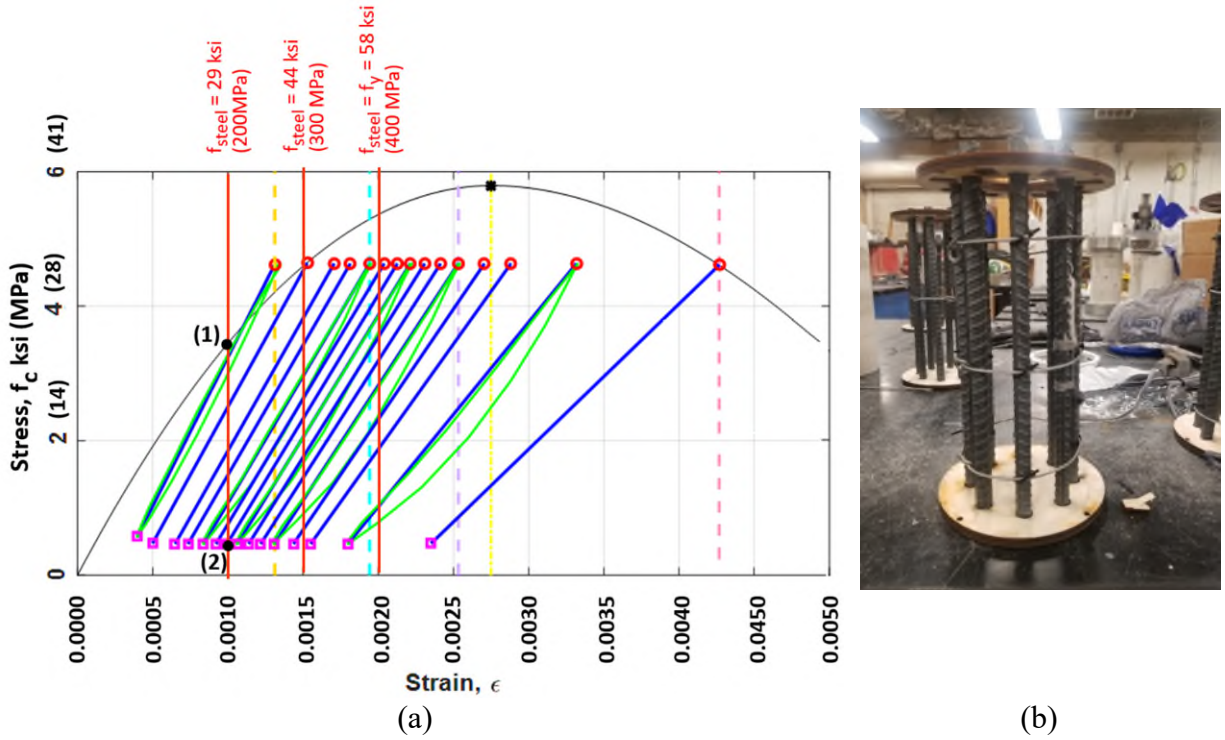

Figure 122 a) Monotonic response of RC (Stress-Strain curve) and loading-unloading lines of fatigue test; b) reinforcement cage used for casting cylindrical specimens made of RC (4 in x 8 in)

The load share between the reinforcing steel and the concrete is expected to vary because of concrete softening and damage accumulation. Early in the fatigue loading history, the stress in the concrete when the strain is equal to 0.0010 is three ksi (21 MPa) as shown as point (1), whereas by midway through the loading history, the strain in the concrete for this level strain is about 0.6 ksi (4 MPa) as shown as point (2). This means that, for an RC structure subjected to a constant variation in forces, there will be a decrease in concrete stresses and increase in steel stresses as the fatigue loading progresses. This effect is not currently considered in design practice nor quantified in existing fatigue models. A significant number of fatigue tests are being conducted on cylinders made of RC to investigate and quantify this effect.

4.3.5.3 Effect of longitudinal reinforcement on fatigue capacity

The use of longitudinal reinforcement had a dramatic effect on the number of load cycles to failure as shown in Figure 123 for the ratios of S_{max}/S_{min} = 0.80/0.05. Six test results are shown, four for specimens made of PC, and two for specimens containing four #3 longitudinal bars. As shown, the addition of reinforcing bars increased the fatigue capacity by a factor of 5-10.

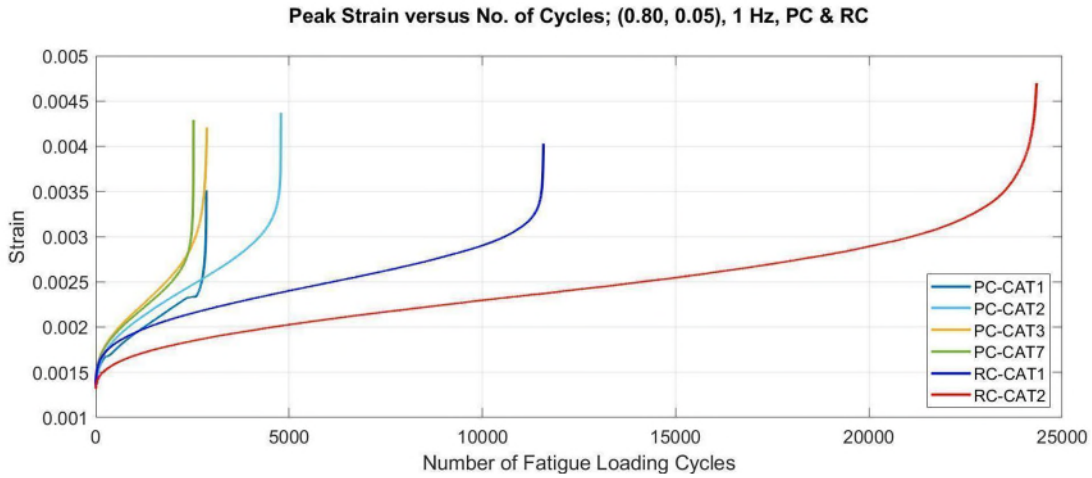

Figure 123 Comparison of the number of cycles to failure in specimens made of PC and RC with S_{max}/S_{min} = 0.80/0.05

4.3.5.4 Plausible explanation for the benefit of longitudinal reinforcement

A likely explanation for this extension of fatigue life through longitudinal reinforcement is that, even in the early segment of cyclic loading, concrete softens considerably, leading to a transfer of load/stress from the concrete to the longitudinal reinforcement. The reduction in compressive stress in the concrete is fairly dramatic, as shown in Figure 124. This stress can be calculated from equilibrium using the following expression:

$$f_c = \frac{Total\ Axial\ Load - Force\ in\ Steel}{Area\ of\ Concrete} = \frac{N - A_s f_s}{A_c}\ where\ f_s = E_s\varepsilon < f_{sy} \qquad Equation\ 2$$

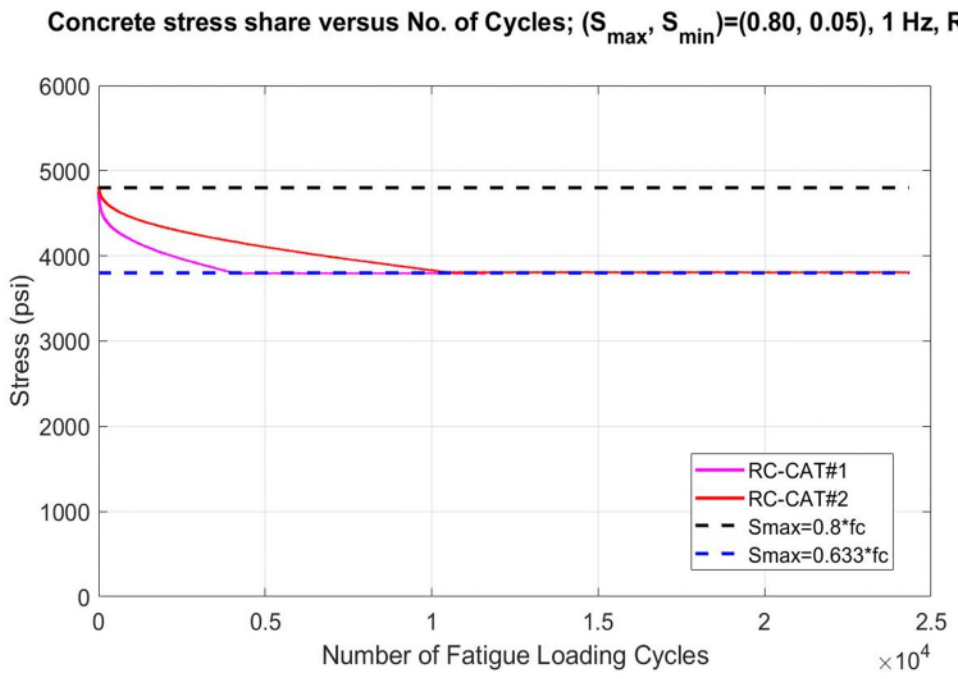

Figure 124 Compressive stress over the loading history caluclated for S_{max}/S_{min} = 0.80/0.05 tests

Since even a small reduction in compressive stress causes a large increase in fatigue strength, the large difference in total number of cycles to failure due to the presence of reinforcement was expected. The fatigue capacity for this range in stresses by the Model Code can be calculated by dividing this curve into a finite set of stresses and associated loading cycles as shown in Figure 125 and Table 24.

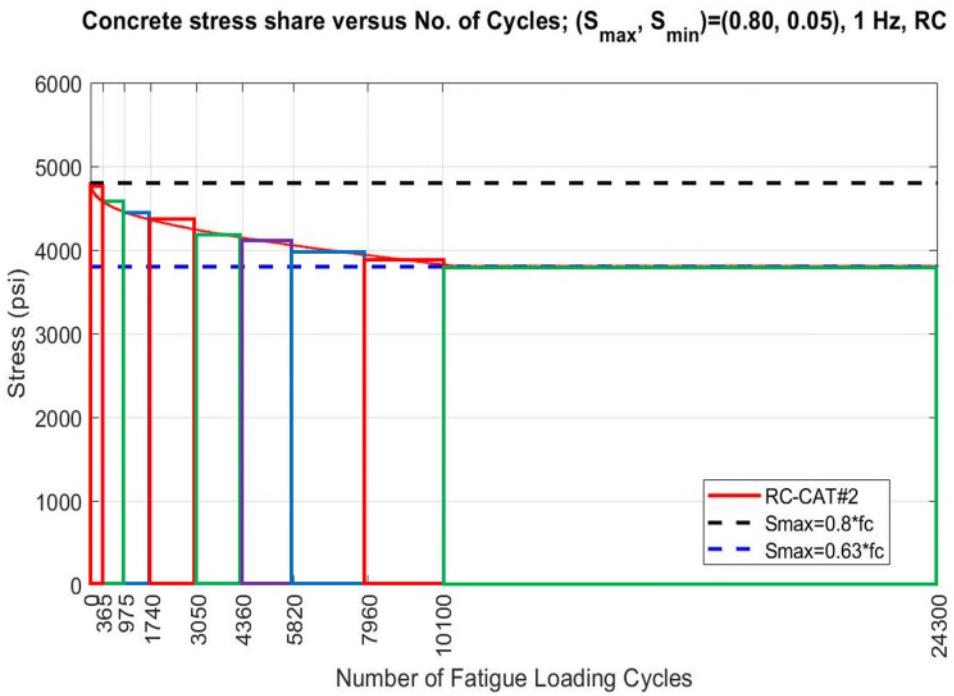

Figure 125 Bands for calculating fatigue capacity utilization.

Table 24 Fatigue capacity utilization based on the Model Code.

Band	Smax_vp1	Smin_vp1	Applied	Nf Model Code	Utilization Ni/Nf
1	0.79	0.05	365	1926	0.189
2	0.76	0.05	610	5554	0.110
3	0.74	0.05	765	12762	0.060
4	0.73	0.05	1310	20091	0.065
5	0.70	0.05	1310	62476	0.021
6	0.69	0.05	1460	98355	0.015
7	0.66	0.05	2140	226005	0.009
8	0.65	0.05	2140	413902	0.005
9	0.63	0.05	14200	651600	0.022
Sum	-	-	24300	-	0.497

4.3.5.5 Impact of reinforcement on uniformity of axial straining around the cylinder's circumference

In the testing on PC cylinders, a significant variation in axial straining around each specimen's circumference was frequently observed. This was expected because of the natural variation in the stiffness of the concrete that would require more strain in the less stiff regions to produce the same level of stress as required because of the use of a spherical seat at the top of the cylinder

(see Figure 93) that ensures a non-moment condition along the centerline of the cylinder. With increasing levels of axial stress in these cylinders, straining and damage often concentrate on one part of the cylinder, and then the failure initiates from this local region of damage. The pattern of deformation and straining needed for this was not consistent with what would occur within the critically stressed region (or any region for that matter) of a large continuous structure for which the kinematic restraints of the surrounding concrete would force a more uniform distribution of strain. The use of at least four equally spaced longitudinally reinforcing bars around the perimeter of the cylinder substantially reduced the variation in axial compressive straining across the cross-section; this reinforcement reduced the likelihood that a less stiff and weaker region could precipitate a failure. This result raises questions about how testing should be done on PC. To better represent the state of stress and kinematic constraints, tests would ideally have the use of a spherical seat to address the non-parallelism of the ends of the cylinders, and this seat would be locked into position once uniform stress conditions have been imposed and the test is past end seating effect.

4.3.5.6 Prediction of compressive stresses in design

While the compressive stress that is applied in fatigue testing can be easily calculated from the known axial load, measured straining, and stress-strain characteristics of the reinforcement, it is challenging to determine how best to estimate the values of these influential factors in the design process. Through discussions with designers and Certification and Verification Agencies (CVA)[14], it was determined that most practitioners consider concrete to be a linear elastic

[14] Certification verification agencies, like DNV (Det Norske Veritas), play a crucial role in the offshore wind industry by ensuring that the design, construction, and operation of wind structures meet established standards and regulatory requirements. Their primary responsibilities include Standards Compliance, Independent Assessment,

material with some accounting for the stiffness of the reinforcing steel and others not. Some practitioners also consider the non-linear stress strain response of concrete as well as some aspects of time-dependent behavior either through creep or a loss in stiffness due to the effects of fatigue loading.

4.4 Effect of saturation on fatigue capacity

After demolding the first cast of concrete, a few cylindrical specimens were submerged and stored in a water tank to preserve the saturated condition for testing. Initially, three monotonic tests were performed on saturated PC specimens, to find the monotonic strength of the wet concrete. Because of the presence of water inside the concrete body, the pore water pressure was elevated by an increase in loading, so the monotonic strength of wet concrete was slightly less than that of dry concrete. The constant amplitude test on the saturated/wet PC cylinders was conducted with the load combination of (Smax, Smin) = (0.80, 0.05) at a frequency of 1 Hz. The results (number of cycles to failure) are listed in Table 25. This table, like Table 22, includes the previous test results with the same load combination on the dry PC specimens and the model predictions for the fatigue capacity. The last three columns show the ratio of the predicted/recorded number of cycles to failure to the predicted number of cycles to failure of three fatigue models of “Model Code 2010”, “DNVGL-ST-C502”, and “Eurocode 2”. These ratios show that the current fatigue models are not useful for predicting the fatigue lifetime of wet concrete. For instance, all of the test results are less than what Model Code 2010 predicted for this load combination. The DNVGL code considered the effect of the presence of water in the damage index by limiting the damage index to 0.33 (rather than 1).

Risk Management, Quality Assurance, Type and Project Certification, Insurance and Financing, & Operational Lifetime Assessment.

Table 25 Fatigue test results versus fatigue model predictions for saturated/wet and dry

Type	Name	N_f	N_f / N_{f_MC2010}	N_f / N_{f-DNV}	$N_f / N_{f-Eurocode2}$
Code	Model Code 2010	1489.5	1.0	4.4	1.9
	DNVGL-ST-C502	336.0	0.2	1.0	0.4
	Eurocode 2	779.5	0.5	2.3	1.0
Dry PC	PC-CAT#1-F1-80-5	2,860	1.9	8.5	3.7
	PC-CAT#2-F1-80-5	4,790	3.2	14.3	6.1
	PC-CAT#3-F1-80-5	2,875	1.9	8.6	3.7
	PC-CAT#4-F1-80-5	2,529	1.7	7.5	3.2
Wet PC	Wet-PC-CAT#1-F1-80-5	589	0.40	1.75	0.76
	Wet-PC-CAT#2-F1-80-5	772	0.52	2.30	0.99
	Wet-PC-CAT#3-F1-80-5	725	0.49	2.16	0.93
	Wet-PC-CAT#4-F1-80-5	813	0.55	2.42	1.04
	Wet-PC-CAT#5-F1-80-5	864	0.58	2.57	1.11
	Wet-PC-CAT#6-F1-80-5	682	0.46	2.03	0.87
	Wet-PC-CAT#7-F1-80-5	1,059	0.71	3.15	1.36

Naming guide: Plain Concrete (PC) – Constant amplitude test number 1 (CAT#1) – Frequency of loading (Hz) # (F1) – Smax percent % (80) - Smin percent % (5)

Figure 126 shows that wet PC test results have a very tight scatter compared to dry PC and RC. It also shows that the presence of water has a considerable effect on the fatigue behavior of concrete. In this specific load combination, the DNVGL code has the most conservative prediction compared to other fatigue models, and the wet concrete test results are still higher than its prediction.

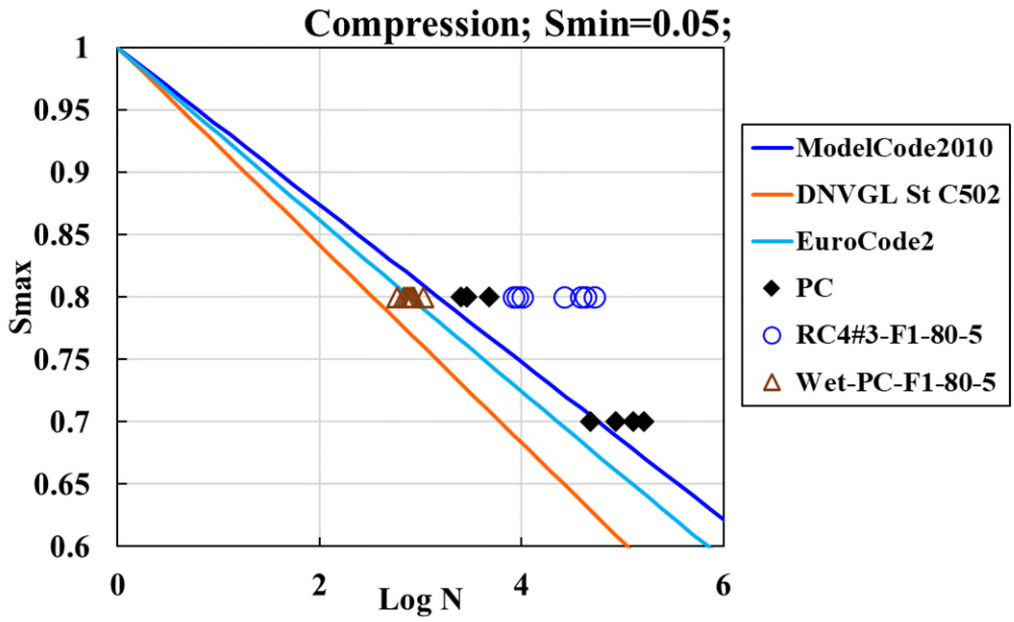

Figure 126 Fatigue test results for saturated/wet cylinders made of PC.

Current research indicates that the saturation level of concrete has a significant effect on its fatigue capacity. Studies have shown that saturated (or submerged) concrete specimens exhibit reduced fatigue capacity due to the presence of moisture, which affects the internal microstructure and accelerates material degradation under cyclic loading (see section for Saturation and presence of water, on page 58). This decrease can be attributed to factors such as increased pore water pressure and reduced interfacial bond strength, leading to earlier onset of fatigue cracking. As a result, accurate consideration of the environmental condition, such as water submergence, is crucial for determining the fatigue capacity of concrete, especially for offshore wind turbine foundations. A new environmental factor has even been proposed to account for these effects in design codes like those of the DNV and Model Code 2020 to ensure safer and more reliable fatigue predictions for concrete structures [59, 86, 117]. After taking the specimens out of water tank, a siren plastic wrap was used to keep the moisture from evaporating while performing the cyclic loading. The present results confirm the hypothesis mentioned

earlier in this paragraph about pore pressure buildup within saturated specimens, and the final fatigue capacity for wet specimens is about 3/4 of the fatigue capacity in the dry condition. (See Figure 127)

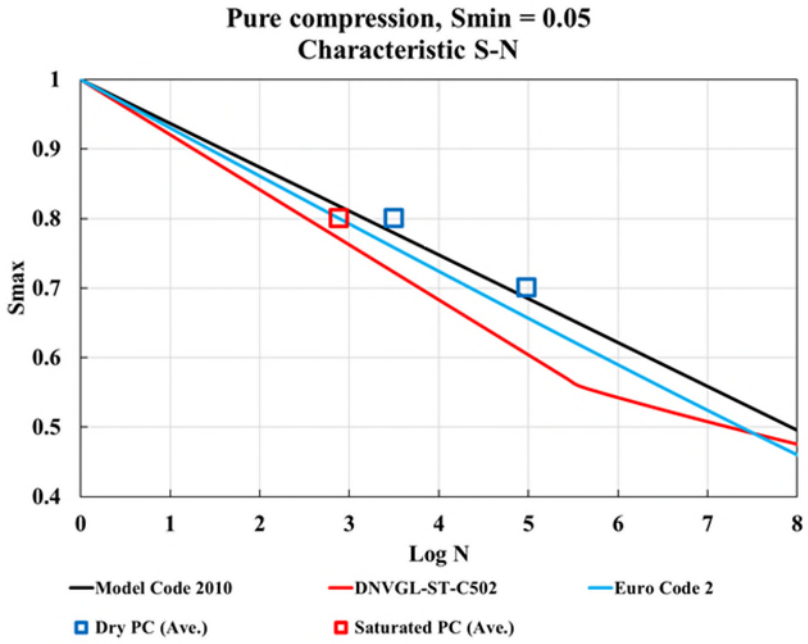

Figure 127 Effect of saturation on the final fatigue capacity.

Figure 128 includes the information that was requested from the participants for this part of the competition. The value of Smax = 0.80 and Smin = 0.05 in these tests, and the loading frequency is 1 Hz, which is the same as for the CATs on RC. Overall, it gives an overview of the minimum, average, and the maximum number of cycles to failure of the wet specimens under fatigue loading of (Smax, Smin) = (0.80, 0.05) and frequency of 1 Hz.

2. Constant Amplitude Tests (CATs) on Saturated Plain Concrete (PC)

Smax	Smin	Freq	Number of Cycles to Failure (Nf)		
(ratio)	(ratio)	(Hz)	Minimum	Average	Maximum
0.8	0.05	1	**589**	**786**	**1059**

Figure 128 Overview of the saturated/wet PC cylinders fatigue test results

4.5 Effect of load eccentricity on fatigue capacity

A series of fatigue tests were conducted under conditions where the loading was eccentric, resulting in compressive stress on one face being up to three times higher than on the opposing face. The results revealed that the fatigue capacity, when measured based on the maximum stress, was significantly higher than if the entire test cylinder had been uniformly subjected to that same stress level. This outcome is particularly promising for structural components exposed to bending and significant strain gradients. Figure 129 shows the setup and strain gradient expected in eccentric loading over a cross-section of the cylindrical sample. An example of the test that has been done and predicted fatigue capacity based on the S-N model of Model Code 2010 is presented in Figure 130.

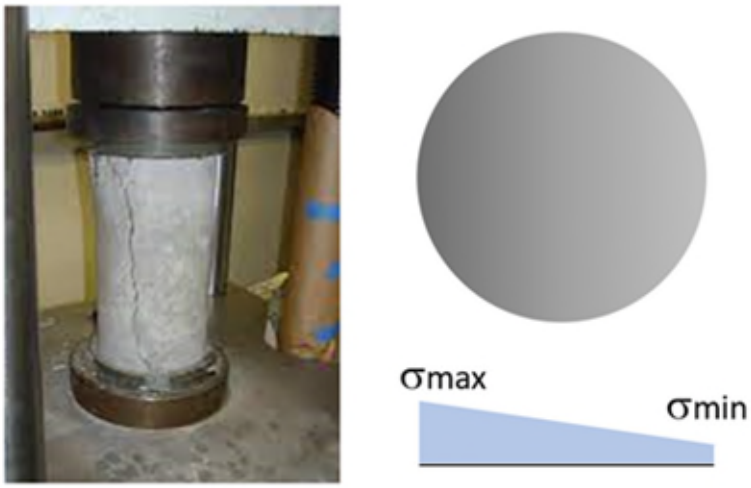

(a) Cylinder (b) Strain Gradient

Figure 129 The setup for eccentric loading.

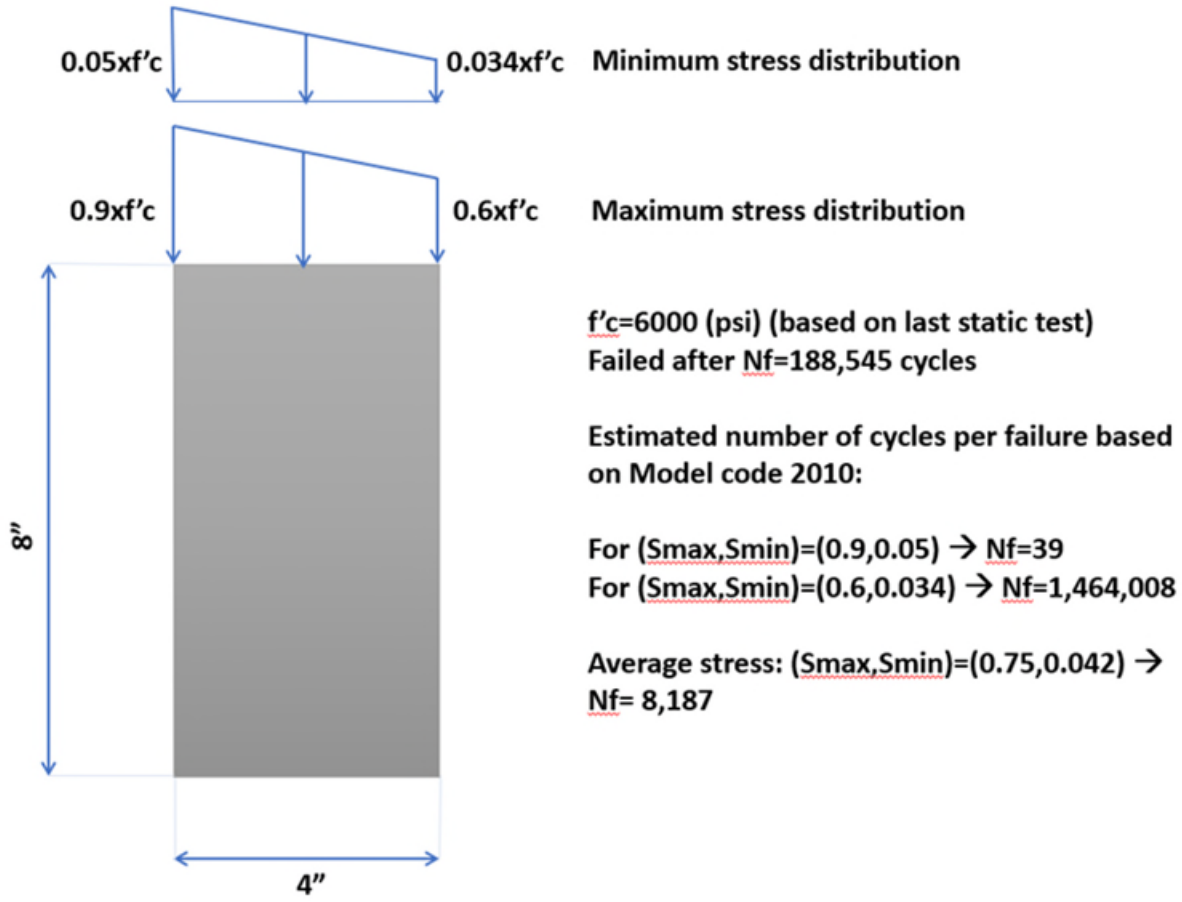

Figure 130 Example of eccentric loading effect on the fatigue capacity.

4.6 Variability in experimental test data and impact of f'c

The collected data is archived in an Excel sheet, where plots and tables have been established so that the results can be viewed in the context of existing data and its significance can be established. The results of the tests were used to evaluate, develop, and propose changes to fatigue standards and models. Figure 131 shows S-N models and the corresponding experimental data points for fatigue tests with varying stress levels for a small range of minimum stress levels, which highlights the large scatter in results. Due to lack of data provided about the concrete mix and loading protocol, it is not clear why there is huge scatter in the fatigue capacity. One significantly contributing factor to this scatter is variability in the concrete monotonic

compressive strength which has the effect that the actual loading ratios (Smax/Smin) were not the intended loading ratios.

4.6.1 Significance of concrete compressive strength in fatigue testing

Concrete fatigue testing involves the repeated loading of specimens to measure their durability. Small errors in estimating monotonic compressive strength, such as a 5% variation, can lead to large discrepancies in the predicted fatigue life. This variability is particularly consequential in fatigue tests, where the number of cycles to failure is sensitive to changes in material properties.

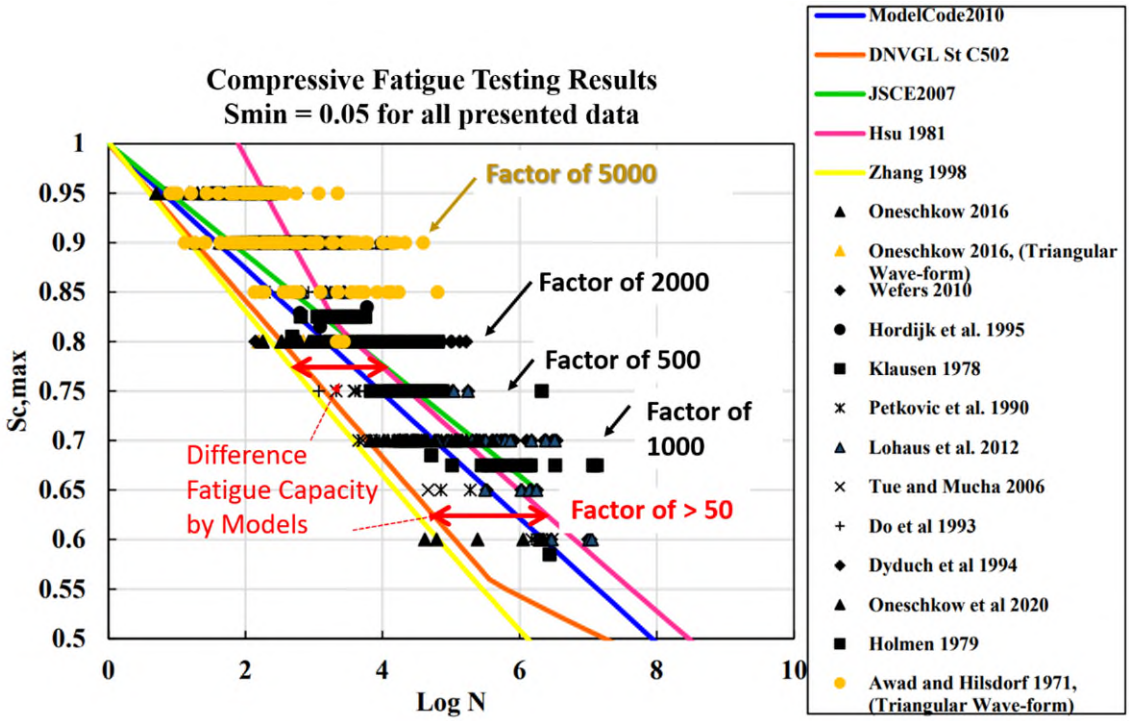

Figure 131 S-N models and experimental data points for a minimum stress level of 0.05. [21, 23, 32, 37, 39, 41, 51, 58, 59, 65, 78, 117-121]

Figure 131 illustrates the relationship between stress (S) and the number of cycles to failure (N_f). Different researchers, using varying assumptions for concrete monotonic compressive strength, produce significantly different predictions for fatigue life. This variability emphasizes the need for accurate strength estimation methods.

4.6.2 Impact — on fatigue capacity — of assumed strength error

Table 26 illustrates the effect of monotonic compressive strength variability, showing the sensitivity of predicted fatigue life to different assumed strengths. Even a 5% error in strength estimation can result in three to five-fold variation in predicted cycles to failure, highlighting the significant impact of small deviations. This underscores the importance of minimizing errors in strength estimation to achieve more reliable results in fatigue testing.

Table 26 Impact of assumed strength error on fatigue capacity using three different fatigue models

fcm	Smax	Smin	Number of cycles to failure (Nf)		
			Model Code 2010	DNV	Eurocode 2
fcm-5% (If strength was 5% lower)	0.84	0.21	1,797	269	386
fcm (Planned Smax=0.80)	0.80	0.20	10,208	1,000	1,711
fcm+5% (If strength was 5% higher)	0.76	0.19	54,996	3,594	7,582
fcm-5% (If strength was 5% lower)	0.63	0.21	33,572,059	417,112	2,208,912
fcm (Planned Smax=0.60)	0.60	0.20	104,199,038	1,000,000	7,220,567
fcm+5% (If strength was 5% higher)	0.57	0.19	322,815,611	2,805,597	23,602,833

4.7 Conclusion

I. **Monotonic compressive strength**: The monotonic compressive strength of concrete is a critical factor that influences the variability of fatigue test results. Errors in strength estimation, even as small as 5%, can lead to significant differences in predicted fatigue life. Ensuring accurate strength estimation is essential to reduce variability and improve the reliability of concrete fatigue testing.

II. **Strain evolution under fatigue loading**: When concrete is subjected to fatigue loading between two stress levels (S_{max} and S_{min}), the strain at the peak stress level and the valley stress level increases significantly with the number of loading cycles. Strains at Smax

increase more rapidly than those at Smin, resulting in a reduction in stiffness with an increasing number of cycles.

III. **Impact of load eccentricity**: Load eccentricity introduces additional variability in fatigue capacity. Specimens subjected to eccentric loading show reduced fatigue life compared to those under concentric loading.

IV. **Effect of saturation**: Saturated concrete has a significantly reduced fatigue capacity compared to dryer concrete, highlighting the importance of moisture content in design considerations.

V. **Variability (scatter) in fatigue capacity**: There is an exceptionally large scatter in the measured compressive fatigue capacity of concrete, up to three orders of magnitude, making it difficult to develop accurate models and set design standards.

VI. **Causes of variability (scatter)**: The measured scatter is due to many causes beyond just the inherent (or aleatory) uncertainty in the behavior of concrete in fatigue. These causes include variability in monotonic strengths of concrete specimens cast from the same batch, differences in loading frequency, differences in loading waveform, and differences in aggregate types.

VII. **Comparison of plain and reinforced concrete**: RC exhibits enhanced fatigue performance compared to PC due to the redistribution of stress from concrete to reinforcement, reducing stress demand on concrete as stiffness degrades. The presence of longitudinal reinforcing steel is expected to significantly affect fatigue capacity, as the reduction in concrete stiffness shifts the load from concrete to steel, decreasing stress demand on the concrete as the number of loading cycles increases.

VIII. **Correlation between visual damage and strain**: Visual damage progression correlates strongly with strain evolution. Visual damage can indicate the remaining fatigue life.

IX. **Challenges in availability and reporting of data**: Limited sharing of test data — especially industry-funded results — hampers model improvement. Public funding may be necessary to ensure broader access to high-quality test data. Many reports lack detailed data on strain evolution and other critical information, limiting the ability to refine models and standards effectively.

5 3D-Printed Concrete

3D-printed concrete (3DPC) has emerged as an important new type of concrete construction material gaining use across many applications, including as towers that support onshore wind turbines and potentially as foundations for supporting offshore wind turbines. The design of support structures for wind turbines differ from that for most civil infrastructure (e.g. buildings, bridges) in that it is frequently controlled by high-cycle fatigue demands from wind, wave, rotor rotation, and aerodynamic imbalances. While significant research has been done on 3DPC materials, [122, 123], the present study may be the first to examine the high-cycle compression fatigue characteristics of this material. In addition, a new fatigue loading protocol is presented, to reduce the apparent scatter in fatigue capacities.

5.1 Introduction

The relentless pursuit of renewable energy sources has led to the rapid expansion of wind energy technologies, with wind turbines emerging as prominent fixtures in the global energy landscape. As wind turbine structures continue to evolve to meet the demands of increasing power generation capacities and environmental challenges, the reliability and performance of these structures become paramount. Concrete, once primarily associated with traditional construction, has gained significant traction as a material of choice for the support structures of wind turbines, offering economic advantages and environmental sustainability benefits over more conventional steel. Wind towers made of concrete are proving to be more cost-effective, particularly at greater hub heights, which accommodate taller towers [124, 125].

The design and operation of wind turbine structures are subject to various mechanical forces, including cyclic loading induced by wind turbulence, which can lead to fatigue failure over time. Understanding the fatigue behavior of concrete under such conditions is crucial for ensuring the

structural integrity and longevity of wind turbine systems. Despite considerable advancements in concrete technology and structural design, gaps persist in our understanding of concrete fatigue characteristics, particularly concerning the unique loading conditions experienced by wind turbine structures. Offshore structures are subjected to high-cycle fatigue loading due to wind, wave, and operational loads of turbines [126, 127] over their design life (which is typically 25 years).

There is an emerging interest, in the construction industry, in 3DPC as an alternative to conventional cast concrete [128, 129]. Challenges related to time-dependent characteristics of cementitious materials [130], durability [131], integration of reinforcement [132, 133] and structural compliance [134, 135], have been explored at different size scales to allow for the production of innovative and high-quality structures for various specific applications, including concrete towers, fixed bottom GBFs, and gravity-based anchors of floating offshore structures that support wind turbines. Numerous experimental fatigue investigations and analytic studies have been conducted on concrete materials with different material compositions [21, 35, 50, 58, 65, 66, 95, 136, 137]. This paper focuses on 3DPC material, characterizing its fatigue behavior under compressive cyclic loads for the first time. The fatigue characteristics of 3D-printed materials are hypothesized to be affected by the printing layout and the holes/defects between the filaments inside the concrete material. Most work to-date has focused on fatigue life capacity (i.e. number of loading cycles to failure), with some data collected and reported on the behavior (i.e. developing strain behavior) under cyclic fatigue loading [20, 22, 23, 25, 26, 30, 86, 136]. Authors have contributed to some of the work that examines concrete fatigue behavior [25, 26, 138], including the effect of parameters that have not been given significant attention in earlier studies.

5.2 Research significance

This study produced new experimental data on the number of cycles to failure for 3DPC and comparisons of those data with several fatigue life prediction models for 3DPC and with experimental data on conventional concrete. An improved estimated strength method was used to define the experimental fatigue load and reduce the scatter of the final fatigue capacity results, for the first time. The study also delves into the stress-strain and stiffness characteristics of 3DPC under fatigue loading conditions, contributing to a deeper understanding of its behavior.

5.3 Experimental investigation

5.3.1 Materials and specimens

5.3.1.1 Material development

Mortar mixtures for the 3D-printed specimens used in this study consisted of combinations of supplementary cementitious materials (SCMs) for high replacement (40%) of ordinary Portland cement (OPC) and fly ash, silica fume and limestone filler [130]. An iterative process was used to define the proper combination of these materials, to identify the appropriate fresh-state properties for 3D-printing. Material **M13** — consisting of 60% OPC, 20% fly ash class C, 10% silica fume, and 10% limestone filler — was designed based on the results of flow table tests, isothermal calorimetry and compressive strength of mortar cubes. The water-to-cementitious material (w/cm) ratio was set at 0.36. Chemical admixtures including a high-range water-reducer admixture (Master Glenium 7700) and a viscosity modifying admixture (Master Matrix 362), with a dosage of 0.15% and 0.05% by weight of cementitious material, were used to adjust the consistency of the mixture for successful printability.

5.3.1.2 Preliminary durability assessment

Two major durability tests were performed on M13 specimens to determine the durability properties of different printing configurations: Rapid chloride penetration tests and absorption of water. A lower overlap of adjacent filaments increased the porosity of specimens and susceptibility to the ingress of chlorides or water. Configurations with moderate overlap levels (i.e., 26% and 60%) showed comparable performance to cast specimens in charge passed (100-1000 Coulombs) and absorption tests (1.0-2.0 mm). These results indicate that control over the filament interfaces of 3D-printed elements could enhance the durability and mechanical properties of 3D-printed specimens [130].

5.3.1.3 Printing process

A 6-axis robotic arm with a nozzle opening of about 1 in (25-mm) was used to produce 3D-printed solid blocks with dimensions of 36 in (914.4 mm) x 15 in (381 mm) x 10 in (254 mm). The filament height was set to slightly higher than 3/8 in (10 mm), and the nominal filament width for the toolpath was set to about 1 in (25 mm). The selected printing path consisted of the alternation of perpendicular layers, to minimize the anisotropy of the overall 3D-printed element during mechanical testing, ensuring that the interfaces of the filaments were not aligned between consecutive layers (see Figure 1). The 3D-printed filaments had a cross-sectional area of 1in (25.4 mm) in width by 3/8 in (9.525 mm) in height. The filament was extruded at a continuous speed of 200 mm/s.

Figure 132 3D-printed beam (left) and the coring procedure for production of cylindrical specimens (right).

5.3.1.4 Coring procedure

To obtain cored cylindrical specimens with dimensions 4 in (101.6 mm) x 8 in (203 mm) for fatigue testing, the 3D-printed blocks were cured for seven days by covering them with a plastic sheet, and water was continuously applied on their surface to avoid excessive evaporation. After seven days, the samples were extracted from the block using the sequence illustrated in Figure 132. For this purpose, a concrete core-drill was used with a continuous supply of water, to avoid damage to the equipment and to the concrete specimens.

5.3.1.5 Compressive strength

Mechanical testing revealed that 3D-printed samples showed a reduction in compressive strength of about 38% with respect to specimens cast with the same material. Further investigation is needed to determine the effects of the processing or material processing during the different stages of the printing process.

Table 27 shows the monotonic test results for these specimens. The variation was high compared to what has been seen to-date for the cylinders made of casted concrete. The main reason for that

can be the variety in spread of voids between concrete print passes (filaments) [122]. Figure 134 shows the stress versus strain and the high variation of the monotonic test results for 3DPC.

Figure 133 3DPC cylinders.

Table 27 Monotonic test results for 3DPC

Test No.	Load (lb)	Stress (psi)	Strain
3D-PC#1	78127	6217	0.00290
3D-PC#2	74608	5937	0.00276
3D-PC#3	85869	6833	0.00300
3D-PC#4	96095	7647	0.00334
3D-PC#5	92798	7385	0.00313
3D-PC#11	108989	8675	0.00363
3D-PC#20	105152	8368	0.00351
Avg.	85499	6804	0.00302
Standard Deviation	9201	732	0.00022
Std.Dev./Avg.	11%	11%	7%

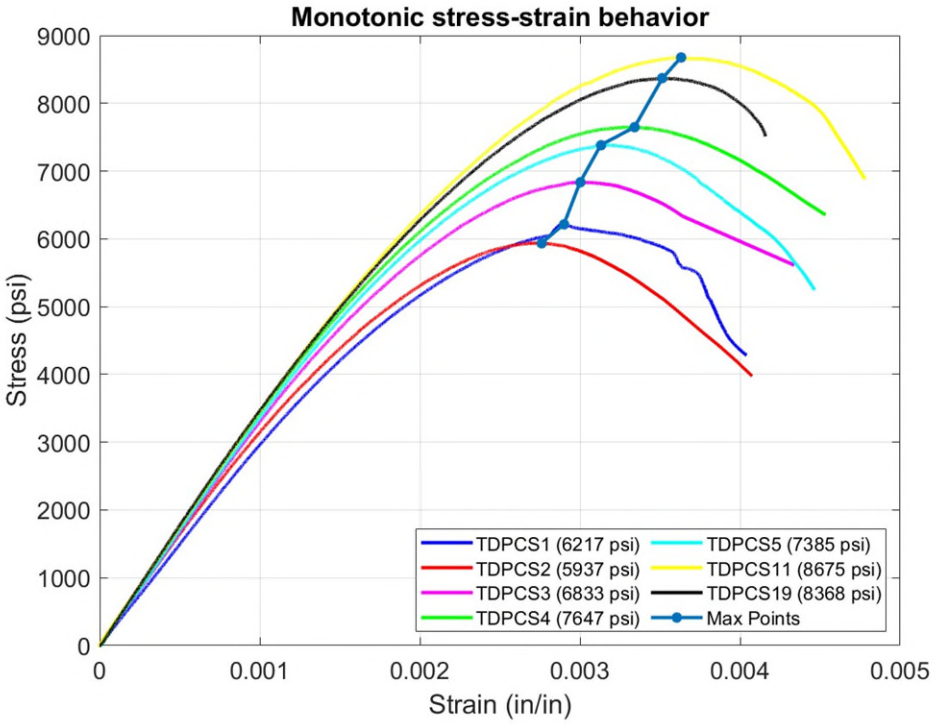

Figure 134 Monotonic test results for 3DPC.

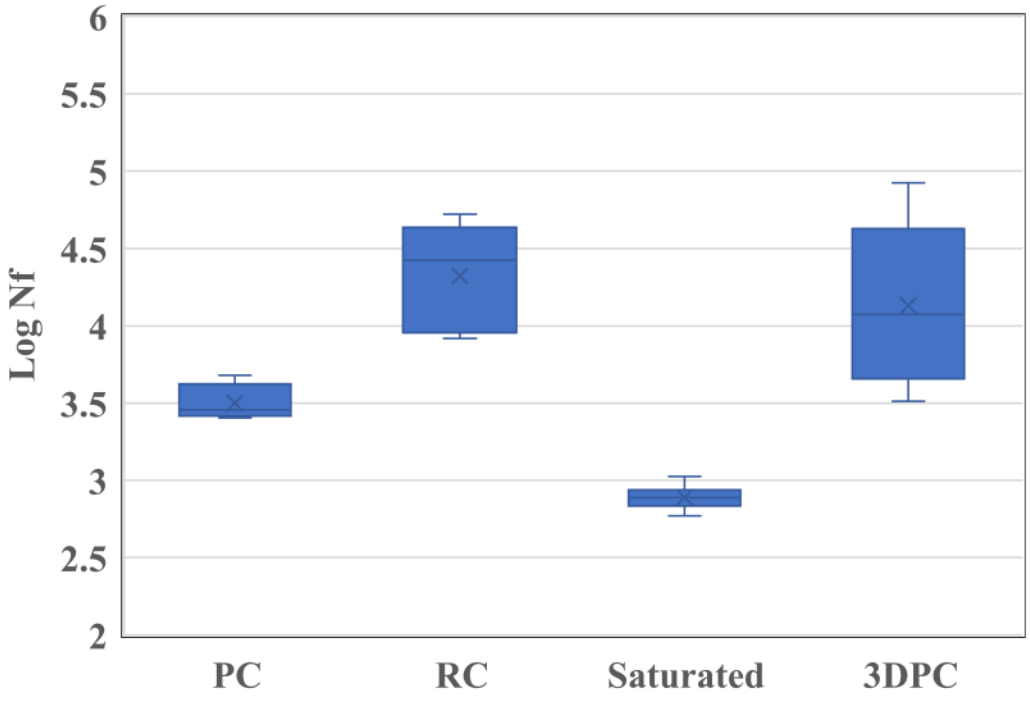

Figure 135 Fatigue test results variation based on the test type (PC; plain concrete, RC; Reinforced concrete, 3DPC; 3D print concrete).

5.4 Experimental results, analysis and discussion

5.4.1 Monotonic test results

The average compressive strength of 3DPC cylinders at 28 days was 5300 psi (36.5 MPa). Seven monotonic tests were conducted following ASTM C39's loading protocol on the 3DPC cylinders right before the start of the fatigue testing program. The average speed of loading was 31-34 psi/sec (0.21-0.23 MPa/sec). 3DPC cylinders varied considerably in strength (5900-8700 psi or 40.5-60 MPa). The coefficient of variation was about 11%, which is high relative to that for cylinders made of casted concrete (see Figure 134 & Table 27). That variation may be due to holes and empty spaces between the filaments of the printed concrete layers, which can vary by size and amount because of printing speed, layout, and other factors still not well understood. [122, 123, 130].

5.4.2 Fatigue test results

5.4.2.1 Capacity

The fatigue load combination of (S_{max}, S_{min}, Frequency) = (0.80, 0.05, 1 Hz) was selected for most of the fatigue tests for three reasons: (1) optimum operational range of the machine; (2) time needed to do the tests; and (3) comparability to other test results. In order to fully understand the fatigue behavior of a specific material, more combinations of (Smax, Smin, and Frequency) would need to be studied. Improved strength estimate method, defined in "Test Setup" section, was used to get an improved estimate of the strength of the cylinders. Then by using the cross-sectional area of the cylinders, and the load combination for fatigue testing of each cylinder was determined.

Most of the tests were carried out up to failure by imposing uniaxial compressive cyclic load of constant amplitude (i.e. one value of S_{max} and S_{min} per test) using a sinusoidal waveform with a predefined frequency of 1 Hz. Two tests were shut down before failure due to technical difficulties in the electricity-related laboratory facilities. The fatigue capacity (Number of cycles to failure; N_f, also called fatigue capacity) is presented in Table 28. Figure 136 shows the average fatigue capacity of the 3DPC compared with plain concretes and also to the three selected characteristic S-N (Stress ratio -number of cycles) curves. In this plot, the maximum nominal stress level (S_{max}) is presented on the vertical axis, and the logarithm of the number of cycles to failure, $\log_{10}$ (N_f), is shown on the horizontal axis. This plot shows on average that the 3DPC N_f values were usually much larger than that given estimation of fatigue life by selected models, and 3DPC can have at least the same fatigue capacity as ordinary casts of similar monotonic strength.

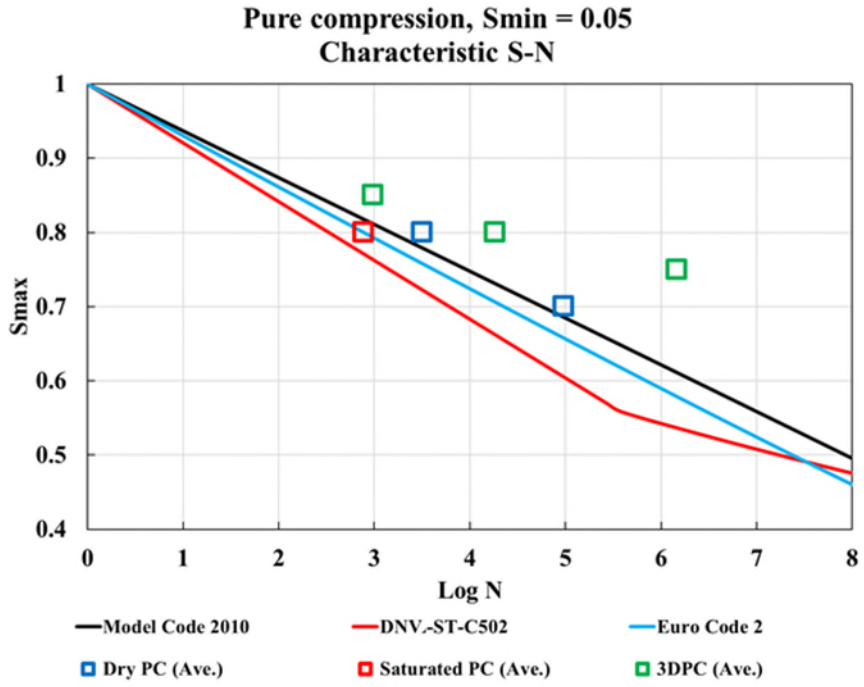

Figure 136 Average fatigue capacity of 3DPC material compared to plain concrete (dry and saturated), and S-N models (EuroCode2, DNV-ST-C502, Model Code 2010).

Figure 137 shows the actual fatigue capacity ($\log_{10} N_f$) compared to the S-N curves. The main observation is that the variation in fatigue capacity is still high, even when the improved strength estimation method, ISEM, is used. This may be because of the location of the holes between filaments, which can affect the rate of microcrack development. This is discussed further in the next section.

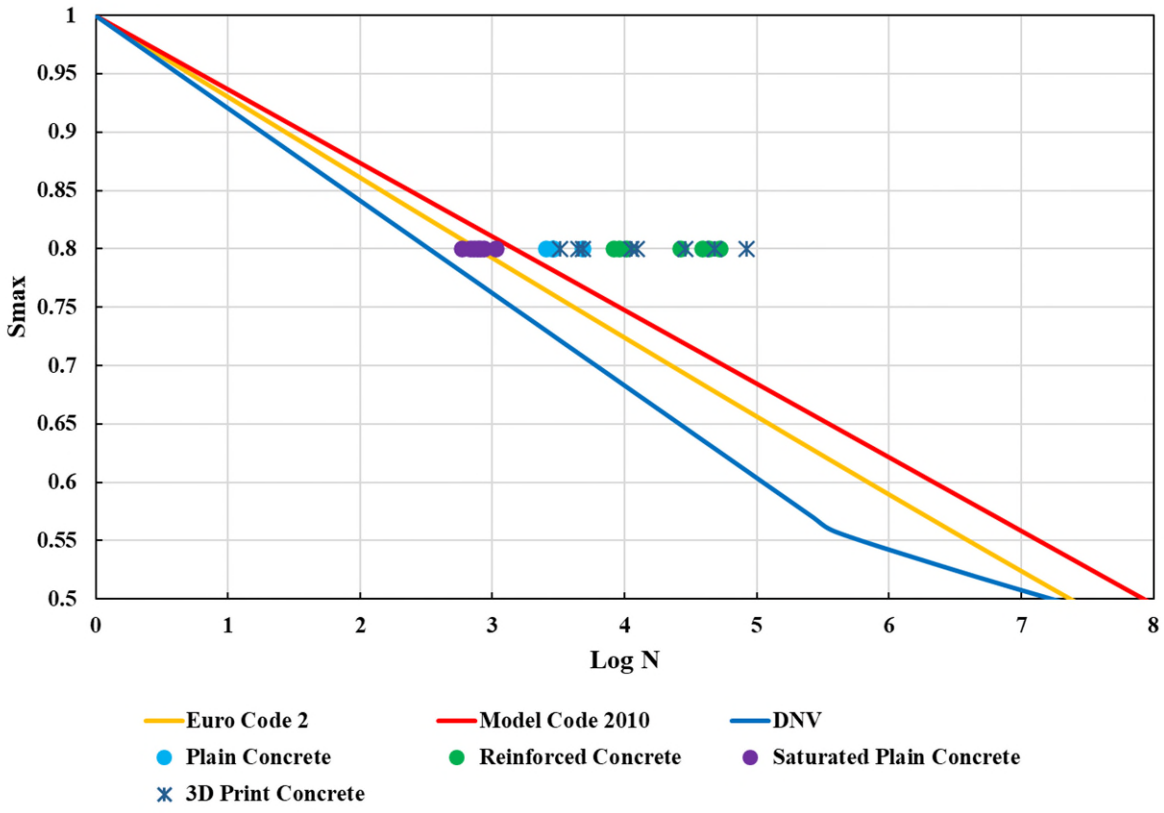

Figure 137 S-N plot (models compared to test results).

Table 28 Fatigue test results for 3DPC specimens

Test Name	Number of cycles to failure
3DPC6-CAT#1-P80-V5-F1	11,233
3DPC9-CAT#2-P80-V5-F1	12,444
3DPC13-CAT#3-P80-V5-F1	48,205
3DPC15-CAT#4-P80-V5-F1	4,448
3DPC10-CAT#5-P80-V5-F1	3,250
3DPC14-CAT#6-P80-V5-F1	4,854
3DPC16-CAT#7-P80-V5-F1	84,165
3DPC7-CAT#8-P80-V5-F1	28,867
3DPC8-CAT#9-P80-V5-F1	26,789
3DPC12-CAT#10-P80-V5-F1	135,414
3DPC19-CAT#13-P75-V5-F1	1,466,691
3DPC22-CAT#15-P85-V5-F1	1,176
3DPC23-CAT#16-P85-V5-F1	797

Naming guide: 3DPC # – Constant amplitude test number 1 (CAT#1) – Frequency of loading (Hz) # (F1) – Peak or S_{max} percent % (P80) – Valley or S_{min} percent % (V5)

5.4.2.2 Strain evolution

The strain progress due to cyclic loading fatigue was captured by two extensometers mounted on opposite sides of the cylinder. Data were acquired at a rate of 2000 Hz and then down-sampled to 25 Hz and logged in a text file. Two high-resolution cameras were used to capture images, from both sides of the cylinder, at predefined time intervals, to show the progress of the cracks and failure along with the measured data. The peak and valley strains are the uniaxial strain related to the maximum and minimum uniaxial compressive load imposed on the test specimen. Strain progression is plotted against the number of cycles (or the normalized number of cycles) in a strain evolution plot (see Figure 138, right side). Figure 138 shows the results of one of the fatigue tests (Test #9 or 3DPC8-CAT#9-P80-V5-F1) in two plots. On the left side, the monotonic stress-strain response of concrete with the same strength (3D-PC#3) is plotted along with a few down-sampled fatigue hysteresis curves (in green). The secant stiffness lines for those hysteresis curves, which are plotted (in blue), are drawn by connecting the maximum and minimum stress-strain points (σ_{max}, ε_{max}) and (σ_{min}, ε_{min}). The test failed when the last loading cycle crossed the descending branch of the monotonic test result. This behavior is typical [24-27]. The peak and valley strain evolution plots are shown on the right side of Figure 8. The strain evolution plot has a S-inverted shape. There are three distinctive phases of strain development in 3DPC as in other concrete materials. *Phase I* has a rapid strain accumulation due to the closing of the holes and pore spaces inside the material and usually continues up to about $0.2*N_f$. *Phase II* has a steady, linear strain accumulation. In *Phase II*, microcracks continue to progress. *Phase III* starts at about $0.8*N_f$ and shows a rapid strain increase due to cyclic loading. The S-inverted behavior is normally concluded to be due to the merging of microcracks and initiation of macrocracks and failure zones [23, 25, 26].

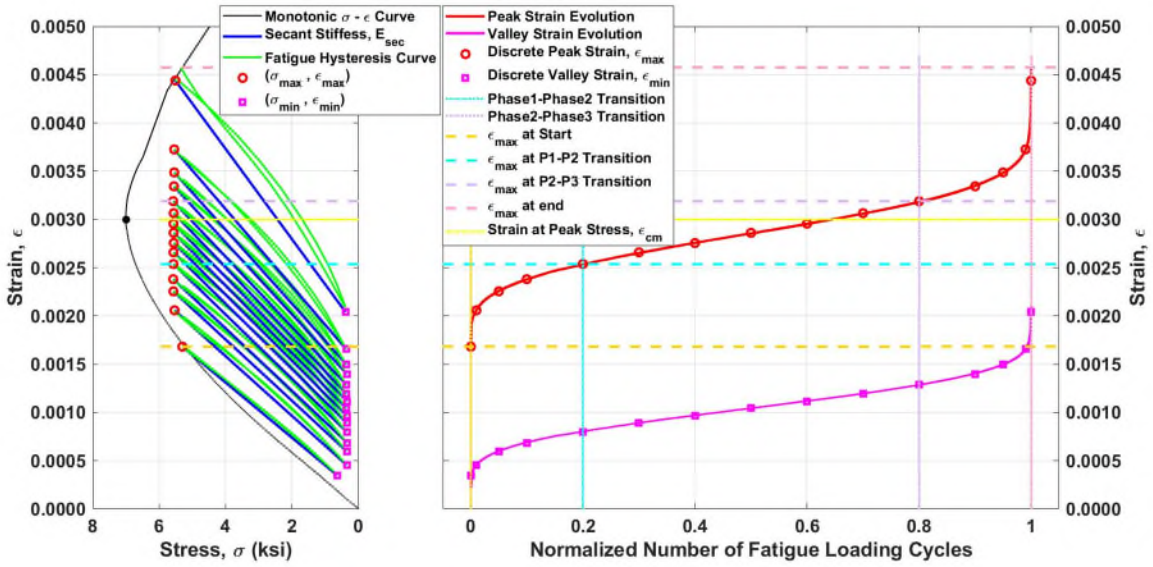

Figure 138 Combined fatigue test results of 3DPC; left side) Stress-strain response of cylinder to monotonic compressive loading, along with a few cycles of hysteresis and peak and valley stress and strain development over the cycles. Right side) The strain evolution plot shows peak and valley strain increments over the cycles of loading up to failure.

The photos taken by the two cameras from the cylinder during the constant amplitude test are shown in Figure 139. The goal was to capture visual crack initiation and progression during the fatigue test. The 3DPC showed a brittle behavior compared to casted concrete tested at Tufts University. Brittle behavior was expected for 3DPC, since that material has very small aggregate sizes (for printability and strength). Visual cracks did not appear until the very end of the test. Figure 139 shows that concrete stayed in contact on the surface up to at least 90% of the number of cycles to failure inside *phase III*, and rapid strain accumulations were observed.

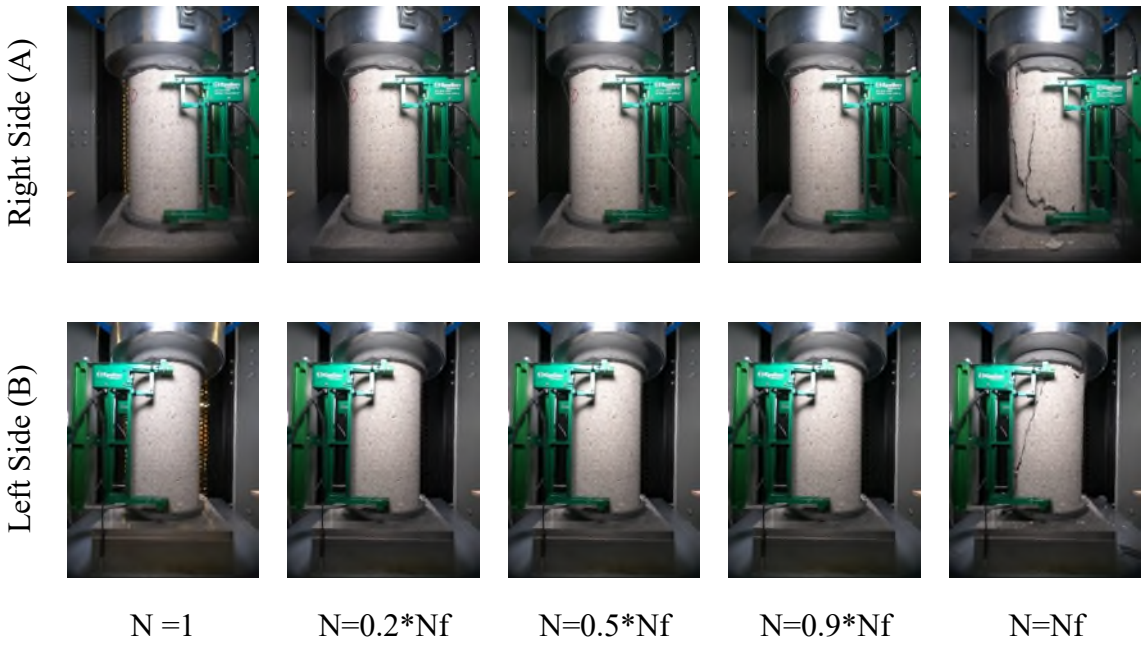

Figure 139 Photos of two sides of the concrete cylinder at certain points during the test (Test #9).

Figure 140 shows the average peak strain along with the individual strain development on both sides of the cylinder. There was a pretty uniform strain behavior around the perimeter of the cylinder, and the side strains started to deviate from each other at around half of the way to failure, but the amount of difference in strain between the two sides is not very high compared to other types of concrete. This may be because of the uniformity and homogeneity of 3DPC and the material's very small aggregate sizes and stronger cement paste which can delay initiation of microcracks and progression until the very end of the test (*phase III*). This is another indication of brittle behavior, indicating the need for additional safety considerations in design.

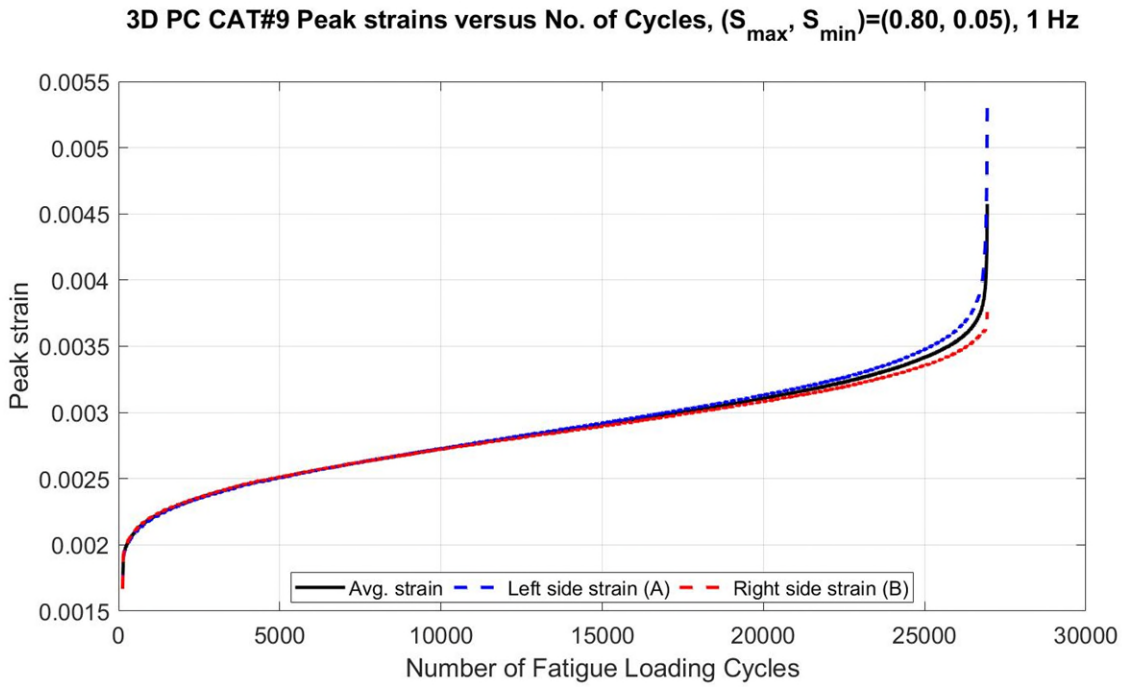

Figure 140 Peak strain recorded on both sides of the concrete cylinder across the testing cycles.

Peak strain evolution for all tests is plotted in Figure 142. Figure 143 shows the normalized strain evolution plot. On the vertical and horizontal axes, respectively, the average measured peak strain is normalized to the initial strain and the number of cycles is normalized to failure. Figure 143 shows that the specimens with very close N_f also have almost the same normalized strain evolution plot, meaning that the normalized strain slope directly correlates to the number of cycles to failure, a pattern noticed previously [20, 23-25].

The peak strains at the final cycles for all the failed specimens are depicted along with normalized monotonic stress-strain response in Figure 144 which shows that the last cycle intersects with the descending branch of the monotonic stress-strain response of concrete to uniaxial compressive loading. Since there was a high variation in monotonic responses, variation in pre-failure peak strain related to fatigue loading is also expected.

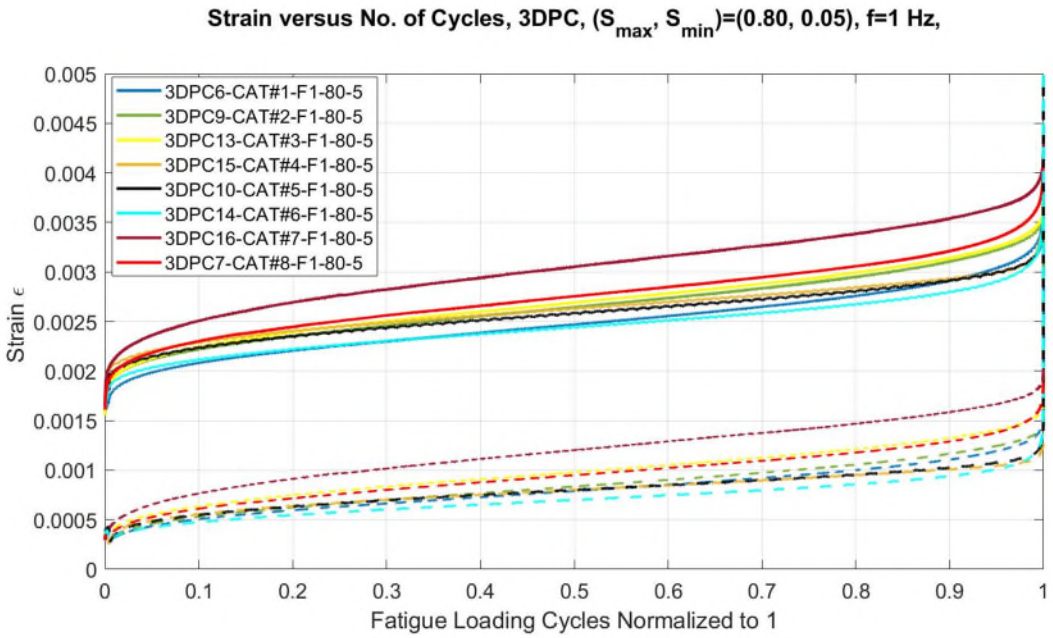

Figure 141 Strain evolution of 3DPC (peak and valley strain vs. normalized number of cycles to failure); Peak solid lines; Valley dashed lines.

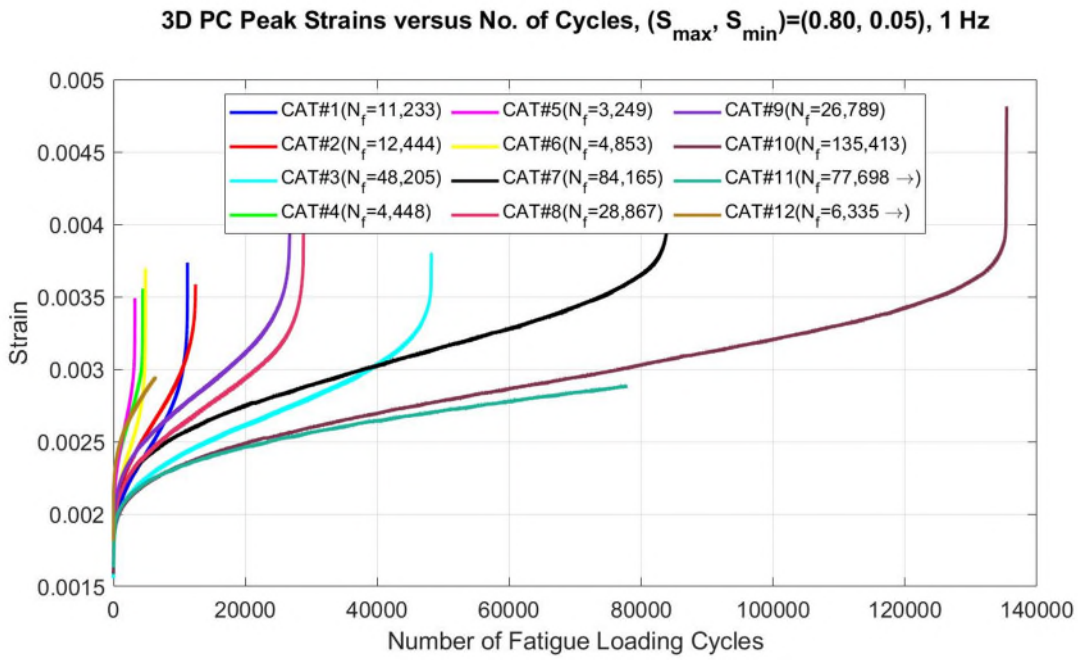

Figure 142 Peak strain evolution for (Smax, Smin)=(0.80, 0.05).

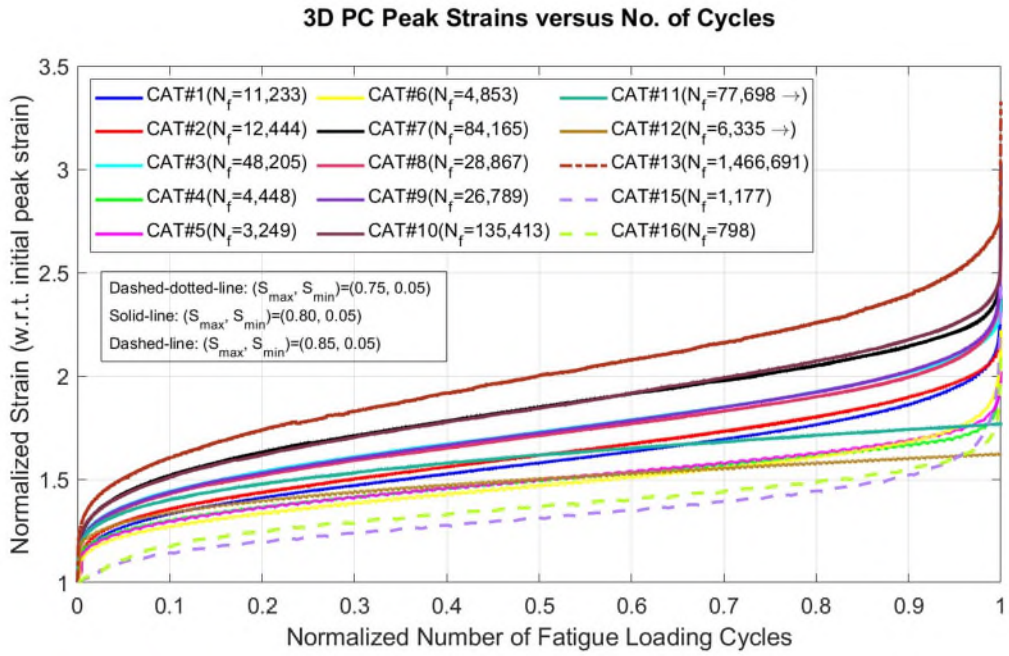

Figure 143 Normalized peak strain evolution plot

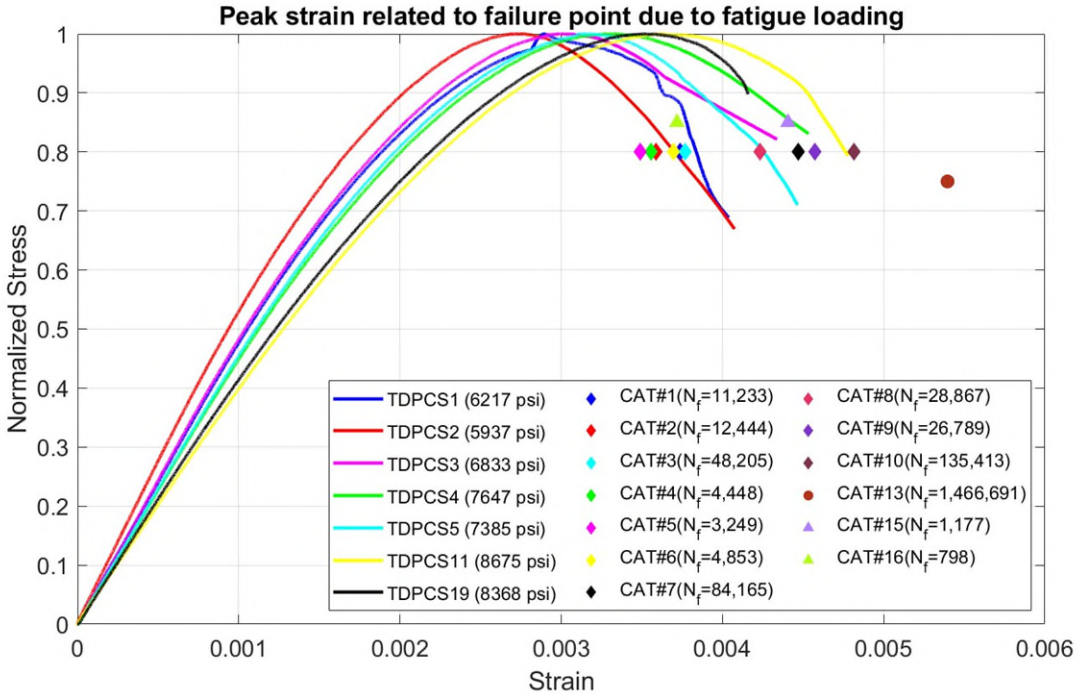

Figure 144 Final peak strain due to fatigue loading versus normalized stress-strain monotonic results.

5.4.2.3 Secant stiffness

The secant stiffness was calculated for each loading cycle using peak and valley stress-strain data points (see *Equation 1*). The secant stiffness at the start and end of each fatigue test versus the log of N_f are shown in Figure 145. Secant stiffness is always lower at the end than at the start, showing the degradation of concrete stiffness due to the fatigue loading. This degradation does not correlate with N_f. The trend lines are shown for the secant stiffness of start and end. There is no considerable trend associated with N_f, . The variation in start and end secant stiffness can be due to normal variations in concrete material mechanical characteristics. The difference between trend lines increases with increased N_f, , meaning that the higher number of cycles to failure has higher stiffness degradation. Since the N_f has strong connections with the loading combination (S_{max}, S_{min}), thus, the stiffness degradation correlates with the loading combination, with lower loading ratios having higher N_f, and greater stiffness degradation.

$$E_{sec} = \left(\frac{\sigma_{max} - \sigma_{min}}{\varepsilon_{max} - \varepsilon_{min}}\right) \qquad \text{Equation 3}$$

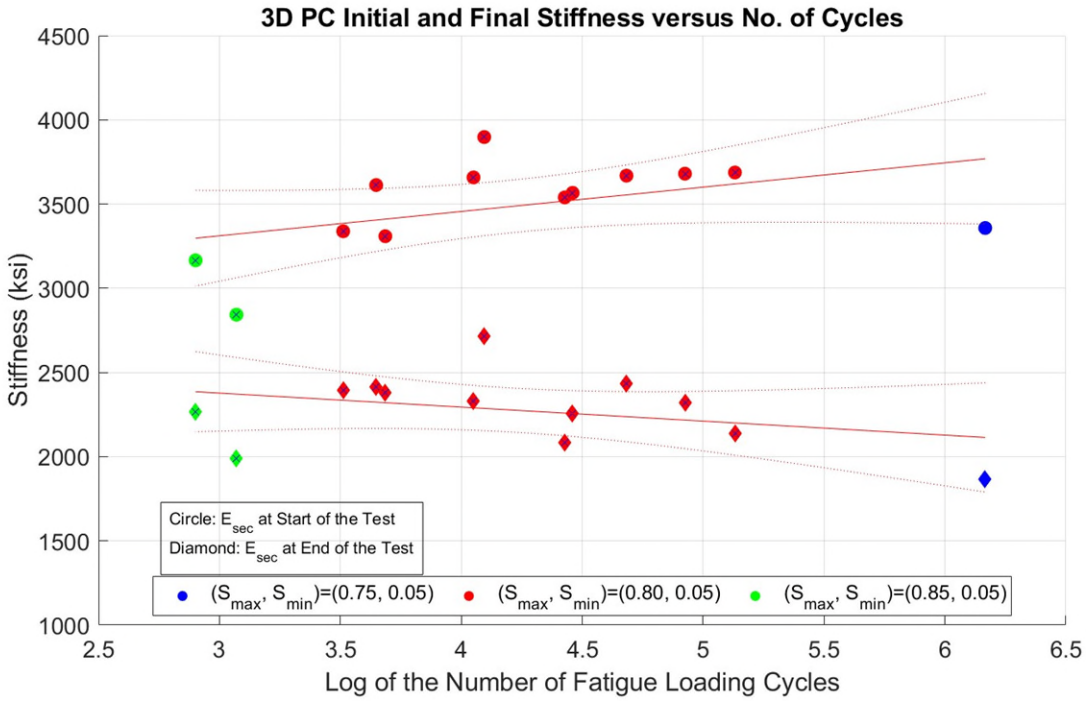

Figure 145 Initial and final stiffness versus the logarithm of the number of cycles to failure.

5.4.2.4 Visual cracks

The approximate number of cycles associated with the first visual crack appearance was calculated for all the tests using the photos of the test specimens that were taken at pre-defined time intervals. Peak strains at those number of cycles were plotted against the maximum stress level along with the normalized monotonic stress-strain response. Some points intersect some of the descending parts of stress-strain curves, indicating brittle behavior. This observation is consistent with the observations from the photos of the test specimen during the test and with the deviation of measured strain between the two sides of the specimen at the very end of the tests.

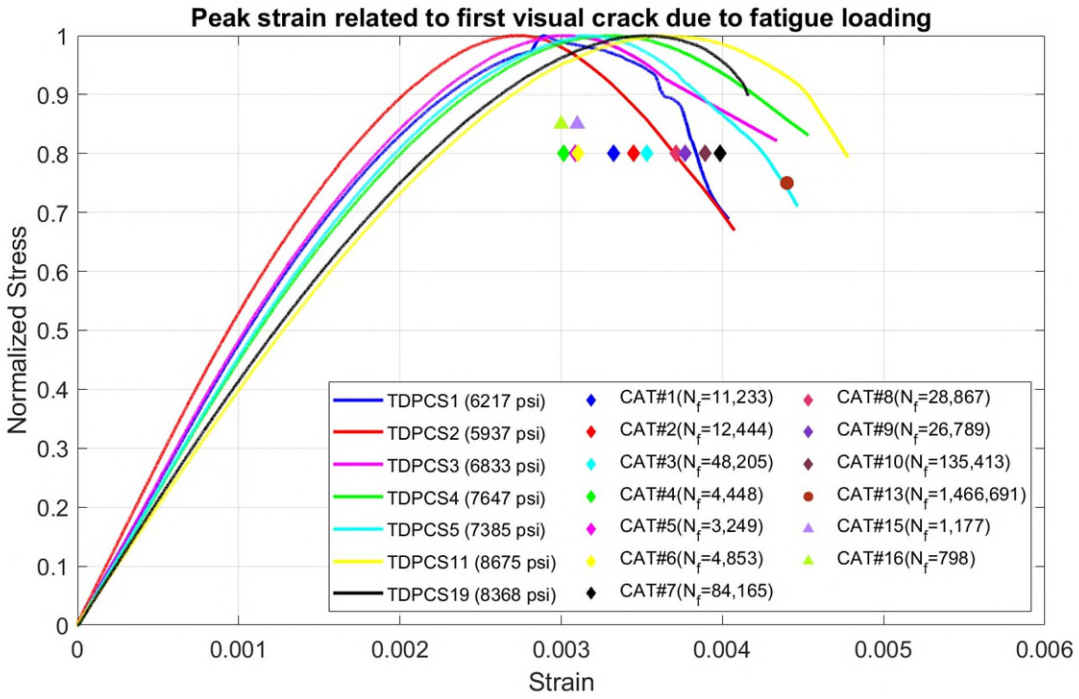

Figure 146 Peak strain related to the first visual crack appearance on the concrete cylinders final due to fatigue loading versus normalized stress-strain monotonic results.

5.4.2.5 Fatigue capacity prediction using strain and stiffness gradients

The correlation between the gradient of strains or stiffness in *phase II* (which is fairly constant) and N_f as has been reported in the literature [23, 25, 26, 86]. To examine the applicability of this theory to the 3DPC material, the number of cycles to failure was used to down-sample the fatigue test results to 23 equally-distanced points. Figure 147-a shows the down-sampled peak strain evolution plotted against the normalized N_f. Figure 147-b shows the gradient of peak strain, which can be assumed to be constant in *phase II*. Figure 147-c shows the zoomed-in version of the gradient peak strain versus the Normalized N_f. The average of the middle 13 gradient values (excluding the five initial and five final points) is considered the representative gradient peak strain of the test specimen. The same process was done for gradient valley strain and stiffness.

Figure 148, Figure 149 & Figure 150, respectively, show the correlation of gradient peak strain, gradient valley strain, and gradient stiffness to the power of two against the normalized N_f. This correlation is linear for these two parameters' logarithm (base 10). The gradient stiffness to the power of two was used because the stiffness gradient is negative, and having a logarithm of a negative value is undefined. The corresponding linear regression equations and their associated coefficients of correlation (R^2) are provided in the plots. The parameters were highly correlated, with the lower the gradient having the higher the number of cycles to failure. These correlations can be used to estimate the minimum number of cycles to failure of the tests that got stopped around mid-life. The gradient of strains and stiffness can be used to predict the remaining fatigue life (by finding N_f and subtracting the number of cycles the run-out tests had experienced). Using these three correlations, the failure number of cycles (fatigue life) for all fatigue tests (including two cut-out compressive fatigue tests) were estimated, and the average, minimum and maximum N_f are listed in Table 29. The results have low error values for the failed tests, showing the method's reliability.

Table 29 Predicted fatigue capacity based on correlations of gradient strains and stiffness

Test Name	Nf	Predicted	Avg. Nf Predicted	Delta/Error %
3DPC6-CAT#1-P80-V5-F1	11,233	8,514-10,790	9,963	11%
3DPC9-CAT#2-P80-V5-F1	12,444	8,803-11,482	10,409	16%
3DPC13-CAT#3-P80-V5-F1	48,205	33,395-49,132	43,385	10%
3DPC15-CAT#4-P80-V5-F1	4,448	4,438-5,224	4,873	10%
3DPC10-CAT#5-P80-V5-F1	3,249	2,665-3,530	3,213	1%
3DPC14-CAT#6-P80-V5-F1	4,853	4,084-5,651	4,942	2%
3DPC16-CAT#7-P80-V5-F1	84,165	48,250-77,668	67,118	20%
3DPC7-CAT#8-P80-V5-F1	28,867	21,767-27,748	25,499	12%
3DPC8-CAT#9-P80-V5-F1	26,789	22,258-24,276	23,363	13%
3DPC12-CAT#10-P80-V5-F1	135,413	103,816-129,159	118,663	12%
3DPC19-CAT#13-P75-V5-F1	1,466,691	1,146,425-1,614,836	139,7695	5%
3DPC22-CAT#15-P85-V5-F1	1,176	1,278-1,086	1131	4%
3DPC23-CAT#16-P85-V5-F1	797	713-755	750	6%
3DPC17-CAT#11-P80-V5-F1	77,698 *	184,659 – 200,000	192329.5	-
3DPC18-CAT#12-P80-V5-F1	6,335 *	12,356 – 12,717	12536.5	-

***** Runout tests

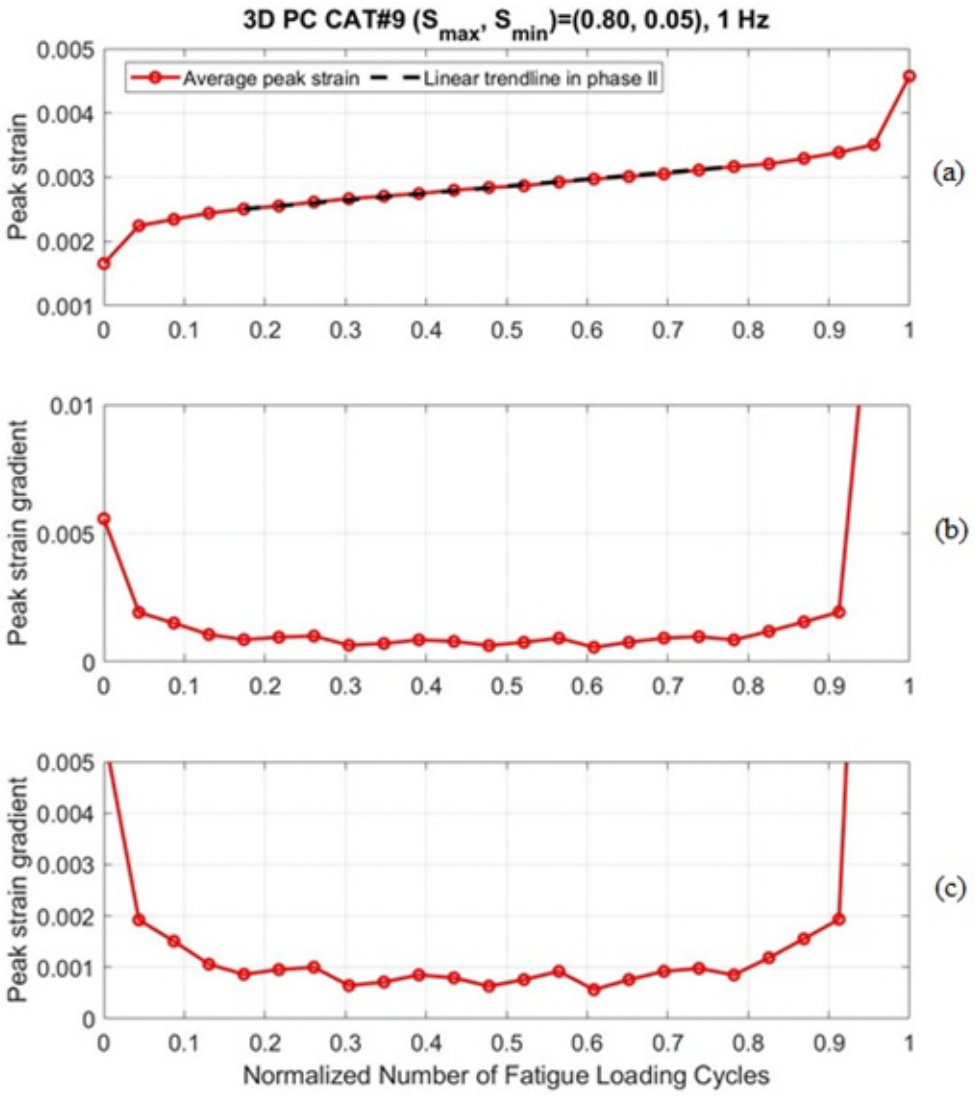

Figure 147 Down-sampled peak strain (Test #9); a) Peak strain evolution plot, b) the gradient of peak strain, c) Zoomed-in gradient of peak strain.

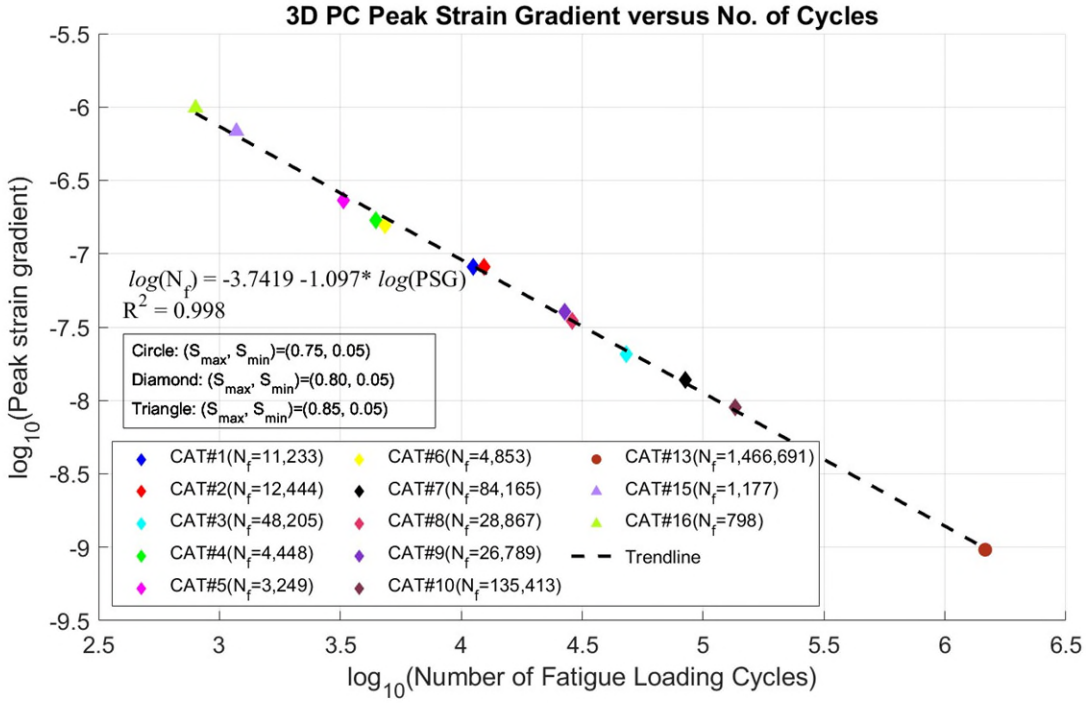

Figure 148 Correlation between the number of cycles to failure and peak strain gradient.

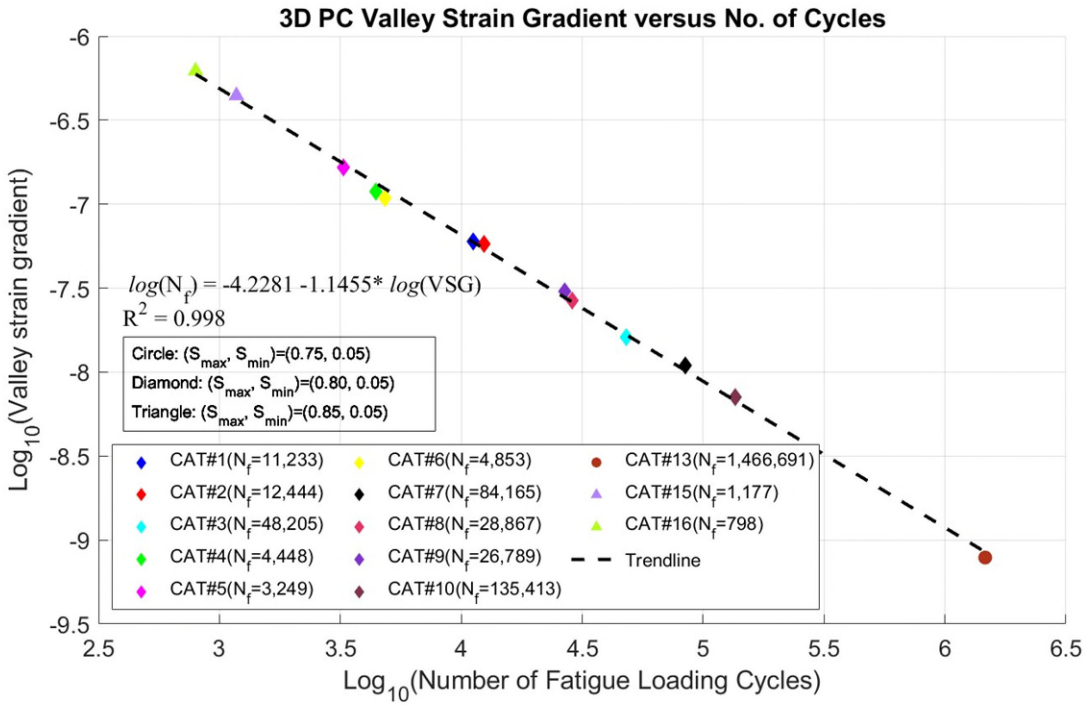

Figure 149 Correlation between the number of cycles to failure and valley strain gradient.

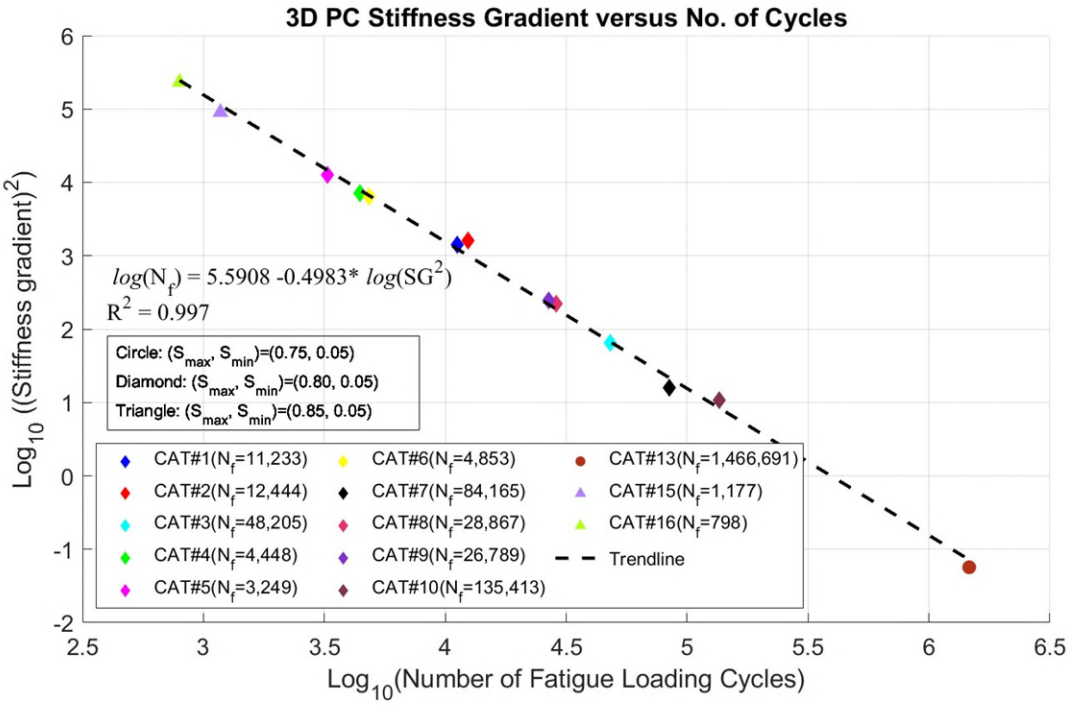

Figure 150 Correlation between the number of cycles to failure and stiffness gradient.

5.5 Conclusions

The fatigue characteristics of 3DPC were investigated through uniaxial compressive cyclic experimental tests. A new, improved strength estimation method for predefining the fatigue load protocol more accurately, ISEM, has been used to reduce the effect of strength variation on the test outcome. Below is a summary of the key takeaways from the experiments and analysis.

I. **Fatigue capacity of 3D-printed concrete**:

3DPC exhibited a higher average fatigue capacity compared to conventional cast-in-place concrete of similar strength, with results exceeding predictions from established models such as EuroCode2, DNV-ST-C502, and Model Code 2010. The experimental results of the constant amplitude compressive fatigue tests show a promising outcome. The average fatigue capacity of

the 3DPC is greater than that estimated by the three selected standard fatigue models. 3DPC behaves similar to normally casted concrete, but the variation in the results is high. This variation is expected in fatigue tests for the 3DPC because of the different locations of the holes and pores among the filaments which can affect the progress of microcracks.

II. **Impact of microstructure**:

The fatigue behavior of 3DPC is influenced by its unique microstructure. The distribution of voids and pores between filaments contributes to the high variability in test results and affects the initiation and propagation of microcracks in 3DPC under cyclic loading.

III. **Strain evolution and stiffness degradation**:

Strain evolution followed a three-phase pattern with an inverted S-shape, while stiffness degradation showed an upright S-shape. These behaviors align with observations of traditional concrete. The progress of peak and valley strain and degradation of secant stiffness due to cyclic loading were studied. The results showed the three distinct phases of strain development and stiffness degradation that are typical of cast concrete. Strain was plotted against the number of cycles to failure for each specimen and took an S-inverted shape. In contrast, the stiffness degradation plot took an S-upright shape. Observations about S-shape behavior resemble those of previous studies [20, 23-25].

IV. **Uniform strain distribution**:

Strain measurements revealed relatively uniform distribution across specimens until late in the fatigue life, attributed to the material's homogeneity, smaller aggregate sizes, and stronger cement paste. The strain measured on both sides of the specimen in almost all cases showed a uniformly distributed strain accumulation. The difference between the measured strains was very

small, and it developed mostly during the last phase of strain accumulation. This is due to the brittle behavior of concrete with small aggregate size, stronger cement paste, and high strength. The normalized strain plot versus the normalized N_f showed that the specimens with almost the same number of cycles have similar strain evolution curves.

V. **Visual crack initiation**:

Visual cracks appeared near the end of the fatigue life, correlating with peak strain values and the descending branch of the monotonic stress-strain curve. This indicates the material's brittle nature and highlights safety considerations for structural applications. The visual cracks become visible on the circumferential surface of the cylinder at the very end of the fatigue life of the cylinders. The associated peak strains were plotted against the maximum stress level, along with the normalized monotonic stress-strain response of 3DPC. The intersection of these peak strains related to visual cracks with the softening part of monotonic responses proved the material's brittleness.

VI. **Fatigue prediction models**:

A strong linear correlation was observed between the logarithmic values of strain gradients in Phase II and the number of cycles to failure. These correlations can enhance predictive models for fatigue capacity of 3DPC. The correlation of the average gradient of peak and valley strain and stiffness in *phase II* and the number of cycles to failure were investigated. There was a linear correlation between these parameters' logarithm and N_f's logarithm. The high coefficient of correlation (R^2) proves a direct correlation between these factors.

VII. **Recommendations for design and testing**:

Given the brittleness of 3DPC, additional safety factors are recommended for structural design with this material. Further research is suggested to refine fatigue models, accounting for unique microstructural effects, different printing directions, and saturation (presence of water) during fatigue testing.

VIII. Additional insights:

Monotonic strength variability: The high coefficient of variation (11%) in monotonic strength highlights the need for standardized production and quality control during 3D printing.

Durability observations: Degree of overlap between filaments significantly affects durability, with moderate overlaps yielding better performance against chloride penetration and water absorption.

6 Effect of Aggregate Size and Shape on Fatigue Behavior of Concrete

6.1 Primary fatigue experimental investigations

In later stages of the studies, 71 concrete specimens were prepared and cast with two different aggregate gradations, to examine the effect of maximum aggregate size and aggregate type on the compressive fatigue capacity of concrete. More information on mix design, aggregate gradation, and strength of concrete, as well as a few results on cyclic fatigue testing, are presented below. The fatigue test and results are shown in Figure 157 and Table 30.

Figure 151 The preparation of materials (sieving aggregates) for casting at Tufts University (March 2023).

Figure 152 Types of aggregates used in the casting of new concrete cylinders.

6.1.1 Riverstone concrete (with 3/8 in maximum aggregate size)

In this round of concrete cast, more round pea pebbles were used with a maximum size of 3/8 in as a coarse aggregate. Round river aggregates are one of the most commonly used sources of concrete material. The sieve analysis result is shown in Figure 153. In this particular concrete, since the coarse aggregate size is relatively small and they are round, it was expected that the microcracks take a longer time to be developed; therefore, the fatigue capacity would be higher. This concrete had an average of 2450 psi strength at the age of 28 days.

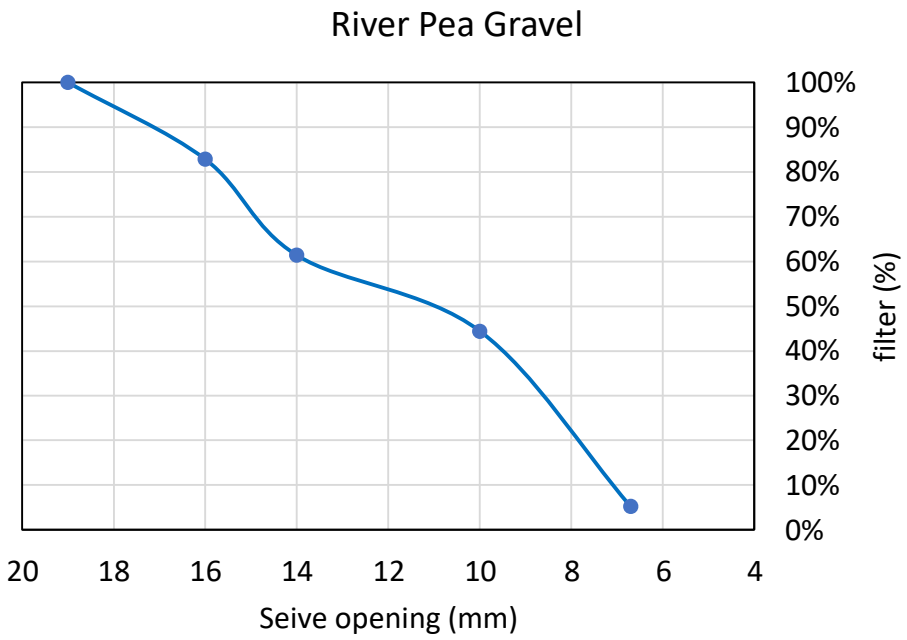

Figure 153 Aggregate gradation for river pea gravel source used for casting.

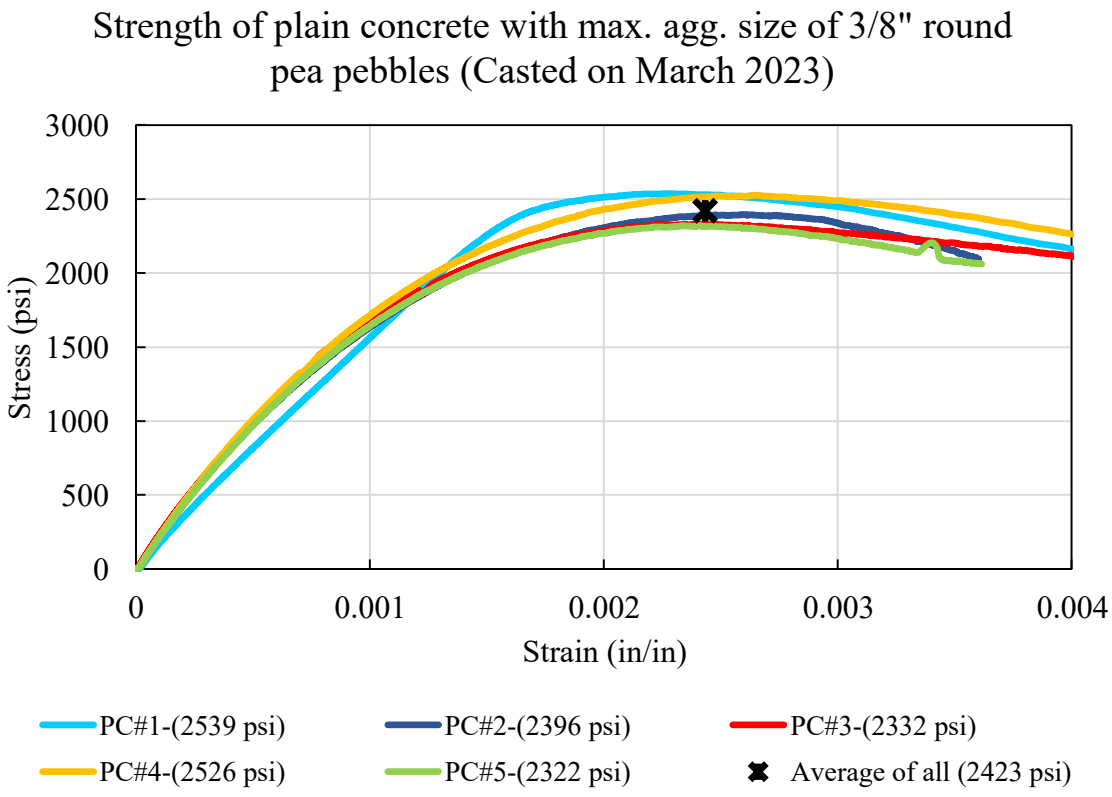

Figure 154 Monotonic strength of concrete cylinders with smaller round aggregate.

Table 30 Monotonic strength of concrete cylinders with smaller round aggregate

Specimen #	Age (days)	Stress (psi)	Avg. Strain
Cast#4-PC#1	28	2539	0.0023
Cast#4-PC#2	28	2396	0.0026
Cast#4-PC#3	28	2332	0.0022
Cast#4-PC#4	28	2526	0.0027
Cast#4-PC#5	28	2322	0.0024
Average		2423	0.0024
CoV		4%	-

6.1.2 Crushed stone concrete (with 3/4 in maximum aggregate size)

The goal of this cast was to have a very different aggregate type and size, and essentially a very different concrete cast, to see the effect of aggregate type and size on fatigue capacity. Therefore, the crushed blue stone aggregates with high sharpness number are used as coarse aggregates. The maximum aggregate size was ¾ in, which is almost double the size of previous aggregates. The sieve analysis result is shown in Figure 155. In this concrete, since the coarse aggregate size is relatively large, expected to have higher strength. This concrete had an average of 3100 psi strength at the age of 28 days. Since the coarse aggregates are crushed stones, they have very sharp angular shapes with linear/straight edges. Thus, it was expected that microcrack initiation and development would be much faster than round small-size concrete. In other words, the fatigue capacity would be lower.

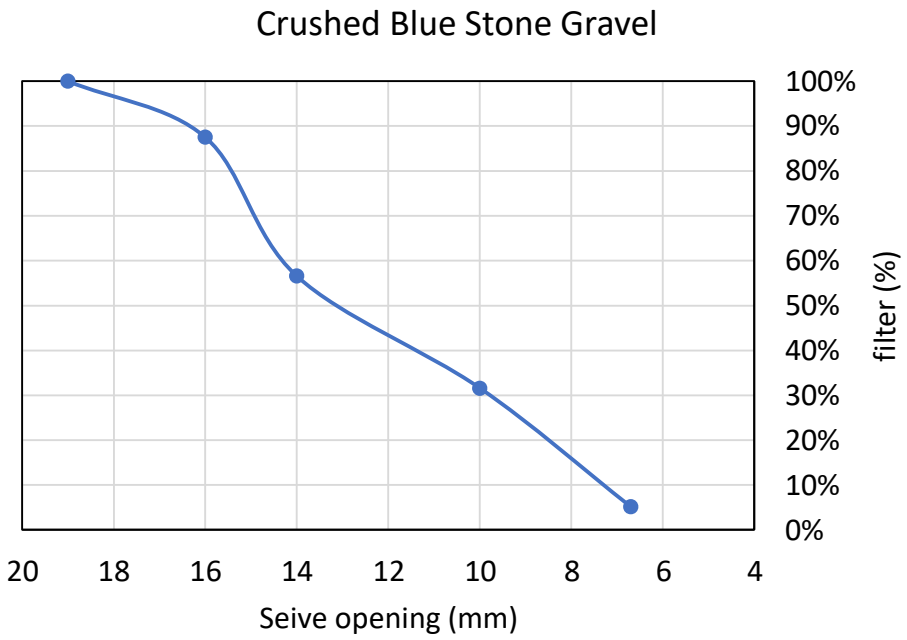

Figure 155 Aggregate gradation for crushed blue stone source used for casting.

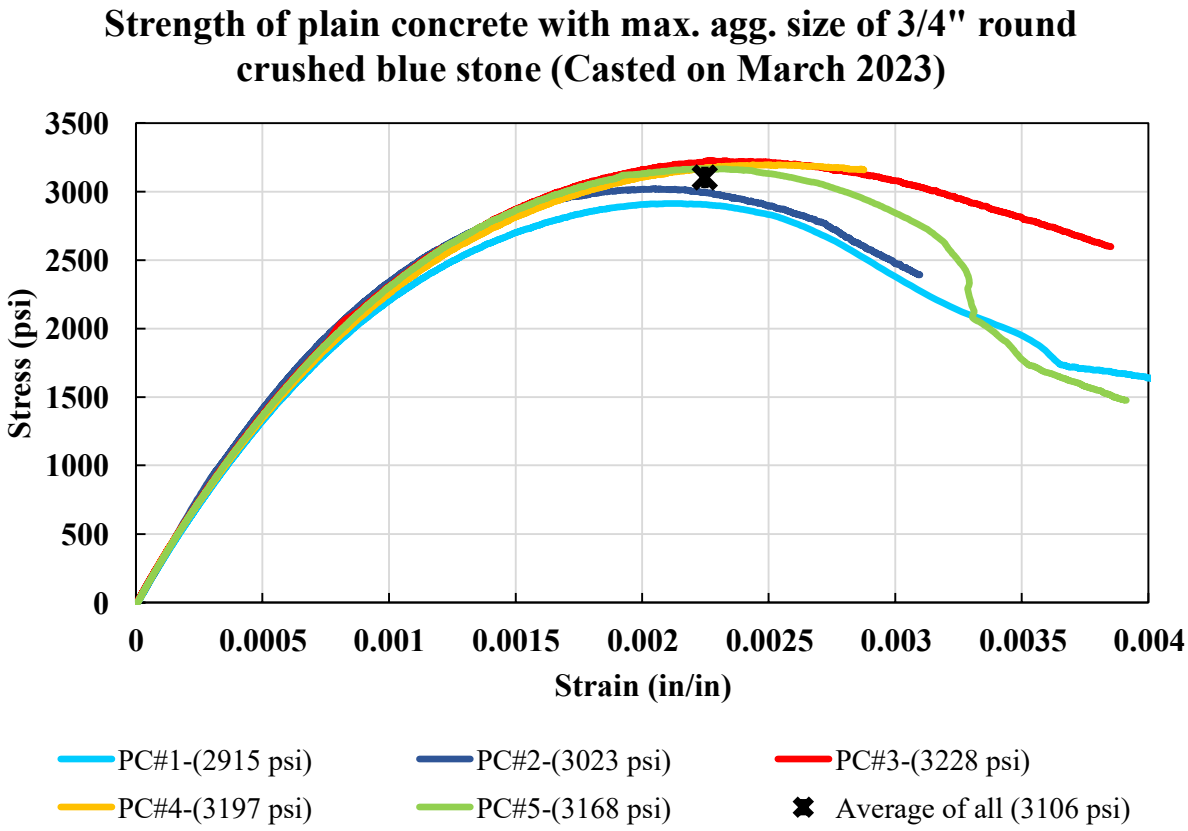

Figure 156 Monotonic strength of concrete cylinders with larger sharp aggregate.

Table 31 Monotonic strength of concrete cylinders with larger sharp aggregate

Specimen #	Age (days)	Stress (psi)	Avg. Strain
Cast#5-PC#1	28	2915	0.00215
Cast#5-PC#2	28	3023	0.00205
Cast#5-PC#3	28	3228	0.00226
Cast#5-PC#4	28	3197	0.00254
Cast#5-PC#5	28	3168	0.00223
Average		3106	0.00225
CoV		4%	

6.1.3 Primary fatigue test results

Initially, the typical (Smax, Smin)=(0.8, 0.05) loading level with the frequency of 1 Hz on a couple of cylinders was performed. The results agree with our hypothesis. The table below shows the actual number of cycles to failure from the tests and their comparison with the predicted capacity using three models suggested by codes and standards. The concrete with smaller, round, coarse aggregate had seven times greater fatigue capacity than the concrete with larger, sharp, coarse aggregate.

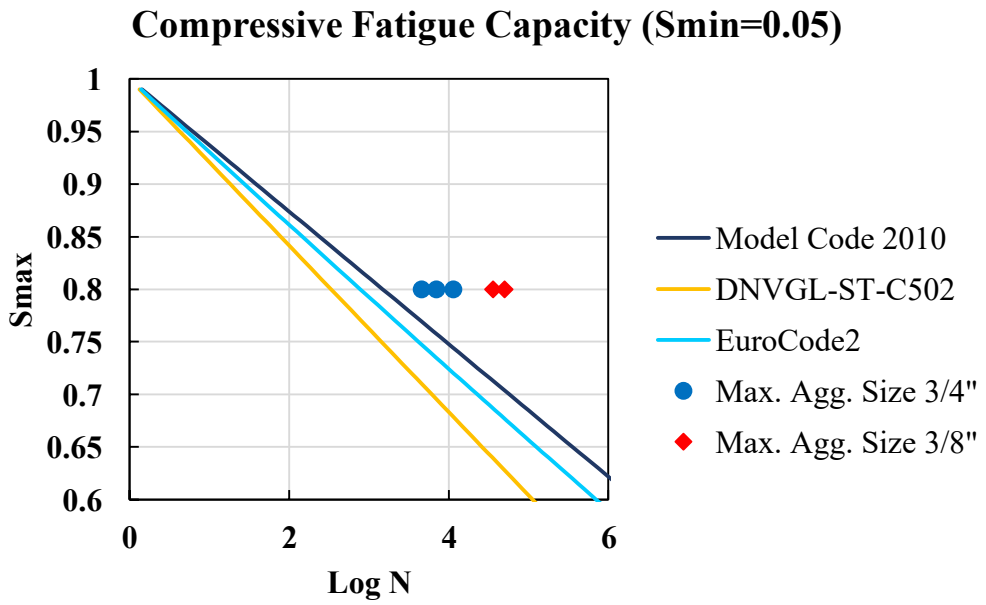

Figure 157 Compressive fatigue capacity test results compared to the codes.

Table 32 Primary fatigue test results

Test name	Predicted Number of cycles to failure			
	Model Code 2010	DNVGL-C502	EuroCode2	Actual Test result (Nf)
Cast#4-CAT#1-80-5-F1	1,490	336	780	36080
Cast#4-CAT#2-80-5-F1	1,490	336	780	50364
~~Cast#4-CAT#1-80-5-F1~~	~~1,490~~	~~336~~	~~780~~	~~6569~~
Cast#5-CAT#1-80-5-F1	1,490	336	780	4582
Cast#5-CAT#2-80-5-F1	1,490	336	780	11350
Cast#5-CAT#3-80-5-F1	1,490	336	780	6980

Naming guide: Cast # – Constant amplitude test number 1 (CAT#1)– Smax percent % (80) - Smin percent % (5) – Frequency of loading (Hz) # (F1)

Note: Cast #4 is the concrete with smaller round coarse aggregate (round pea pebbles with max size of 3/8 in), and Cast#5 is the concrete with larger sharp coarse aggregate (crushed blue stone with max size of ¾ in).

Note: The 3rd fatigue test on Cast#4 failed early due to a very high difference in stiffness of two sides. Sometimes, a concrete cylinder does not have a uniform stiffness around the perimeter due to some unknown/unseen defect. These defects are mostly caused by errors in casting. Therefore, this test is not representative of the sample, and based on the procedure that we defined, this test result is rejected.

6.2 Fabrication of specimens for final casting of various concrete batches

6.2.1 Aggregate sources and details

For the final casting, aggregates were procured from a local concrete company, Thresca Brothers, located in Medfield, MA. The aggregate used in the study was the type of aggregate usually used for structural concrete in this region, including crushed granite coarse aggregate, river-based round coarse aggregate, sand, and lightweight aggregate. The sieve analysis plot and the photos of these types of aggregates are given below (See *Figure 158* to *Figure 163*).

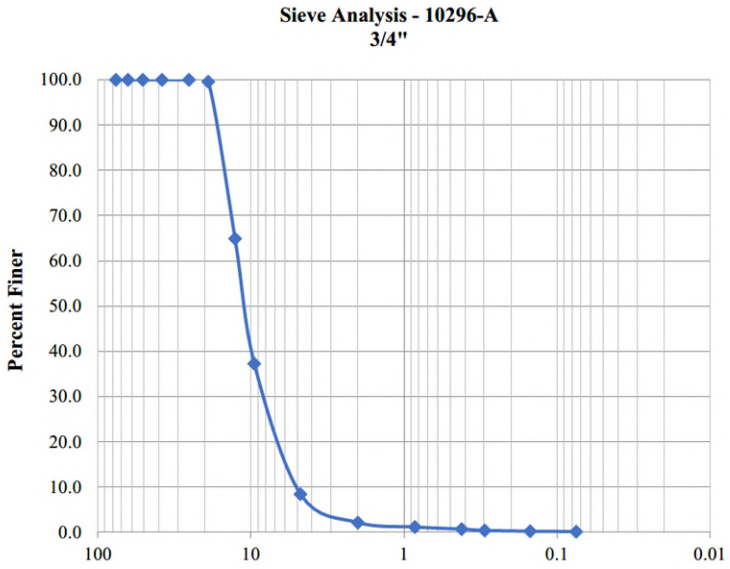

Analysis By Weight, % (USCS)		
Gravel	(Plus #4)	92
Coarse Sand	(#4-10)	7
Medium Sand	(10-40)	1
Fine Sand	(40-200)	0
Silt / Clay	(Minus 200)	0

Figure 158 Gradation results for crushed coarse granite.

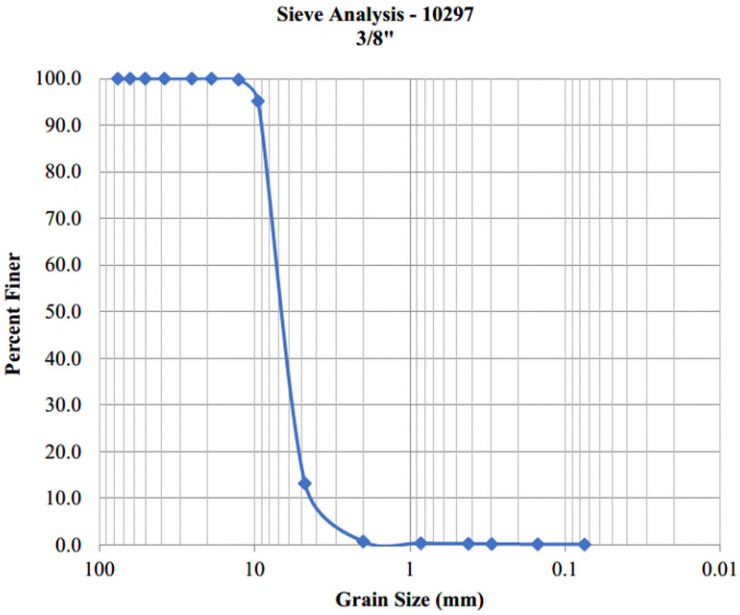

Analysis By Weight, % (USCS)		
Gravel	(Plus #4)	87
Coarse Sand	(#4-10)	12
Medium Sand	(10-40)	0
Fine Sand	(40-200)	0
Silt / Clay	(Minus 200)	0

Figure 159 Gradation results for river based round aggregate.

Figure 160 Coarse crushed granite aggregate; Left) max aggregate size of ¾ in; Right) max aggregate size of 3/8 in.

Figure 161 River based round aggregate with max size of 3/8 in.

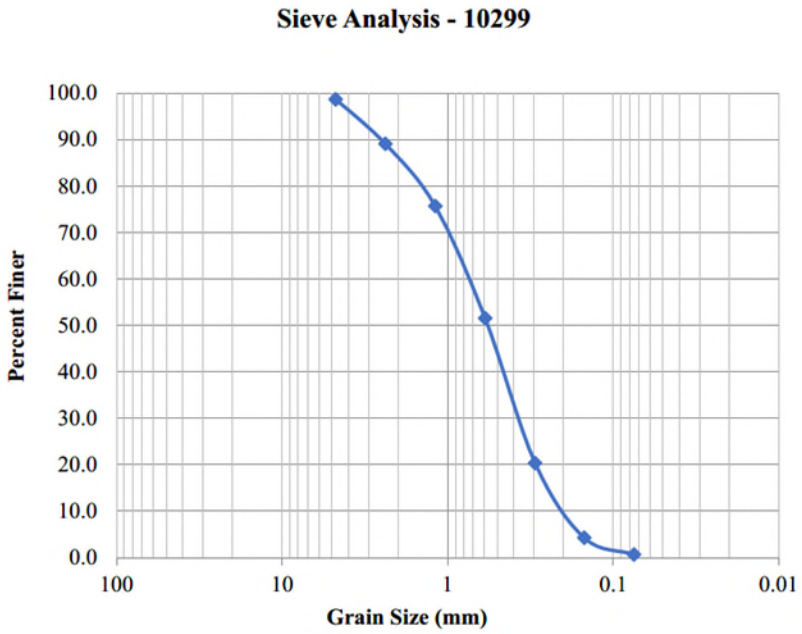

Analysis By Weight, % (USCS)		
Gravel	(Plus #4)	1
Coarse Sand	(#4-10)	10
Medium Sand	(10-40)	38
Fine Sand	(40-200)	51
Silt / Clay	(Minus 200)	1

Figure 162 Gradation results for sand.

Figure 163 Sand.

6.2.2 Selection of desired mix designs by casting trial batches

The desired strength was chosen to be around 5000 psi, a typical strength for normal structural concrete. To achieve this goal, 11 different batches of concrete have been poured and tested at the age of 7 days (a few at six days) to verify and find the best mix design for target strength. Concrete material usually reaches to 70% of its strength by the age of 7 days. Therefore, the

desired strength by the age of 7 days was 3500 psi. *Figure 164* entails a few of photos related to the trial batches casting campaign. *Table 33* shows the monotonic test results of trial batches.

Figure 164 A few photos from the trial batches (mixing process and results of the slump test).

Table 33 Monotonic test results for trial batches of concrete

Trial Batch #	Concrete Type	Target Strength (psi) At the age of 7 days	Avg. Strength (psi) at the age of 7 days
10300	Round coarse aggregate	3500	3806
10301	Round coarse aggregate	3500	3913
10302	Crushed granite coarse aggregate	3500	3847
10303	Round coarse aggregate	3500	4810
10304	Crushed granite coarse aggregate	3500	4233
10305	Crushed granite coarse aggregate	3500	2603
10306	Round coarse aggregate	3500	3753
10307	Round coarse aggregate	3500	2256
10308	Crushed granite coarse aggregate	3500	3510
10309	Round coarse aggregate	3500	3380
10310	Light-weight aggregate	3500	3050
10311	Light-weight aggregate	3500	2770

6.2.3 Final selected types of concrete

After a careful review of the trial batches results, the best four mix designs selected. Figure 165 shows a couple of photos of the first type of concrete casting and primary tests. Table 34 presents the mix design target strength and final test results at the age of 28 days. These specimens will be tested in the next couple of months to examine and prove the effectiveness of the proposed techniques for testing for compressive fatigue testing and also developing fatigue capacity estimation model using experimental testing.

Figure 165 A few photos from concrete 10321, with round coarse aggregate and the slab with crushed granite aggregate (mixing process, entrained air test, and results from the slump test).

Table 34 Monotonic test results for the final mix designs of concrete

Final Batch #	Concrete Type	Target Strength (psi) At the age of 28 days	Avg. Strength (psi)	Age of testing days
10321	Round coarse aggregate	5000	5170	28 days
10323	Crushed granite coarse aggregate	5000	5220	28 days
10324	Slab	5000	5200	28 days
10328	Lightweight aggregate	5000	5190	28 days

Figure 166 The first two sets of concrete cylinders delivered to Tufts University.

6.3 Experimental testing

6.3.1 Overview

This study explores the interplay between strain gradient, stiffness degradation, and the fatigue capacity of concrete under uniaxial compressive fatigue loading. By synthesizing previous research on concrete fatigue, it highlights significant variations in fatigue capacity and overlooked internal mechanisms that extend material service life. Experimental results reveal a strong linear relationship between stiffness degradation in cylindrical specimens, suggesting potential applications to structural components under specific stress gradients. While Model Code 2010 incorporates a stress gradient factor, efforts to refine deformation and stiffness degradation characterization are ongoing. This study includes over 200 fatigue tests on various concrete mixes, complemented by existing data. We also examined the strain at the first visual crack appearance due to fatigue loading, confirming its occurrence around the end of phase 2 and start of phase 3 of strain evolution. Findings demonstrate significant correlations, offering valuable insights for structural design and materials engineering.

6.3.2 Introduction

Extensive studies have been conducted on fatigue capacity (number of cycles to failure) of concrete specimens [20-26, 29, 50, 65, 66, 86, 95, 136, 138]. The findings were condensed into S-N curves and incorporated into standards that aid in designing fatigue-loaded concrete structures. Considerable variation in fatigue capacity has been observed. Within concrete, internal processes and mechanisms exist that extend the service life of the material at the member scale. However, these processes are not accounted for in the S-N curves. The primary factors contributing to this extended service life are the deformation behavior and stiffness

degradation of fatigue-loaded concrete [26]. Experimental testing showed a strong correlation between the stiffness results obtained from tests on cylindrical specimens and beams. Findings from cylindrical tests can be extrapolated to structural components, provided that the stress gradient within components can be simplified into segments with uniform stresses across the cross-section [139]. Model Code 2010 incorporates this consideration in a simplified manner through a stress gradient factor [119], to provide a more precise description of the deformation characteristics and stiffness deterioration of fatigue-loaded concrete.

These efforts tried to establish a relationship between the ultimate fatigue strain and the deformation characteristics under continuously increasing loads. Within this framework, three primary hypotheses are outlined in the literature. First, the ultimate fatigue strain is either slightly smaller or insignificantly larger than the ultimate strain observed under continuously increasing, force-controlled compressive load [23, 26, 29, 140]. Second, the ultimate fatigue strain occurs within the descending branch of the envelope curve [25, 26, 48, 141]. Third, the ultimate fatigue strain is located above the descending branch of the envelope curve [58]. (see Figure 102 as an example).

It is important to highlight that both the ultimate strain under continuously increasing load and the envelope curve are influenced by the compression test's loading rate [142]. To simplify, it is commonly assumed that strains observed in fatigue tests comprise both elastic and plastic components. The plastic strains are believed to arise from material degradation and crack formation as the number of cycles increases. However, a few research studies demonstrate that ultimate fatigue strains are also affected by time-dependent viscous deformations [37, 52, 143]. Tests with longer durations yielded larger ultimate fatigue strains compared to tests with shorter durations, despite having the same maximum and minimum stress levels but different load

frequencies. Additionally, cyclic loading induces a temperature rise in the specimens during fatigue tests, leading to thermal strains and simultaneous thermal expansion alongside deformations caused by cyclic loading [55].

To fill the existing gap of our understanding of concrete fatigue, This study is focused on the secondary strain rate correlation with the fatigue capacity of the concrete under compressive uniaxial fatigue loading. For this purpose, 160 fatigue tests were carried out using 3 different concrete mixes. In addition to the experimental testing performed by the author, results from other studies were summarized in the analysis to show its feasibility and conclusions.

6.3.3 Mechanical properties and mix design of material

The experimental testing was conducted on air-cured PC cylindrical samples with an average of 5200 psi 28 days strength. The mix design and mechanical properties of each concrete are listed in the following table.

Table 35 Concrete specifications and mix design

Concrete Type	Aggregate Type / Max. Size	Mix design C:S:A	w/c	Entrained air	Strength at 28 days
RBAC	River base round - ¾ in	1:2.85:3.5	0.6	3.1%	5170 psi
CGAC	Crushed granite angular – ¾ in	1:2.85:3.5	0.60	5%	5220 psi
LWAC	River base aggregate – 3/8 in & 20% Lightweight aggregate replacement	1:2.75:1.25	0.55	4%	5190 psi

The specimens were cylinders with 4 in diameter and 8 in height. Crushed granite coarse aggregate and also river-based round coarse aggregate, both commonly used in New England for structural concrete, were used to cast plain concrete cylinders. Type I Portland cement was used in these concretes. 75% of the specimens were cast in plastic molds and air cured. In addition to specimens from molds a slab was cast using crushed granite aggregate and cored to create some

specimens. This was done to investigate the effect of coring on fatigue capacity. The fatigue tests were done after the age of 90 days, when the strength growth of the concrete was almost finished.

6.3.4 Improved method for estimating the strength

The fatigue loading protocol was defined using the Improved Strength Estimation Method (ISEM) to ensure precision. The compressive loading protocol consisted of maximum and minimum loading ratios (S_{max}, S_{min}). Typically, the average strength from recent monotonic tests is used as the monotonic strength, but this can lead to unrealistic results due to variations in specimen strength. To address this, a new method was implemented (ISEM) to better estimate each cylinder's strength before fatigue testing. Each cylinder was loaded up to $0.95 * S_{max}$ (based on the batch's average strength) at the standard rate defined in ASTM C39. The resulting stress-strain response was then compared to monotonic test results to identify the closest match, thus providing an improved strength estimate. For example, Figure 167 shows that fatigue test #7 of 3DPC aligns most closely with monotonic test #5 of 3DPC, resulting in an estimated strength of 7400 psi (51 MPa) for defining the fatigue loading protocol, rather than the batch's average strength of 6800 psi (47 MPa).

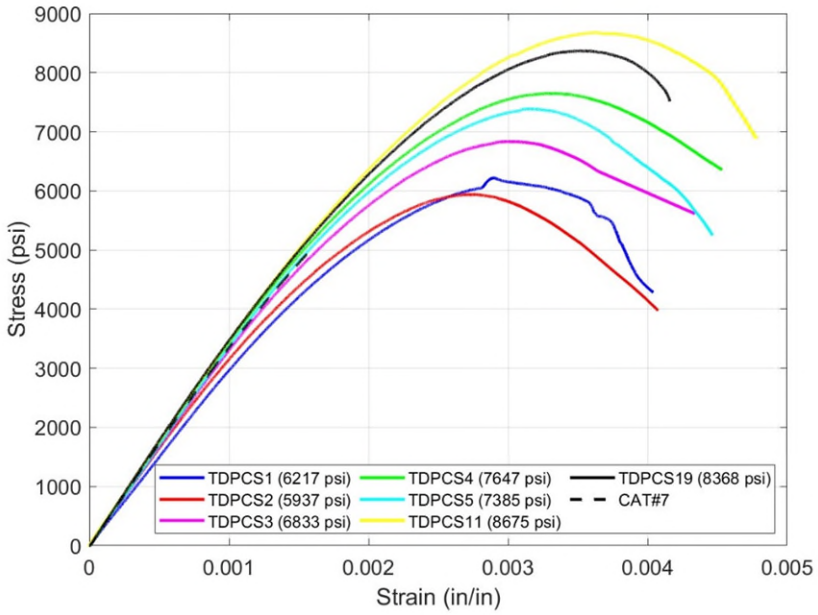

Figure 167 Example of plotting the stress-strain response of a concrete cylinder to compressive monotonic loading using ISEM to estimate the actual strength of the cylinder (3DPC).

6.3.5 Results and discussion

6.3.5.1 Fatigue capacity

The different fatigue load combinations of S_{max}, S_{min}, and frequency were selected to cover a range of testing with a maximum number of cycles of less than 1 million to perform the tests. Considering the use of ISEM to find a more precise strength value for each cylinder, the loading protocol is defined for each individual cylinder for fatigue testing.

All of the tests were carried out to failure by imposing a uniaxial compressive constant amplitude cyclic load (i.e., one value of S_{max} and S_{min} per test) with a sinusoidal waveform and a predefined frequency of 1 Hz. The fatigue capacity (Number of cycles to failure; N_f) for each tested specimen are presented in Table 36, Table 37, and Table 38. Figure 168 and Figure 169 show the fatigue capacity of all types of tested concrete compared to characteristic S-N (Stress ratio - number of cycles) curves from three different codes. In these plots, the maximum nominal stress

level (S_{max}) is presented on the vertical axis, and the logarithm of the number of cycles to failure, log10 (N_f), is shown on the horizontal axis. These plots show that the concretes based on material characteristics has different fatigue capacity (even with the same range of strength).

The other main observation from S-N test results is that the variation in fatigue capacity is considerably reduced using the improved strength estimation method (ISEM), compared to data base observations.

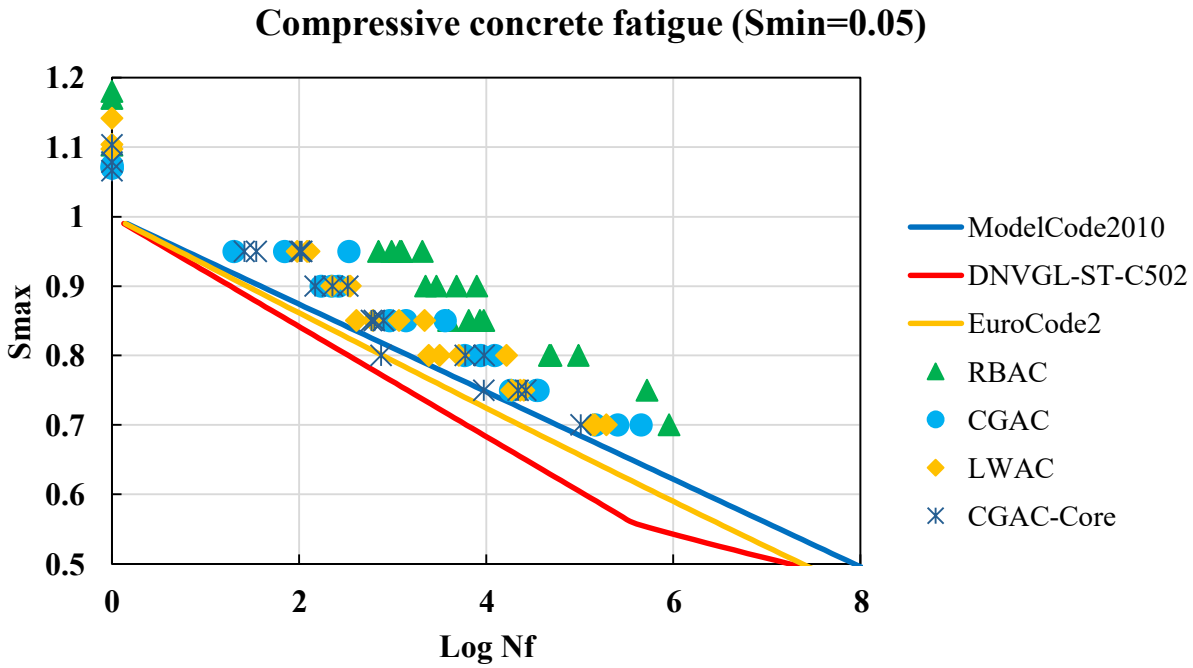

Figure 168 S-N curve plot for uniaxial compressive fatigue testing with Smin of 5%.

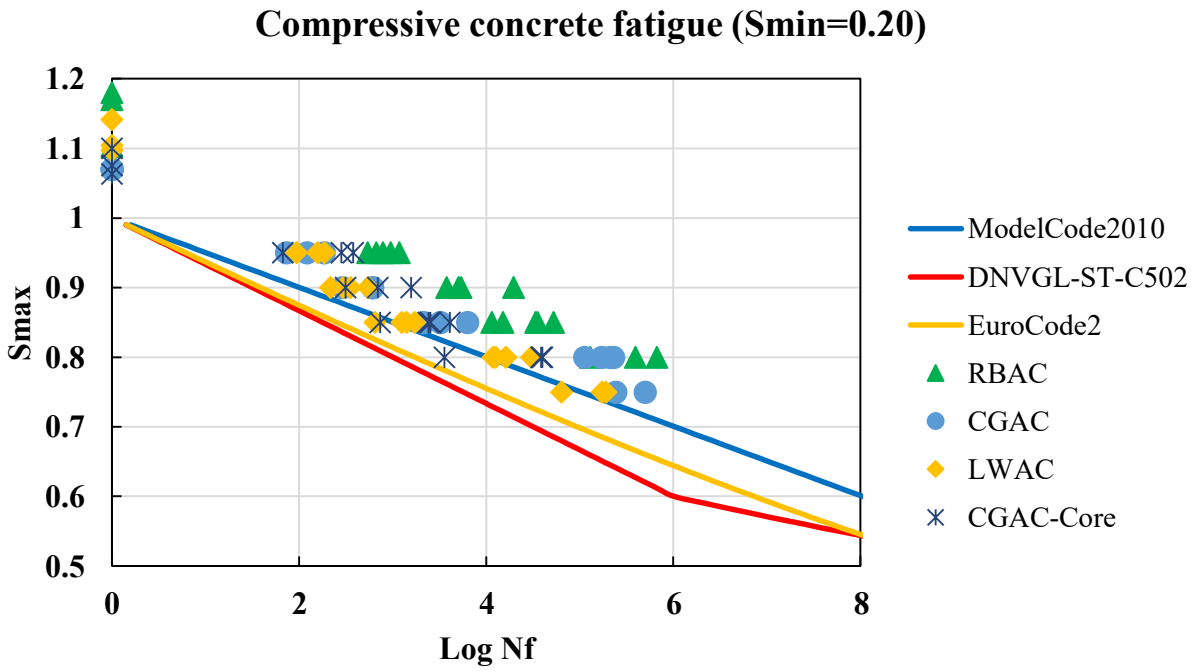

Figure 169 S-N curve plot for uniaxial compressive fatigue testing with Smin of 20%.

Table 36 Fatigue test results of PC specimens with river base round coarse aggregate (maximum size of 3/8 in)

Test Name	Smax	Smin	Fre. (Hz)	Number of cycles to failure	Test Name	Smax	Smin	Fre. (Hz)	Number of cycles to failure
RBAC-CAT#1	0.95	0.05	1	1,195	RBAC-CAT#19	0.95	0.20	1	1,174
RBAC-CAT#2	0.95	0.05	1	1,240	RBAC-CAT#20	0.95	0.20	1	955
RBAC-CAT#3	0.95	0.05	1	2,068	RBAC-CAT#21	0.95	0.20	1	540
RBAC-CAT#4	0.95	0.05	1	976	RBAC-CAT#22	0.95	0.20	1	785
RBAC-CAT#5	0.95	0.05	1	708	RBAC-CAT#23	0.95	0.20	1	667
RBAC-CAT#6	0.90	0.05	1	4,795	RBAC-CAT#24	0.90	0.20	1	5,355
RBAC-CAT#7	0.90	0.05	1	2,931	RBAC-CAT#25	0.90	0.20	1	5,039
RBAC-CAT#8	0.90	0.05	1	7,912	RBAC-CAT#26	0.90	0.20	1	19,480
RBAC-CAT#9	0.90	0.05	1	2,246	RBAC-CAT#27	0.90	0.20	1	3,756
RBAC-CAT#10	0.85	0.05	1	8,576	RBAC-CAT#28	0.85	0.20	1	35,272
RBAC-CAT#11	0.85	0.05	1	3,938	RBAC-CAT#29	0.85	0.20	1	52,287
RBAC-CAT#12	0.85	0.05	1	9,395	RBAC-CAT#30	0.85	0.20	1	15,037
RBAC-CAT#13	0.85	0.05	1	6,481	RBAC-CAT#31	0.85	0.20	1	11,430
RBAC-CAT#14	0.80	0.05	1	46,953	RBAC-CAT#32	0.85	0.20	1	33,538
RBAC-CAT#15	0.80	0.05	1	96,695	RBAC-CAT#33	0.80	0.20	1	665,194
RBAC-CAT#16	0.80	0.05	1	48,931	RBAC-CAT#34	0.80	0.20	1	394,911
RBAC-CAT#17	0.75	0.05	1	522,174	RBAC-CAT#35	0.80	0.20	1	130,188
RBAC-CAT#18	0.70	0.05	1	897,468	-				

Table 37 Fatigue test results of plain concrete specimens with crushed granite (angular) coarse aggregate (maximum size of 3/4 in)

Test Name	Smax	Smin	Fre. (Hz)	Number of cycles to failure	Test Name	Smax	Smin	Fre. (Hz)	Number of cycles to failure
CGAC-CAT#1	0.95	0.05	1	340	CGAC-CAT#19	0.95	0.20	1	185
CGAC-CAT#2	0.95	0.05	1	70	CGAC-CAT#20	0.95	0.20	1	73
CGAC-CAT#3	0.95	0.05	1	20	CGAC-CAT#21	0.95	0.20	1	121
CGAC-CAT#4	0.90	0.05	1	171	CGAC-CAT#22	0.90	0.20	1	607
CGAC-CAT#5	0.90	0.05	1	222	CGAC-CAT#23	0.90	0.20	1	606
CGAC-CAT#6	0.90	0.05	1	263	CGAC-CAT#24	0.90	0.20	1	290
CGAC-CAT#7	0.85	0.05	1	1,373	CGAC-CAT#25	0.85	0.20	1	6,264
CGAC-CAT#8	0.85	0.05	1	3,621	CGAC-CAT#26	0.85	0.20	1	3,216
CGAC-CAT#9	0.85	0.05	1	924	CGAC-CAT#27	0.85	0.20	1	2,116
CGAC-CAT#10	0.80	0.05	1	8,674	CGAC-CAT#28	0.80	0.20	1	210,322
CGAC-CAT#11	0.80	0.05	1	5,867	CGAC-CAT#29	0.80	0.20	1	228,515
CGAC-CAT#12	0.80	0.05	1	12,265	CGAC-CAT#30	0.80	0.20	1	171,556
CGAC-CAT#13	0.75	0.05	1	34,394	CGAC-CAT#31	0.80	0.20	1	111,600
CGAC-CAT#14	0.75	0.05	1	18,078	CGAC-CAT#32	0.75	0.20	1	240,998
CGAC-CAT#15	0.75	0.05	1	35,606	CGAC-CAT#33	0.75	0.20	1	500,000
CGAC-CAT#16	0.70	0.05	1	145,945	-				
CGAC-CAT#17	0.70	0.05	1	254,299					
CGAC-CAT#18	0.70	0.05	1	450,000					

Table 38 Fatigue test results of PC specimens with lightweight coarse aggregate

Test Name	Smax	Smin	Fre. (Hz)	Number of cycles to failure	Test Name	Smax	Smin	Fre. (Hz)	Number of cycles to failure
LWAC-CAT#1	0.95	0.05	1	128	LWAC-CAT#21	0.95	0.20	1	94
LWAC-CAT#2	0.95	0.05	1	96	LWAC-CAT#22	0.95	0.20	1	158
LWAC-CAT#3	0.95	0.05	1	122	LWAC-CAT#23	0.95	0.20	1	186
LWAC-CAT#4	0.90	0.05	1	223	LWAC-CAT#24	0.90	0.20	1	354
LWAC-CAT#5	0.90	0.05	1	343	LWAC-CAT#25	0.90	0.20	1	548
LWAC-CAT#6	0.90	0.05	1	353	LWAC-CAT#26	0.90	0.20	1	216
LWAC-CAT#7	0.85	0.05	1	1,169	LWAC-CAT#27	0.90	0.20	1	296
LWAC-CAT#8	0.85	0.05	1	613	LWAC-CAT#28	0.85	0.20	1	1,715
LWAC-CAT#9	0.85	0.05	1	409	LWAC-CAT#29	0.85	0.20	1	649
LWAC-CAT#10	0.85	0.05	1	2196	LWAC-CAT#30	0.85	0.20	1	1,254
LWAC-CAT#11	0.80	0.05	1	16,434	LWAC-CAT#31	0.85	0.20	1	1,407
LWAC-CAT#12	0.80	0.05	1	5,066	LWAC-CAT#32	0.80	0.20	1	30,380
LWAC-CAT#13	0.80	0.05	1	2,420	LWAC-CAT#33	0.80	0.20	1	11,821
LWAC-CAT#14	0.80	0.05	1	3,180	LWAC-CAT#34	0.80	0.20	1	12,585
LWAC-CAT#15	0.75	0.05	1	25,073	LWAC-CAT#35	0.80	0.20	1	16,187
LWAC-CAT#16	0.75	0.05	1	23,012	LWAC-CAT#35	0.75	0.20	1	63,751
LWAC-CAT#17	0.75	0.05	1	18,575	LWAC-CAT#36	0.75	0.20	1	190,975
LWAC-CAT#18	0.70	0.05	1	145,073	LWAC-CAT#37	0.75	0.20	1	174,091
LWAC-CAT#19	0.70	0.05	1	192,336	-				
LWAC-CAT#20	0.70	0.05	1	137,706					

Table 39 Fatigue test results of cored plain concrete specimensfrom slab with crushed granite (angular) coarse aggregate (maximum size of 3/4 in)

Test Name	Smax	Smin	Fre. (Hz)	Number of cycles to failure	Test Name	Smax	Smin	Fre. (Hz)	Number of cycles to failure
CCGAC-CAT#1	0.95	0.05	1	26	CCGAC-CAT#18	0.95	0.20	1	67
CCGAC-CAT#2	0.95	0.05	1	35	CCGAC-CAT#19	0.95	0.20	1	284
CCGAC-CAT#3	0.95	0.05	1	102	CCGAC-CAT#20	0.95	0.20	1	378
CCGAC-CAT#4	0.95	0.05	1	107	CCGAC-CAT#21	0.9	0.20	1	1572
CCGAC-CAT#5	0.9	0.05	1	149	CCGAC-CAT#22	0.9	0.20	1	697
CCGAC-CAT#6	0.9	0.05	1	331	CCGAC-CAT#23	0.9	0.20	1	315
CCGAC-CAT#7	0.9	0.05	1	228	CCGAC-CAT#24	0.85	0.20	1	4062
CCGAC-CAT#8	0.85	0.05	1	594	CCGAC-CAT#25	0.85	0.20	1	733
CCGAC-CAT#9	0.85	0.05	1	801	CCGAC-CAT#26	0.85	0.20	1	2528
CCGAC-CAT#10	0.85	0.05	1	636	CCGAC-CAT#27	0.85	0.20	1	2409
CCGAC-CAT#11	0.8	0.05	1	751	CCGAC-CAT#28	0.8	0.20	1	39497
CCGAC-CAT#12	0.8	0.05	1	5,956	CCGAC-CAT#29	0.8	0.20	1	38332
CCGAC-CAT#13	0.8	0.05	1	9,437	CCGAC-CAT#30	0.8	0.20	1	3557
CCGAC-CAT#14	0.75	0.05	1	9,379	-				
CCGAC-CAT#15	0.75	0.05	1	26,338					
CCGAC-CAT#16	0.75	0.05	1	21,775					
CCGAC-CAT#17	0.7	0.05	1	102,476					

Table 40 Comparison of the average and minimum fatigue capacity of normal concrete with similar strength but different aggregate type and size (Smin = 5%)

Smax	Smin = 0.05					
	N_f Min			N_f avg		
	RBAC	CGAC	ratio	RBAC	CGAC	ratio
0.95	708	20	35.4	1237.4	143	8.6
0.9	2246	171	13.1	4471	219	20.4
0.85	3938	924	4.3	7097.5	1973	3.6
0.8	46953	5867	8.0	64193	8935	7.2
0.75	522174	18078	28.9	522174	29359	17.8
0.7	897468	145945	6.1	897468	283415	3.2

Table 41 Comparison of the average and minimum fatigue capacity of normal concrete with similar strength but different aggregate type and size (Smin= 20%)

Smax	Smin = 0.20					
	Nf Min			Nf avg		
	RBAC	CGAC	ratio	RBAC	CGAC	ratio
0.95	540	73	7.4	824.2	126	6.5
0.9	3756	290	13.0	8407.5	501	16.8
0.85	11430	2116	5.4	28506.5	3865	7.4

6.3.5.2 Strain evolution

The same test setup defined in Chapter 4 is used for these testing. The peak and valley stains are the uniaxial strains related to the maximum and minimum uniaxial compressive load imposed on the test specimen.

The development of strain depicted versus the number of cycles (or the normalized number of cycles) is called the strain evolution plot (see Figure 170, right side). Figure 170 shows the results of one of the fatigue tests (Test #9 or 3DPC8-CAT#9) in two plots. On the left side, the monotonic stress-strain response of the concrete with the same strength (3D-PC#3) is plotted along with a few down-sampled fatigue hysteresis curves (in green). It also depicted the secant stiffness lines for those hysteresis curves, which are plotted (in blue) by connecting the maximum and minimum stress-strain points (σ_{max}, ε_{max}) and (σ_{min}, ε_{min}). Failure of specimen was determined when the last loading cycle crossed the descending branch of the monotonic test

result. This is a typical behavior observed in other experiments [24-27]. The peak and valley strain evolution plots are shown on the right side of Figure 8. The strain evolution plot has a S-inverted shape. Like other concrete materials, there are three distinctive phases of strain development. Phase I has a rapid strain accumulation due to the closing of the holes and pore spaces inside the material, and it usually continues up to about $0.2*N_f$. Phase II has a steady and constant linear strain accumulation. In Phase II, the microcracks continue to progress. Phase III starts at about $0.8*N_f$ and shows a rapid strain increase due to cyclic loading. The S-inverted behavior is traditionally explained by microcracks merging and initiating macrocracks and failure zones [23, 25, 26].

The photos taken by two cameras from the cylinder during the constant amplitude test are shown in Figure 171 to Figure 139. The goal was to capture visual crack initiation and progression during the fatigue test.

Figure 170 shows the average peak strain of 3DPC specimen along with the individual strain development on both sides of the cylinder. This plot shows that there was a quantifiably uniform strain behavior around the perimeter of the cylinder, and the side strains start to deviate from each other at around half of the way to failure, but the amount of difference between these two sides measured strains is not very high compared to the other types of concrete tested by author. The reason for that might be the uniformity and homogeneity in the material itself and having small aggregate sizes, and stronger cement paste, which can delay the initiation of microcracks and the progression/development of microcracks until the end of the test (phase III). In other words, this is another indication of brittle behavior, and will require additional safety considerations in design.

There is an interesting observation in Figure 172. It shows the normalized strain evolution plot. In the vertical axis, the average measured peak strain normalized to the initial strain and the normalized number of cycles to failure in the horizontal axis. The specimens with very close N_f also have almost the same normalized strain evolution plot. It means that the normalized strain slope directly correlates to the number of cycles to failure. This observation was made by previous studies [20, 23-25].

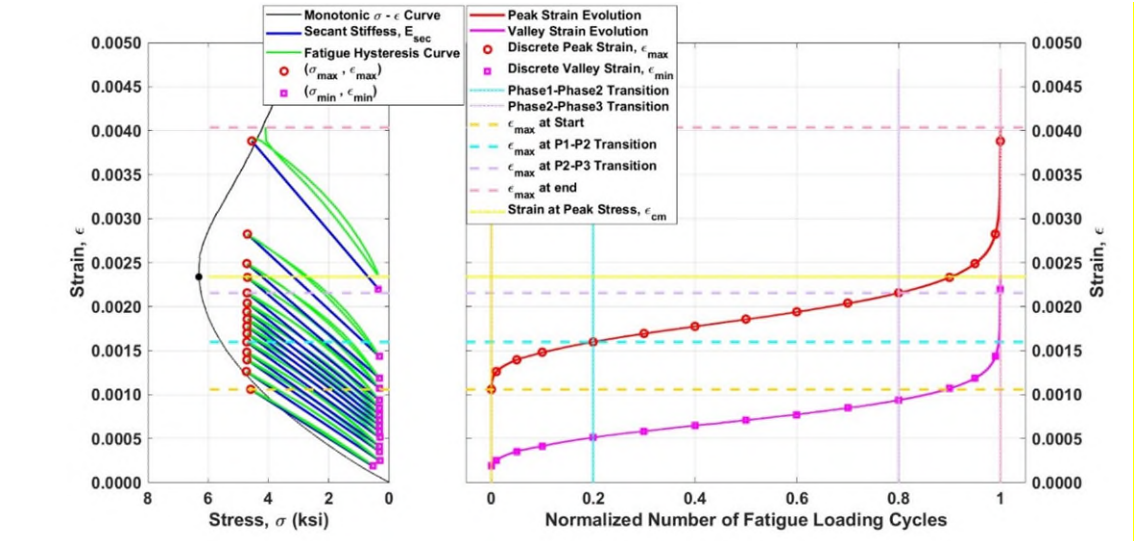

Figure 170 Combined fatigue test result plot of 3D-printed concrete; left side) Stress-strain response of cylinder to monotonic compressive loading, along with a few cycles of hysteresis and peak and valley stress and strain development over the cycles. Right side) Strain evolution plot showing peak and valley strain increment over the cycles of loading up to failure.

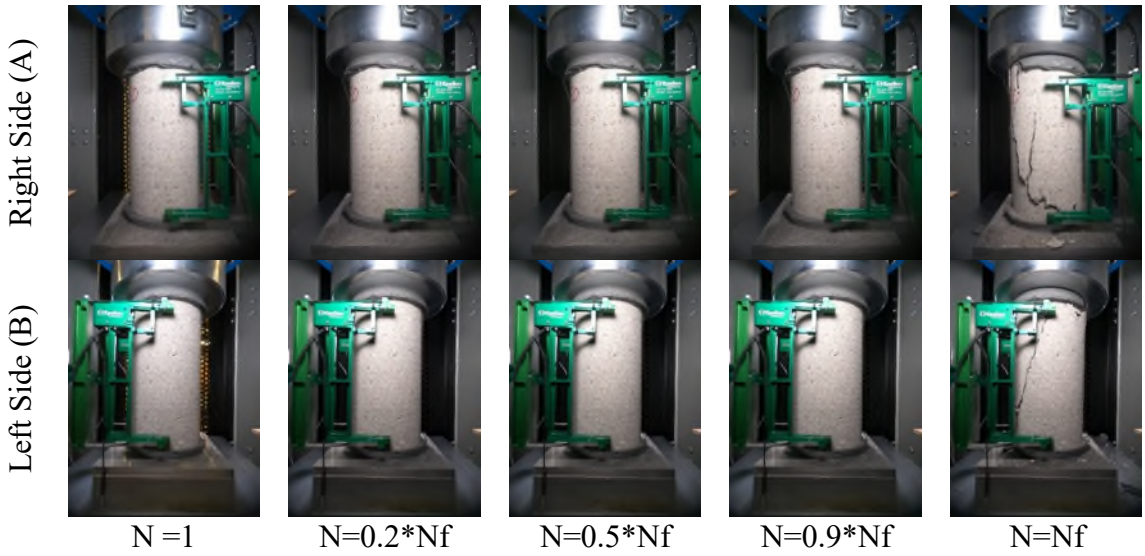

Figure 171 Photos of two sides of the concrete cylinder at certain points during the test (Test #9).

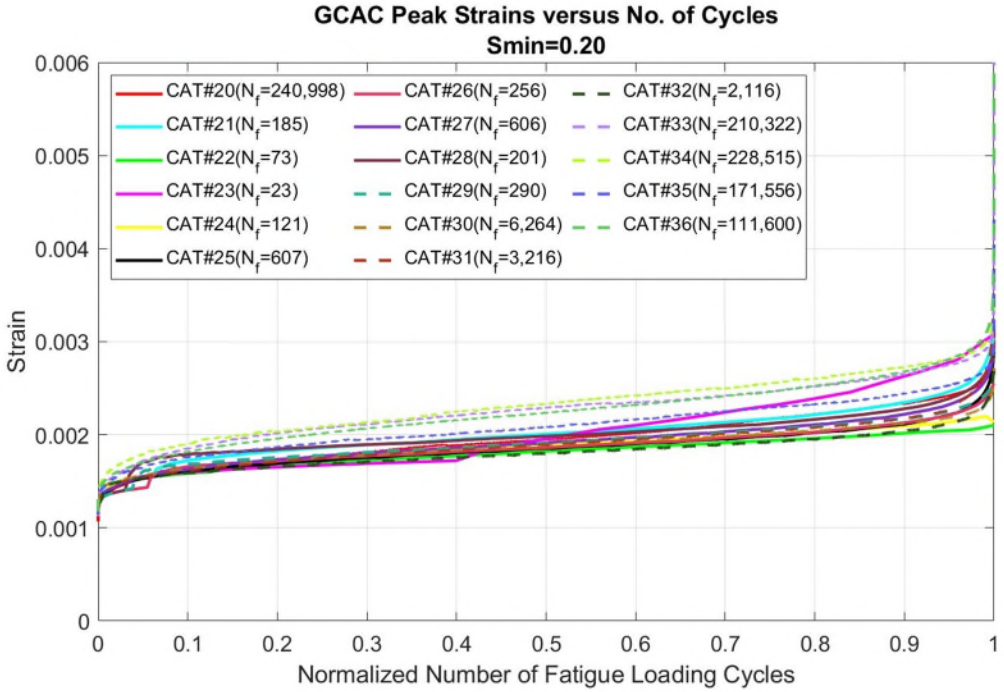

Figure 172 Normalized peak strain evolution plot.

6.3.5.3 Fatigue capacity prediction using strain and stiffness gradients

The correlation between the gradient of strains or stiffness in phase II (which is fairly constant) and N_f has been reported in the literature [23, 25, 26, 86]. To examine the applicability of this theory, the fatigue test results were down-sampled to 23 equally distanced points based on the failure number of cycles. Figure 173-a shows the down-sampled peak strain evolution plot against the normalized N_f. Figure 173-b shows the gradient of peak strain, which can be assumed constant in phase II. Figure 173-c shows the zoomed-in version of the gradient peak strain versus the Normalized N_f. The average of the middle 13 gradient values (excluding the five initial and five final points) is considered the representative gradient peak strain of the test specimen. The same process has been done for gradient valley strain and stiffness.

Figure 174, Figure 175, and Figure 176 show the correlation of gradient peak strain, gradient valley strain, and gradient stiffness to the power of two against the normalized N_f. This correlation is linear for these two parameters' logarithm (base 10). Since the stiffness gradient is negative and having a logarithm of a negative value is undefined, the gradient stiffness to the power of two was used. The corresponding linear regression equations and their associated coefficients of correlation (R^2) are provided in the plots. The high coefficient correlation value shows a strong correlation between the parameters. The lower the gradient, the higher the number of cycles to failure. These correlations can be used to estimate the minimum number of cycles to failure of the run-out tests. In other words, in a run-out test that got stopped around mid-life, the gradient of strains and stiffness can be used to predict the remaining fatigue life (by finding N_f and subtracting the number of cycles the run-out tests had experienced).

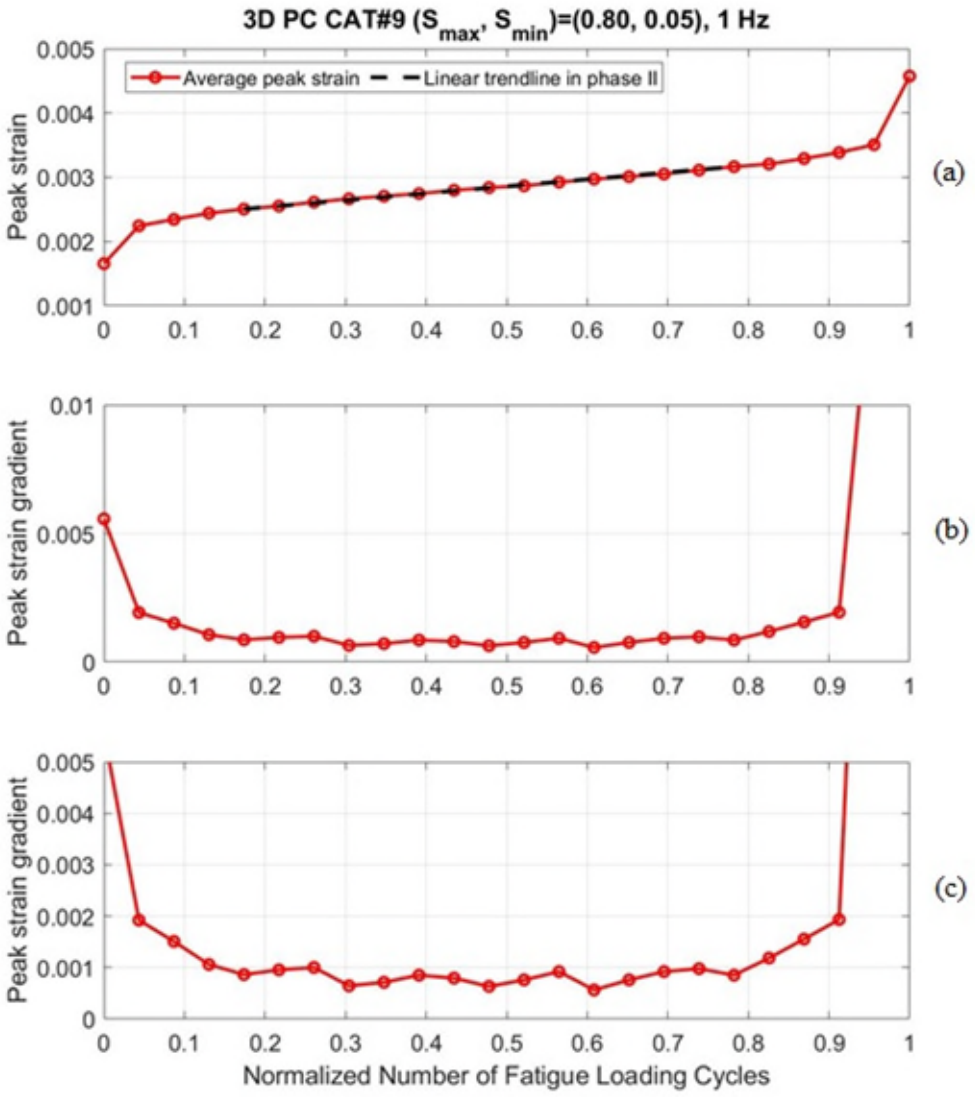

Figure 173 Down-sampled peak strain (3DPC Test #9); a) Peak strain evolution plot, b) the gradient of peak strain, c) Zoomed-in gradient of peak strain.

6.3.5.3.1 Peak Strain Gradient vs. Nf

$$log(Nf) = a + b * log(PSG)$$ Equation 4

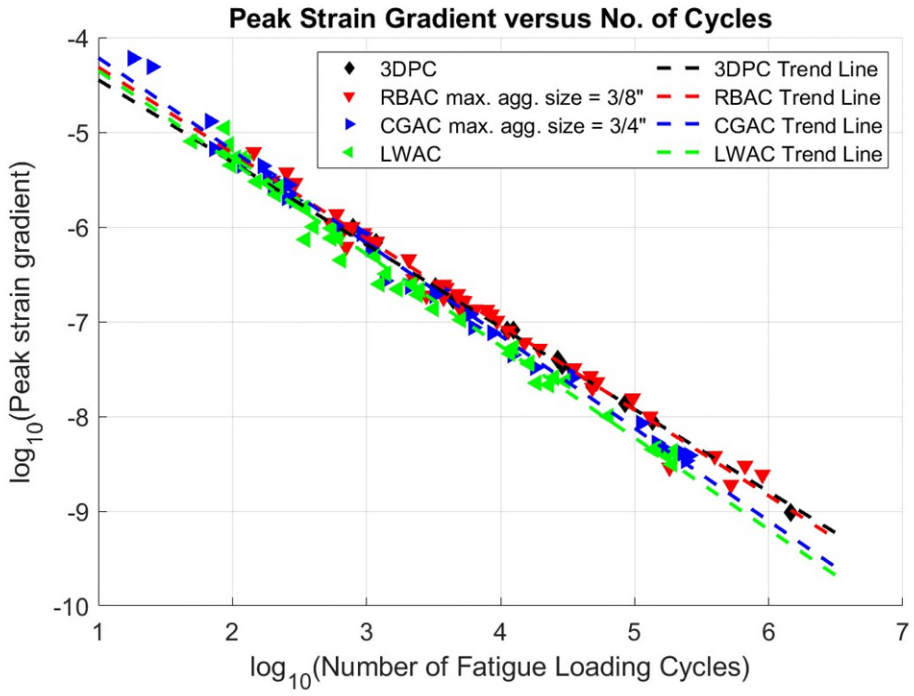

Figure 174 Correlation between the number of cycles to failure and peak strain gradient.

Table 42 shows the parameters of the linear equation between the peak strain gradient in phase II of strain evolution and the fatigue capacity. The correlation coefficient and number of data points in each case are listed as well. A few parameters from the oldest to newest literature review are also included in this table to show the applicability of this correlation for different concrete materials. Table 43 and Table 44 show the same content for the valley strain gradient and stiffness gradient, respectively.

Table 42 Parameters of peak (maximum) strain gradient correlation with fatigue capacity

Concrete Name	a	b	R^2	Number of test results
3DPC	-3.7419	-1.0970	0.998	12
RBAC	-3.6666	-1.0900	0.987	44
CGAC	-3.2562	-1.0147	0.992	45
LWAC	-3.4241	-1.0220	0.99	45
High-strength concrete [23]	-3.364	-1.013	0.981	123
PC [26]	-3.9512	-1.1352	0.9845	38
Normal strength concrete [20]	-3.919	-0.865	0.964	47
Gravel concrete [35]	-2.6716	-0.89	-	24
Limestone concrete [35]	-2.9508	-0.98	-	24
Lytag Concrete [35]	-2.7852	-1.06	-	24
Normal strength concrete II [24]	-3.0458	-0.972	-	-

6.3.5.3.2 Valley Strain Gradient vs. Nf

$$\log(Nf) = a + b * \log(VSG)$$ Equation 5

Table 43 Parameters of valley (minimum) strain gradient correlation with fatigue capacity

Concrete Type	a	b	R^2	Number of test results
3DPC	-4.2281	-1.1455	0.998	12
RBAC	-4.0313	-1.1308	0.987	44
CGAC	-3.6149	-1.0512	0.992	45
LWAC	-3.7953	-1.0520	0.99	45
High-strength concrete [23]	-3.571	-1.014	0.966	123
PC [26]	-4.3537	-1.1791	0.9866	38
Normal strength concrete [20]	-4.280	-0.817	0.927	47

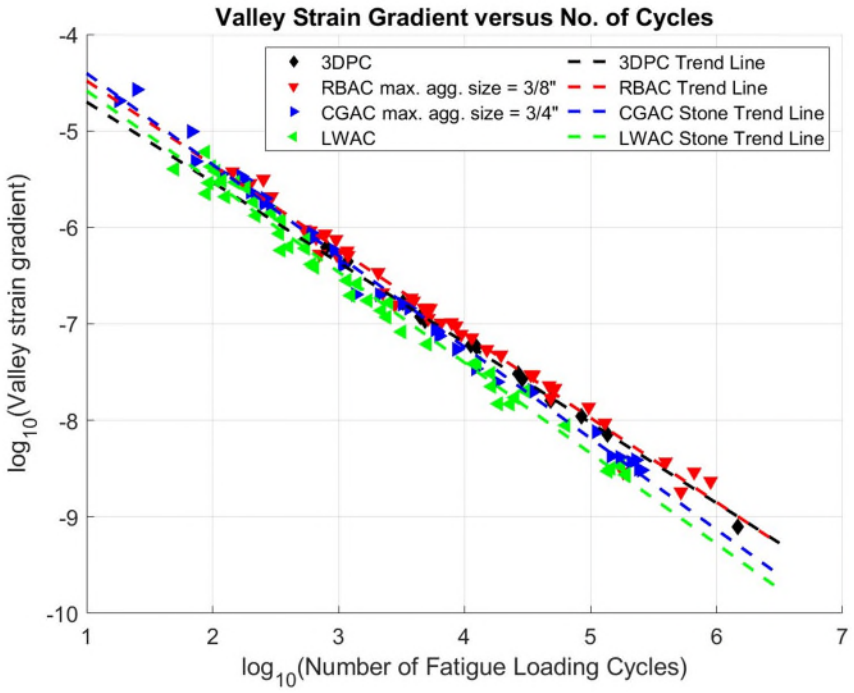

Figure 175 Correlation between the number of cycles to failure and valley strain gradient.

6.3.5.3.3 Stiffness degradation gradient vs. Nf

$$log(Nf) = a + b * log(SSG^2)$$ Equation 6

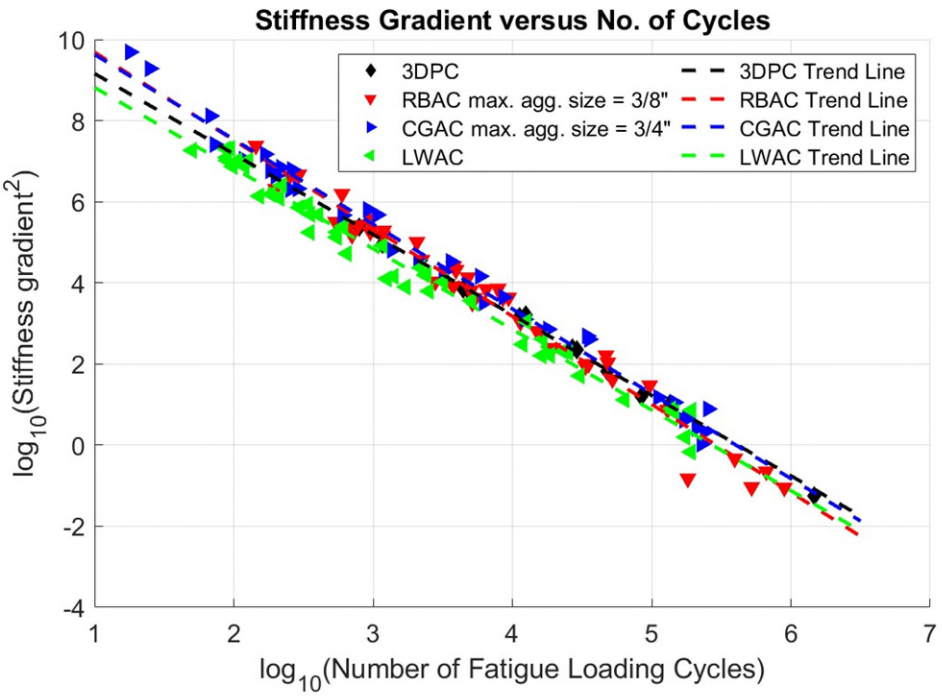

Figure 176 Correlation between the number of cycles to failure and stiffness gradient.

Table 44 Parameters of Stiffness degradation gradient correlation with fatigue capacity

Concrete	a	b	R^2	Number of test results
3DPC	5.5908	-0.4983	0.997	12
RBAC	5.4242	-0.4498	0.976	44
CGAC	5.5769	-0.4722	0.987	45
LWAC	5.3981	-0.4944	0.982	45

6.3.5.4 Appearance of visual cracks

One of the primary objectives of this experimental campaign was to determine the timing of visual crack formation on the concrete surface under fatigue loading and to investigate any potential correlation between the visual crack appearance and the strain evolution stage or fatigue capacity. As mentioned in description of the test setup, to achieve this goal, two GoPro cameras were positioned on opposite sides of a concrete cylindrical specimen subjected to fatigue loading, where the strain gauges were mounted. The cameras captured images at

predefined intervals. Following the failure of the specimen, the images from both sides were analyzed to identify the moment when the first visual crack appeared on the surface. The corresponding average strain at this moment was then considered as the strain value at which the surface crack occurred.

Figure 177 shows the peak strain related to visual crack appearance plotted versus the normalized monotonic stress-strain test results of the same concrete batch for river-based coarse aggregate concrete. The main observation is that these peak strain points related to the first visual crack mostly fall within the range of strain related to the strength (peak stress) of concrete under monotonic uniaxial testing collected from the monotonic test results of the same batch of concrete. Figure 178 and Figure 179 show the same plot for crushed granite coarse aggregate concrete and lightweight coarse aggregate concrete, respectively. The only difference is that the peak strain related to the first visual crack for lightweight concrete mostly falls before the range of strain related to the strength of the concrete. This observation is reasonable considering the brittle failure of the lightweight concrete under monotonic tests.

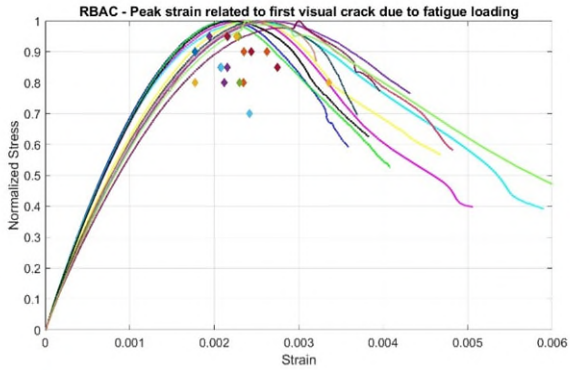

Smin = 0.05

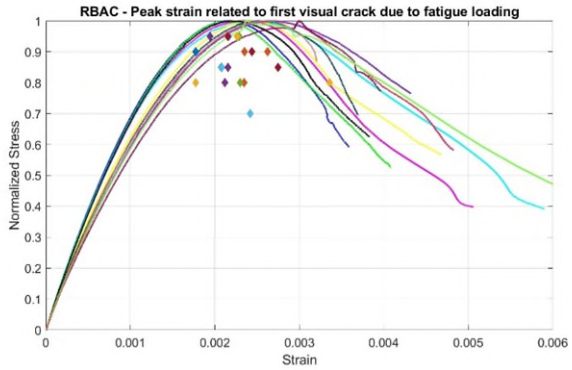

Smin = 0.20

Figure 177 Peak strain related to the stag of visual crack appearance due to fatigue loading for river base aggregate concrete.

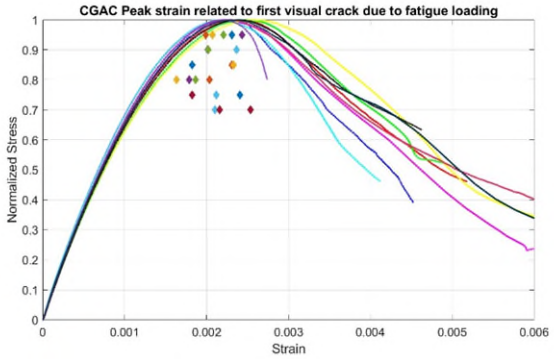

Smin = 0.05

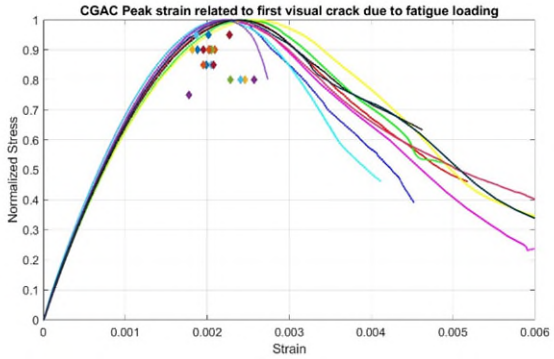

Smin = 0.20

Figure 178 Peak strain related to the stag of visual crack appearance due to fatigue loading for crushed granite coarse aggregate concrete.

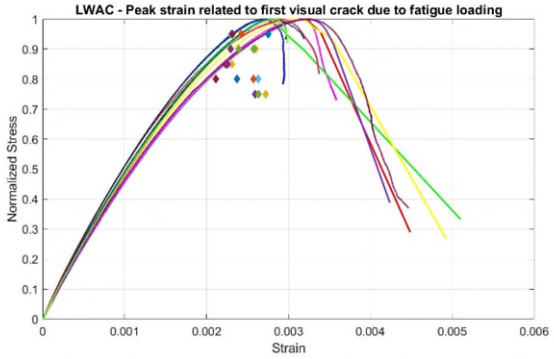

Smin = 0.05

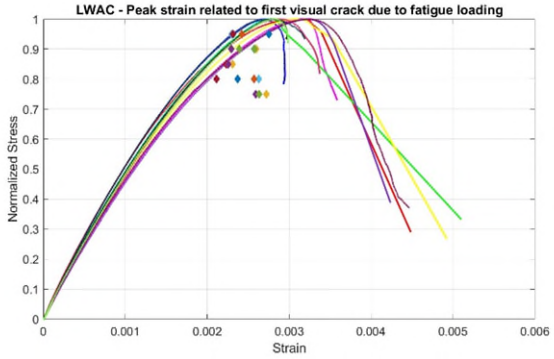

Smin = 0.20

Figure 179 Peak strain related to the stag of visual crack appearance due to fatigue loading for lightweight coarse aggregate concrete.

The observations show that the first visual crack appears at around 70% to 80% of fatigue life. A literature review of strain evolution under fatigue loading and our testing shows the concrete transition from phase II (linear) to phase III (final phase) at around 80% to 90% of fatigue life.

This means that a visual crack appears on the concrete surface just before the transition point to phase III. Another important observation was that the first visual crack appeared earlier in fatigue life for a higher minimum stress ratio of fatigue loading.

Table 45 Ratio of the fatigue life (capacity) at which the first visual crack observed

Concrete type	Minimum stress level of the fatigue loading	The ratio of the fatigue life (capacity) at which the first visual crack was observed	
		Median	Mean
RBAC	Smin = 0.05	0.65*Nf	0.65*Nf
	Smin = 0.20	0.78*Nf	0.75*Nf
CGAC	Smin = 0.05	0.77*Nf	0.75*Nf
	Smin = 0.20	0.74*Nf	0.70*Nf
LWAC	Smin = 0.05	0.83*Nf	0.78*Nf
	Smin = 0.20	0.71*Nf	0.70*Nf

6.3.6 Conclusions

In this study, the strain-related fatigue characteristics of 3 different concrete types were investigated using uniaxial compressive cyclic experimental tests. A new improved strength estimation method, ISEM, for predefining the fatigue load protocol more accurately was also used to reduce the effect of strength variation on the outcome of the tests. Here is the summary of the findings:

I. **Effect of aggregate size and type on fatigue capacity**:

Concrete with smaller, round, coarse aggregates (river-based) exhibited significantly higher fatigue capacity compared to concrete with larger, angular, coarse aggregates (crushed granite). This difference highlights the critical role of aggregate geometry and size in influencing microcrack development and fatigue life.

The smaller round aggregates delayed microcrack initiation, resulting in greater durability under cyclic loading.

Also, it has been observed that rounded aggregates (e.g., river gravel) lead to better packing and reduced voids due to their smooth surfaces and ease of movement during compaction. This generally results in lower porosity in the concrete. In contrast, angular aggregates (e.g., crushed stone) have more irregular shapes and sharp edges, which can lead to higher interlocking. While interlocking can improve strength, it may increase voids and porosity if not well-compacted [144]. Higher porosity in the concrete leads to earlier microcrack formation and lower fatigue capacity.

II. Difference between cast-in concrete cylinder and cored cylinder's fatigue capacity

A notable observation emerged from the comparison of fatigue capacities between cylinders cast in plastic molds and those extracted from slabs using the same concrete mix. Although the average fatigue capacities of both sample types were similar, the cored cylinders exhibited greater variability in their results. This increased variability is likely due to early crack initiation in certain specimens with high stress concentrations, especially those containing large aggregates near the edges.

III. **Strain evolution and stiffness degradation**:

The strain-related fatigue characteristics showed three distinct phases of strain evolution and stiffness degradation, consistent with findings in normal concrete. Strain evolution plots displayed an inverted S-shape, while stiffness degradation followed an upright S-shape [20, 23-25]. These patterns affirm prior research and provide a robust framework for interpreting fatigue behavior.

IV. **Correlation between strain metrics and fatigue life**:

The study established a strong linear correlation between the logarithm of the average gradients of peak and valley strain in Phase II and the logarithm of cycles to failure. This relationship allows for predictive modeling of fatigue capacity in run-out tests with high accuracy. The correlation of the average gradient of peak and valley strain, stiffness in phase II, and the number of cycles to failure is a linear correlation between these parameters' logarithm and N_f's logarithm. The high correlation coefficient (R^2) proves a direct relationship between these factors. Therefore, these linear equations can serve to predict the fatigue capacity of run-out tests.

V. **Impact of minimum stress ratios on crack formation**:

Higher minimum stress ratios accelerated the appearance of visual cracks, emphasizing the sensitivity of fatigue life to loading conditions. Visual cracks typically formed at 70–80% of the fatigue life, just before the transition to Phase III strain evolution.

VI. **Improved method for estimating strength (ISEM)**:

The ISEM successfully improved fatigue test reliability by reducing variability in strength estimation. This precision allowed for better-defined fatigue load protocols, mitigating the effects of strength variation across specimens and enhancing consistency in fatigue testing outcomes.

VII. **Behavior of lightweight concrete**:

Lightweight aggregate concrete demonstrated a brittle failure mode, with visual cracks appearing earlier in the fatigue life compared to normal concrete specimens. This reflects its inherent material characteristics and challenges its application in high-fatigue environments.

VIII. **Role of visual monitoring of cracks**:

The use of synchronized imaging allowed precise detection of the first visual cracks on specimen surfaces. These cracks correlated strongly with critical strain values, validating their importance as indicators of impending failure. The analysis revealed that for river-based coarse aggregate concrete, the peak strain points related to the first visual crack fell within the strain range associated with the concrete's strength. However, for lightweight concrete, the first visual crack appeared earlier compared to other normal concrete specimens, reflecting its brittle nature under monotonic tests. Additionally, it was observed that visual cracks appeared at around 70% to 80% of the concrete's fatigue life, just before transitioning to phase III of strain evolution. Higher minimum stress ratios in fatigue loading led to earlier crack appearances, highlighting the influence of loading conditions on fatigue behavior.

IX. **Code comparisons and observations**:

Experimental results often surpassed the fatigue capacities predicted by established standards such as Model Code 2010, DNVGL-C502, and EuroCode2. This suggests a need for revising fatigue models to reflect advancements in material characterization and testing methods.

X. Additional considerations

The experimental framework could be expanded to include the effects of other environmental and loading parameters (e.g., temperature and humidity) on aggregate behavior. Also, the strong correlation between material-specific fatigue characteristics and overall structural performance underscores the need for continued development of tailored design guidelines.

7 Recommendations for Fatigue Testing

A task group was established within ACI Committee 215 on Fatigue to shepherd this through the development and revision of two technotes. The titles of these technotes were chosen to be "*Technote 4 - ACI 215 Recommended Practice for Compression Fatigue Testing of Concrete*", and "*ACI Technote 5: Recommended Procedure for Development of an S-N Curve for a Specific Concrete Mix*". The numbering is based on the process of ACI Committee 215.

7.1 ACI Technote #4 - Recommended Practice for Compression Fatigue Testing of Concrete

As mentioned in Chapter 3, the misreporting of data in concrete fatigue testing research frequently results in unreliable conclusions and inconsistent outcomes across different studies. One of the important factors that has a huge impact on the concrete fatigue testing result is the assumed strength of the specimen. The variability of the strength has a considerable impact on the fatigue loading protocol setup and, consequently, on the final fatigue life observed during the testing. To address this issue, the Improved Strength Estimation Method (ISEM) and its Neural Network-based variant (NNISEM) were introduced. These methods aim to improve the accuracy of predicting concrete's fatigue life by carefully accounting for key influencing factors and ensuring thorough data documentation. ISEM employs five distinct base datasets to boost prediction accuracy, reducing the average error to 2.68% compared to 3.57% with traditional methods. NNISEM further enhances precision by using augmented data and optimizing hyperparameters, lowering the average error to 1.92%. Both approaches highlight the importance of detailed reporting, such as mix design, curing processes, and strain measurement, to increase the reliability and repeatability of fatigue test outcomes. Standardized protocols are essential for

deepening the understanding of concrete's behavior under fatigue loading and creating more accurate predictive models.

7.1.1 Introduction

The incomplete or inconsistent reporting of data in scientific papers, particularly in the context of concrete fatigue testing, can significantly undermine the reliability and applicability of research findings. Many studies fail to provide critical information about influencing factors and testing conditions, which leads to inconsistencies and variability in the data. For example, differences in specimen geometry, material properties, and loading protocols are often not adequately documented or explained. These omissions can result in large variations in fatigue life predictions, making it difficult to draw accurate conclusions or compare results across different studies. Therefore, it is essential for researchers to thoroughly document and report all relevant variables and conditions to ensure the reproducibility and comparability of experimental results.

The motivation for the proposed fatigue testing protocol is driven by the very large scatter in the measured number of fatigue cycles to failure by different researchers for the same fatigue Smax/Samin stress ratios (Smax, Smin), which have been shown to range by a factor of more than 1000 (shown in Figure 180). This wide range is likely the reason why fatigue stress models and standards, which are derived from different subsets of test results, can vary by more than a factor of 10 (shown in Figure 180).

Although there is an inherent degree of randomness (aleatory uncertainty) in the measured number of fatigue cycles to failure, the scale of this variation is considerable. This can be attributed to differences in fatigue testing methods used by researchers and the lack of reporting and consideration of significant influencing factors.

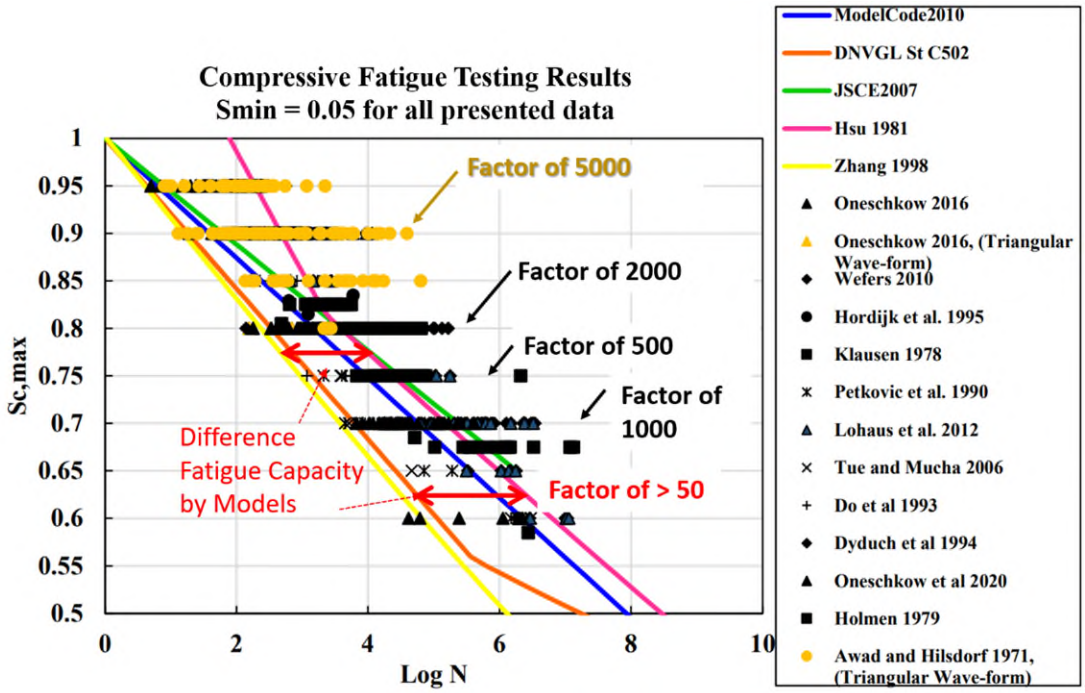

Figure 180 S-N models and experimental data points for a minimum stress level of 0.05[23, 32, 37, 39, 41, 51, 58, 60, 65, 66, 78, 86, 119-121, 145]

The analysis of the sensitivity of fatigue models to concrete strength reveals that a 5% error in estimating material strength can result in a four to fivefold variation in predicted fatigue life. For instance, if the desired fatigue loading is (Smax, Smin) = (0.80, 0.20), and the assumed strength is accurate, the DNV fatigue model predicts a failure after 1,000 cycles. However, if there is a 5% error in the assumed strength, the predicted number of cycles to failure would range from 269 to 3,594 cycles. For more information, see Table 46.

Table 46 Impact of assumed strength error on fatigue capacity using three different fatigue models

fcm	Smax	Smin	Number of cycles to failure (Nf)		
			Model Code 2010 [119]	DNV [60]	Eurocode 2 [146]
fcm-5% (If strength was 5% lower)	0.84	0.21	1,797	269	386
fcm (Planned Smax=0.80)	0.80	0.20	10,208	1,000	1,711
fcm+5% (If strength was 5% higher)	0.76	0.19	54,996	3,594	7,582
fcm-5% (If strength was 5% lower)	0.63	0.21	33,572,059	417,112	2,208,912
fcm (Planned Smax=0.60)	0.60	0.20	104,199,038	1,000,000	7,220,567
fcm+5% (If strength was 5% higher)	0.57	0.19	322,815,611	2,805,597	23,602,833

To address these issues, a comprehensive and standardized methodology for reporting fatigue test data is crucial. The development of the Improved Strength Estimation Method (ISEM), a human-based method, and the use of NN methods could exemplify such an effort. This method involves detailed steps for establishing stress-strain relationships, conducting monotonic and fatigue testing, and analyzing results with specific criteria for data inclusion and exclusion. By adhering to such standardized protocols, researchers can minimize the impact of aleatory uncertainties and improve the accuracy of fatigue life predictions. Additionally, creating detailed databases that include all relevant and necessary test parameters and results, as demonstrated by the experimental test data repository, can significantly enhance the understanding of concrete behavior under fatigue loading and facilitate the development of more reliable predictive models.

7.1.2 Methodology

7.1.2.1 Improved Strength Estimation Method (a human-based guestimating method)

The proposed fatigue testing protocol is outlined below:

1. Establish stress-strain relationships from monotonic testing using the ASTM C-39 "Concrete Cylinder Compressive Testing" specified loading rate of 35±7 psi/second. Conduct at least five compressive cylinder tests. If any maximum stresses vary by more

than 6% from the mean of all five tests, discard those results and perform replacement tests until five satisfactory results are obtained. Additionally, discard and replace test results if boundary condition failures are suspected or there is significant non-linear distribution of axial strain around the perimeter before failure. The measured strain (ε_c) in each test should be the average of at least two strain measurements taken around the perimeter of the test cylinder. The average of the five acceptable test results is denoted as fcm_ave_C39.

2. Plot the results from the five or more compressive cylinder tests on the same graph and examine if the fc versus ε_c curves is adequately separated (e.g., higher strength concrete has higher fc values for most of the loading history). If the curves are not adequately separated, conduct replacement tests until the relative shape of the five curves is deemed acceptable.
3. For each fatigue test, begin by loading up to 95% of Smax calculated using fcm_ave_C39 at the C-39 loading rate, then reduce and hold the load at Smean (Smax/2 + Smin/2). Calculate an improved estimate of the monotonic strength (fcm) for that particular cylinder based on the pattern of measured strain up to 95% of Smax calculated using fcm_ave_C39 relative to that measured for the five representative cylinders tested until failure. This calculation should take no more than five minutes. The measured strain should be the average of at least two measurements around the perimeter of the test cylinder.
4. For each combination of Smax and Smin, conduct a minimum of three tests. Tests with an abnormally low number of cycles to failure may be ignored if sufficiently justified, such as due to an end region failure, significant variation in measured strain around the

cylinder circumference, or an unrealistic failure type. If a test is stopped before failure, report the average axial strain at Smax and Smin in the last loading cycle. The stress-strain response should be measured for all fatigue test results, with the average value based on at least three measured axial deformations around the cylinder circumference.

For instance, a set of compressive fatigue tests on 3DPC cylinders were done at Tufts University. Figure 181 shows the monotonic test results of a few of these cylinders with a high variation in the final strength (The coefficient of variation is about 11%). The high variation in the strength was not preventable due to the nature of the 3DPC mixture and production process. The importance of this method of defining the fatigue loading based on this protocol is highlighted in this case. Figure 181 shows that fatigue test #7 has the closest stress-strain behavior to monotonic test result #5. Thus, the estimated strength of this specimen for defining the fatigue loading protocol using ISEM method would be 7400 psi (rather than 6800 psi, which is the average strength of this batch of concrete).

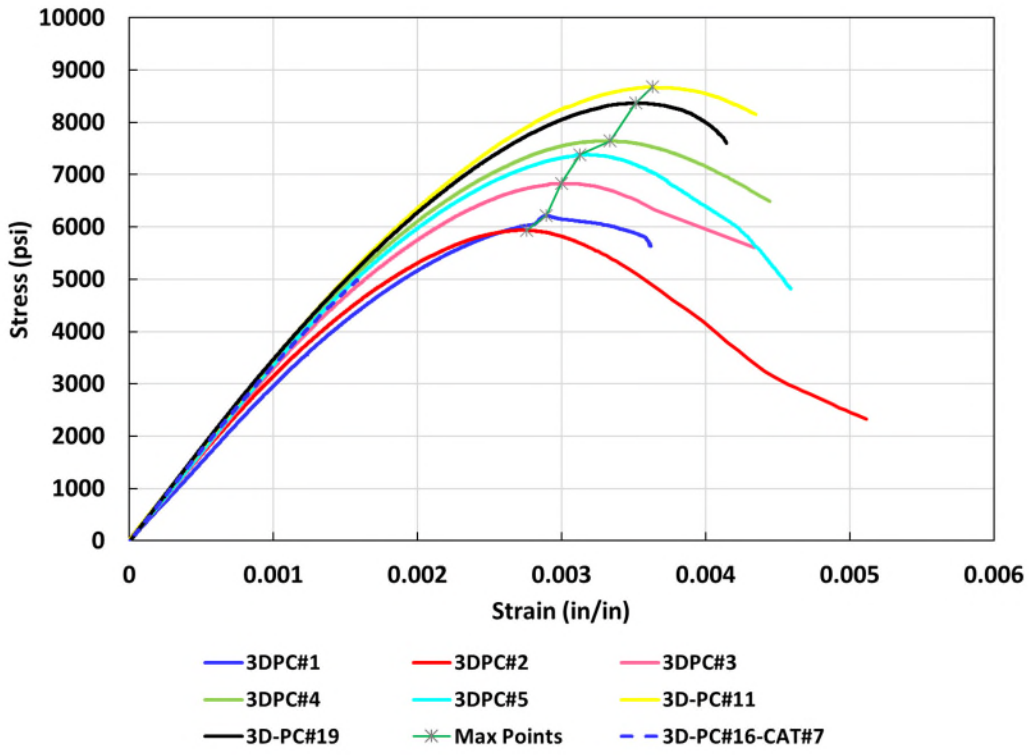

Figure 181 3D-printed concrete monotonic test results

7.1.2.2 Neural Network Improved Strength Estimation Method (NNISEM)

In this method, we utilize the same data to estimate the material strength using a modified version of the ISEM method combined with a Neural Network (NN). The key distinction in this approach is that, in step 3 of the ISEM method, a trained NN model is employed to predict the strength of the material that will be subjected to fatigue loading. To enhance the model's accuracy, the training dataset is expanded and augmented. Subsequently, hyperparameters are fine-tuned to prevent overfitting. Finally, a random forest regressor model is used to train the NN. These steps are briefly outlined below, with the results discussed in the discussion section.

7.1.2.2.1 Data Loading and Augmentation

The methodology begins with the systematic loading and augmentation of the dataset. The code reads multiple text files from a specified directory, each containing data on stress and strain

measurements. To enhance the robustness and generalizability of the model, data augmentation techniques are applied. Specifically, the `augment_data` function adds noise to the stress and strain values to simulate variability and create multiple augmented datasets from each original file. This augmentation process is repeated a specified number of times, helping to prevent overfitting and ensure that the model can generalize well to new, unseen data.

7.1.2.2.2 Model Training with Hyperparameter Tuning

After data augmentation, the code proceeds to train a Random Forest regression model. A significant enhancement in this methodology is the incorporation of hyperparameter tuning using Grid Search. The `hyperparameter tuning` function explores a range of hyperparameters, such as the number of estimators, maximum depth of the trees, and feature selection strategies. This tuning is performed using cross-validation to ensure the model's parameters are optimized based on the training data's performance. The best hyperparameters identified through Grid Search are then used to configure the final Random Forest model, which is trained on the full augmented dataset.

7.1.2.2.3 Evaluation and Visualization

The final phase of the methodology involves evaluating the model's performance and visualizing the results. A set of test files is randomly excluded from the training process to serve as a validation set. The model's performance is assessed by predicting the maximum stress values for these test files and comparing the predicted values with the actual values. Various error metrics, including percentage error and mean squared error, are calculated to quantify the model's accuracy. The results are visualized through a bar plot, where the errors for the training and test sets are distinctly colored, providing a clear visual representation of the model's performance. Additionally, the plot includes average error lines for a comprehensive comparison. This

approach ensures that the model's strengths and weaknesses are easily identifiable, guiding further refinement and application.

7.1.3 Experimental Testing

A few normal-strength concrete cylindrical samples have been used after two years from the casting date to do the monotonic compressive test and establish a small database. The concrete specimens had an average strength of 5975 psi, and the coefficient of variation was 4%, which is typical variation for normally casted concrete. There is no information about the mix design and aggregate characteristics available. Table 47 presents a statistical summary of the test results. Table 48 presents the detailed information about all the test results. The data include the peak load, maximum experienced stress, strain related to maximum experience stress, type of failure, shape of failure, and average loading rate (to make sure the tests are in agreement with the standard required loading rate). Figure 182 shows the stress-strain plots of every single monotonic test result. This plot depicts the variation in load pathes and the strength of each specimen from the same batch of concrete. Figure 183 shows the different failure shapes defined by ASTM C39 standard [147].

Table 47 Statistic summary of the monotonic test results of OCNC concrete

	Load (lb)	Stress (psi)	Strain
Avg.	75085	5975	0.00204
Standard Deviation	3259	259	0.00015
Std.Dev./Avg.	4%	4%	7%
Max	83392	6636	0.00239
Min	70435	5605	0.00178

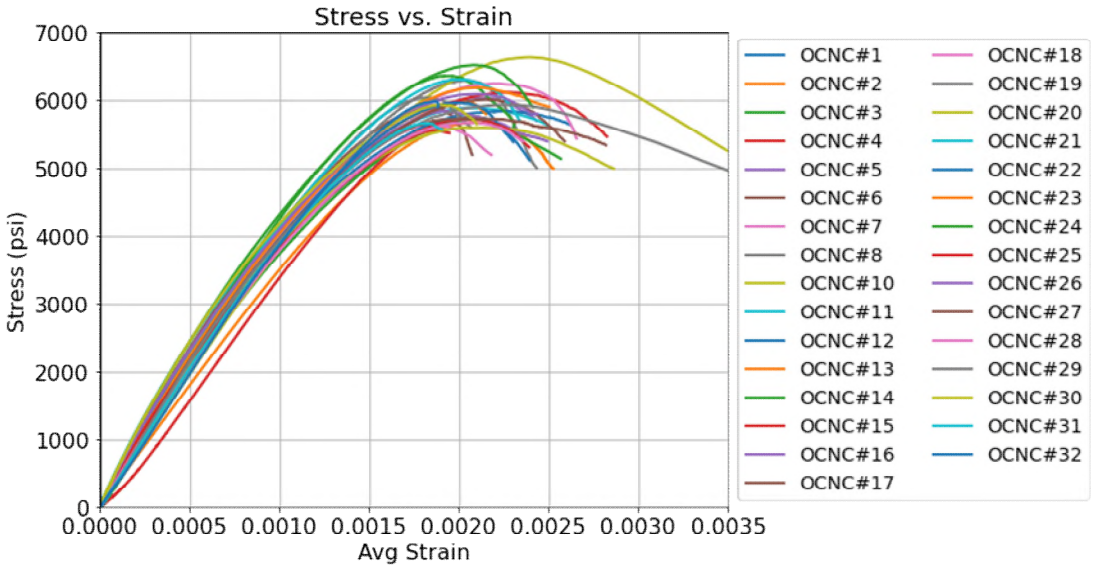

Figure 182 Monotonic stress-strain test results of the concrete named OCNC

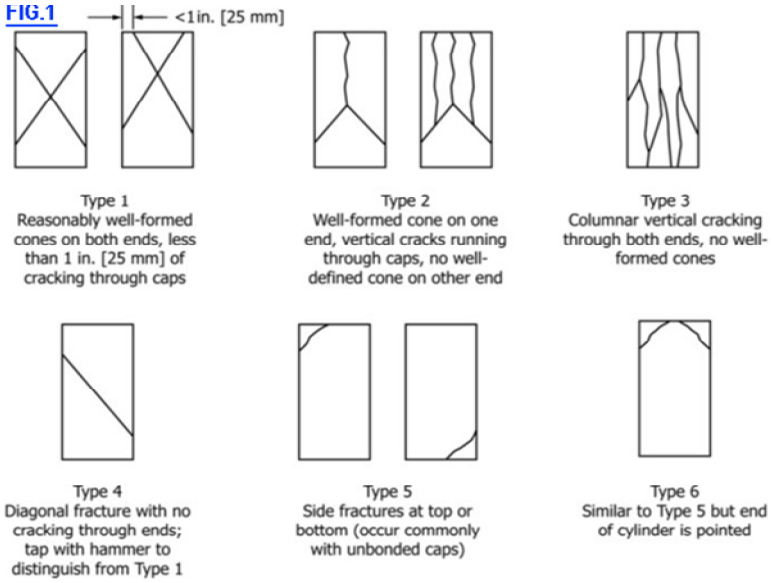

Figure 183 Shape of the concrete cylindrical specimen failure under monotonic compressive loading [147]

Table 48 Monotonic test results of concrete (called OCNC)

Test No.	Load (lb)	Stress (psi)	Avg. Strain	Failure type	Failure shape	Loading rate (psi/sec)
OCNC#1	72362	5758	0.00209	Ductile	Type 1	38
OCNC#2	71476	5688	0.00209	Ductile	Type 2	36
OCNC#3	72008	5730	0.00207	Brittle	Type 4	31
OCNC#5	75945	6044	0.00210	Ductile	Type 2	35
OCNC#6	74343	5916	0.00185	Ductile	Type 3	33
OCNC#7	71039	5653	0.00186	Ductile	Type 1	32
OCNC#8	76379	6078	0.00178	Ductile	Type 2	28
OCNC#10	83392	6636	0.00239	Brittle	Type 1	44
OCNC#11	74053	5893	0.00206	Brittle	Type 1	37
OCNC#12	73487	5848	0.00224	Ductile	Type 1	39
OCNC#13	75218	5986	0.00200	Ductile	Type 1	39
OCNC#14	79950	6362	0.00194	Ductile	Type 4	42
OCNC#15	76920	6121	0.00227	Ductile	Type 4	45
OCNC#16	73486	5848	0.00191	Ductile	Type 1	34
OCNC#17	75592	6015	0.00215	Ductile-brittle	Type 4	38
OCNC#18	78598	6255	0.00219	Ductile	Type 1	37
OCNC#19	75902	6040	0.00183	Ductile	Type 4	39
OCNC#20	70435	5605	0.00203	Brittle	Type 1	40
OCNC#21	79318	6312	0.00196	Ductile	Type 1	41
OCNC#22	75012	5969	0.00197	Ductile	Type 4	38
OCNC#23	77820	6193	0.00210	Ductile-brittle	Type 4	30
OCNC#24	81973	6523	0.00208	Ductile	Type 1	34
OCNC#25	72105	5738	0.00204	Ductile-brittle	Type 1	35
OCNC#26	76567	6093	0.00211	Ductile	Type 1	38
OCNC#27	72136	5740	0.00203	Ductile	Type 4	32
OCNC#28	71379	5680	0.00209	Ductile	Type 4	35
OCNC#29	74572	5934	0.00228	Brittle	Type 1	35
OCNC#30	74625	5938	0.00190	Brittle	Type 1	33
OCNC#31	71248	5670	0.00181	Brittle	Type 1	34
OCNC#32	75201	5984	0.00186	Brittle	Type 1	42

7.1.4 Discussion and Results

7.1.4.1 ISEM

In this method, the five most discernible data were set aside as base test results. Figure 184 depicts the stress-strain response of the base test results. Then, other test data was filtered to

exclude any data above certain stress thresholds (in this case, 80% of average strength). The filtered data error with respect to five base test results was calculated, and the strength of any of the base test results with the lowest error amount was assigned as representative strength of that data. The error of the results shows that the ISEM method generally performs better than the old-fashioned method (assuming the average strength as the strength of the whole batch) (see Table 49). The average error using ISEM method is 2.68%, which is better than 3.57% error of using the old-fashioned method. The improved accuracy of the ISEM method is attributed to its ability to account for variations in individual test conditions and material properties. This approach helps in identifying outliers and anomalies more effectively. Moreover, the use of multiple base datasets provides a more robust reference for error calculation. Consequently, this method enhances the reliability of strength predictions in fatigue-loaded concrete specimens. The study's findings support the adoption of the ISEM method in routine testing to achieve more accurate and reliable results.

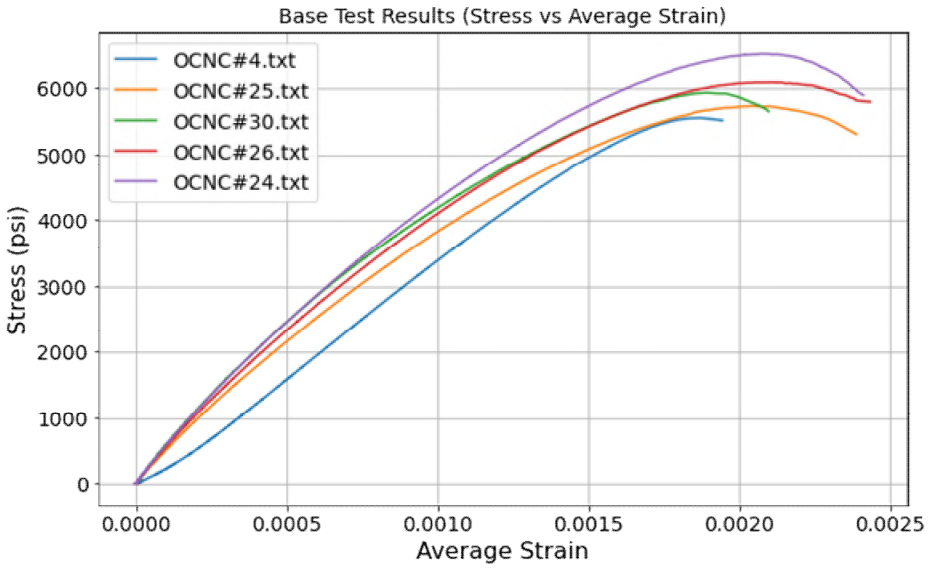

Figure 184 Base test results used to predict the strength using ISEM method

Table 49 Performance of ISEM method compared to old fashioned method (assuming the average strength for all the specimens)

Test #	Actual Strength	Predicted Strength (ISEM)	% Error	% Error Old-fashioned	Data Type
OCNC#1	5758.4	5737.95	0.36	3.63	Test
OCNC#2	5687.91	5558.09	2.28	4.8	Test
OCNC#3	5730.2	5737.95	0.14	4.1	Test
OCNC#4	5558.09	5558.09	0	6.98	Base
OCNC#5	6043.52	5737.95	5.06	1.15	Test
OCNC#6	5916.01	6093.02	2.99	0.99	Test
OCNC#7	5653.1	5737.95	1.5	5.39	Test
OCNC#8	6298.3	5737.95	8.9	5.41	Test
OCNC#11	5892.97	5938.44	0.77	11.06	Test
OCNC#12	5847.94	5737.95	1.88	1.37	Test
OCNC#13	5985.65	6093.02	1.79	2.13	Test
OCNC#14	6362.25	6093.02	4.23	0.18	Test
OCNC#15	6121.07	5737.95	6.26	6.48	Test
OCNC#16	5847.8	5737.95	1.88	2.44	Test
OCNC#17	6015.39	5737.95	4.61	2.13	Test
OCNC#18	6254.59	6093.02	2.58	0.68	Test
OCNC#19	6040.1	6093.02	0.88	4.68	Test
OCNC#20	5605.07	5737.95	2.37	1.09	Test
OCNC#21	6311.92	6093.02	3.47	6.19	Test
OCNC#22	5969.25	5737.95	3.87	5.64	Test
OCNC#23	6192.69	6093.02	1.61	0.1	Test
OCNC#24	6523.19	6523.19	0	3.64	Base
OCNC#25	5737.95	5737.95	0	9.17	Base
OCNC#26	6093.02	6093.02	0	3.97	Base
OCNC#27	5740.36	5737.95	0.04	1.98	Test
OCNC#28	5680.13	5737.95	1.02	3.93	Test
OCNC#29	5934.21	5737.95	3.31	4.93	Test
OCNC#30	5938.44	5938.44	0	0.68	Base
OCNC#31	5669.74	5737.95	1.2	0.61	Test
OCNC#32	5984.32	5737.95	4.12	5.11	Test

7.1.4.2 NNISEM

Initially, the impact of the number of monotonic test results in the database on the mean squared error (MSE) was investigated. Random samples of 5, 10, 15, 25, and 30 monotonic test data were

used for model training, with 20% of each dataset reserved for testing. The model identifies features from the stress-strain data up to a specific stress level, which is 80% of the average strength in this case. For each test, strains measured on two sides of the cylinder are used to train the neural network (NN) model, rather than using just the average strain. These features serve as the model inputs, while the output is the material strength, defined as the maximum stress the specimen can withstand under monotonic compressive loading. Figure 185 demonstrates that the test data MSE generally decreases as the number of input data increases. Consequently, the entire available dataset was used to train and test the NN model.

Techniques were employed to augment the database to further enhance model performance and reduce MSE, effectively multiplying the input data. In this study, each monotonic test result was reproduced using augmentation techniques four times, increasing the database size to 150 entries. This augmented dataset was then used to train and test the model, resulting in an approximately 30% reduction in MSE for both training and test sets. Additionally, to further strengthen the model, a 5-fold cross-validation was conducted.

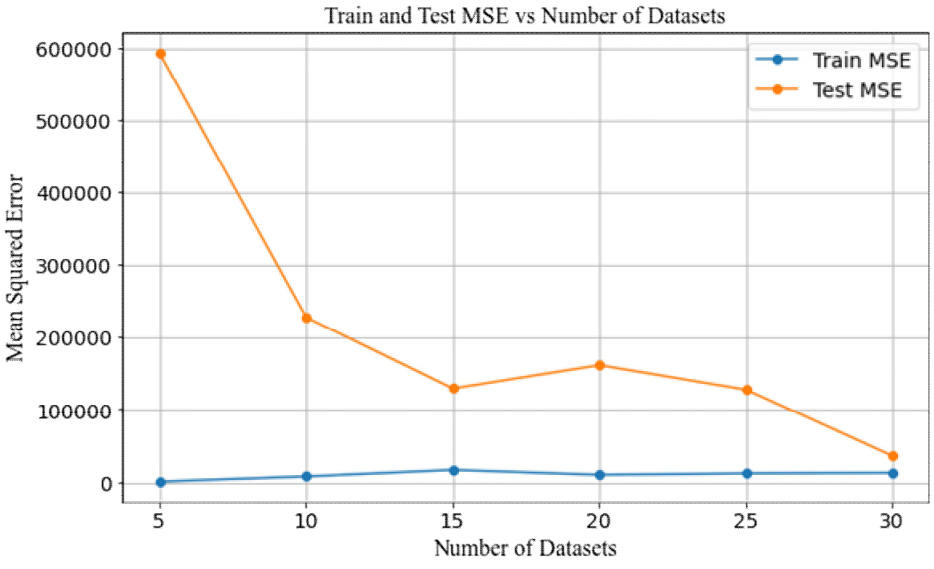

Figure 185 Effect of the number of input data on the model error

The final trained model using data augmentation, hyperparameter tuning, and cross-validation was used to randomly choose 5/6 of the data to train the data and use 1/6 of the data to test it. Table 50 shows the NNISEM method considerably performs well in training the model, and the error percentage in predicting the actual strength is 1.92% on average compared to 2.68% for ISEM method and 3.57% using the old-fashioned method, which we use the average strength of the monotonic test as the assumed strength of all the specimens. Table 51 presents all the input data, predicted strength using NN, actual strength, amount of error using both techniques and features of which data is used as a test data set or not.

Figure 186 shows the error in the prediction of strength as a bar plot. The blue and red bars are the train and test data, respectively, using the NN method to predict the strength. The gray bars represent the number of errors, considering the average strength as the strength of all the specimens. The average error using NNISEM method is shown as a dashed line, and the average error in the average strength method is shown as a solid line.

Table 50 NN model performance on average

Method	Average percentage error	
	Train model	Test model
NNISEM	1.92%	5.56%
Average Strength method (assuming the average strength)	3.57%	5.41%

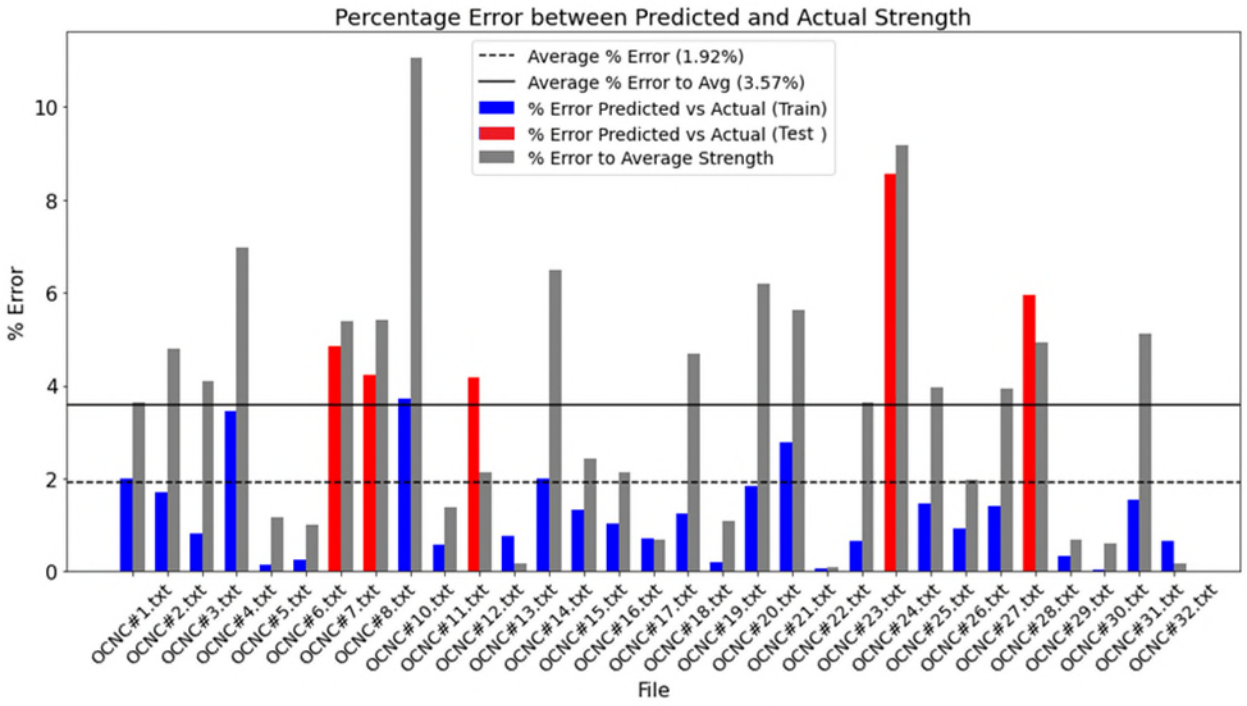

Figure 186 bar-plot comparing the error of the NNISEM model and old-fashioned model

Table 51 Performance of NN model compared to old fashioned method (assuming the average strength for all the specimens)

Specimen Name	Predicted Strength (psi)	Actual Strength (psi)	% Error NNISEM	% Error Old-fashioned	Data Type
OCNC#1	5873.35	5758.4	2	3.63	Train Data
OCNC#2	5784.68	5687.91	1.7	4.8	Train Data
OCNC#3	5776.66	5730.2	0.81	4.1	Train Data
OCNC#4	5750.59	5558.09	3.46	6.98	Train Data
OCNC#5	6034.59	6043.52	0.15	1.15	Train Data
OCNC#6	5901.32	5916.01	0.25	0.99	Train Data
OCNC#7	5927.33	5653.1	4.85	5.39	Test Data
OCNC#8	6031.37	6298.3	4.24	5.41	Test Data
OCNC#10	6389.9	6636.13	3.71	11.06	Train Data
OCNC#11	5859.13	5892.97	0.57	1.37	Train Data
OCNC#12	6092.55	5847.94	4.18	2.13	Test Data
OCNC#13	5940.84	5985.65	0.75	0.18	Train Data
OCNC#14	6234.49	6362.25	2.01	6.48	Train Data
OCNC#15	6040.04	6121.07	1.32	2.44	Train Data
OCNC#16	5908.77	5847.8	1.04	2.13	Train Data
OCNC#17	6057.98	6015.39	0.71	0.68	Train Data
OCNC#18	6176.15	6254.59	1.25	4.68	Train Data
OCNC#19	6028.45	6040.1	0.19	1.09	Train Data
OCNC#20	5707.67	5605.07	1.83	6.19	Train Data
OCNC#21	6135.81	6311.92	2.79	5.64	Train Data
OCNC#22	5965.68	5969.25	0.06	0.1	Train Data
OCNC#23	6152.37	6192.69	0.65	3.64	Train Data
OCNC#24	5964.73	6523.19	8.56	9.17	Test Data
OCNC#25	5821.18	5737.95	1.45	3.97	Train Data
OCNC#26	6036.35	6093.02	0.93	1.98	Train Data
OCNC#27	5820.86	5740.36	1.4	3.93	Train Data
OCNC#28	6017.79	5680.13	5.94	4.93	Test Data
OCNC#29	5914.38	5934.21	0.33	0.68	Train Data
OCNC#30	5936.94	5938.44	0.03	0.61	Train Data
OCNC#31	5757.14	5669.74	1.54	5.11	Train Data
OCNC#32	6023.87	5984.32	0.66	0.16	Train Data

7.1.5 Recommended Data Gathering Items

Unfortunately, most of the published papers on concrete fatigue that present experimental data lack basic information about the critical parameters. To tackle this issue and have a baseline for experimental fatigue testing and reporting on concrete, the following items are recommended to be reported:

i. Reporting of mix design, including the amount, type, and maximum size of coarse aggregate
ii. Curing regime and moisture conditions at the time of testing
iii. Reporting of strain evolution and how this was measured
iv. Reporting of type of observed failure
v. Reporting on when the first external damage was observed
vi. Cast cylinders months before fatigue testing is started so that there is little strength gain over the duration of testing (at least 90 days)
vii. Recommendations for ensuring the inclusion of a test result in a future evaluation database (for discussion)
    - Items (ii) – (v) above
    - 2-3 measurements of compressive straining around the circumference
    - The cylinder did not have irregular surface conditions

7.1.6 Conclusion

The study emphasizes the critical importance of accurate data representation in concrete fatigue testing to ensure the reliability and consistency of research findings. The development of the Improved Strength Estimation Method (ISEM) and its Neural Network-based variant (NNISEM) highlights a significant advancement in predicting the fatigue life of concrete specimens. By using five discernible base datasets, ISEM effectively reduces the average prediction error to 2.68%, compared to the 3.57% error of traditional methods that assume the average strength for

all specimens. This improvement is attributed to ISEM's ability to account for variations in test conditions and material properties, enhancing the robustness of strength predictions.

NNISEM further refines the prediction process by employing data augmentation and hyperparameter tuning, resulting in an even lower average error of 1.92%. This method leverages advanced machine learning techniques to more accurately model the stress-strain behavior of concrete under fatigue loading. The use of augmented datasets, where each test result is reproduced multiple times with added variability, ensures that the model can generalize well to new, unseen data. Hyperparameter tuning optimizes the model configuration, further enhancing its predictive accuracy. This approach demonstrates the potential of integrating traditional engineering methods with modern data science techniques to improve testing outcomes.

The findings underscore the necessity for comprehensive and standardized reporting of experimental conditions, including mix design, curing regime, and strain evolution, to improve the reproducibility and comparability of results across different studies. Detailed documentation of testing protocols and conditions helps in identifying outliers and anomalies more effectively, contributing to a more robust understanding of concrete behavior under fatigue loading. The adoption of these enhanced methodologies and detailed documentation protocols can significantly advance the understanding of concrete behavior under fatigue loading, leading to more reliable predictive models and better-informed engineering practices. This study advocates for the integration of standardized testing methods and modern analytical techniques to achieve more accurate and reliable results in concrete fatigue research.

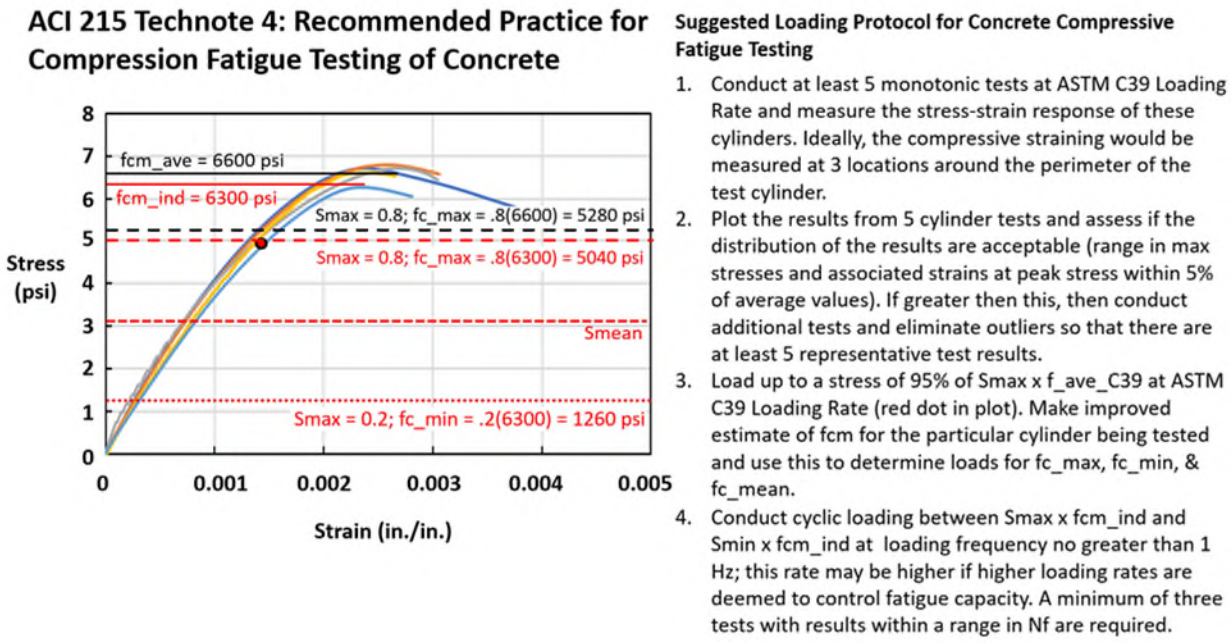

Figure 187 Improved Strength Estimate Method

7.2 ACI Technote #5 - Recommended Procedure for Development of a S-N Curve for a Specific Concrete Mix

A standardized approach to developing S-N curves for concrete through compressive fatigue testing is defined. The was created to enhance the predictability of concrete fatigue behavior by conducting extensive fatigue tests on various types of concrete.

7.2.1 Overview

This study presents a standardized methodology for developing compressive fatigue S-N curves for concrete through extensive experimental testing. The research explores the fatigue behavior under cyclic compressive loading by conducting 160 fatigue tests on four different concrete types. The testing program varies stress levels and records the number of cycles to failure, enabling the construction of S-N curves that accurately represent fatigue life. Additionally, probabilistic S-N curves are generated to account for the variability in fatigue performance, providing a comprehensive range of outcomes. This approach enhances the predictability of concrete fatigue behavior, improving structural design and durability. The results contribute to the existing literature by offering detailed experimental data and methodologies, addressing gaps related to the fatigue performance of different concrete compositions. This study is particularly valuable for infrastructure and high-rise buildings subjected to repetitive loading.

7.2.2 Introduction

Concrete's structural integrity and long-term durability are paramount in civil engineering, particularly in infrastructure and high-rise construction, where concrete is subjected to repetitive loading over its service life. Unlike static loading, where the material's behavior under a constant load is well understood, cyclic or fatigue loading presents a unique challenge. Fatigue in concrete

is characterized by the progressive deterioration of the material under repeated stress, leading to eventual failure even at stress levels well below its static strength. Understanding the fatigue behavior of concrete is essential for predicting its service life, especially in structures subjected to fluctuating stresses, such as bridges, pavements, high-rise buildings, and wind turbine support structures.

The S-N curve typically represents the relationship between applied stress and the number of cycles to failure in materials, where 'S' denotes the stress amplitude, and 'N' represents the number of cycles to failure. For concrete, S-N curves provide insights into how various stress levels impact fatigue life, guiding engineers in designing structures that can endure repeated loads without failing prematurely. Developing S-N curves for concrete, particularly under compressive fatigue, has been the subject of extensive research over the past several decades [15, 21, 25, 26, 35, 51, 65, 104, 138]. These curves provide critical insights into the fatigue performance of concrete and are crucial for designing and assessing structures where fatigue loading is a primary concern.

Early research into the fatigue behavior of concrete focused primarily on tensile and flexural fatigue, driven by the need to understand the performance of concrete pavements and other horizontally loaded structures. However, with the growing importance of high-rise buildings and infrastructure subjected to significant compressive stresses like wind turbine support structures, the focus has gradually shifted towards compressive fatigue.

Recent research has introduced advanced models and methods for constructing and interpreting S-N curves for concrete. Zhang and Wang (2021) developed an energy dissipation method to investigate the impact of stress levels on the fatigue performance of PC, emphasizing the importance of energy-based parameters in predicting fatigue life [148]. Viswanath et al. (2021)

examined the compressive strain behavior of concrete under uniaxial fatigue loading, contributing to more accurate fatigue life predictions through detailed strain measurements [26].

Further advancements include the use of artificial neural networks (ANN) and machine learning techniques to predict concrete fatigue behavior. Abambres and Lantsoght (2019) utilized ANN to estimate the fatigue strength of concrete under compression, showcasing the potential of machine learning in enhancing fatigue life predictions. These modern approaches offer a comprehensive understanding of concrete fatigue, incorporating various factors such as stress amplitude, loading frequency, and material composition [149].

While early studies by Tepfers and Kutti (1979) laid the foundation for understanding the fatigue strength of different concrete types, more recent research has expanded on these findings [70]. For instance, Holmen (1979) investigated the fatigue behavior of concrete under constant and variable amplitude loading, highlighting the intricate interaction between stress levels, loading frequencies, and concrete properties [51]. Zhang and Wu (1997) explored the residual fatigue strength and stiffness of ordinary concrete under bending, providing deeper insights into the impact of cyclic loading on concrete's structural integrity [15].

Despite significant progress, several gaps remain in the literature. Most studies focus on specific concrete types or loading conditions, limiting the generalizability of their findings. Additionally, there is a lack of comprehensive experimental data covering a wide range of concrete compositions and loading scenarios. Existing fatigue models often rely on empirical data from limited tests for a particular concrete mix, which may not accurately capture the behavior of different concrete mixes.

The motivation for this procedure is that the compressive fatigue capacity is observed to be highly dependent on the composition of the concrete, particularly the amount, size, angularity,

and stiffness of the coarse aggregate relative to the hardened paste, as well as other features such as the presence of fibers. Using fatigue models derived from tests on concretes forming the lower bound of expected fatigue capacity will unduly underestimate the fatigue capacity of most concretes.

This study aimed to develop a standardized procedure for generating fatigue S-N curves for concrete through comprehensive compressive experimental testing. By conducting 160 fatigue tests on four different types of concrete, this research sought to investigate the fatigue behavior of various concrete compositions under cyclic compressive loading. The goal was to develop S-N curves that accurately represent the fatigue life of each concrete type and provide a detailed experimental methodology for future studies. Ultimately, the adoption of this approach will contribute to the development of more accurate fatigue models, enhancing the design and durability of concrete structures.

Definitions

- fcm_ave_C39 is the average monotonic compressive strengths of cylinders loaded at the ASTM C39 specified rate of 35±7 psi/second
- $f_{cm\_ave\_high}$ is the average monotonic compressive strength of cylinders loaded at a stress rate within a factor of 2 to that of the average stress range and frequency of the fatigue testing program
- fcm is the monotonic strength of an individual cylinder
- Smax is the ratio of the maximum applied stress in a cycle to the monotonic compressive strength by ASTM C-39
- Smin is the ratio of the minimum applied stress in a cycle to the monotonic compressive strength by ASTM C-39

- $N_{fm\_Smax\_Smin}$ is the measured number of cycles to failure for a particular combination of Smax and Smin. For example, if Smax = 0.80 and Smin = 0.05 and the measured number of cycles at failure were 10500, then this would be expressed as $N_{fm\_80\_05}$ = 10500 cycles.

7.2.3 Methodology

This methodology outlines a six-step procedure designed to develop an S-N curve for concrete fatigue within a two-week timeframe. The steps are designed to optimize testing time while ensuring accurate and reliable data. This process is based on a combination of short-duration and long-duration fatigue tests, following the initial establishment of the concrete's compressive strength.

7.2.3.1 Step 1: Establish Monotonic Strength at Fatigue Stress Rate (1 Day of Testing)

Before conducting fatigue tests, the monotonic compressive strength of concrete at a higher loading rate must be established. This differs from the standard compressive strength measured using the ASTM C-39 method, which determines the average compressive strength ($f_{cm\_ave\_C39}$) at a specified loading rate.

For this step:

- Conduct tests to determine the compressive strength of concrete at a higher loading rate, referred to as $f_{cm\_avg\_high}$.
- This step involves preparing and testing concrete cylinders or prisms under a monotonic compressive load applied at a higher rate, simulating the fatigue loading conditions.
- The data obtained will be crucial for setting the stress levels in subsequent fatigue tests.

This step should take approximately one day and ensures that the stress levels used in the fatigue tests are based on the material's behavior under relevant loading conditions.

7.2.3.2 Step 2: Conduct Initial Short-Duration Fatigue Tests (4 Days of Testing)

In this step, fatigue tests are conducted at high stress levels to gather data quickly. The goal is to complete at least two tests per day over four days, yielding results that provide an initial understanding of the S-N relationship.

For the example case where Smin is equal to 0.05 (5% of the maximum stress):

- Perform fatigue tests at three different maximum-to-minimum stress ratios: 0.90/0.05, 0.85/0.05, and 0.80/0.05.
- Each test should involve subjecting the concrete samples to cyclic loading until failure, recording the number of cycles to failure (Nf) for each stress level.

The data from these tests will allow for the establishment of the initial slope of the S-N curve. This step provides essential information on the fatigue life of concrete under high stress, which can be extrapolated to lower stress levels.

7.2.3.3 Step 3: Establish the Initial Slope of the S-N Curve

Using the data from Step 2, plot the initial S-N curve on a logarithmic scale. The maximum stress (S) will be plotted on the y-axis, and the number of cycles to failure (Nf) on the x-axis.

- Fit a line to the data points to define the initial slope of the S-N curve.
- This initial curve, represented as the blue line in Figure 188, will provide a preliminary indication of the relationship between stress and fatigue life for concrete.

The initial S-N curve typically shows a steep decline at high stress levels, and this line will be extended to much lower stress levels as more data is collected.

7.2.3.4 Step 4: Establish S-N Curve for Long-Duration Tests

A more comprehensive set of data is required to refine the S-N curve. This involves determining the stress level at which long-duration tests will yield meaningful results without extending the testing time excessively.

- Using the initial S-N curve, identify the maximum number of cycles that will be useful for determining the final S-N curve's slope.
- This step involves plotting a second S-N curve (shown as the purple line in Figure 188) with a slightly less steep slope based on the anticipated results of longer-duration tests.

This purple line serves as a guide for when to stop the long-duration tests, ensuring that testing is efficient and avoids unnecessary cycles beyond what is needed to define the S-N relationship accurately.

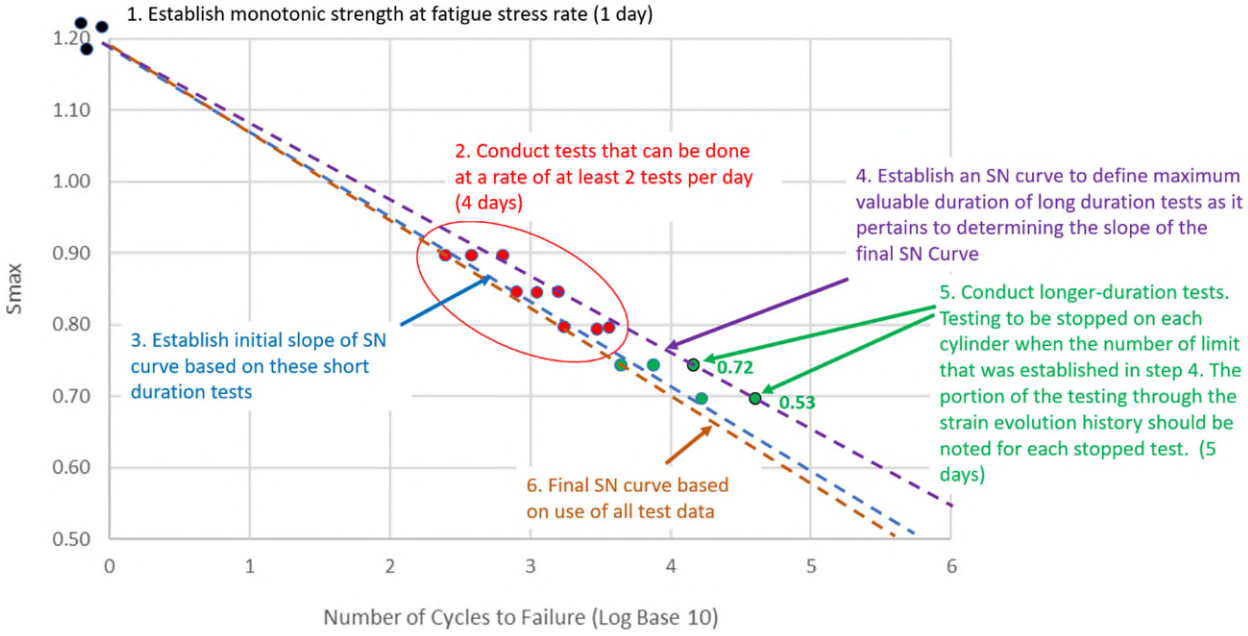

Figure 188 Example of development of an S-N Curve by certification by testing procedure

7.2.3.5 Step 5: Conduct Long-Duration Fatigue Tests (5 Days of Testing)

With the criteria established in Step 4, conduct longer-duration fatigue tests at lower stress levels. These tests aim to capture data on the fatigue life of concrete under conditions that more closely resemble real-world applications.

- For each test, stop loading when the number of cycles reaches the limit established in Step 4.
- Record the strain evolution history and note any significant changes in the material's behavior throughout the test.

This step will take approximately five days, and the data collected will be essential for refining the final S-N curve.

7.2.3.6 Step 6: Develop Final S-N Curve

In this final step, all the data from both short-duration and long-duration tests will be compiled to develop the final S-N curve.

- Plot the combined data points and fit a line that represents the overall relationship between stress and fatigue capacity or life.
- The final S-N curve should provide a comprehensive understanding of the concrete's fatigue behavior across a range of stress levels and cycle counts.

Depending on the design, it may be desired to establish this for more than one level of Smin or another different characteristic (e.g. saturated concrete, RC). Figure 189 provides an example of two fatigue curves in which the second curve was derived from testing at Smax/Smin = 0.90/0.20, 0.85/0.20, 0.80/0.20, and 0.75/0.20.

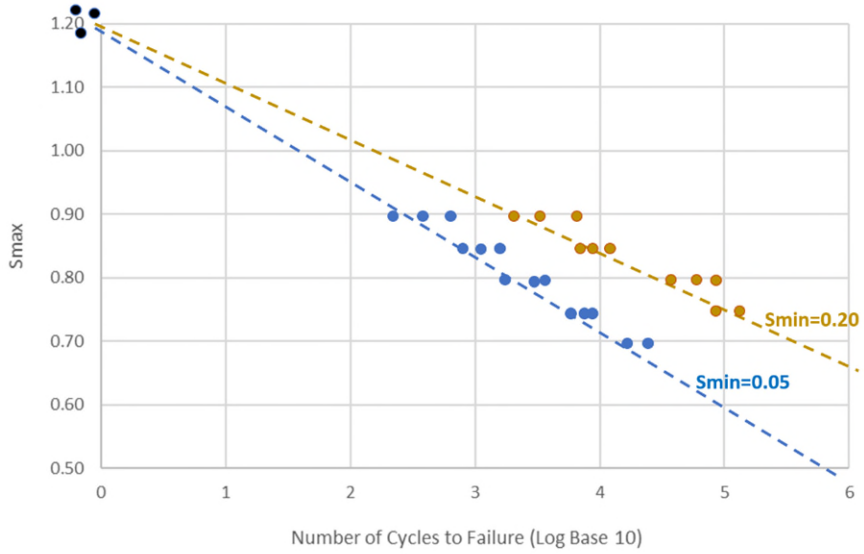

Figure 189 Development of Two S-N Curves

7.2.4 Experimental Testing Example

For instance, a testing campaign was conducted at Tufts University on a normal strength concrete cylinders, and the defined fatigue S-N curves are shown in the following figures:

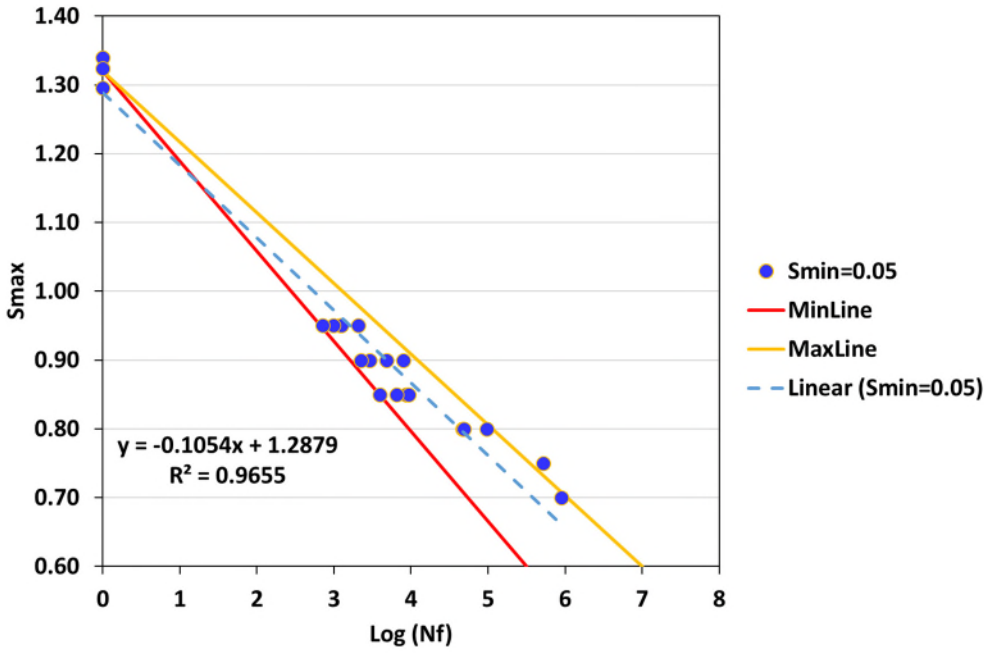

Figure 190 Developed S-N curve for a particular normal strength concrete at Smin=0.05 & frequency=1 Hz

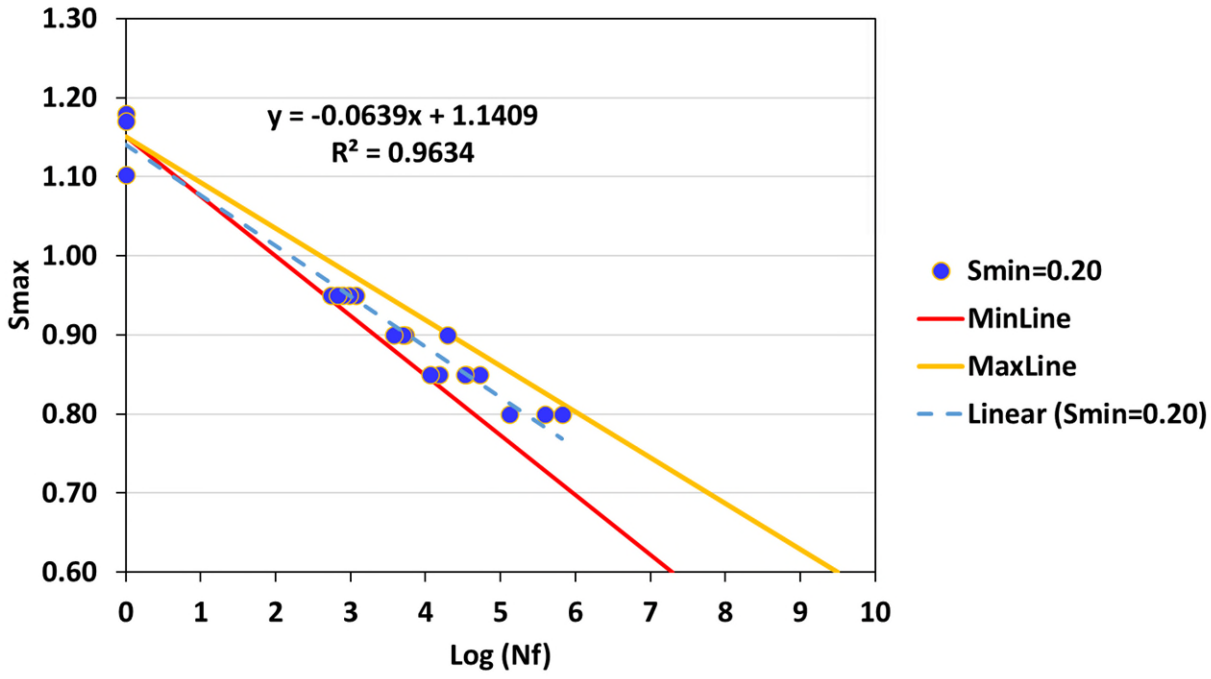

Figure 191 Developed S-N curve for a particular normal strength concrete at Smin=0.20 & frequency=1 Hz

7.2.5 Discussion and Results

The proposed methodology is employed to generate proper S-N curve formulation for specific concrete mixes. The different fatigue load combinations of (S_{max}, S_{min}, frequency) were selected to cover a range of testing with the number of cycles to failure of less than 1 million cycles in order to have a reasonable time to perform the tests. Using the method defined in the "Test setup" section, using the improved estimate of the strength of the cylinders, their cross-sectional area, and the load combination used to define the actual maximum (peak) and minimum (valley) loads to be imposed on the test specimen.

Almost all of the tests were carried out up to failure by imposing uniaxial compressive constant amplitude cyclic load (i.e., one value of S_{max} and S_{min} per test) using a sinusoidal waveform with a predefined frequency of 1 Hz. The fatigue capacity (Number of cycles to failure; N_f, also

called fatigue capacity) is presented in Chapter 6. Figure 192 and Figure 193 show the fatigue capacity of all types of tested concrete compared. In this plot, the maximum nominal stress level (S_{max}) is presented on the vertical axis, and the logarithm of the number of cycles to failure, log10 (N_f), is shown on the horizontal axis. These plots show that the concretes based on material characteristics have different fatigue capacities (even with the same range of strength).

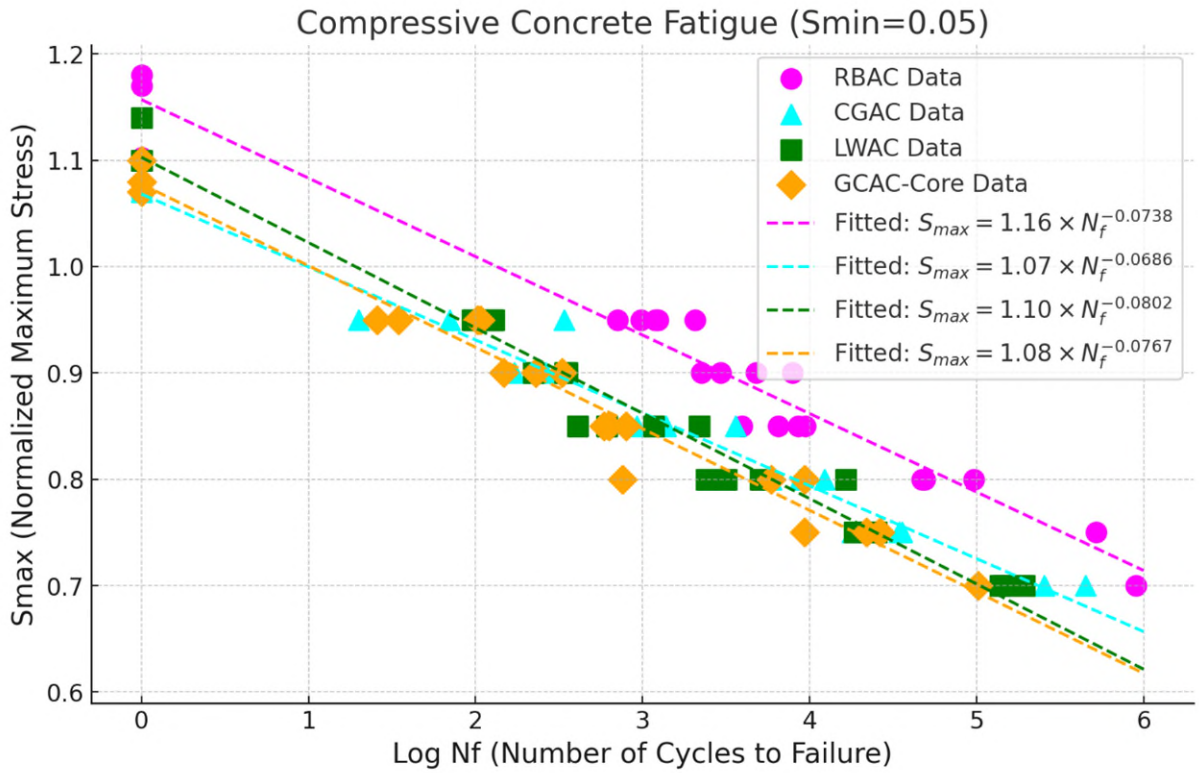

Figure 192 S-N curve plot for uniaxial compressive fatigue testing with Smin of 5%

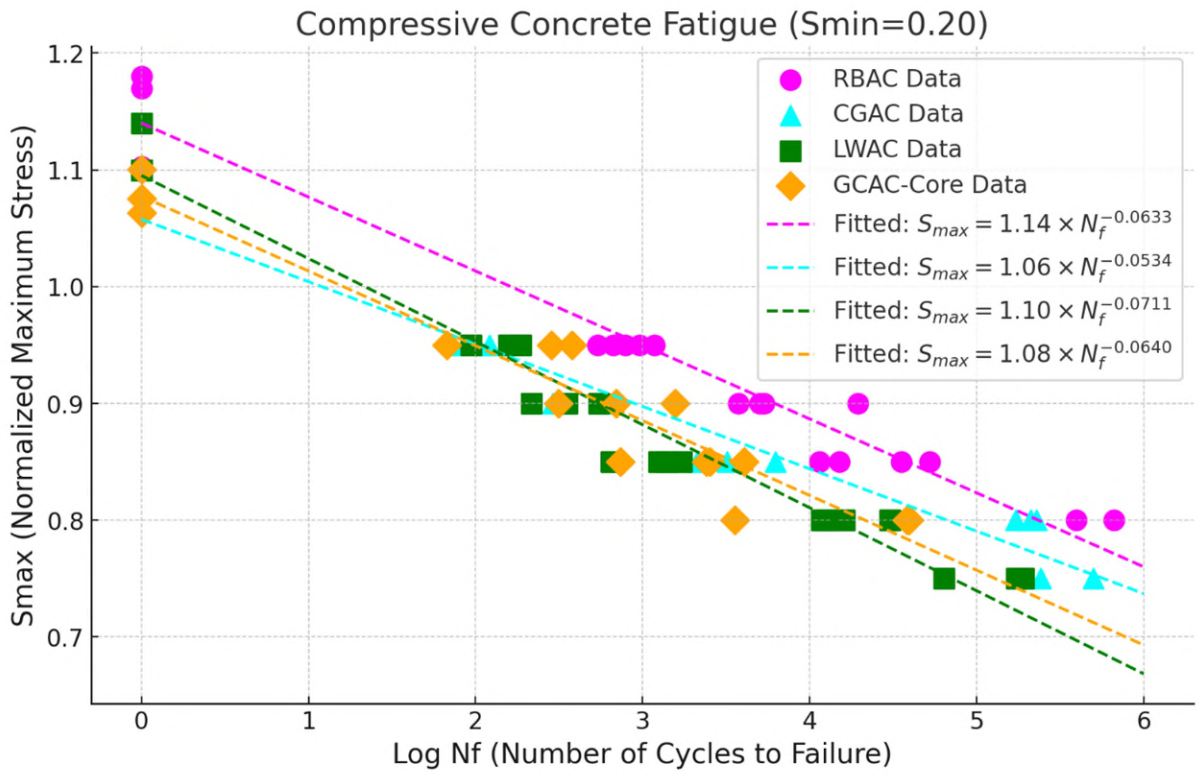

Figure 193 S-N curve plot for uniaxial compressive fatigue testing with Smin of 20%

The two plots represent the S-N curves for compressive concrete fatigue with different minimum stress ratios, Smin=0.05 and Smin=0.20. The first plot shows that as the number of cycles to failure increases, the maximum stress Smax that the concrete can withstand decreases significantly. The different datasets (RBAC, CGAC, LWAC, and GCAC-Core) show varying rates of decline, with RBAC (magenta) exhibiting the steepest decline in maximum stress, indicating a more sensitive response to fatigue loading. The fitted S-N curves suggest that the relationship between Smax and the number of cycles to failure can be described by a power-law decay, with the RBAC dataset having the most pronounced slope, implying a faster reduction in fatigue strength compared to the other concrete types.

In the second plot, where Smin=0.20, the general trend remains consistent with the first plot, but the overall stress levels are slightly higher, and the slopes of the fitted curves are less steep. This

suggests that increasing the minimum stress ratio allows the concrete to maintain higher maximum stress levels across the same number of cycles to failure. However, the relative differences between the datasets persist, with RBAC still showing the fastest decline in fatigue strength. The GCAC-Core dataset shows a more moderate slope, indicating a better performance under cyclic loading compared to RBAC. The differences between the two plots highlight the importance of the minimum stress ratio in fatigue behavior, as a higher Smin reduces the rate of strength degradation, which could be crucial for designing concrete structures subjected to cyclic loading.

7.2.6 Probabilistic Approach

7.2.6.1 Overview

The development of fatigue S-N curves for concrete under compressive loading using probabilistic methods provides a robust framework for accounting for variability in material properties, loading conditions, and environmental influences. This approach acknowledges that concrete fatigue life is inherently stochastic, exhibiting significant scatter in experimental data. Probabilistic methods allow for the quantification of uncertainty, enabling more reliable and efficient design of concrete structures subjected to cyclic loading.

7.2.6.2 Methodologies in Probabilistic Fatigue Analysis

Probabilistic fatigue analysis for concrete primarily employs statistical distributions to represent the variability in fatigue life. Commonly used distributions include the Weibull distribution, log-normal distribution, and exponential models. These distributions characterize the relationship between stress levels and the number of cycles to failure, capturing the inherent scatter observed in experimental data.

7.2.6.2.1 Weibull Distribution

The Weibull distribution is widely used in fatigue analysis due to its flexibility in modeling different failure behaviors. The probability density function (PDF) of the Weibull distribution is expressed as:

$$f(N_f) = \frac{k}{\lambda}\left(\frac{N_f}{\lambda}\right)^{k-1} e^{-\left(\frac{N_f}{\lambda}\right)^k} \qquad \textit{Equation 7}$$

Where:

- N_f is the number of cycles to failure,
- λ is the scale parameter,
- k is the shape parameter.

The cumulative distribution function (CDF), representing the probability of failure occurring at or before a given cycle count, is:

$$F(N_f) = 1 - e^{-\left(\frac{N_f}{\lambda}\right)^k} \qquad \text{Equation 8}$$

Holmen (1982) demonstrated the use of Weibull distributions in analyzing fatigue life variability, providing a foundation for modern probabilistic approaches [51]. They demonstrated that the fatigue life of concrete exhibits significant variability due to material and environmental factors, and he effectively modeled this variability using Weibull distributions. His study highlighted the influence of Weibull parameters, showing that the shape parameter (k) reflects the scatter in fatigue life while the scale parameter (λ) represents the characteristic life at specific failure probabilities. Holmen also emphasized the dependency of these parameters on stress levels, reinforcing the probabilistic nature of fatigue behavior. His work provided a quantitative framework for reliability-based design, enabling engineers to account for fatigue life randomness

and design safer, more efficient concrete structures. This research laid the foundation for modern probabilistic approaches in concrete fatigue analysis.

7.2.6.2.2 Log-Normal Distribution

The log-normal distribution is particularly suited for fatigue life data spanning several orders of magnitude. The probability density function (PDF) for the log-normal distribution is:

$$f(N_f) = \frac{1}{N_f \sigma \sqrt{2\pi}} e^{-\frac{\left(\ln N_f - \mu\right)^2}{2\sigma^2}} \qquad \text{Equation 9}$$

Where:

- μ is the mean of *ln* N_f,
- σ is the standard deviation of *ln* N_f.

The cumulative distribution function (CDF) for the log-normal distribution is:

$$F(N_f) = \frac{1}{2}\left[1 + erf\left(\frac{\ln N_f - \mu}{\sigma\sqrt{2}}\right)\right] \qquad \text{Equation 10}$$

Where *erf* is the error function.

Petkovic et al. (1993) showed how log-normal distributions can effectively represent the fatigue behavior of high-strength concrete [33]. They demonstrated that log-normal distributions are highly effective in modeling the fatigue behavior of high-strength concrete, capturing the wide variability in cycles to failure observed in experimental data. Their study revealed that the logarithmic transformation of fatigue life data produces a normal distribution, enabling straightforward statistical analysis and reliable prediction of fatigue performance. They also highlighted that the parameters of the log-normal distribution, such as the mean (μ) and standard deviation (σ) of the logarithmic fatigue life, vary with stress levels, making the model adaptable to different loading conditions. This work established log-normal distributions as a robust tool

for probabilistic fatigue analysis, particularly suited to materials with fatigue life spanning multiple orders of magnitude.

7.2.6.2.3 Bayesian Updating

Bayesian approaches integrate prior knowledge with new experimental data, refining probabilistic models. The posterior probability is calculated using Bayes' theorem:

$$P(\theta|D) = \frac{P(D|\theta)P(\theta)}{P(D)} \qquad \text{Equation 11}$$

Where:

- $P(\theta|D)$ is the posterior probability of the model parameters given the data,
- $P(D|\theta)$ is the likelihood of the data given the model parameters,
- $P(\theta)$ is the prior probability of the model parameters,
- $P(D)$ is the marginal probability of the data.

Bayesian methods in fatigue analysis and its applications in integrating multi-source data to refine S-N curves are explored by Li and Wang (2011) [150]. They explored the application of Bayesian methods in fatigue analysis to integrate multi-source data and refine S-N curves for improved predictive accuracy. Their study demonstrated how Bayesian updating combines prior knowledge with experimental data to iteratively enhance fatigue life models, particularly under conditions of data scarcity or uncertainty. By incorporating information from various sources, their approach reduced variability and improved the reliability of fatigue predictions. They also emphasized the adaptability of Bayesian methods in accommodating new data, making it a powerful tool for refining S-N curves across different materials and loading conditions. This work highlighted the utility of Bayesian approaches in probabilistic fatigue modeling and reliability-based design.

7.2.6.3 Key Parameters and Limitations

Probabilistic models typically use a minimal parameter set, focusing on stress range, stress ratio, material strength, and fatigue life. While these parameters provide a practical balance between simplicity and predictive accuracy, they may overlook complex interactions, such as those involving environmental conditions or aggregate properties.

7.2.6.4 Applications in Design and Analysis

Probabilistic S-N curves are critical for reliability-based design, allowing engineers to quantify the likelihood of failure under specific loading conditions. These curves are often compared to deterministic models, such as those in DNVGL-ST-C502 and Eurocode 2, highlighting the enhanced predictive capability of probabilistic approaches.

7.2.6.5 The use of the probabilistic method in experiments on concrete samples with different aggregate type

The probabilistic S-N curves for compressive concrete fatigue were constructed by first fitting a baseline S-N curve to the experimental data for each concrete type (RBAC and GCAC) with a minimum stress ratio Smin=0.05. The relationship between the maximum stress Smax and the logarithm of the number of cycles to failure logNf was modeled using a linear function. The baseline curve, which serves as the central tendency of the data, was determined by fitting the parameters a and b in the equation $S_{max}=a-b\cdot\log N_f$. This curve represents the average fatigue behavior of the concrete under cyclic loading.

To account for the variability inherent in concrete fatigue performance, the residuals between the observed Smax values and those predicted by the baseline curve were calculated. The standard deviation of these residuals was then used to quantify the spread of the data around the baseline

curve. By incorporating this standard deviation, we generated probabilistic S-N curves that represent different probabilities of failure: 5%, 50%, and 95%. These curves were obtained by adjusting the baseline curve according to the z-values from the normal distribution corresponding to the desired probability of failure. Specifically, the 95% probability of failure curve (red) was generated by shifting the baseline curve downward by 1.645× the standard deviation, while the 5% probability of failure curve (yellow) was generated by shifting the curve upward by the same amount.

The resulting probabilistic S-N curves for both RBAC and GCAC concretes show that higher probabilities of failure are associated with steeper slopes, indicating a faster decline in allowable stress as the number of cycles increases. The 95% probability of failure curve is the most conservative, predicting failure at lower stress levels for a given number of cycles. In contrast, the 5% probability of failure curve allows for higher stress levels for the same number of cycles, reflecting better fatigue performance. The separation between these curves illustrates the variability in fatigue life and provides a range of possible outcomes, allowing for more informed decision-making in design and analysis.

These probabilistic S-N curves are crucial for understanding the fatigue behavior of concrete under compressive loading, particularly when considering safety and reliability in structural design. By incorporating different probabilities of failure, the curves offer a more comprehensive view of the potential performance of concrete, accounting for both the average behavior and the extremes. This approach ensures that the full range of possible outcomes is considered, enabling engineers to make more informed choices regarding safety factors and expected service life in concrete structures subjected to cyclic loading.

The two plots illustrate the probabilistic S-N curves for RBAC and GCAC concrete types under compressive fatigue with a minimum stress ratio Smin=0.05. In both plots, the solid data points represent the experimental data, while the dashed lines indicate the fitted S-N curves corresponding to different probabilities of failure: 95% (red), 50% (orange), and 5% (yellow). The curves show that as the probability of failure increases, the slope of the S-N curve becomes steeper, predicting failure at lower stress levels for a given number of cycles. The 95% failure curve is the most conservative, reflecting a higher likelihood of failure, while the 5% failure curve is the least conservative, indicating better fatigue performance. These probabilistic curves highlight the variability in fatigue life and provide a range of possible outcomes for each concrete type under cyclic loading. See Figure 194 and Figure 195.

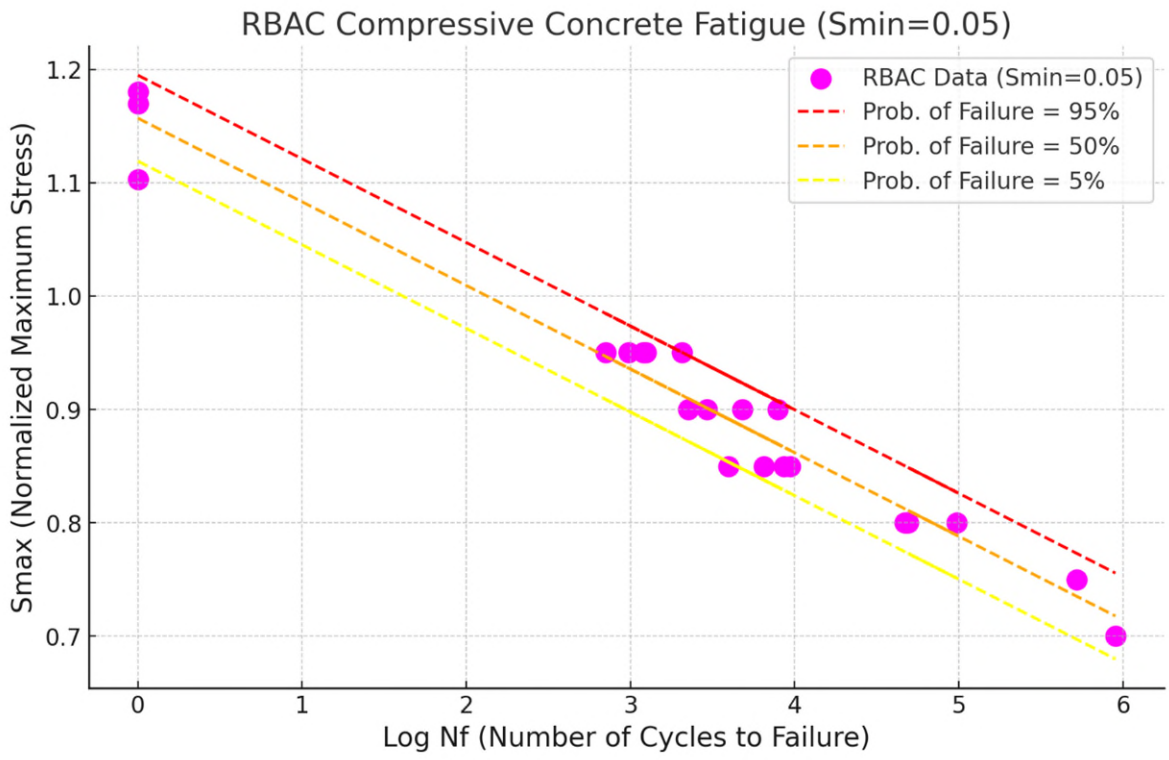

Figure 194 Probabilistic S-N curve plot for uniaxial compressive fatigue testing for RBAC

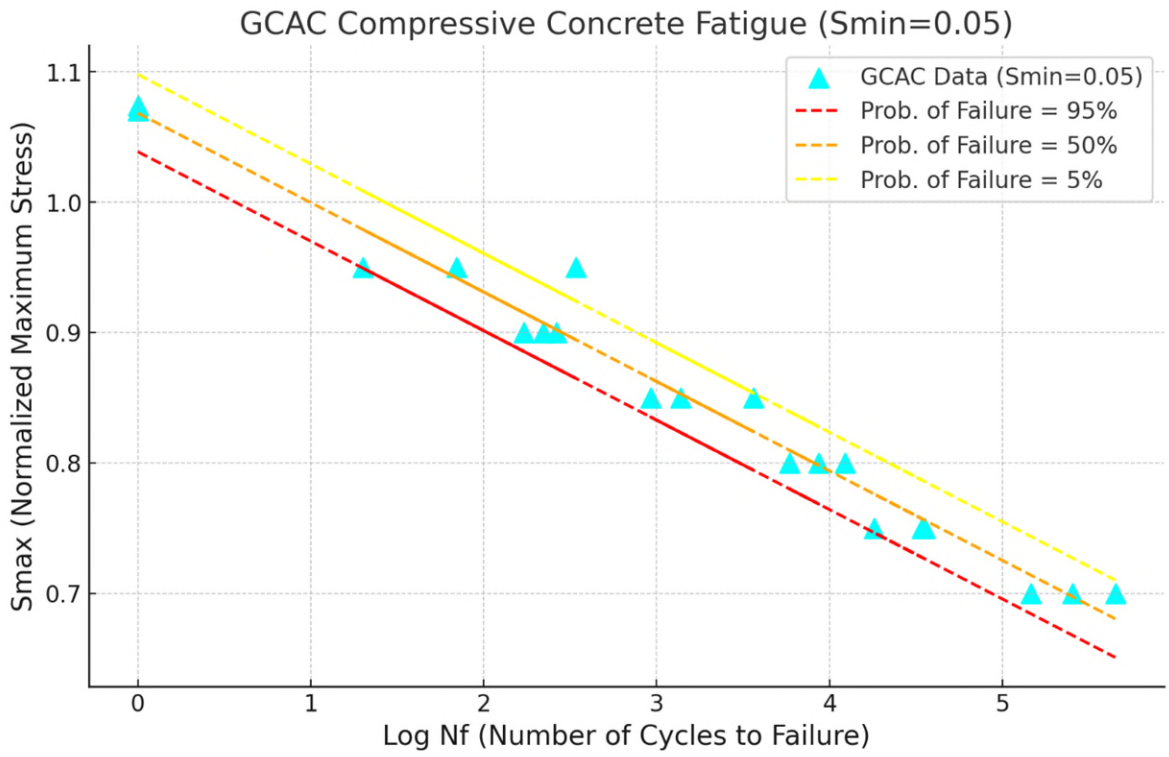

Figure 195 Probabilistic S-N curve plot for uniaxial compressive fatigue testing for GCAC

7.2.7 Conclusion

This study has developed a systematic approach for constructing fatigue S-N curves for concrete through compressive experimental testing, with a focus on four distinct concrete types. The research not only establishes a baseline methodology for testing but also incorporates a probabilistic approach to account for the variability in concrete fatigue performance. The findings highlight the importance of understanding the relationship between applied stress and the number of cycles to failure, which is critical for predicting the service life of concrete structures under cyclic loading.

The experimental results show that different concrete compositions exhibit varying fatigue behaviors, particularly in response to changes in stress levels. The S-N curves developed in this study provide valuable insights into the fatigue life of these concrete types, revealing that factors

such as aggregate type and mix composition significantly influence fatigue performance. The probabilistic S-N curves further enhance this understanding by offering a range of potential outcomes based on different probabilities of failure. This approach allows for more informed decision-making in the design and analysis of concrete structures, particularly those subjected to repetitive loading.

Moreover, the research addresses existing gaps in the literature by providing comprehensive experimental data and a robust methodology for fatigue testing. The probabilistic approach ensures that the full range of possible outcomes is considered, enabling engineers to design more resilient structures. This study underscores the need for continued research into concrete fatigue behavior, particularly as infrastructure demands increase and new materials are introduced.

In practical terms, the methodology developed here can be applied to various concrete types and loading scenarios, making it a versatile tool for both research and industry. The results demonstrate that accurate fatigue predictions can be made within a reasonable timeframe, supporting the design of safer and more durable concrete structures. Future work should focus on expanding the dataset to include more concrete types and exploring the effects of additional variables such as loading frequency and environmental conditions. By continuing to refine these models, the field can move closer to achieving comprehensive and reliable fatigue predictions for all types of concrete.

8 Summary of Findings and Recommendations for Future Research

8.1 Overview of dissertation objectives and scope

Through new physical testing and the collection and analysis of a comprehensive database of concrete fatigue test results, this research yielded new and important insights into the fatigue behavior of concrete, with implications for fatigue models and for the design of support structures — including wind turbines — made of concrete. The new experiments included an examination of the effects of previously untested or lightly considered factors. The analysis of the new test results, together with those already in the technical literature, point to the need for — and facilitate the development of — more accurate fatigue models and improved design practices. The primary objectives of this work were to:

- Understand the influence — on fatigue performance — of material properties, including aggregate type, reinforcement, and saturation, on various types of concrete, including normal plain, lightweight, and 3DPC. These are new test experiments which will inform us on the performance and behavior of concrete under compression fatigue.
- Create a comprehensive, user-friendly database of publicly-available concrete fatigue tests; study the effect of various factors on concrete fatigue; and investigate the potential use of neural network models in fatigue.
- Propose standardized methods for testing and tailor fatigue models to improve the reliability and cost-effectiveness of concrete structures subjected to high-cycle fatigue. This is novel and new approach which will lead to a better, and more compatible data for future analysis and better understanding of concrete fatigue.

The variability in wind and wave loadings — coupled with the dynamic forces from wind turbine operations — subject towers and foundations of wind turbines to significant cyclic loadings. These fatigue demands often govern the design of these support structures. While concrete structures generally exhibit superior fatigue resistance compared to steel, current fatigue design models and standards for structures made of concrete remain overly conservative and fail to account for many critical factors. Excessive conservatism can result in concrete structures that are unnecessarily large and costly.

The primary goals of this research were to enhance the understanding of the compressive fatigue of concrete and to develop more reliable and cost-effective methodologies for the design and assessment of concrete structures that support wind turbines. The research began with a collection and analysis of all publicly available fatigue data; fatigue models, which are all empirical, have been derived from subsets of this data. This analysis revealed the deficiency of existing fatigue models and a lack of standardization among data on the compressive fatigue capacity of concrete.

A preliminary experimental program that explored the effects of key variables guided the scope and design of a subsequent and more detailed testing series. The results from these experiments demonstrated relatively consistent fatigue capacity (measured number of cycles to failure within a factor of five for specific Smax/Smin stress ranges). However, the scatter across the entire collected database, which included data from various researchers, often spanned more than three orders of magnitude. This variability was attributed to differences in the details of the concrete mix. The testing procedures for most previous test results were not sufficiently detailed to enable the development of a more comprehensive and accurate model for fatigue.

Given these challenges, the research shifted toward providing a pragmatic approach for improving fatigue practice in the near term by developing recommended procedures and ACI Technotes for generating S-N curves for specific concrete mixes, as well as in the long term by proposing procedures for improving the reliability of fatigue tests. Extensive material characterization and experimental measurements were conducted throughout the study to inform these recommendations. All existing and newly generated test results were organized into an accessible Excel spreadsheet[15] to support future research and model development.

Going forward, the field could benefit from standardization of fatigue tests, improved reporting of material properties, and acquisition and reporting of the measured response to imposed loadings. This would allow for the continued improvement of fatigue models, including considering a wide range of influencing factors. Continued refinement of testing protocols and dissemination of findings will be critical in advancing the field and enabling the construction of more efficient and durable concrete structures.

The next few sections will focus on key findings. Section 8.2 presents the findings from the experimental testing, including the effects of longitudinal reinforcement, effects of saturation, effects of load eccentricity, effects of aggregate size and shape, effects of variability in monotonic compressive strength, performance of 3DPC, and the formation of visible cracks due to fatigue loading. Section 8.3 presents the findings from the analysis of the comprehensive fatigue testing database, including a discussion of dashboard development, variability in fatigue capacity, variations among standards, reporting gaps in the literature, and the effects of loading frequency. Section 8.4 presents the recommendations for standardized fatigue testing, based on

[15] https://tufts.box.com/s/rimeao5efwblmcdecr2gopiq5i47phj1

the findings and observations from the database, to improve fatigue testing methodologies for enhanced structural reliability and cost efficiency. Section 8.5 presents recommendations for future research, including exploration of complex stress states, fatigue-induced stress softening, testing of structural joints, and computed tomography investigations.

These sections collectively consolidate the research findings and provide actionable insights and future directions for advancing the understanding and application of concrete fatigue in structural engineering. The key findings are summarized below.

8.2 Findings from new experiments

The new fatigue test program examined the influence — on compressive fatigue capacity and performance — of seldom-considered factors, including:

- Longitudinal reinforcement
- Saturation
- Load eccentricity
- Aggregate size and shape
- Variation in monotonic strength
- Fatigue of 3DPC
- Appearance of cracks in material under fatigue

8.2.1 Effect of longitudinal reinforcement

The inclusion — in concrete specimens — of longitudinal reinforcing steel impacts compressive fatigue performance significantly. Unreinforced concrete bears the entirety of the applied stress, but in RC, the load is redistributed. As cyclic loading progresses, strain damage accumulates in the concrete matrix, gradually reducing the material's stiffness and shifting the load-bearing

responsibility increasingly onto the steel reinforcement. Since the reinforcement remains elastic up to its yield point, it effectively reduces the stress demand on the concrete, thereby enhancing the overall fatigue resistance of the composite system.

This redistribution mechanism significantly boosts the fatigue capacity of RC, often by approximately an order of magnitude compared to unreinforced specimens. Steel's ability to sustain cyclic stresses without significant damage delays the onset of critical fatigue failure in the concrete. As a result, the RC system exhibits improved durability and prolonged service life under repeated loading conditions. These findings underscore the importance of longitudinal reinforcement in structural applications, particularly for components subjected to high-cycle compression fatigue, such as wind turbine towers or bridge elements, where long-term performance and resilience are critical.

8.2.2 Effect of saturation

The saturation of concrete has a substantial detrimental effect on the material’s fatigue capacity. Saturated concrete specimens consistently exhibited fatigue capacities up to an order of magnitude lower than their unsaturated counterparts. This significant reduction is primarily attributed to the role of pore water, which, under cyclic loading, generates additional stresses within the concrete matrix. These pore water stresses accelerate crack initiation and propagation, weakening the material and reducing its ability to withstand repeated cycles of stress. This phenomenon is particularly relevant for underwater sections of wind turbine support structures.

While some existing design codes partially address the impact of saturation on fatigue capacity, many do not fully account for this effect, leading to potential underestimation of structural vulnerability. These findings highlight the importance of considering moisture conditions in both experimental testing and fatigue model development. By incorporating the influence of

saturation into design standards and testing protocols, engineers can better predict the performance of concrete in marine and similar high-moisture environments, ensuring the safety and durability of critical infrastructure.

8.2.3 Effect of load eccentricity

Load eccentricity significantly influenced the fatigue capacity of concrete. Eccentric loading creates uneven stress distributions, leading to localized stress concentrations that accelerate material degradation. This effect highlights the need for accurate modeling of eccentric loads in structural design, as ignoring this factor can result in an overestimation of fatigue capacity and a subsequent compromise in structural safety.

8.2.4 Effect of aggregate size and shape

The experimental testing on the effects of aggregate size and shape in Chapter 6 provided critical insights into the fatigue behavior of concrete. Concrete mixes incorporating large, angular aggregates exhibited significantly lower fatigue capacity compared to those with smaller, rounder aggregates. This disparity, often amounting to a reduction in fatigue capacity by an order of magnitude, underscores the influence of aggregate geometry on crack initiation and propagation.

The reduced performance of concrete with angular aggregates can be attributed to increased stress concentrations at the sharp edges and corners of these particles. Under cyclic loading, these stress concentrations promote early crack formation and accelerate crack propagation through the concrete matrix. Conversely, smaller, rounder aggregates distribute stresses more evenly, reducing the likelihood of crack initiation and enhancing overall fatigue resistance.

Also, it has been observed that rounded aggregates (e.g., river gravel) lead to better packing and reduced voids due to their smooth surfaces and ease of movement during compaction. This generally results in lower porosity in the concrete. In contrast, angular aggregates (e.g., crushed stone) have more irregular shapes and sharp edges, which can lead to higher interlocking. While interlocking can improve strength, it may increase voids and porosity if not well-compacted [144]. Higher porosity in the concrete leads to earlier microcrack formation and lower fatigue capacity.

These findings highlight the importance of aggregate selection in mix design, particularly for structures subjected to high-cycle fatigue loading, such as wind turbine foundations or bridge components. By prioritizing aggregates with favorable size and shape characteristics, engineers can improve the durability and longevity of concrete structures, ensuring their reliability under demanding service conditions.

Another important insight was gained by comparing the fatigue capacity of cylinders cast in plastic molds with those cored from slabs made using the same mix. While both types of concrete samples exhibited similar average fatigue capacities, the cylinders cored from the slabs showed greater variability in the results. This increased scatter is likely attributed to early crack initiation in some specimens with high stress concentration, particularly those with large aggregates located near the edges.

8.2.5 Lightweight aggregate concrete

Lightweight aggregate concrete (LWAC) demonstrated a reduced fatigue capacity compared to normal concrete and other types of structural concrete. The research revealed that LWAC specimens tended to fail earlier under cyclic loading due to weaker aggregate mechanical characteristics. The inherent porosity of the lightweight aggregates accelerates microcrack

initiation and propagation. Additionally, the stiffness of LWAC degraded faster over the fatigue cycles, resulting in less resistance to cyclic loading. LWAC's failure was characterized by a more brittle response and shorter fatigue life compared to normal concrete, which exhibited more gradual damage accumulation and extended strain phases under similar loading conditions.

8.2.6 Effect of variability in monotonic compressive strength

Variability in the monotonic compressive strength of test cylinders cast from the same concrete batch emerged as a significant factor contributing to the observed scatter in fatigue capacity. Experimental results from Chapters 4 through 6 consistently demonstrated that even small differences in the compressive strength of specimens can lead to substantial variations in fatigue performance, often by up to an order of magnitude. This variability is particularly critical in fatigue assessments, where accurate predictions of fatigue life depend heavily on a reliable estimation of the material's baseline strength. Factors such as inconsistencies in specimen preparation, curing conditions, and aggregate distribution within the concrete matrix exacerbate this scatter, complicating the development of robust fatigue models and design standards.

To address this challenge, this research developed and validated an Improved Strength Estimation Method (ISEM) that enhances the accuracy of monotonic strength estimations. By incorporating additional parameters, like statistical corrections, the ISEM comparatively reduces variability in strength estimates. This improvement enables more consistent fatigue testing and analysis, ultimately leading to better-informed fatigue models and design protocols. These findings emphasize the importance of standardizing strength estimation practices to mitigate variability and improve the accuracy of fatigue assessments in concrete engineering.

8.2.7 Performance of 3D-printed concrete

The experimental testing on 3DPC revealed remarkable findings, showcasing its considerable fatigue performance compared to traditional cast-in-place concrete of similar strength. This enhanced fatigue capacity is largely attributed to the unique microstructure of 3DPC, which is characterized by controlled material deposition and a more homogeneous internal structure. These features effectively minimize stress concentrations and improve resistance to crack initiation and propagation under cyclic loading. The results indicate that 3DPC has a distinct advantage in applications where high-cycle fatigue loading is a critical concern.

Additionally, the layer-by-layer deposition process inherent in 3D printing allows for greater control over the placement of material, reducing voids and inconsistencies commonly associated with cast-in-place methods. This controlled deposition not only contributes to improved fatigue performance but also allows for customized designs and material optimization to meet specific structural demands. The findings also highlighted that 3DPC specimens exhibited consistent strain evolution patterns, further validating its reliability under dynamic loading conditions.

These results underscore the potential of 3DPC for innovative structural applications, particularly in renewable energy infrastructures such as wind turbine support systems. Its superior fatigue capacity, coupled with the flexibility of additive manufacturing, opens up new possibilities for efficient, durable, and cost-effective construction. However, further research is warranted to address variability in printing parameters, long-term durability, and scalability to ensure its broader adoption in critical structural applications.

8.2.8 Appearance of visual cracks due to fatigue loading

The investigation into visual crack appearance across various concrete types revealed significant insights into the correlation between crack formation and fatigue behavior. In all tested specimens (PC, RC, and 3DPC), visual cracks typically appeared during the latter stages of fatigue life, often aligning with the transition to Phase III of strain evolution. This phase is characterized by rapid stiffness degradation and accelerated strain accumulation, indicating that visual cracks serve as a precursor to structural failure. The strain at which these cracks appeared was found to vary based on material properties and loading conditions, with higher minimum stress ratios accelerating their occurrence.

For concrete with river-based aggregates, the strain at the first visual crack often corresponded to the strain associated with the monotonic strength of the material, highlighting a predictable relationship between crack initiation and mechanical performance. In contrast, lightweight concrete demonstrated earlier visual crack formation, reflecting its brittle nature and reduced ability to redistribute stresses. RC specimens delayed the onset of visual cracks due to load transfer from the degrading concrete to the reinforcing steel, thereby extending the material's fatigue life. Similarly, 3DPC showed unique crack formation patterns influenced by its microstructure, with cracks appearing closer to failure but following predictable strain thresholds.

These findings emphasize the importance of monitoring visual cracks as an indicator of fatigue damage progression. The ability to correlate crack appearance with specific stages of strain evolution and fatigue life provides engineers with a valuable tool for assessing structural health in real time. This knowledge is particularly critical for designing structures like wind turbine

support systems, where fatigue-induced failure must be minimized, and early warning signs of damage can inform maintenance and repair strategies.

8.3 Findings from analysis of the complete fatigue testing database

A comprehensive database of experimental fatigue test results was developed to enhance the understanding of concrete fatigue under compressive cyclic loading. This database integrates both previously published data and new experimental results, capturing a wide range of material types, testing conditions, and performance metrics. The data compilation process gathered, when available, all key parameters influencing fatigue performance, such as stress ratios, aggregate characteristics, and loading conditions. The database incorporates results from journals and technical reports as well as the new data that was collected as part of this thesis work, as presented in Sections 4-6 and 8.2 of this study.

To streamline the exploration and analysis of this extensive dataset, an Excel-based dashboard was developed. This user-friendly tool organizes data into clear categories, such as material mix, loading conditions, etc., and provides interactive visualization capabilities. Researchers and engineers can analyze trends, compare experimental results against established fatigue models, and identify gaps in the data. Key features include customizable filters, overlay comparisons with S-N curves from standards like EuroCode2, and tools for gap identification, guiding future research efforts. The dashboard's intuitive interface ensures accessibility for a broad audience, enabling efficient data driven decision making.

The database and dashboard together constitute an important resource for advancing concrete fatigue research. They provide a robust foundation for exploring the effects of various parameters on fatigue behavior and offer actionable insights to refine design and testing practices

for improving models and, thereby, the durability and performance of concrete structures sensitive to fatigue.

Key findings from the development and use of this database for the equation of models are as follows:

8.3.1 Insufficient reporting in the literature

In the development of the database, it was unfortunately found that relatively limited information about the test specimen, loading, or measured response was provided in the technical literature. The database was analyzed to assess data availability. Some characteristics exhibit full data completeness, with 100% availability, including loading levels like maximum and minimum stress level and fatigue capacity. Some of the research publications fail to report important items like frequency of loading or loading rates, aggregate type, etc. "Frequency of Loading" is recorded in ~75% of the dataset, and "Specimen Type" data is available in ~80%. However, there are some important items that are less frequently reported, such as those related to specific material properties or test conditions, that may have data available in only ~30% of entries. This detailed assessment highlights the strengths of the dataset while identifying areas with substantial data gaps, helping prioritize efforts for improvement, and ensuring more robust analyses in the future.

This significantly limited the number of test results from the entire dataset that is available for more in-depth analyses. An important obstacle is the lack of detailed information on material composition and testing procedures in prior studies. This lack of transparency also makes it difficult to identify and exclude outliers, complicating the development of reliable general-purpose models.

8.3.2 Effect of loading frequency

In the review of the entire available dataset, it was observed that fatigue capacity decreases as loading frequency increases. This was expected because the use of a lower loading frequency led to longer times at peak stress, which allowed more time for crack propagation and damage. For wind turbine support structures, test data with loading frequencies of 2 Hz or less are most relevant for accurate design and analysis.

8.3.3 Scatter in fatigue capacity

The observed scatter in measured fatigue capacity for any given stress range (Smax/Smin) was observed to be extremely large, often spanning three or more orders of magnitude. This variability is attributed to material differences, unconsidered influencing factors, and inconsistent testing protocols.

Based on the literature review and experimental testing results, the following listed factors were observed to impact fatigue capacity (number of cycles to failure for a particular combination of strength ratios). Beside each of these factors is their estimated impact on the number of measured cycles to failure

i. Frequency of loading; Fatigue life varies significantly with loading frequency, with higher frequencies (e.g., 5 Hz) reducing fatigue capacity by approximately a factor of 3 compared to lower frequencies (e.g., 1 Hz).
ii. Uncertainty in monotonic strength of a specific test cylinder; Variability in the monotonic compressive strength of test specimens leads to scatter in fatigue results, especially for high-stress levels (Smax), influencing fatigue life by a factor of approximately 8.

iii. Effect of reinforcing steel; The inclusion of reinforcing steel enhances fatigue capacity substantially, increasing it by a factor of approximately 12 compared to plain concrete under similar loading conditions.

iv. Effect of degree of saturation; The level of saturation in concrete significantly impacts fatigue performance. Saturated specimens exhibit approximately 4 times lower fatigue capacity than dry specimens.

v. Effect of specific composition of concrete; Concrete composition, including aggregate type and size, mix design, and water-to-cement ratio, can influence fatigue capacity by up to a factor of 10, highlighting the importance of tailored material selection for specific applications.

This last factor includes the size, shape, stiffness, and distribution of coarse aggregate, as well as the strength of the concrete, with high-strength concrete having a generally lower fatigue strength for the same Smax/Smin values than for normal-strength concrete.

The combination of these factors is much more than 1000, so the variation in the fatigue capacities presented in the literature (and thereby fatigue models) is not surprising. Since researchers do not consider or report (i) uncertainty in the monotonic strength of a test cylinder or (ii) coarse aggregate size distribution, the collected test database does not provide the information needed to produce a much better fatigue model than in the literature. This was illustrated through the development of a trained neural network (on 4/5 of the collected test data) to predict the fatigue capacity of the remaining 1/5 of the database for different group selections.

8.3.4 Variability in fatigue models

The empirical fatigue models and standards derived from subsets of available data in the literature showing significant variation in estimated fatigue capacity. These differences can lead

to vastly divergent service life predictions, with some standards estimating 50 years while others predict 5 years or less for the same structure. This was not surprising since different researchers and standards committees used different subsets of data for the validation of models. Also, fatigue models, including both deterministic and probabilistic approaches, typically rely on a limited number of parameters to balance simplicity, efficiency, and applicability. Commonly used parameters include the stress range ($\Delta S = S_{max} - S_{min}$), which governs the magnitude of fatigue damage; the stress ratio ($R = S_{min}/S_{max}$) capturing the mean stress effects; material strength (f'_c), which represents the variability in concrete properties; and the number of cycles to failure (N_f), representing material durability under cyclic loading. Additionally, the limited availability of experimental data often constrains the validation of models with extensive parameters. It is also important to consider using traditional approaches of standardization focusing on dominant factors like stress range and material strength to achieve robust predictions without unnecessary complexity and ensure broad applicability across different concrete types and loading conditions. However, this approach will increase the level of conservatism. Nowadays, there are very advanced computational methods available to perform a more robust and complex analysis and decrease the conservatism of estimations. Having a comprehensive database and standardized method of testing will ensure that.

8.4 Recommendations for the advancement of fatigue testing and design practice

These findings collectively highlight the complexity of concrete fatigue behavior and underscore the importance of improved testing methodologies, comprehensive data reporting, and refined fatigue models to advance the reliability and cost-effectiveness of concrete structures.

A major contribution of this work is the proposed standardized testing protocols for uniaxial compressive fatigue tests that were reported in chapter 7 and will be published as a technote by

the American Concrete Institute. These protocols include detailed recommendations on specimen preparation, loading conditions, and data collection, ensuring consistency and comparability across experiments. By adopting these guidelines, researchers and practitioners can minimize variability in test results and improve the reliability of fatigue models. The proposed methods also emphasize the importance of monitoring strain evolution and stiffness degradation, which are critical indicators of fatigue damage progression.

Another significant product of this research is the development of procedures for generating customized S-N curves tailored to specific concrete mixes, which was also presented in Chapter 7 and will be published as an ACI technote. The chapter also highlights the need for probabilistic approaches to fatigue design, incorporating the inherent variability of concrete properties and loading conditions to achieve safer and more efficient designs.

These two contributions aim to bridge the gap between experimental research and engineering practice, supporting the development of fatigue-resistant concrete structures for renewable energy infrastructure and other demanding applications. The proposed guidelines and methodologies not only address current challenges but also set the foundation for advancing fatigue research and design practices in the future.

8.5 **Recommendations for future research**

While it is considered that this study has contributed significantly to available and detailed experimental data sets on the compression fatigue capacity and behavior of concrete, that the dissemination of the large Excel database of available data is significant, and that the procedures in the Technotes can significantly improve research and professional practice, there is much to be done to be able to make greatly improved and more reliable assessments of the fatigue

capacity and performance of concrete structures. One of these is simply additional compression fatigue testing on different types of concretes with different levels and types of reinforcement conditions. Other recommendations for future work are described below:

8.5.1 Influence of complex states of stress

Limited research on the effect of lateral confining pressure on fatigue capacity has found that the lateral confining pressure greatly enhanced the fatigue capacity and that the influence was stronger and lower the peak stress levels. This will have a very significant effect on the final results and strain progression, but it is not considered in the codes and provisions of RC structure designs for fatigue. This confinement can be bi-axial or tri-axial. Therefore, there is a need for a new apparatus or facility to be able to do high-cycle fatigue testing on concrete elements that can be subjected to bi-axial or tri-axial fatigue loading, which is common in many field structures.

8.5.2 Assessment of impact — on stress demands — of softening due to fatigue

As observed in this project, the presence of steel reinforcement has a significant effect on the strain evolution, microcracks initiation and progression inside the structure, and on concrete softening due to cracks development and load transfer from concrete to steel; this greatly affects fatigue demand and capacity and has only just begun to be studied. Although there are some studies on developing analytical or numerical models, no numerical or analytical tool is capable of considering this softening effect under high-cycle fatigue loading. The complex geometry of upcoming floating wind turbine structures, environmental conditions, and loading will increase the importance of such a study. The test variables of such a study should include the number of reinforcements, direction of loading relative to reinforcements, and strain variation across the dimensions of the test specimen.

8.5.3 Structural joint test

Finally, the most greatly needed area of future study regarding the fatigue capacity of concrete wind turbine support structures is on the fatigue capacity of joints, which is what is most likely to control the fatigue life of these structures. The variables that need to be investigated for the high-cycle fatigue capacity of joints include the shape of connected panels, construction sequence, use of grout, type of grout, thickness of grout, surface of joint (intentionally roughened, match cast, smooth, CNC – machined flat), type of concrete, type of connectors (long unbonded strands, short unbonded strands, bolted), and under what conditions is gaping allowed. The design of a testing program on joints should be informed by an examination of industry practices and extensive field monitoring campaigns.

8.5.4 Computed tomography investigation

The literature review highlighted a significant gap in understanding the development of microcracks in concrete under fatigue loading, which can be effectively studied using ultra-high-resolution X-Ray Computed Tomography (CT). Conducting extensive CT scanning on a diverse range of concrete and reinforced concrete specimens, as well as field samples, would provide valuable insights into microcrack initiation, progression, and patterns. Such a research program could significantly improve the assessment of fatigue capacity utilization and the prediction of remaining service life in field structures while also informing better design practices [151-155].

Key areas for investigation include the effect of aggregate type, size, and shape on microcracking, including how fatigue loading influences crack progression and the extent of cracks penetrating aggregates. Evaluating cores from onshore and offshore field structures that have undergone fatigue loading could offer critical observations on crack growth in high-stress

zones and bridge the gap between lab results and in-situ performance. Additionally, examining the impact of reinforcement on crack growth and strain evolution under fatigue loading is essential, as almost all concrete structures are reinforced. Understanding these factors will contribute to more accurate lifetime predictions and enhanced design standards for fatigue-resistant concrete structures.

9 References

1. Larson, E., et al., *Net-Zero America: Potential Pathways.* Infrastructure, and Impacts, interim report, Princeton University, Princeton, NJ, 2020.
2. Protection, C.D.o.E.a., *Integrated Resources Plan, Pathways to achieve a 100% zero carbonelectric sector by 2040*. 2020.
3. Research, E.E., *Energy Pathways to Deep Decarbonization, A Technical Report of the Massachusetts 2050 Decarbonization Roadmap Study*. 2020.
4. Williams, J.H., et al., *Pathways to deep decarbonization in the United States*. 2015: Energy and Environmental Economics, Incorporated.
5. Fried, S., et al., *Low-Carbon, Bio-Enhancing Concrete Gravity-Based Foundations for Offshore Wind Turbines*. 2022, Tufts University. p. 67.
6. Momber, A.W., A. Krenz, and S. Buchbach, *The corrosion of carbon steel under delaminating repair coatings after long-term marine splash zone exposure.* Materials and Corrosion, 2022. **73**(6): p. 897-902.
7. Momber, A.W., et al., *The corrosion protection performance of repair coatings for offshore wind power constructions after long-term splash zone site exposure.* Materials and Corrosion, 2022. **73**(4): p. 526-539.
8. Delwiche, A. and I. Tavares. *Retrofit strategy using aluminium anodes for the internal sections of windturbine monopiles*. in *NACE CORROSION*. 2017. NACE.
9. Krebs, D.-I.T. *ICCP system for internal protection of monopiles for offshore wind farms*. in *NACE CORROSION*. 2018. NACE.
10. Offshore, A.C.I.C. and M.S.K. Marine Concrete Structures, *SP-337: Offshore and Marine Concrete Structures: Past, Present, and Future.* ACI Symposium Publication. **337**.
11. Bromage, A., A. Tricklebank, and B.J. Magee, *Concrete Towers for Onshore and Offshore Wind Farms*. 2012, The Concrete Centre and Gifford.
12. Lesny, K. and W. Richwien, *Design, construction and installation of support structures for offshore wind energy systems*, in *Wind Energy Systems*. 2011, Elsevier. p. 479-518.
13. Bennett, E. *Cumulative fatigue damage of plain concrete in compression*. in *The Proceedings of the Southampton 1969 Civil Engineering Materials Conference*. 1969.
14. Shah, S.P. and S. Chandra. *Fracture of concrete subjected to cyclic and sustained loading*. in *Journal Proceedings*. 1970.
15. Zhang, B. and K. Wu, *Residual fatigue strength and stiffness of ordinary concrete under bending.* Cement and concrete research, 1997. **27**(1): p. 115-126.
16. Destrebecq, J.-F., *Cyclic and Dynamic Loading Fatigue of Structural Concrete*, in *Mechanical Behavior of Concrete*. 2013. p. 185-224.
17. Sakata, Y. and M. Ohtsu, *Spectral response and acoustic emission of reinforced concrete members under fatigue bending.* 1997.
18. Weigler, H. and D. Klausen, *Ermüdungsverhalten von Beton. Auswirkung einer Beanspruchung im Dauerfestigkeitsbereich.* BETONWERK U FERTIGTEIL-TECH, 1979. **45**(4).
19. Yuyama, S., et al., *Evaluation of fatigue damage in reinforced concrete slab by acoustic emission.* NDT & e International, 2001. **34**(6): p. 381-387.

20. Hümme, J., et al., *Fatigue behaviour of a normal-strength concrete–number of cycles to failure and strain development.* Structural Concrete, 2016. **17**(4): p. 637-645.

21. Zhang, B., D. Phillips, and K. Wu, *Effects of loading frequency and stress reversal on fatigue life of plain concrete.* Magazine of concrete research, 1996. **48**(177): p. 361-375.

22. Saucedo, L., et al., *A probabilistic fatigue model based on the initial distribution to consider frequency effect in plain and fiber reinforced concrete.* International journal of fatigue, 2013. **48**: p. 308-318.

23. Oneschkow, N., *Fatigue behaviour of high-strength concrete with respect to strain and stiffness.* International Journal of Fatigue, 2016. **87**: p. 38-49.

24. Isojeh, B., M. El-Zeghayar, and F.J. Vecchio, *Concrete damage under fatigue loading in uniaxial compression.* ACI Mater. J, 2017. **114**(2): p. 225-235.

25. Viswanath, S., D.A. Kuchma, and J.M. LaFave, *Experimental Investigation of Concrete Fatigue in Axial Compression.* ACI Structural Journal, 2021. **118**(1).

26. Viswanath, S., J.M. LaFave, and D.A. Kuchma, *Concrete compressive strain behavior and magnitudes under uniaxial fatigue loading.* Construction and Building Materials, 2021. **296**: p. 123718.

27. Fan, Z. and Y. Sun, *A study on fatigue behaviors of concrete under uniaxial compression: testing, analysis, and simulation.* Journal of Testing and Evaluation, 2021. **49**(1): p. 160-175.

28. Ahmed, T., E. Burley, and S. Rigden, *The effect of alkali—silica reaction on the fatigue behaviour of plain concrete tested in compression, indirect tension and flexure.* Magazine of Concrete Research, 1999. **51**(6): p. 375-390.

29. Kim, J.-K. and Y.-Y. Kim, *Experimental study of the fatigue behavior of high strength concrete.* Cement and Concrete Research, 1996. **26**(10): p. 1513-1523.

30. Klcriber, F.W., *The effects of air content, water-cement ratio, and aggregate type on the flexural fatigue strength of plain concrete.* Special Publication, 1982. **75**: p. 111-132.

31. Raithby, K. and J. Galloway, *Effects of moisture condition age, and rate of loading on fatigue of plain concrete.* Special Publication, 1974. **41**: p. 15-35.

32. Petkovic, G., et al., *Fatigue of high-strength concrete.* Special Publication, 1990. **121**: p. 505-526.

33. Petkovic, G. and R. Lenschow, *Properties of concrete related to fatigue damage*, in *Fracture and Damage of Concrete and Rock*, H.P. Rossmanith, Editor. 1993, CRC Press: Vienna. p. 217-226.

34. Hsu, T.T., et al. *Microcracking of plain concrete and the shape of the stress-strain curve*. in *Journal Proceedings*. 1963.

35. Sparks, P.R. and J. Menzies, *The effect of rate of loading upon the static and fatigue strengths of plain concrete in compression.* Magazine of concrete research, 1973. **25**(83): p. 73-80.

36. Sparks, P., *The influence of rate of loading and material variability on the fatigue characteristics of concrete.* Special Publication, 1982. **75**: p. 331-342.

37. AWAD, M.E.-M., *Strength and deformation characteristics of plain concrete subjected to high repeated and sustained loads*. 1971: University of Illinois at Urbana-Champaign.

38. Takhar, S., I. Jordan, and B. Gamble, *Fatigue of concrete under lateral confining pressure.* Special Publication, 1974. **41**: p. 59-70.

39. Do, M.-T., O. Chaallal, and P.-C. Aïtcin, *Fatigue behavior of high-performance concrete.* Journal of Materials in civil Engineering, 1993. **5**(1): p. 96-111.

40. Grzybowski, M. and C. Meyer, *Damage accumulation in concrete with and without fiber reinforcement.* Materials Journal, 1993. **90**(6): p. 594-604.

41. Dyduch, K., M. Szerszeń, and J.-F. Destrebecq, *Experimental investigation of the fatigue strength of plain concrete under high compressive loading.* Materials and Structures, 1994. **27**: p. 505-509.

42. Lohaus, L. and S. Anders. *High-cycle Fatigue of "Ultra-High Performance Concrete" and "Grouted Joints" for Offshore Wind Energy Turbines*. in *Wind Energy: Proceedings of the Euromech Colloquium*. 2007. Springer.

43. Bahn, B.Y. and C.-T.T. Hsu, *Stress-strain behavior of concrete under cyclic loading.* Materials Journal, 1998. **95**(2): p. 178-193.

44. Medeiros, A., et al., *Effect of the loading frequency on the compressive fatigue behavior of plain and fiber reinforced concrete.* International Journal of Fatigue, 2015. **70**: p. 342-350.

45. von der Haar, C. and S. Marx, *Development of stiffness and ultrasonic pulse velocity of fatigue loaded concrete.* Structural Concrete, 2016. **17**(4): p. 630-636.

46. Oneschkow, N., *Influence of loading frequency on the fatigue behaviour of highstrength concrete.* Proceedings of the 9th FIB International PhD Sym-posium in Civil Engineering. July 22nd to 25th, 2012: p. 235-240.

47. Li, Q., et al., *Compressive fatigue damage and failure mechanism of fiber reinforced cementitious material with high ductility.* Cement and Concrete Research, 2016. **90**: p. 174-183.

48. Park, Y.J., *Fatigue of concrete under random loadings.* Journal of Structural engineering, 1990. **116**(11): p. 3228-3235.

49. von der Haar, C. and S. Marx, *A strain model for fatigue-loaded concrete.* Structural Concrete, 2018. **19**(2): p. 463-471.

50. Cachim, P.B., J.A. Figueiras, and P.A. Pereira, *Fatigue behavior of fiber-reinforced concrete in compression.* Cement and concrete composites, 2002. **24**(2): p. 211-217.

51. Holmen, J.O., *Fatigue of concrete by constant and variable amplitude loading.* Special Publication, 1982. **75**: p. 71-110.

52. Whaley, C. and A. Neville, *Non-elastic deformation of concrete under cyclic compression.* Magazine of Concrete Research, 1973. **25**(84): p. 145-154.

53. Gao, L. and C.-T.T. Hsu, *Fatigue of concrete under uniaxial compression cyclic loading.* Materials Journal, 1998. **95**(5): p. 575-581.

54. Breitenbücher, R., H. Ibuk, and H. Alawieh. *Influence of cyclic loading on the degradation of mechanical concrete properties*. in *Advances in Construction Materials 2007*. 2007. Springer.

55. Deutscher, M., N.L. Tran, and S. Scheerer, *Experimental investigations on the temperature increase of ultra-high performance concrete under fatigue loading.* Applied Sciences, 2019. **9**(19): p. 4087.

56. béton, C.e.-i.d. and F.I.d.l. Précontrainte, *CEB-FIP model code 1990: Design code*. Vol. 1993. 1993: Thomas Telford Publishing.

57. béton, C.e.-i.d. and F.I.d.l. Précontrainte, *CEB-FIP model code for concrete structures 2010*. 2013: Wiley.

58. Lohaus, L., N. Oneschkow, and M. Wefer, *Design model for the fatigue behaviour of normal-strength, high-strength and ultra-high-strength concrete.* Structural Concrete, 2012. **13**(3): p. 182-192.

59. International, f., *fib Model Code for Concrete Structures (2020)*. 2020: fib.

60. DNV, *DNV-ST-C502; Offshore Concrete Structures.* 2018, Det Norske Veritas: Høvik, Norway.

61. CSN, E., *1-2: 2011 Eurocode 2:"Design of concrete structures-Part 1-1: General rules and rules for buildings"*. 2011, UNMZ.

62. NO.15, J., *Standard specifications for concrete structures "Design"* 2007, Japanese society of civil engineering.

63. CEN, *Eurocode 2: Design of concrete structures - Concrete bridges - Design and*

detailing rules. NEN-EN 1992-2+C1:2011. 2011, Comité Européen de Normalisation. p. 113.

64. Structures", C.C.T.F.f., *Regulations for*

concrete - Bridges - Structural requirements and calculation methods, NEN 6723:2009. 2009. p. 72.

65. Hsu, T.T. *Fatigue of plain concrete*. in *Journal Proceedings*. 1981.

66. Zhang, B., D. Phillips, and D. Green, *Sustained loading effect on the fatigue life of plain concrete.* Magazine of Concrete Research, 1998. **50**(3): p. 263-278.

67. Lantsoght, E., *Fatigue of concrete under compression: database and proposal for high strength concrete.* Report nr. 25.5-14-04, 2014.

68. Lantsoght, E.O., C. van der Veen, and A. de Boer, *Proposal for the fatigue strength of concrete under cycles of compression.* Construction and Building Materials, 2016. **107**: p. 138-156.

69. Reinhardt, H.W., H.A. Cornelissen, and D.A. Hordijk, *Tensile tests and failure analysis of concrete.* Journal of structural engineering, 1986. **112**(11): p. 2462-2477.

70. Tepfers, R. and T. Kutti. *Fatigue strength of plain, ordinary, and lightweight concrete*. in *Journal Proceedings*. 1979.

71. Lenschow, R. *Concrete Platforms in the North Sea and Some Related Research on Fatigue*. in *Ocean Space Utilization'85: Proceedings of the International Symposium Nihon University, Tokyo, Japan, June 1985 Volume 2*. 1985. Springer.

72. Siemes, A., *Miner's rule with respect to plain concrete variable amplitude tests.* Special Publication, 1982. **75**: p. 343-372.

73. Becks, H. and M. Classen, *Mode II behavior of high-strength concrete under monotonic, cyclic and fatigue loading.* Materials, 2021. **14**(24): p. 7675.

74. Becks, H., et al. *Experimental and Numerical Characterization of High-Strength Concrete Under Monotonic and Fatigue Mode II Loading with Active Control of Lateral Compression*. in *International Symposium of the International Federation for Structural Concrete*. 2023. Springer.

75. Lee, D.-Y., F.W. Klaiber, and J.W. Coleman, *Fatigue behavior of air-entrained concrete.* Transportation Research Record, 1978(671).

76. Klaiber, F., T. Thomas, and D. Lee, *Fatigue behavior of air-entrained concrete: phase II*. 1979.

77. Ramakrishnan, V. and T.B.V. Malhotra, *Fatigue strength and endurance limit of lightweight concrete.* Special Publication, 1993. **136**: p. 397-420.

78. Hordijk, D., G. Wolsink, and J. De Vries, *Fracture and fatigue behaviour of a high strength limestone concrete as compared to gravel concrete.* HERON-ENGLISH EDITION-, 1995. **40**: p. 125-146.

79. Gray, W.H., J.F. McLaughlin, and J.D. Antrim. *Fatigue properties of lightweight aggregate concrete*. in *Journal Proceedings*. 1961.

80. Scheiden, T. and N. Oneschkow, *Influence of coarse aggregate type on the damage mechanism in high-strength concrete under compressive fatigue loading.* Structural Concrete, 2019. **20**(4): p. 1212-1219.

81. You, F., S. Luo, and J. Zheng, *Experimental study on residual compressive strength of recycled aggregate concrete under fatigue loading.* Frontiers in Materials, 2022. **9**: p. 817103.

82. Grassl, P., H.S. Wong, and N.R. Buenfeld, *Influence of aggregate size and volume fraction on shrinkage induced micro-cracking of concrete and mortar.* Cement and concrete research, 2010. **40**(1): p. 85-93.

83. Akçaoğlu, T., *Determining aggregate size & shape effect on concrete microcracking under compression by means of a degree of reversibility method.* Construction and Building Materials, 2017. **143**: p. 376-386.

84. Sinaie, S., et al., *Effect of size on the response of cylindrical concrete samples under cyclic loading.* Construction and Building Materials, 2015. **84**: p. 399-408.

85. Andersen, M.S. and C. Ertel. *Concrete compression fatigue-Design rules and focus areas for testing*. in *International Symposium on Multiscale Experimental Mechanics: Multiscale Fatigue*. 2017.

86. Oneschkow, N., J. Huemme, and L. Lohaus, *Compressive fatigue behaviour of high-strength concrete in a dry and wet environment.* Construction and Building Materials, 2020. **262**: p. 119700.

87. Basaldella, M., N. Oneschkow, and L. Lohaus, *Influence of the specimen production and preparation on the compressive strength and the fatigue resistance of HPC and UHPC.* Materials and Structures, 2021. **54**: p. 1-14.

88. Reineck, K.-H., et al., *Shear database for reinforced concrete members without shear reinforcement.* Structural Journal, 2003. **100**(2): p. 240-249.

89. Issa, S., et al., *Specimen and Aggregate Size Effect on Concrete Compressive Strength.* Cement, Concrete and Aggregates, 2000. **22**(2): p. 103-115.

90. Mena-Alonso, Á., et al., *Size effect on the flexural fatigue behavior of high-strength plain and fiber-reinforced concrete.* Construction and Building Materials, 2024. **411**: p. 134424.

91. Daneshfar, M., et al., *Experimental Model for Study of Thickness Effect on Flexural Fatigue Life of Macro-Synthetic-Fiber-Reinforced Concretes.* Buildings, 2023. **13**(3): p. 642.

92. Wan-Wendner, L., R. Wan-Wendner, and G. Cusatis, *Age-dependent size effect and fracture characteristics of ultra-high performance concrete.* Cement and Concrete Composites, 2018. **85**: p. 67-82.

93. Waagaard, K. *Fatigue of offshore concrete structures-design and experimental investigations*. in *Offshore Technology Conference*. 1977. OTC.

94. Waagaard, K. *Design Verification of Offshore Concrete Structures*. in *The Fourth International Offshore and Polar Engineering Conference*. 1994.

95. Waagaard, K., *Fatigue strength evaluation of offshore concrete structures.* Special Publication, 1982. **75**: p. 373-397.

96. Tomann, C. and N. Oneschkow, *Influence of moisture content in the microstructure on the fatigue deterioration of high-strength concrete.* Structural Concrete, 2019. **20**(4): p. 1204-1211.

97. Ali, M.A., et al., *Influence of the load frequency and moisture content on fatigue deterioration of high-strength concrete.* ce/papers, 2023. **6**(6): p. 849-855.

98. Wu, L., et al., *Peridynamic modeling for impact failure of wet concrete considering the influence of saturation.* International Journal of Damage Mechanics, 2022. **31**(9): p. 1448-1474.

99. Kesler, C.E. *Effect of speed of testing on flexural fatigue strength of plain concrete*. in *Proceedings, Highway Research Board*. 1953.

100. Murdock, J.W., *A critical review of research on fatigue of plain concrete.* University of Illinois. Engineering Experiment Station. Bulletin; no. 475, 1965.

101. Félix, E.F., R. Carrazedo, and E. Possan, *Fatigue life of concrete: Experimental study on the influence of loading conditions and material strength.* Revista ALCONPAT, 2022. **12**(1): p. 1-15.

102. Keerthana, K. and J.C. Kishen, *Micromechanical effects of loading frequency on fatigue fracture in concrete.* Journal of Engineering Mechanics, 2021. **147**(12): p. 04021111.

103. Lenschow, R., *Long term random dynamic loading of concrete structures.* Matériaux et Construction, 1980. **13**: p. 274-278.

104. Karna, S., P. Deb, and S. Mondal, *Consequences of fatigue in concrete structures: a state-of-the-art review and possible remedial measures.* Innovative Infrastructure Solutions, 2024. **9**(8): p. 320.

105. McCall, J.T. *Probability of fatigue failure of plain concrete*. in *Journal Proceedings*. 1958.

106. Murdock, J.W. and C.E. Kesler, *Effect of range of stress on fatigue strength of plain concrete beams.* TAM R 130, 1958.

107. Johnston, C.D. and R.W. Zemp, *Flexural fatigue performance of steel fiber reinforced concrete--influence of fiber content, aspect ratio, and type.* Materials Journal, 1991. **88**(4): p. 374-383.

108. Jun, Z. and H. Stang, *Fatigue performance in flexure of fiber reinforced concrete.* Materials Journal, 1998. **95**(1): p. 58-67.

109. Lee, M. and B. Barr, *An overview of the fatigue behaviour of plain and fibre reinforced concrete.* Cement and Concrete Composites, 2004. **26**(4): p. 299-305.

110. Reineck, K.-H., et al., *ACI-DAfStb Databases for Shear Tests on Slender Reinforced Concrete Beams with Stirrups.* ACI Structural Journal, 2014. **111**(5).

111. Kuchma, D.A., et al., *Development of the One-Way Shear Design Provisions of ACI 318-19 for Reinforced Concrete.* ACI Structural Journal, 2019. **116**(4): p. 285-296.

112. Seleemah, A.A., *A neural network model for predicting maximum shear capacity of concrete beams without transverse reinforcement.* Canadian Journal of Civil Engineering, 2005. **32**(4): p. 644-657.

113. Institute, A.C., *Building Code Requirements for Structural Concrete (ACI 318-19): An ACI Standard ; Commentary on Building Code Requirements for Structural Concrete (ACI 318R-19)*. 2019: American Concrete Institute.

114. ACI Committee. *Building code requirements for structural concrete (ACI 318-08) and commentary*. 2008. American Concrete Institute.

115. Son, J. and S. Yang, *A new approach to machine learning model development for prediction of concrete fatigue life under uniaxial compression.* Applied Sciences, 2022. **12**(19): p. 9766.

116. Lloyd, D.N.V.G., *Fatigue design of offshore steel structures*. 2019: Recommended Practice. p. 285.

117. DNVGL, *DNVGL-ST-C502: Offshore concrete structures*. 2018, Det Norske Veritas: Norway.

118. Béton, C.E.-I.d., *CEB-FIP model code 1990: Design code*. 1993: Thomas Telford Publishing.

119. Du Béton, F.I., *fib model code for concrete structures 2010*. 2013: Wiley-vch Verlag Gmbh.

120. Tue, N.V. and S. Mucha, *Ermüdungsfestigkeit von hochfestem Beton unter Druckbeanspruchung.* Bautechnik, 2006. **83**(7): p. 497-504.

121. Klausen, D., *Strength and damage of concrete by frequently repeated stress*. 1978, Technische Hochschule Darmstadt Darmstadt, Germany.

122. Le, T.T., et al., *Hardened properties of high-performance printing concrete.* Cement and Concrete Research, 2012. **42**(3): p. 558-566.

123. Hou, S., et al., *A review of 3D printed concrete: Performance requirements, testing measurements and mix design.* Construction and Building Materials, 2021. **273**: p. 121745.

124. Grünberg, J. and J. Göhlmann, *Concrete structures for wind turbines*. 2013: John Wiley & Sons.

125. LaNier, M.W., *LWST Phase I project conceptual design study: Evaluation of design and construction approaches for economical hybrid steel/concrete wind turbine towers; June 28, 2002--July 31, 2004*. 2005, National Renewable Energy Lab.(NREL), Golden, CO (United States).

126. Partovi-Mehr, N., et al., *Fatigue Analysis of a Jacket-Supported Offshore Wind Turbine at Block Island Wind Farm.* Sensors, 2024. **24**(10): p. 3009.

127. Shid-Moosavi, S., et al., *Modeling and experimentally-driven sensitivity analysis of wake-induced power loss in offshore wind farms: Insights from Block Island Wind Farm.* Renewable Energy, 2024: p. 122126.

128. Siddika, A., et al., *3D-printed concrete: Applications, performance, and challenges.* Journal of Sustainable Cement-Based Materials, 2020. **9**(3): p. 127-164.

129. Diggs-McGee, B.N., et al., *Print time vs. elapsed time: A temporal analysis of a continuous printing operation for additive constructed concrete.* Additive Manufacturing, 2019. **28**: p. 205-214.

130. Rodriguez, F.B., et al. *Evaluation of Durability of 3D-Printed Cementitious Materials for Potential Applications in Structures Exposed to Marine Environments*. in *RILEM International Conference on Concrete and Digital Fabrication*. 2022. Springer.

131. Nodehi, M., et al., *Durability properties of 3D printed concrete (3DPC).* Automation in Construction, 2022. **142**: p. 104479.

132. Pham, L., P. Tran, and J. Sanjayan, *Steel fibres reinforced 3D printed concrete: Influence of fibre sizes on mechanical performance.* Construction and Building Materials, 2020. **250**: p. 118785.

133. Marchment, T. and J. Sanjayan, *Mesh reinforcing method for 3D Concrete Printing.* Automation in Construction, 2020. **109**: p. 102992.

134. Wolfs, R., F. Bos, and T. Salet, *Hardened properties of 3D printed concrete: The influence of process parameters on interlayer adhesion.* Cement and Concrete Research, 2019. **119**: p. 132-140.

135. Rahul, A., et al., *Mechanical characterization of 3D printable concrete.* Construction and Building Materials, 2019. **227**: p. 116710.

136. Abubakar Ali, M., et al., *Influence of Moisture Content and Wet Environment on the Fatigue Behaviour of High-Strength Concrete.* Materials, 2022. **15**(3): p. 1025.

137. Miner, M.A., *Cumulative damage in fatigue.* 1945.

138. Kuchma, D.A., et al. *HIGH CYCLE FATIGUE BEHAVIOR OF REINFORCED CONCRETE*. in *6th fib International Congress on Concrete Innovation for Sustainability, 2022*. 2022. fib. The International Federation for Structural Concrete.

139. Birkner, D., R.E.B. Gutiérrez, and S. Marx, *Comparison of stiffness degradation in fatigue-loaded concrete cylinders and large-scale beams.* Engineering Structures, 2024. **302**: p. 117360.

140. Kono S, H.H., Mori K, Ichioka Y, Sakashita M, Watanabe F. *Low cycle fatigue characteristics of high strength concrete*. in *Eighth International Symposium on Utilization of High-Strength and High-Performance Concrete Vol. 1*. 2008.

141. Papa, E., *A damage model for concrete subjected to fatigue loading.* European journal of mechanics. A. Solids, 1993. **12**(3): p. 429-440.

142. Rüsch, H., *Researches toward a general flexural theory for structural concrete.* Journal of the American Concrete Institute, 1960. **57**(1): p. 1-28.

143. Rostásy, F., W. Alda, and K. Teichen, *Kriechen und Schwingkriechen von Leichtbeton.* Bauingenieur, 1975. **50**(12).

144. Neville, A.M., *Properties of concrete [by] AM Neville*. 1973: Wiley.

145. Uomoto, T., et al., *Standard Specifications for Concrete Structures-2007 by Japan Society of Civil Engineers.* Concrete Journal, 2008. **46**(7): p. 3-14.

146. BS-EN, *Eurocode 2: Design of concrete structures*. 1992.

147. International, A., *ASTM C39/C39M-21: Standard Test Method for Compressive Strength of Cylindrical Concrete Specimens*. 2021, ASTM International: West Conshohocken, PA, USA.

148. Zhang, Q. and L. Wang, *Investigation of stress level on fatigue performance of plain concrete based on energy dissipation method.* Construction and Building Materials, 2021. **269**: p. 121287.

149. Abambres, M. and E.O. Lantsoght, *ANN-based fatigue strength of concrete under compression.* Materials, 2019. **12**(22): p. 3787.

150. Li, M. and L. Wang, *Feature fatigue analysis in product development using Bayesian networks.* Expert Systems with Applications, 2011. **38**(8): p. 10631-10637.

151. Jung, J., et al. *Analysis of damage in specimen under cyclic uniaxial loading test by X-ray CT method*. in *ISRM International Symposium-Asian Rock Mechanics Symposium*. 2014. ISRM.

152. Sharma, R., et al. *Micro-mechanisms of concrete failure under cyclic compression: X-ray tomographic in-situ observations*. in *Proceedings of the 9th International Conference on Fracture Mechanics of Concrete and Concrete Structures (FraMCoS-9), Berkeley, CA, USA*. 2016.

153. Obara, Y., et al., *Evaluation of micro-damage of concrete specimens under cyclic uniaxial loading by X-ray CT method.* Journal of Advanced Concrete Technology, 2016. **14**(8): p. 433-443.

154. Vicente, M.A., et al., *CT-Scan study of crack patterns of fiber-reinforced concrete loaded monotonically and under low-cycle fatigue.* International Journal of Fatigue, 2018. **114**: p. 138-147.

155. Mínguez, J., et al., *Plain and fiber-reinforced concrete subjected to cyclic compressive loading: study of the mechanical response and correlations with microstructure using CT scanning.* Applied Sciences, 2019. **9**(15): p. 3030.